Towards Scalable Fabrication of Plasmonic Devices via Nanoimprint Lithography (NIL)

by

Muhammad Faris Shahin Shahidan

ORCID:0000-0002-7807-4662

A thesis submitted in total fulfillment for the
degree of Doctor of Philosophy

in the
Faculty of Science
School of Physics
THE UNIVERSITY OF MELBOURNE

July 2021

THE UNIVERSITY OF MELBOURNE

Abstract

Faculty of Science
School of Physics

Doctor of Philosophy

by Muhammad Faris Shahin Shahidan
ORCID:0000-0002-7807-4662

Advances in theoretical and computational techniques for advancing concepts in nanophotonics along with major development in nanofabrication technologies has enable the realization of nanoscale optical device with unprecedented ability to control light such as plasmonic metasurface. Fabrication of plasmonic devices, however, has long been relying on conventional lithography technique such as electron beam lithography (EBL), focused ion beam (FIB) milling and photolithography (PL). While these lithography techniques have enable construction of sub-wavelengths nanostructures, their reliance on the interaction between charged particles or light beam with polymer resist during pattern writing process require intricate control systems and usually require high operating and maintenance cost. In fact, for FIB and EBL, the writing time can be very slow depending on the pattern area. These approaches, therefore, are unsuitable for industrial scale production thus hindering commercial uptake of metasurfaces. Therefore, there is a need for an alternative low-cost, high-throughput nano-manufacturing approach to overcome the bottleneck in conventional lithography methods.

With this motivation in mind, this thesis focused on utilizing the nanoimprint lithography (NIL) technique for fabrication of the designated plasmonic device. NIL uses pattern transfer approach whereby a predefined pattern on a mould is used to replicate the pattern onto another surface. NIL offers scalability and high-throughput large area manufacturing of nanostructures. In this thesis, the versatility and capability of NIL for producing plasmonic device, particularly plasmonic colours, with a potential of scalability is investigated. This includes the investigation of the dynamic flow of the resist during the nanoimprinting process through various process parameters. With this information, it will be shown that NIL is capable of producing multi height, grayscale-like structures through a careful control of the flow of the resist, without relying on control of charged particle or light beams.

This novel technique was then utilised as a method to print the plasmonic colouration device, with ability of controlling the hue and saturation of the resulting colours via tuning of the vertical gap size of the structure. Additionally, an investigation of multispectral, polarisation-selective iridescence plasmonic colour will also be shown in this thesis. This was achieved via the elongation of the spatial dimension of plasmonic structure which results in multiple resonances in both visible and infrared region of the spectrum. Such multispectral system will be very useful especially for optical security device. Finally, a novel plasmonic colour designed to preserve the vividness of the resulting colour under unpolarised ambient lighting condition will be demonstrated in this thesis. This involves production of polarization-independent plasmonic structure featuring symmetric cross structures. It will be shown that this device produced excellent colours with preserved hue and vividness, regardless of polarization state of light.

Declaration of Authorship

I, Muhammad Faris Shahin Shahidan, declare that this thesis titled, 'Towards Scalable Fabrication of Plasmonic Devices via Nanoimprint Lithography (NIL)' and the work presented in it are my own. I confirm that:

- The thesis comprises only my original work towards the degree of Doctor of Philosophy except where indicated in the preface;
- due acknowledgement has been made in the text to all other material used; and
- the thesis is fewer than the maximum word limit in length, exclusive of tables, maps, bibliographies and appendices as approved by the Research Higher Degrees Committee.

Signed: ______________________________________

Date: ______________________________________

Preface

This thesis contains unpublished original work by the author except where acknowledgements and references are made to previous work. Some of the figures used in this thesis have been taken from other works. In these instances the appropriate source has been cited at the end of the figure caption to acknowledge the source and permission obtained from the publisher for reproduction.

Dr Jingchao Song must be recognised for the fabrication of the Si moulds used throughout this research at the Melbourne Centre for Nanofabrication (MCN). The Si moulds were used for sample fabrication via nanoimprint lithography (NIL) which were performed by me using facilities in the Nanofabrication Lab, Swinburne University of Technology. Nanoimprinted samples were coated using thin film deposition (metal and dielectric) with Dr Song's assistance. All these samples were presented in Chapter 4, 5, 7 and 8.

Dr Timothy James and Dr Jasper Cadusch gave expert advice regarding plasmonic colours and NIL fabrication techniques during my various process development stages. Heyou Zhang assisted with atomic force microscopy (AFM) measurement and training during early NIL parameter optimisation. Dr Nicholas Kirkwood synthesised the quantum dots used in Chapter 8.

Experimental advice in regard to device development and optical characterisation was given by Dr Timothy James, Dr Jingchao Song, Dr Jasper Cadusch, Dr Evgeniy Panchenko, Prof Paul Mulvaney, and Prof Ann Roberts. Over the course of this work several publications and presentation were based on the work presented herein. They are listed below for reference.

The PhD candidature of the author was supported with scholarships from The University of Melbourne as a Melbourne Research Scholarships (MRS) and projects cost provided by the Australian Research Council through the Linkage Projects Scheme (LP160100054).

List Of Publications

Publication arising from this thesis

M. F. S. Shahidan, J. Song, T. D. James, and A. Roberts, “Multilevel nanoimprint lithography with a binary mould for plasmonic colour printing,” *Nanoscale Advances*, vol. 2, no. 5, pp. 2177–2184, 2020, doi: 10.1039/d0na00038h.

M. F. S. Shahidan, J. Song, T. D. James, P. Mulvaney, and A. Roberts, “Scalable and consistent fabrication of plasmonic colors via nanoimprint lithography,” *SPIE Micro + Nano Materials, Devices, and Applications 2019*, Dec. 2019, doi: 10.1117/12.2539079.

M. F. S. Shahidan, J. Song, T. D. James, and A. Roberts, ”Polarisation-selective, Multispectral Iridescent Plasmonic Pixels,” *In Preparation*

M. F. S. Shahidan, J. Song, T. D. James, and A. Roberts, ”Polarisation Independent Plasmonic Colour with Preserved Vividness Under Ambient Condition,” *In Preparation*

Other Publications

Zhang, H., Liu, Y., **Shahidan, M. F. S.**, Kinnear, C., Maasoumi, F., Cadusch, J., Akinoglu, E. M., James, T. D., Widmer-Cooper, A., Roberts, A., Mulvaney, P., Direct Assembly of Vertically Oriented, Gold Nanorod Arrays. *Adv. Funct. Mater.* 2020, 2006753. https://doi.org/10.1002/adfm.202006753

Acknowledgements

First and foremost, I would like to express my sincere gratitude to my supervisor, Professor Ann Roberts, who without her continuous guidance, advice and support, I will never have a courage to complete this thesis. I should also thank Professor Roberts for her support when my research was impacted by the pandemic. Special thanks to Dr Jingchao Song who played a very important role during the progress of this thesis. His assistance in fabrication of the Si mould used for nanoimprinting and deposition of thin films have helped to establish plasmonic devices presented in this thesis.

I would like to also thank Dr Timothy James for fruitful discussions concerning plasmonic colouration, nanoimprinting, characterisation techniques which had help in the development of this thesis. I also would like to acknowledge the other members of my supervisory panel, Prof Paul Mulvaney and Dr Christian Reichardt for their support throughout my PhD. Advice from Dr Jasper Cadusch regarding nanoimprinting and quantum dots measurements, and from Dr Evgeniy Panchenko regarding nanofabrication and optical characterisations, were very helpful to the author.

To my dearest friends Lukas Wesemann, Heyou Zhang, Arun Ashokan, thanks for the laughs, miscellaneous rants and advices. Thanks to Lukas who had assisted in fabricating my sample, together with Dr Song, when I had no access to NIL facilities due to the pandemic. Heyou patiently trained me using AFM, lent me various pieces of equipment and gave me useful insights into academic writing. Both Heyou and Arun have provided me handy advice in dealing with chemicals in their laboratory in Chemistry. Big thanks to members of the ARC Centre of Excellence for Exciton Science for welcoming me to their lab in Chemistry and were very helpful during time spent in the lab. Shout out to Niken and Jon who make my office more lively. I should also thank Niken who kindly help me to evaporate metal on the last samples. I want to also acknowledge Dr Tomas Katkus from Swinburne University who arranged access to and provided advice about the NIL facility at the Nanofabrication Lab.

This thesis is dedicated to my family, especially my mum and dad. Without their endless support and prayers, I would not have been able to undertake this project. Special thanks to my sisters and brother, Nabila, Almas and Ash who always lend their hands and ears. To my loving wife, Shima, thanks for always there for me and for being patient and passionate every time I threw a tantrum. I don't think I would continue doing what I'm doing without her motivational and emotional support.

Contents

List of Figures

List of Tables

Chapter 1

Introduction

Current advances in optics are aimed at developing new devices and materials to improve light generation, manipulation and detection. Historically, technologies utilised conventional materials such as glass to control light based on basic optical phenomena including reflection, refraction, diffraction and interference. Such devices, however, have limitations as they depend inherently on the path length of the light beam as it propagates through the materials [1] which consequently requires relatively bulky devices to manipulate light. Such space-consuming shapes are impractical in modern electronic and photonic technologies which are pushing towards optimal device miniaturisation.

The parallel development of theoretical and computational techniques for advancing concepts in nanophotonics alongside massive progress in nanofabrication technologies has paved the way to a new paradigm of flat optics where devices with planar configurations can be used to control light. Many nanofabrication techniques have been developed utilising either bottom-up or top-down approaches to accommodate the production of structures with nanoscale geometries. With state-of-the-art lithography techniques, not only do we have more degrees of freedom to design subwavelength structures of various geometries, but we also have the capacity to create a new category of material termed optical 'meta-materials' or 'meta-surfaces', which are artificial electromagnetic materials that comprise arrays of nanostructures as building blocks (or in the case of metasurfaces, their two-dimensional analogues) [1, 2] .

The concept of a metamaterial emerged from Veselago's discussion of the optical properties of a hypothetical negative refractive index material [3]. Unlike conventional materials with optical properties determined solely by their constituent atoms and molecules, 'metamaterials' have properties that are tailored by artificially modifying the geometry and, hence, the resonances of the material unit cell. Optical metamaterials thus enable control of the amplitude, phase and polarisation of scattered light arising from resonances of subwavelength structures upon illumination with light [4]. In the optical regime, however, fabricating three-dimensional (3D) metamaterials requires complex fabrication techniques with nanoscale precision which has become the roadblock that has limited practical applications of metamaterials. Even with existing state-of-the-art nanofabrication technologies, the complexity of 3D geometries is an enormous engineering challenge [5]. Therefore, although initially the focus was on 3D materials, the fabrication challenges and a growing awareness that a two dimensional arrangement of optical resonators could replicate many of the interesting properties envisaged for metamaterials, has led to a shift of interest toward ‘metasurfaces’. This strategy can reduce the size of an optical component such as a lens by many orders of magnitude allowing massive miniaturization of devices.

Metasurfaces, the two-dimensional counterparts of metamaterials, are essentially an array of optical nanoantennas, which can be composed of metals, to create plasmonic devices, or dielectric materials. The focus of this work is mainly on plasmonic devices. Plasmonic metasurfaces comprise an arrangement of nanoscale metallic films and particles (also known as ‘meta-atoms’ or ‘optical antennas’) on a planar surface. Figure 1.1 shows some examples of plasmonic metasurfaces comprising various shapes and dimensions of nanoantennas. These are resonant systems that have the capacity to manipulate light by controlling the amplitude, phase, polarisation and direction of scattered light. From a fabrication point of view, planar metasurfaces require less complex fabrication than those of 3D structures. Metasurfaces have a similar tailoring flexibility as metamaterials and can achieve specific optical properties and functionalities comparable to those of metamaterials but with a reduced size, weight and fabrication time. Metasurfaces usually have unit cells with subwavelength dimensions, therefore nanofabrication techniques with a resolution of sub-100 nm is required.

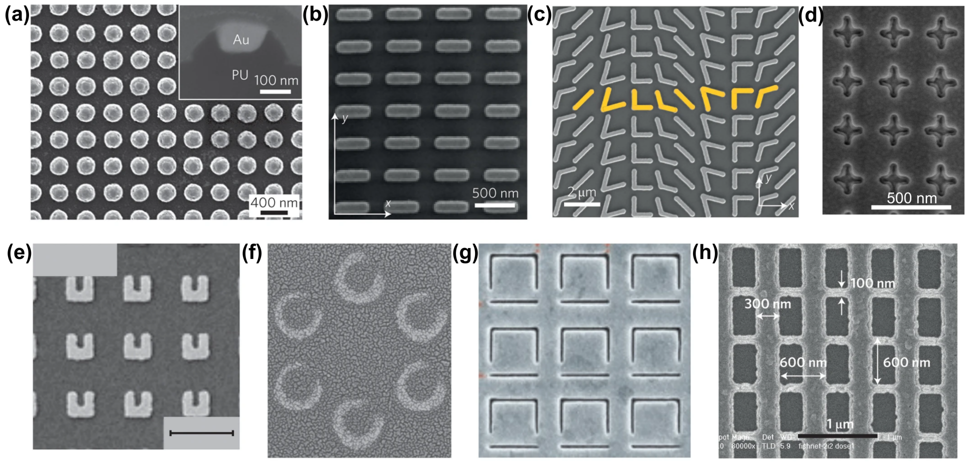

Figure 1.1: Examples of plasmonic metasurface comprised of 'meta-atoms' of various shapes and dimensions. (a) Nanodisks [6], (b) Nanorod antennas [7], (c) V-shaped antennas at different orientations and opening angles [8], (d) cross-shaped structures, (e) U-shape split ring resonators [9], (f) Crescent shape split ring resonators [10],(g) Inverse asymmetric split-ring resonators [11], (h) Double fishnet structures [12].

1.1 Focus of This Thesis

The thesis has two main themes:

1. **Scalable Nanofabrication**

   Conventional clean-room lithography techniques such as electron beam lithography (EBL) and focussed ion beam milling (FIB) have been used to produce metasurfaces and nanoantenna arrays with various types of structural configurations as shown in Figure 1.1, owing to their nanoscale resolution and precision. These direct-write lithography techniques, however, suffer from low-throughput processing (for EBL and FIB), high-cost and require high-end tools, which are unsuitable for industrial scale production thus hindering commercial uptake of metasurfaces [13, 14]. Additionally, these approaches also rely on intricate control of dosage of charged particles and light beams. To address the aforementioned issues, an inexpensive, simple, high-throughput technique is highly desirable for production of plasmonic devices over a large areas. With this motivation in mind, the work presented here focuses on utilising a low-cost pattern transfer lithography technique called Nanoimprint Lithography (NIL) and investigates its versatility and capability for producing various plasmonic devices with a potential for scalability.

2. **Production and Design of Plasmonic Devices**

   In addition to the investigation of the fabrication technique, this thesis is also focussed on the production of plasmonic metasurfaces with specific properties. The main device of interest here is one that produces a characteristic structural colour simply referred to as plasmonic colour. Metal-insulator-metal (MIM) plasmonic metasurfaces, in particular, that comprise metallic nanoantennas of various geometries elevated above their complementary perforated Babinet film, can behave as a near-perfect plasmonic absorber by exploiting the plasmonic coupling between the surface plasmons generated on the metal particles and on the film to produce plasmonics-based structural colouration [15, 16]. Plasmonic metasurfaces have the ability to generate a wide range of vivid colours by varying the spatial geometry and orientation of the constituent nanostructures. The advantages of plasmonic colouration are multifold including the fact that they can be tailored to be diffractive or non-diffractive, are resistant to photobleaching, are mechanically robust, have an ultra-thin thickness and nanoscale resolution, and also have the potential for polarisation sensitivity or iridescence i.e have a tailorable colour variation with angle of incidence. Additionally, plasmonic colour can be realised by using a restricted set of materials i.e. metals such as gold (Au), silver (Ag) or aluminum (Al) and dielectric spacers and coatings such as polymer or silica layer, which are non-toxic and potentially recyclable. Plasmonic surfaces can also be designed to have multispectral features that expand the potential functionality. In contrast, conventional colourants such as dyes and inks are often chemically unstable and suffer from photobleaching leading to the vividness of the colours deteriorating over time. Traditional dyes also contain potentially harmful chemicals that contribute to pollution and threaten the environment. In terms of design, MIM plasmonic colour devices have a fairly simple configuration amenable to nanoimprinting and thus have potential for mass fabrication. In this work, the focus is on producing nanostructures of various shapes, by utilising the NIL technique, for producing surface colouration. High-density optical data storage, tunable colour filters, highly sensitive colorimetric sensors, advanced optical security devices, are some of the anticipated technological applications that will benefit from the large scale fabrication of plasmonic-based colouration.

1.2 Thesis Outcomes

The main aim of this thesis is to progress development of fabrication approaches to produce plasmonic devices exhibiting surface colouration at large scale by using nanoimprint lithography (NIL) and subsequent metallization process. Prior to a large area fabrication attempt, investigation of the NIL process is required to determine the capability of the fabrication method to produce specific nanostructures. This involves the investigation and understanding of the dynamic flow of the resist during the nanoimprinting process which is primarily governed by: (i) the NIL parameters, (ii) the chemical and physical properties of the resist and (iii) the geometry and other properties of the mould and the substrate. In this thesis, these aspects of NIL will be presented and thoroughly discussed. It will be shown that NIL is a versatile technique that is capable of producing not only two-dimensional structures, but also structures of various heights (three-dimensional) – a feature that resembles multilevel, grayscale structures via harnessing dynamics of the resist. This novel multilevel NIL technique is performed through a careful management of the aspects mentioned above. With proper understanding and control of the dynamic flow of the resist, a large area production of plasmonic colour (on the scale of a centimeter) has also been demonstrated.

Since this thesis focuses on plasmonic colouration using a MIM configuration, where the generated colour is highly sensitive to the vertical dimensions of the structure, the production of multi-height structures from the multilevel NIL process was adapted for controlling the hue and saturation of the resulting colours, in addition to the investigation of the dynamics of resist flow. Further to utilising the control of the vertical dimension, the transverse geometry of the structure can be tailored to produce plasmonic colouration with specific responses to the polarisation state of incident light and viewing angle. In this thesis, an investigation of polarisation-selective, non-diffractive iridescent plasmonic colour is demonstrated. It is also shown that this device can be tuned to exhibit multispectral resonances including in the near infrared (NIR) region of the spectrum in addition to its polarisation selective iridescence under visible light. This type of optical response is highly relevant as an optical security device with both overt and covert features. It should also be noted here that due to unavoidable reasons[1], this device was not able to be fabricated and the discussion presented here regarding this particular device is based on simulation results. Although the fabrication of this device was halted, it was designed with mass-fabrication in mind and other results presented in the thesis demonstrate that the structure is amenable for NIL.

While polarisation tunable plasmonic colour is preferable for certain applications, it is however, undesirable in many situations that require fixed colouration under ambient lighting conditions. Polarisation dependent plasmonic colour suffers from crosstalk when devices are used with unpolarised ambient light leading to colour desaturation or even a change in hue. In this thesis, a novel plasmonic colour device designed to preserve the vividness of the resulting colour in unpolarised ambient lighting conditions is also demonstrated. Finally, the demonstration of centimeter scale fabrication using NIL of plasmonic colour device that can be either dependent or independent of the polarisation

---

[1] Access to the NIL tool used in this thesis was unavailable during the final 10 months of candidature due to COVID-19 related restrictions introduced. Also, due to a major EBL failure requiring a substantial amount of time to be rectified and access to engineers who were unavailable as a result of Australia's border closure, fabrication of a viable proof-of-concept sample was unsuccessful.

state of incident light will be presented. The final chapter of this thesis presents potential future work building on nanoimprinted plasmonic colour as a colourimetric refractive index sensor. Furthermore, it will be shown that NIL can also be used to produce a plasmonic device comprising arrays of nanocavities coupled to quantum emitters to control the emission properties of the emitters such as directionality and polarisation states. Although the work completed was only a preliminary investigation, it led to the design of an experiment that would permit collimation of the emitted radiation.

1.2.1 Summary of Thesis Outcomes

In summary, to progress towards the goals of this thesis for producing plasmonic colouration devices with specific spectral and colour response using NIL process, the specific outcomes of this thesis are summarized below:

1. Development of novel multilevel NIL to produce three-dimensional structures via harnessing the nanofluidics dynamics of the resist using only a binary mould.
2. Demonstration of the utilisation of multilevel NIL as a method for printing plasmonic colouration devices with gap-tunable hue and saturation.
3. Development of a novel multispectral, polarisation selective, iridescent plasmonic pixels with an IR signature for potential optical security features.
4. Development and fabrication of a novel polarisation independent plasmonic colour device comprising symmetric cross-shaped structure to preserve the vividness of the colours under ambient light.
5. Demonstration of the scalable production of plasmonic colouration device using NIL.
6. Development of a process sheet for conventional and multilevel NIL process for future reference.

1.3 Thesis Outline

Chapter 2 presents a review of relevant literature and briefly discusses background relevant to the thesis. Chapter 3 provides a general discussion of the fabrication methods used to produce the devices, characterisation techniques and the numerical methods used to simulate the electromagnetic behaviour of the plasmonic structures investigated here. Chapter 4 provides a detailed introduction to the nanoimprint lithography (NIL) process including thermal and UV-assisted NIL, and optimisation for the research presented in this thesis. Chapter 5 presents original research concerning the use of NIL as a printing tool to produce plasmonic colour with the capacity to tune the resulting colour via careful control of the vertical dimension of the fabricated nanostructure. Chapter 6 presents a design for an optical security device comprising a novel iridescent multi-spectral plasmonic colouration device in the visible light while exhibiting a signature in the IR region. Chapter 7 discusses the production of plasmonic colours with the aim of preserving the hue and vividness of the output colour under ambient light. Finally, the outlook for future research and a summary of the research findings discussed in this thesis are presented in Chapter 8 and Chapter 9 respectively.

Chapter 2

Literature Review and Background

This chapter introduces the concept of structural colour, both naturally occurring and man made, and fabrication approaches to create the nanostructures required for producing surface colouration. The first section includes a brief discussion of the origin of structural colouration occurring in nature with examples from various organisms. This section also provides an in-depth discussion of plasmonic-based structural colouration involving two major configurations: (i) the insulator-metal-insulator (IMI) and (ii) the metal-insulator-metal (MIM) approaches. A discussion of the various ways in which colour can be quantified follows. This includes a brief explanation of basic colourimetry, colour mapping, colour models and the correlation between hue, saturation and brightness (HSV) of colours, and spectral properties. The final section pertains to a review of some of the techniques previously demonstrated for producing plasmonic structures. This also includes a discussion and comparison of relevant scalable fabrication approaches including nanoimprint lithography.

2.1 Structural Colourations

In today's world, dyes and pigments are the most commonly used materials to produce colour and are widely used in consumer products such as fabrics, toys and billboards as well as in colour filters in digital displays and cameras. This is a result of their vibrant colour which is independent of the polarisation of the incident illumination and viewing angle, and the ease with which they are produced in abundance. Despite being successfully used for millennia they are not, however, chemically stable at high temperatures and experience photobleaching under prolonged exposure to intense ultraviolet (UV) illumination [13, 14, 17]. Additionally, many dyes and pigments consist of toxic chemicals, which are not environmentally friendly and present issues for recycling. Furthermore, since the optical performance of dyes and pigments is based on volumetric absorption, their performance dramatically deteriorates once the thickness of the pigment layer decreases below the micron scale, resulting in challenges for use in advanced colour displays and spectral imaging devices that require device miniaturisation and high spatial resolution [17]. Additionally, in print registration, using inks requires an overlay of separate cyan, magenta, yellow and black (CMYK) prints which can lead to inaccuracy when aligning them at high resolution. These drawbacks call for a new approach to colour generation with better chemical stability, lower toxicity, reduced sets of materials and higher resolution for demanding advanced applications. Structural colouration serves an important role as an alternative to conventional colouration approaches in future technologies.

Recently, studies into structural 'pigments' have attracted substantial attention due to their promising application as a new class of colourants with potential for large scale, mass fabrication [18]. Colour generation via structural colour does not depend on the interaction of light with molecule i.e. on energy level transitions in the molecules as in the case with dyes and pigments, but rather on the geometry of the constituent micro- or nanostructures. Nature already exhibits fascinating structural colour generation via microstructures on the exoskeletons in some species of bugs and butterflies or even on the surface of flower petals [19] (Figure 2.1). The origins of naturally occuring structural colours have been discussed in detail in several reviews [18–23]. Generally, the structural colouration is a result of light scattering, interference and diffraction thus allowing ranges of wavelengths of visible light to be selectively reflected or absorbed producing a particular colouration of the material. Interestingly, structural colour in nature often involves intricate micro and nanopatterns which usually result in polarisation-dependent or/and 'iridescent' colours i.e colour that depends strongly on the incident or viewing angle. In terms of material, structural colouration usually depends on the presence of a refractive index difference between materials, which in this case are naturally occuring polymers such as beta-keratin, chitin, collagen and melanin ($n \sim 1.5-2$), and air voids, leading to a substantial refractive index difference ($\Delta n \sim 0.5-1$) [22].

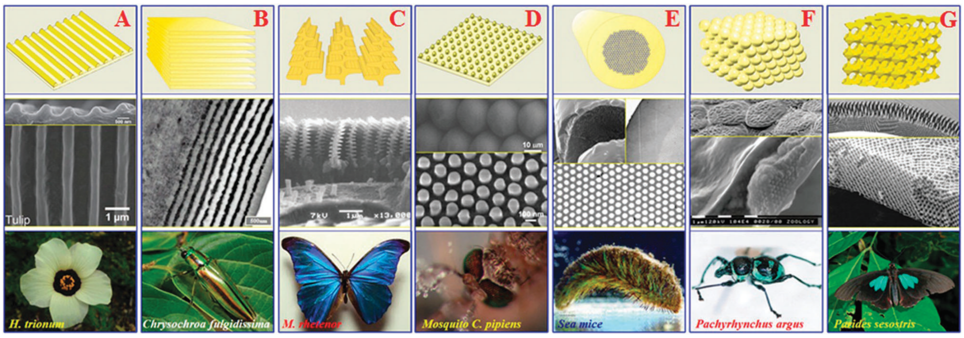

FIGURE 2.1: Common photonic nanostructures in natures comprising nanostructures such as diffraction gratings, multilayers structure and photonics crystals. [20]

A diffraction grating is a commonly found type of structure that generates structural colouration. A grating typically consists of one-dimensional subwavelength patterns that are arranged periodically with a spacing of d on a planar surface (Figure 2.2(a)). Diffraction gratings have been used for decades in optical devices due to their excellent capability for colour routing where the reflected spectrum exhibits peaks located at characteristic wavelengths, λ_m, satisfying $m\lambda_m = d(\sin\theta_i - \sin\theta_r)$ whereby θ_r is the reflection angle, θ_i is the angle of incidence and m is an integer [18, 24]. Examples of structural colouration obtained from natural diffraction gratings include iridescence from flowers such as *Hibiscus trionum* and *Tulipa* species [25], *L.nitida* butterfly scales [26], mollusk (*Haliotis Glabra*) shells [27] and *Serica Sericea* beetles [28].

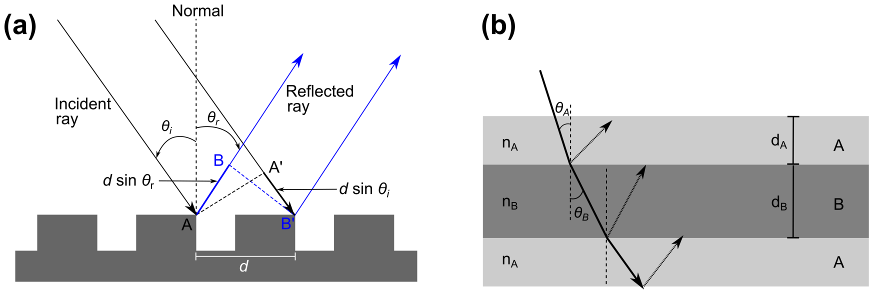

FIGURE 2.2: Ray diagram showing light interaction with (a) diffraction gratings and (b) multilayer thin-film structure.

Another simple structure that can produce colour is a multilayer stack comprising thin films of different refractive indices that are periodically stacked parallel to the reflecting interface. The difference in refractive indices leads to interference that can be constructive or destructive [18]. Due to interference effects, the reflected spectrum thus exhibits a set of peaks or minima at particular wavelengths. For two layers of film labelled A and B (Figure 2.2(b)), with thicknesses of d_A and d_B, and refractive indices of n_A and n_B, respectively, constructive interference occurs when [23]

$$2(n_A d_A \cos\theta_A - n_B d_B \cos\theta_B) = m\lambda. \tag{2.1}$$

Multilayer thin film structural colouration is very common in biological photonic structures and can be found in many organisms, including beetles [29, 30], birds [31, 32], fish [33, 34], mollusk [35–37] and fruit [38]. Due to the simple design, they are suitable for mass fabrication using thin-film deposition techniques which have been conventionally used to produce optical components such as Bragg mirrors, anti-reflection coatings and thin-film sensors [39].

In addition to grating and multilayer films, photonic crystal structures can also be found in naturally occuring structural colours. Photonic crystals are ordered nano and microstructures comprising materials with a spatially varying periodic refractive index, with the lattice size comparable to the wavelength of the incident light [18, 19]. Depending on the nature of the periodic lattice, photonic crystals can be categorised as one-, two- or three-dimensional (1D, 2D or 3D). The multilayer thin film structure discussed above is an example of a 1-dimensional (1D) photonic crystal. Two-dimensional (2D) photonic crystals are biperiodic while photonic crystals with three-dimensional (3D) arrangement, have periodicities in all spatial dimensions allowing light to be confined and controlled in three spatial dimensions [18]. Natural 2D and 3D photonic crystals underpin the colouration of several marine animals [40–43], birds [44, 45] and in insects [46]. This natural structural colouration has inspired scientists to adopt similar concepts in artificial materials such as photonic crystals and metasurfaces to create new type of colourants [14, 47] which manipulate the reflectivity, transmittivity and absorptivity of visible light. Interestingly, recent developments in plasmonic-based structural colouration have provide an alternative method of producing colours via structure, i.e nano-patterned metallic films. These metallic nanostructures enable light manipulation, and thus colour production, via their surface plasmon resonance, a mechanism that does not occur in biological systems [18].

2.1.1 Plasmonics-based Structural Colour

When a metal is exposed to an external electric field, the free electrons experience a displacement force due to the interaction of their charge with the field. The collective displacement of the electron cloud back and forth from its equilibrium position results in the longitudinal oscillation of the electron density in the metal called a plasmon [48, 49]. This then creates an electric field that perturbs the excitation field. As with electromagnetic photons in free space, plasmons can be considered a quasi-particle as a result of the quantisation of the electromagnetic wave in a metal. The plasma frequency ω_p

can be defined as the natural frequency of free oscillation of the electron [48]. Metals such as gold (Au), silver (Ag) and aluminium (Al) are the most widely used materials for production of plasmonic devices due to their intrinsic abundance of free electrons and plasma frequency in the visible spectrum. A two-dimensional plasmon called a surface plasmon polariton (SPP) is an electromagnetic excitation evanescently propagating on the boundary between a metal and a dielectric. On the other hand, localised surface plasmon (LSP) are non-propagating plasmons on, or in the vicinity of, metallic nanostructures coupled to an electromagnetic field. The LSP is a result of oscillations of electron density, confined and localised within the subwavelength volume of a metal nanoparticle or a nanocavity in a metal film, and appear as a plasmonic standing wave [48].

One of the remarkable breakthroughs in the study of plasmonics is the development of artificial materials based on surface plasmon phenomena referred to as metamaterials and their planar counterparts; metasurfaces. Plasmonic metasurfaces, which are the focus of this thesis, are composed of arrays of metallic nanostructures arranged on a planar surface. The optical properties of the metasurface is controlled by the spatial geometry and arrangement of the nanostructures, in conjunction with the intrinsic properties of the material of which it is made. A plasmonic metasurface can have absorption cross-sections significantly greater than their geometric cross-sections [48, 50]. This remarkable optical property enables them to selectively absorb and/or scatter a particular region of the visible spectrum producing colour-related phenomena termed ‘plasmonic colour’. For example, gold and silver nanoparticles typically have resonances falling in the visible region of the electromagnetic spectrum, thus producing bright colours exhibited both in transmission and reflections. This plasmonics-based *structural colour* effect has been used for many hundreds of years mainly due to its aesthetic value and examples include the Roman Lycurgus Cup [51] in which the embedded Au-Ag alloy nanoparticles exhibit dichroism in reflection and transmission. Another example is stained glass windows in Medieval churches where the colouration of some glasses is due to the inclusion of silver nanoparticles of various sizes [52]. With advances in nanofabrication opening new roads to the creation of novel structures such as metasurfaces, and also the potential for mass production, plasmonics-based structural colouration has considerable promise as an alternative colourant [53, 54].

Recently, surfaces decorated with structural colour including plasmonics-based structures have received significant attention due to their excellent colour production, ability to produce ultra-high resolution prints, fabrication simplicity, large viewing-angle tolerance and the possibility of more advanced technological application [13, 14, 17, 55]. Additionally, the use of non-toxic materials such as aluminum and gold not only environmentally friendly but also produce fade-resistant colours. Some of the anticipated potential applications of structural colouration include high-density data storage [56, 57], high-resolution colour printing [58, 59], optical security devices, advanced sensing, and display technologies [60–64]. Unlike the optical absorption of selective wavelengths that occur in dyes and pigments, plasmon-based colouration is a result of surface plasmon resonances that are dependent on the geometry and material of the constituent structure. By tuning the geometry, spatial dimension and surrounding conditions of the plasmonic structure, the resonance frequency and thus the resulting colour can be adjusted [13, 14, 17]. Recent developments in nanofabrication have led to major advances in plasmonic colour technology since it is possible to accurately manipulate the geometry, size, position and orientation of the nanoparticles or nanoholes and engineer more complex designs.

The basis of plasmonic colouration is that metallic nanostructures selectively absorb particular wavelengths of light while reflecting and transmitting the remainder of the spectrum. Furthemore, the plasmonic optical losses are lower on the metal-dielectric interface than inside the bulk of a metal. It is worth mentioning that the losses are helpful in this case since they produce a broader resonance than those created by dielectric structures leading to more vivid colouration [14]. Various implementations of surface plasmon resonances have been reported, based on metallic nanoparticles, nanoprotrusions, nanoapertures and gaps that make up the metasurfaces. Generally, plasmonic colour configurations can be broadly categorised into insulator-metal-insulator (IMI) or metal-insulator-metal (MIM) configurations. Depending on applications and the availability of fabrication tools, approaches to generating plasmonic colour need to be carefully designed based on these configurations in order to produce the desired colour with a highest quality e.g. saturation and brightness.

An IMI configuration consists of a single layer of nanostructured metal film or an array of metal nanoantennas sandwiched between two insulator layers. The surface of a thin layer of metallic film deposited on a substrate can be patterned to create corrugations that establish localised surface plasmon resonances that function as plasmonic pixels. Some examples of plasmonic colouration produced with the IMI configuration are shown in Figure 2.3. As an example, plasmonic colour elements have been formed on a corrugated all-metal surface e.g. silver (Ag) and aluminum (Al) [65–68], comprising nanoprotrusions and nanogratings (Figure 2.3(a-b)). By increasing the size of the protrusions and the lattice period, a wide colour gamut can be produced in reflection and also in transmission (which produces complementary colours to those seen in reflection). In addition to a corrugated surface, a metallic thin-film can also be perforated to create arrays of nanoapertures on its surface which are also suitable for producing colour particularly in transmission [69–72]. Interestingly, apart from symmetric geometries, nanostructures with asymmetric shapes such as cross-shaped nanoapertures (Figure 2.3(c)) have been utilised to produce polarisation tunable colours whereby the shape has different lengths along orthogonal directions thus permitting a selected colour to be transmitted when illuminated with linearly polarised light with an electric field parallel to either orientation of the axis [71, 72]. Previous studies also show that plasmonic metasurfaces consisting of an array of metallic nanoantennas of various geometry such as the rod-shaped nanoantenna shown in Figure 2.3(d), sandwiched between dielectric layers produce excellent colours in reflection and transmission [73, 74]. Similar to nanoapertures, depending on the symmetry of the geometry of the nanoantenna, the generated colours can be either polarisation dependent or independent.

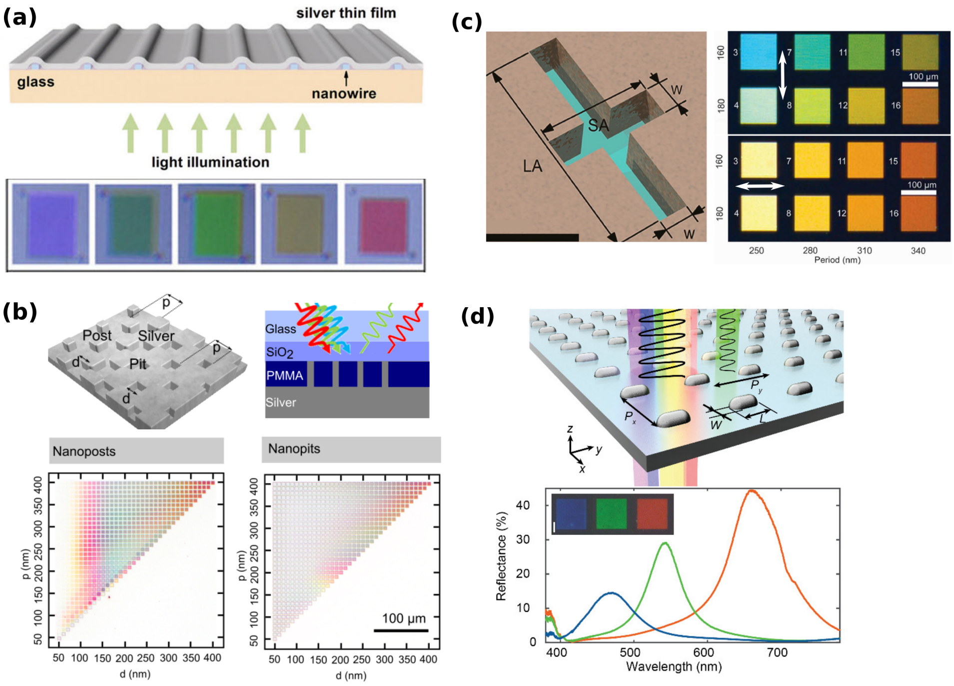

Figure 2.3: Examples of plasmonic colours with insulator-metal-insulator (IMI) configurations comprising (a-b) corrugated metallic thin films and [65, 67] (c) perforated metal films [71] and (d) metallic nanoparticle [75]

In addition to the IMI configuration, plasmonic metasurfaces featuring the metal-insulator-metal (MIM) geometry have been widely utilised to introduce absorption centred on single or multiple wavelengths when at resonance. This configuration comprises two thin metal layers separated by a thin layer of dielectric. One category of MIM plasmonic metasurfaces absorber is one that comprises an array of metallic nanoantennas vertically displaced from a metallic film (either perforated or non-perforated) [14–16, 47, 59, 76–82]. Some examples of MIM plasmonic colouration are shown in Figure 2.4. The plasmonic hybridisation between the top nanoantenna/nanostructured film and the bottom metal film introduces plasmonic energy splitting and can be utilised to further tailor the resonance wavelengths and hence the colour produced [14, 16].

While the intrinsic colours produced by MIM plasmonic stuctures can be tuned by changing the dimensions, shapes and periodicities of the nanoparticles or nanoholes, the separation distance between the top and bottom metallic layers controls the plasmonic coupling strength and, thus, the resonance wavelength [15]. This feature adds an additional degree of freedom in tuning the colours generated by MIM structures. For example, although a wide range of hue and saturation of colours can be produced by changing the dimension of a nanoantenna of various shapes [15, 77, 81, 83] and tuning the period of an array, a similar colour response can be generated by carefully adjusting the vertical gap size [15, 84, 85]. The perception of colour also depends on the initial state of the incident light such as its spectrum, polarisation state and angle of incidence. In response, the colour produced can be directional – changing with tilting angle, incidence angle or polarisation direction. This feature can be undesirable, but for some applications such as optical security devices or for controlling radiation by embedded emitters, the directionality of colours is an important property [86, 87]. Some MIM devices, therefore, used for generating plasmonic colours were designed to have a response to the incident angle or state of polarisation of the incoming light. This property adds further capacity to vary the colours generated by the plasmonic devices which cannot be performed with a pigmented surface. As mentioned previously, the use of a metallic nanoantenna with an asymmetric shape such as rectangular [15] or elliptical [81] nanorods leads to a resonance that changes with the direction of linear polarisation. With this configuration, the generated colours are switched when the electric field of the incident light is polarised either parallel or perpendicular to the long-axis of the rod.

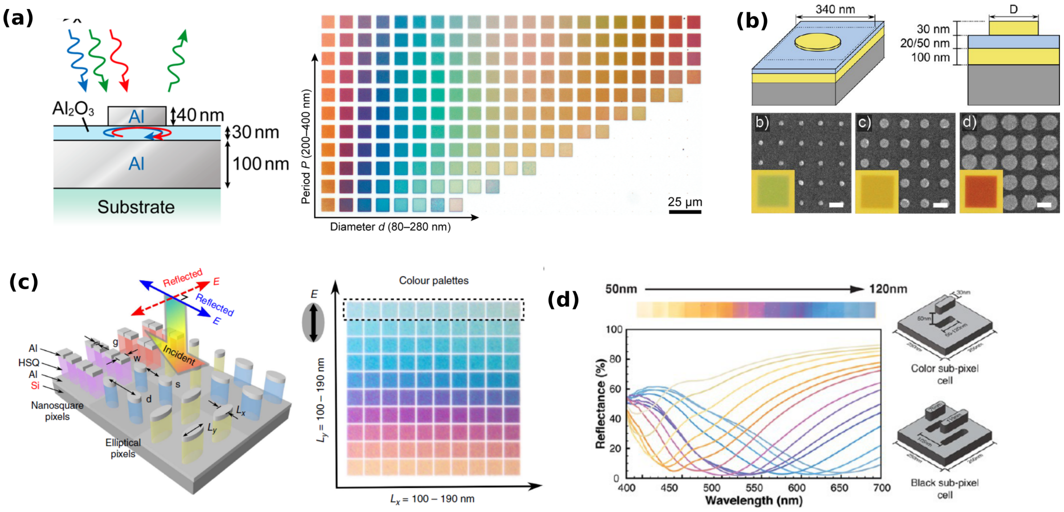

Figure 2.4: Examples of metal-insulator-metal (MIM) plasmonic colours with various nanostructures. (a)[83], (b)[77], (c)[81],(d)[15]

Despite many proposed designs and interesting colour effects, the real challenge however, is to produce plasmonic colour, either directional or polarisation sensitive or not, over a large area utilising a high-throughput fabrication method [13, 14]. In fact, the visual effect exhibited by plasmonic approaches to colouration can usually only be easily seen by the unaided eyes when the pattern covers at an area of the order of a few tenths of a square millimeter [17, 88]. For most industrial applications, a low-cost, high-throughput fabrication process is required to mass produce plasmonic colour with minimum defects. However, the low-throughput conventional fabrication methods are not only time consuming but also tend to introduce defects at larger scales which causes the intended geometry to produce poor colour quality. In fact some nanofabrication methods such as electron beam lithography (EBL) are based on intrinsically sophisticated systems such that the cost of operation and maintenance are uneconomical for mass production. Among top-down fabrication methods, nanoimprint lithography (NIL) is a technique that has promising potential to fulfil those requirements. Some studies have utilised NIL to produce plasmonic colour [59, 89]. However, a detailed discussion into the capability of this technique for plasmonic colour printing, particularly using the MIM structures considered here, has not been undertaken. Colours produced by plasmonic means are sensitive to changes in the geometry of the constituent nanostructures. Therefore, the research presented in this thesis is designed to develop a detailed understanding of the NIL process used not only to produce desired results but also to further explore details of its fabrication capacity. For this purpose, devices with various geometries exhibiting plasmonic colouration, with a design that is most amenable for NIL – specifically, a nanoantenna coupled to its complementary nanohole MIM geometry (see Figure 2.4(d)), have been investigated and are presented in this thesis. More detailed aspects of NIL such as dynamics of polymer resist, parameter optimisation, spatial resolutions, materials and defect control are discussed in Chapter 4.

2.1.2 Colour Perception, Basic Colourimetry and Colour Mapping

Humans use colour information in order to identify objects, materials and even decide the time of day. As light interacts with objects, its spectrum changes with wavelength-dependent absorption, reflection, scattering or transmission, and colours can be seen [90]. Colour perception depends upon both the physical properties of the light, detection by light-sensitive cells in the eye and the complex neurological processing by the brain which integrates properties of the stimulus with experience [90, 91]. To appreciate the quality of colour produced by a device exhibiting structural colour, it is advantageous to understand how humans perceive colours and how colour is characterised. With the aid of advanced optical detection and processing devices such as cameras, displays, spectrometers and colourimeters, it is possible to quantify colours, understand their spectral properties and catalogue them efficiently and precisely. It is, therefore, important to implement an understanding of colour properties and perception when developing approaches to plasmonic or any type of structural colour. This section introduces the basic concepts of colourimetry and colour mapping. Various colour models and colour quality will be discussed and the relationship to the physically measurable spectral information presented.

The colour appearance of an object depends on three components – the light source, the properties of the object and the human visual system. Since the perception of a colour involves all three elements, they must also be quantified in order to create a reliable physical colourimetry system. Colourimetry is simply defined as the measurement of colour, and serves as the foundation of colour appearance specification [90]. The first component for colour production – the light source, constitutes the electromagnetic energy needed to establish visual perception. The fact that the light source itself has its own colour profile, means that the perceived colour of the object will be highly sensitive to the type of light source. The properties of a light source can be described by its spectral intensity distribution. The intensity or irradiance of light at a particular wavelength can be defined as the radiant power (flux) per unit surface area ($I(\lambda) = \Phi(\lambda)/A$) with units of Watts per square meter ($\mathrm{W/m^2}$) [92]. In the colourimetric measurements of stimuli used in the colour appearance specification, it is important to use the actual spectral power distribution of the light source. For simple colourimetry, the determination of the colour properties and spectral power distribution of light sources is carried out in two ways — by calculation and standardisation [90].

Once the nature of the light produced by the source is specified, the next step is the characterisation of its interaction with the object. The interaction between electromagnetic energy and materials obeys the law of conservation of energy as such the sum of the absorbed, reflected, and transmitted light is equal to the energy of incident radiant at each wavelength, as seen in Equation 2.2, assuming the absence of wavelength conversion processes such as fluorescence, [90].

$$\Phi(\lambda) = R(\lambda) + T(\lambda) + A(\lambda) \tag{2.2}$$

where $\Phi(\lambda)$, $R(\lambda)$, $T(\lambda)$ and $A(\lambda)$ are the incident, reflected, transmitted and absorbed fluxes respectively. Since the total of reflection, transmission, and absorption must be equal to the incident flux, they are usually measured as the percentages of the incident flux. Thus reflectance, transmittance and absorptance, each can be defined as the ratio of the reflected, transmitted and absorbed energy to the incident energy, respectively [93]. However, it is worth mentioning that the reflectance or transmittance of an object is not only dependent on the wavelength of the incident light but also on the properties of the illumination, viewing angle and roughness of the surface of the material [90].

Analysis of the perceived colour requires a quantitative technique to predict the response of the human visual system. With the aid of photoreceptors called cones, the human eye is able to detect colour. The quantification of the human visual sensory system is, therefore, based on light energy absorbed into the cones. The human eye has three types of cone cells that respond to varying wavelength stimuli and are referred to as L, M and S cones. The LMS letters refer to the peak absorption bands of each type of cone and specifically to the long-wavelengths (564–580 nm), middle-wavelengths (534-545 nm) and short-wavelength (420–440 nm) sensitive cones respectively [90, 94]. Hence, colourimetry is based on the ability of an average observer to predict when two stimuli match. The properties of human colour matching are defined by the spectral responsiveness, $L(\lambda)$, $M(\lambda)$and $S(\lambda)$, of the three cone types (Figure 2.5).

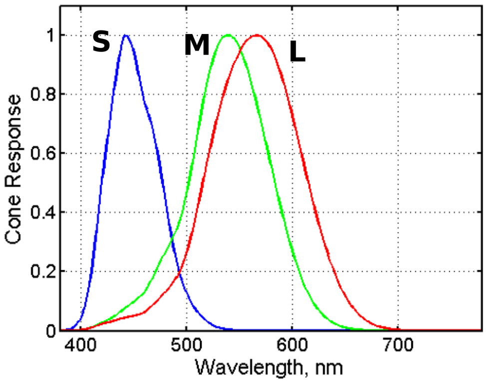

FIGURE 2.5: Spectral responsiveness of the L, M, and S cones [95].

The aim of the colour matching approach is to determine, assuming the spectral responsiveness of the three cone types are known, whether two stimuli will match in colour within the limits of perception. These are characterised by their spectral power distributions $\Phi_1(\lambda)$ and $\Phi_2(\lambda)$, and they are said to match if the product of their spectral power distributions and the relevant cone responsivities, integrated over all wavelengths are equal [90, 96], i.e.

$$\int_\lambda \Phi_1(\lambda)\, L(\lambda)\, d\lambda = \int_\lambda \Phi_2(\lambda)\, L(\lambda)\, d\lambda \tag{2.3a}$$

$$\int_\lambda \Phi_1(\lambda)\, M(\lambda)\, d\lambda = \int_\lambda \Phi_2(\lambda)\, M(\lambda)\, d\lambda \tag{2.3b}$$

$$\int_\lambda \Phi_1(\lambda)\, S(\lambda)\, d\lambda = \int_\lambda \Phi_2(\lambda)\, S(\lambda)\, d\lambda \tag{2.3c}$$

The CIE (acronym stands for Commission Internationale de l'Eclairage or the International Commission on Illumination) system was first established in 1931 and is considered the benchmark for colourimetry that enables the specification of colour for an average observer. The CIE system also quantitatively describes an observer's spectral sensitivity curves as the colour matching functions $[\bar{x}, \bar{y}, \bar{z}]$ [17]. Figure 2.6 below shows the spectra of the colour matching functions.

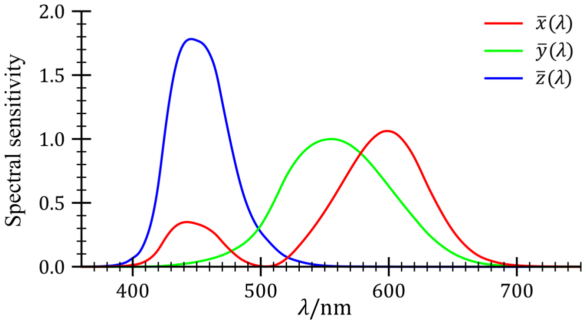

FIGURE 2.6: Colour matching functions $[\bar{x}, \bar{y}, \bar{z}]$ defined by CIE 1931 [97]

The colour perceived by humans is a product of the combination of the responses of the three groups of cone cells, and all colour stimuli can be generated and thereby perceived by the eye by adequate mixing of these stimuli. As a consequence, a mixed set of values correlated with the amount of primary illumination will describe any hue. This set of values is called the tristimulus value. For a given relative spectral power distribution of the illuminating light $\Phi(\lambda)$, and reflection spectrum $R(\lambda)$, the tristimulus values (X, Y, Z) can be determined by the equation below, integrated across the wavelength, λ range of 380–780 nm:

$$X = k \int_{\lambda} \bar{x}(\lambda)\, \Phi(\lambda)\, R(\lambda)\, d\lambda \tag{2.4a}$$

$$Y = k \int_{\lambda} \bar{y}(\lambda)\, \Phi(\lambda)\, R(\lambda)\, d\lambda \tag{2.4b}$$

$$Z = k \int_{\lambda} \bar{z}(\lambda)\, \Phi(\lambda)\, R(\lambda)\, d\lambda \tag{2.4c}$$

where k is a normalisation factor defined as $k = \frac{100}{\int_{\lambda} \Phi(\lambda)\, \bar{y}(\lambda)\, d\lambda}$ [90]. The CIE created a two-dimensional chromaticity diagram also known as the CIE XY diagram, to provide a perception colour map. An example of this diagram is shown in Figure 2.7. Each point with coordinate of *(x,y)* on the diagram represents a colour presented by its tristimulus value. The relation between the coordinates and the tristimulus values is

$$x = \frac{X}{X+Y+Z} \tag{2.5a}$$

$$y = \frac{Y}{X+Y+Z} \tag{2.5b}$$

$$z = \frac{Z}{X+Y+Z} \tag{2.5c}$$

where x+y+z =1. The CIE chromaticity diagram is commonly utilised in characterising the plasmonic colour in order to show the range of colour that can be produced by changing the geometry of the nanoparticles or their arrangement. The chromaticity coordinates, however, attempt to simplify a three-dimensional quantity with only two variables and, hence, they should be used cautiously. Chromaticity coordinates alone, do not include details of the colour appearance of stimuli because they do not contain the brightness value.

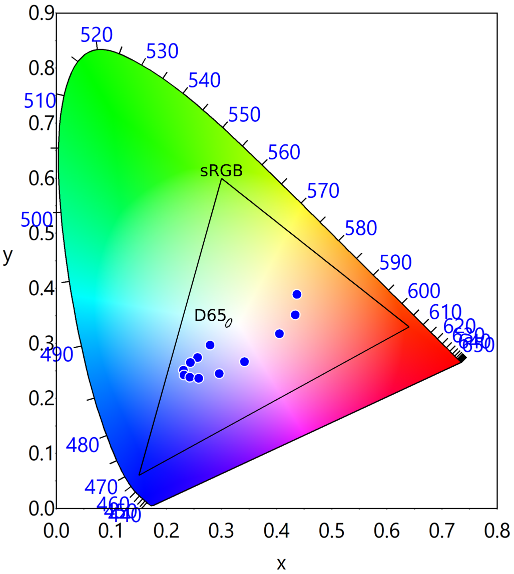

Figure 2.7: An example of CIE 1931 xy chromaticity diagram. The area under the solid line represent the sRGB colour space. The ellipse in the middle of the diagram shows the coordinate of the standard D65 illuminant. Blue dots represent examples of colours in various coordinates of the diagram.

2.1.3 Basic Colour Models

The colour matching function discussed above correlates with the spectral sensitivity of three types of receptors in the human eye denoted as L, M and S, suggestive of red, green,and blue (RGB) sensitivities. The standard RGB (sRGB) colour model was established in 1996 [98] along with the development of advanced computer graphics and monitor displays. The RGB colour model is an additive colour space whereby the additive combinations of the primaries with maximum relative intensity results in a white colour. Table (2.1) below shows the tristimulus values for both additive and subtractive colour systems. Quantitatively, red (R), green (G) and blue (B) colours encode a value in the range of 0-255, whereby R=[255,0,0], G=[0,255,0] and B=[0,0,255]. Any combination of these colours results in another set of values, for example yellow (Y) is a result of combinations of an equal amount of red and green thus giving Y=[255,255,0]. Using this model white and black therefore, have RGB values of [255,255,255] and [0,0,0] respectively. This colour space is especially useful for computer monitors since the colours are controlled by changing RGB light emitters' relative intensities. [94].

Colour	**RGB**	**CMY**	**HSV**
Red	(255, 0, 0)	(0,255,255)	(0°,1,1)
Green	(0, 255, 0)	(255,0,255)	(120°,1,1)
Blue	(0, 0, 255)	(255,255,0)	(240°,1,1)
Cyan	(0, 255, 255)	(255,0,0)	(180°,1,1)
Magenta	(255,0,255)	(0,255,0)	(300°,1,1)
Yellow	(255,255,0)	(0,0,255)	(60°,1,1)
White	(255,255,255)	(0,0,0)	(0°,0,1)
Black	(0,0,0)	(255,255,255)	(0°,0,0)

TABLE 2.1: Table shows different values in trichromatic colour systems i.e. RGB, CMY and HSV.

Another widely used colour model is the CMYK approach, which is an abbreviation of cyan, magenta, yellow, and black [99]. CMYK is considered a subtractive colour model since cyan, magenta and yellow are obtained due to absence of red, green and blue from white light, respectively. Unlike the additive RGB colour, the additive mixture of primaries in the CMYK colour model results in black . Similar to the sRGB system, CMYK colours can be quantified with values ranging from 0-255, where, cyan (C), magenta (M), yellow (Y) and black (K) colour have values of C=[255,0,0], M=[0,255,0], Y=[0,0,255] and K=[255,255,255]. Other colours, therefore, are characterised by a combination of these values, red, for example is produced in the absence of green and blue or, alternatively that it is a combinations of magenta and yellow and has a value of R=[0,255,255].

The CMYK colour model is most appropriate for colour printing due to its subtractive nature, as inks produce colours by absorbing a particular region of the visible spectrum and reflecting the rest of the spectrum. [94].

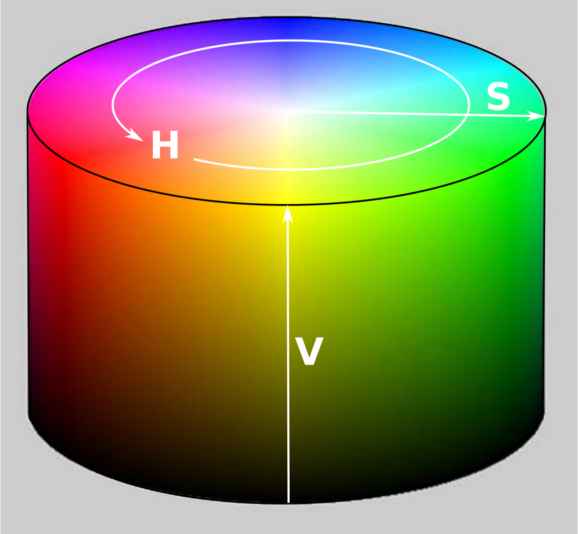

FIGURE 2.8: Schematic of 3-dimensional, cylindrical HSV colour space. The hue (H) is represented by the azimuthal angle of the cylinder starting from red (0°), passing through green and blue (120° and 240° respectively) and wrapping back to red (360°). The saturation of colour increases as the position moves radially outward (from 0 to 1). The vertical axis represents the brightness of colour ranging from 0 (black) to 1 (white) [100].

A more versatile colour model is the three dimensional HSV colour space (also known as HSB). The HSV colour model is a cylindrical-coordinate (or conical) representation of the RGB colour space that uses its hue (H), saturation (S), and brightness (V) to encode colour information (Figure 2.8). The coordinates of the colour are described by an azimuthal coordinate (H), a radial coordinate (S), and the height (V) axis [99]. The hue (H), defined by an angle revolves from $0 - 360°$ relative to the central axis of the cylinder, with red at an angle of 0° or 360°, green at 120° and blue at 240°. The saturation of the colour is characterised by the radius of the cylinder. By moving radially outward from the central axis along S, the saturation increases from 0 to 1, with 1 corresponding to a completely pure or saturated colour and 0 represent a completely unsaturated hue i.e some shade of gray. Additionally, moving up along V increases the colour brightness from 0 to 1 where 0 is always black; depending on the saturation and 1 may be white or a more or less saturated colour. Therefore, the property of a colour can be easily described using a set of three values $[h, s, v]$, pure red colour for example, has a value of [0,1,1]. The HSV model has been used to determine the colour quality produced by plasmonic colouration and also for colour mixing strategies. The tristimulus value

(R,G,B) obtained from a spectra can be converted to the HSV system from the RGB system by using RGB-to-HSV conversion formula given by [99]

$$
\begin{aligned}
R' &= R/255 \\
G' &= G/255 \\
B' &= B/255 \qquad (2.6a) \\
V_{max} &= max(R', G', B') \\
V_{min} &= min(R', G', B') \qquad (2.6b) \\
\Delta &= V_{max} - V_{min} \qquad (2.6c)
\end{aligned}
$$

The hue value, H (or h) can be calculated using

$$
H = \begin{cases} 0^\circ & , \Delta = 0 \\ 60^\circ \times (\frac{G'-B'}{\Delta} \mathrm{mod} 6) & , V_{max} = R' \\ 60^\circ \times (\frac{B'-R'}{\Delta} + 2) & , V_{max} = G' \\ 60^\circ \times (\frac{R'-G'}{\Delta} + 4) & , V_{max} = B' \end{cases} \qquad (2.7)
$$

where *mod6* is the remainder after dividing by 6, while the saturation, S (or s) and brightness, V (or v) value are given by

$$
S = \begin{cases} 0 & , V_{max} = 0 \\ (\frac{\Delta}{V_{max}}) & , V_{max} \neq 0 \end{cases} \qquad (2.8a)
$$

$$
V = V_{max} \qquad (2.8b)
$$

2.1.4 Relationship Between the Spectral Properties and HSV

The CIE chromaticity diagram and a simplified two-dimensional HSV value plot can be used to quantify vividness of colours. Figure 2.9 shows the relationship between nominal spectral properties of the reflectance from a hypothetical sample of interest, HSV values and the coordinate of the colours in the corresponding CIE chromaticity diagram (x, y). Here the hue value is normalised to 1 by dividing the values with 360° for convenience.

For simplicity, Gaussian spectral distributions (i.e. spectra with a Gaussian peak or dip), are assumed. Equation 2.9 below is the Gaussian function used to obtain a spectral peak

$$f(x) = \frac{1}{\sigma\sqrt{2\pi}} e^{-\frac{1}{2}(\frac{\lambda-\lambda_m}{\sigma})^2} \tag{2.9}$$

where σ is the width, λ is wavelength, λ_m is the central wavelengths, while a Gaussian dip is defined as $1 - f(x)$. Either the maximum (for additive colour) or the minimum (for subtractive colour) of each of the spectra is set at 650 nm which correspond to either red (additive colour) or cyan (subtractive colour). In the case of structural colour this would correspond to a resonance wavelength of the device. The spectral linewidths are varied (achieved by varying σ) and the values of the maximum/minimum reflectance are changed to see their relationship with the properties of the colour (hue, saturation and brightness). The reflectance spectra are then converted to corresponding colours and HSV values using customised MATLAB code based on Equation 2.4 - 2.8 by considering illumination from a D65 light source.

Figure 2.9(a) shows Gaussian reflectance spectra with various linewidths for an additive colour achieved by varying the linewidth from $\sigma = 5$ to 100 nm. For the spectra exhibiting a maximum, the narrower linewidths indicate more saturated colours as shown in the HSV plot in Figure 2.9(b). The saturation rapidly decreases once $\sigma > 50$ nm while the brightness exponentially increases with the linewidth. Increasing the standard deviation from 5 to 30 nm, however, does not change the hue but as σ increases beyond 30 nm the hue gradually increases from 0 to 0.1, meaning the colour starts to deviate from 'pure' red (0) to orange (0.11). The inset in Figure 2.9(b) shows the simulated colours as a result of varying the spectral linewidth and the corresponding hue, saturation and brightness value. The corresponding colours are also mapped to the CIE diagram and plotted in Figure 2.9(c). It should be noted that when the saturation of the colour reached 1 (fully saturated), its *(x,y)* coordinates are positioned on the boundary of the CIE diagram while the central white point corresponds to a completely desaturated colour. The black points in Figure 2.9(c) show the effect of increasing linewidth for additive colours where the increase in hue and reduction in saturation moves the coordinate towards the centre part of the CIE diagram.

Figure 2.9(d), on the other hand shows reflectance spectra representing substractive colour with varying linewidth. These consist of a Gaussian 'dip' in the spectrum. The effect is complementary to that seen with additive colour with a lower value of σ associated with unsaturated colours and larger σ associated with more saturated colour, as can be seen in Figure 2.9(e). The hue and brightness of the colour, however, experiences an insignificant change with increasing linewidth. The slight increase in the hue value, however, still results in a colour change from cyan to a darker blue colour. The colour swatch in the inset of Figure 2.9(e) shows the colour change from white to cyan and blue due to the significantly increased saturation value from unsaturated (0) to saturated (1). The blue points inside the CIE diagram of Figure 2.9(f) moves from the middle towards the edge of the diagram, represent the increasing saturation as a result of broadening linewidth in the Gaussian spectra for substractive colours.

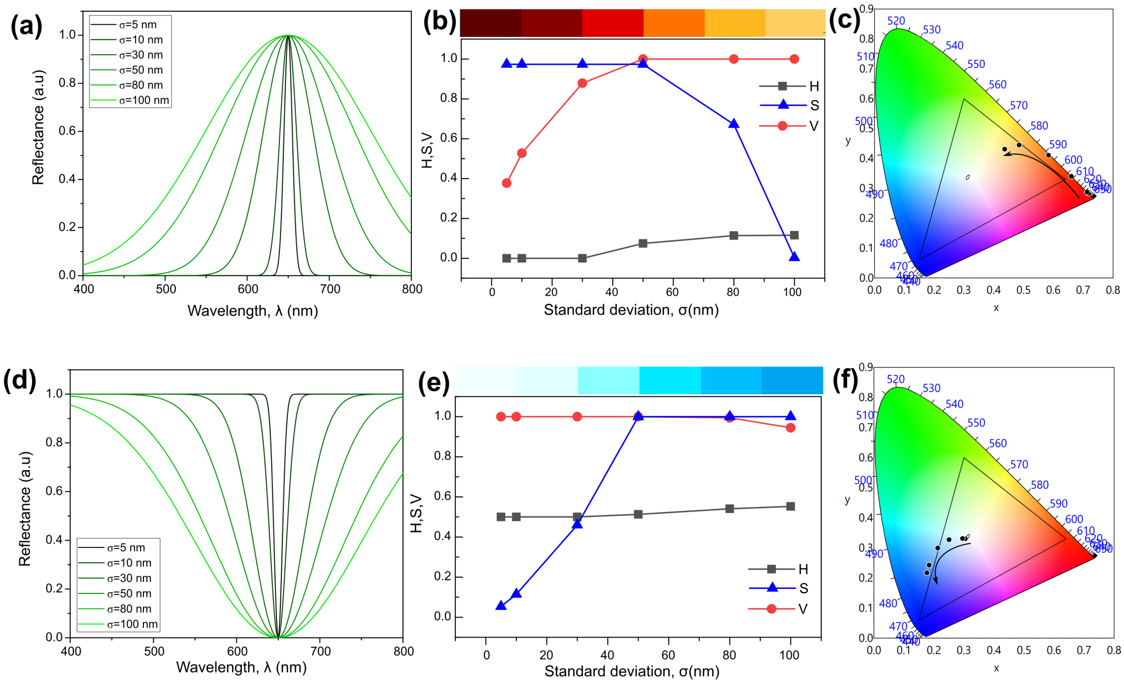

FIGURE 2.9: (a,d) Customised Gaussian-shaped reflection spectra for additive and substractive colours with different linewidths with peak and dip at 650 nm, respectively. Standard deviation σ varies from 5 to 100 nm. (b,e) Two-dimensional HSV plot corresponds to the varying linewidth in (a,d). Insets at the top shows the resulting colours. (c,f) Chromaticity coordinate of the colours in (b,e) in the CIE XY diagram.

For structural colour exhibiting an approximately Gaussian reflectance spectrum, the fraction of light reflected can vary depending on several factors such as the dimensions and even defects arising from the fabrication process. Figure 2.10 (a) shows reflectance spectra with a reflectance maximum ranging from 10% to 100%. The resonance wavelength and linewidth are both fixed at $\lambda = 650$ nm and $\sigma = 30$ nm. As shown in Figure 2.10(b), the brightness increases due to increasing efficiency in reflectance, while, unsprisingly, both saturation and hue remain constant. The colour swatch shown in the inset of Figure 2.10(b) clearly shows the effect on the resulting colour of the increasing brightness (from dark red to brighter red).

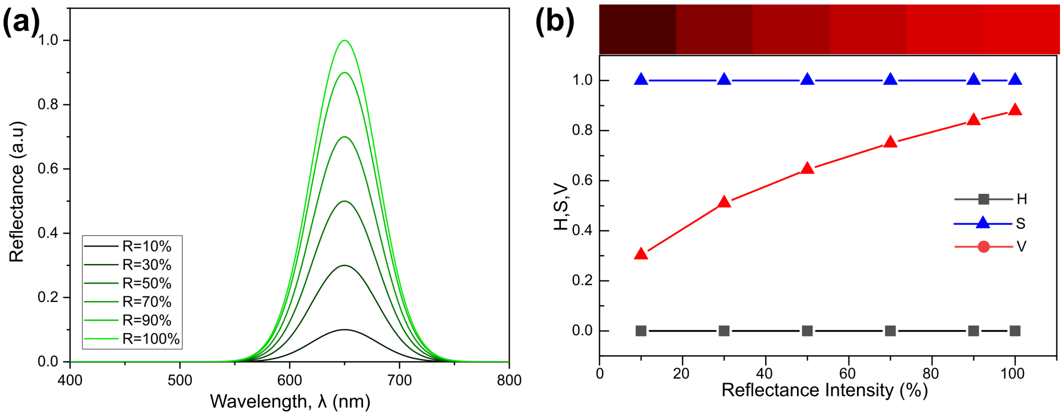

Figure 2.10: (a) Gaussian-shaped reflection spectra for additive colours with reflectance intensity varying from 10% to 100% with peak and standard deviation fixed at λ =650 nm and σ =30 nm respectively. (b) HSV plot and corresponding colour swatch (inset) for various reflectance intensity.

For structural colour exhibiting a reflectance minimum due to enhanced absorption or transmission, there are two possible conditions: either the maximum or minimum reflectance can vary (Figure 2.11 (a) and (c)). Plasmonic colour usually exhibits these type of spectral properties which represent variations in the transmission or absorption efficiency. Figure 2.11(a) shows the reflectance spectra with a maximum reflectance increasing from 10% to 100% while the wavelength corresponding to the minimum and the linewidth are both remains fixed at $\lambda = 650$ nm and $\sigma = 30$ nm. As in the previous case, the increase in the reflectance results in a brighter colour as shown in the HSV plot in Figure 2.11(b), meanwhile, the hue and saturation value remain constant. As a result, the colour changes from very dark to a lighter cyan as shown in the inset of Figure 2.11(b). Figure 2.11(c) on the other hand shows the reflectance spectra corresponding to increasing absorption where the minimum in the spectrum reduces from 90% to 0% while keeping the maximum fixed at 100%. As shown in the HSV plot in Figure 2.11(d), the saturation increases almost exponentially as the absorption efficiency increases, while the hue and brightness remain constant as the reflectance intensity and position of the resonance wavelength are fixed. As a result of increasing saturation, the colour changes from white to a more saturated cyan colour as shown in the inset in Figure 2.11(d).

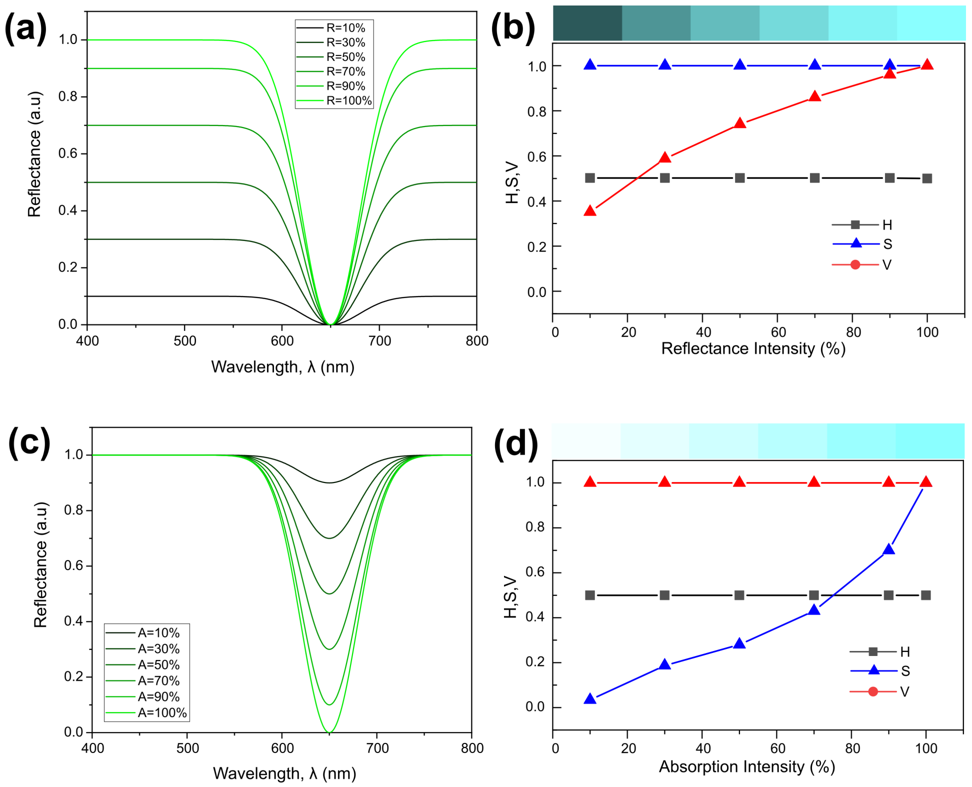

FIGURE 2.11: (a,c) Gaussian-shaped reflection spectra for substractive colours with varying reflectance and absorption intensity respectively. (b,d) HSV plots and colour swatches corresponds to the various reflection and absorption efficiency in (a,c).

In conclusion, structural colour can be tuned to produce either a minimum or a maximum in the reflectance spectra depending on the mechanism involved. In most cases, structural colour often involves more complex spectral characteristics such as Fano-like spectra. Here we are more interested in the case where there is a minimum in reflectance since plasmonic colour produced by MIM devices, which is the main focus of this thesis, relies on the selective absorption of wavelength of light. By increasing the linewidth of the spectral distribution, the saturation of the colour can be increased. On the other hand, if the linewidth is fixed, it is possible to vary the saturation and brightness of the colour by controlling either the reflectance and absorption intensity.

2.2 Fabrication Methods for Plasmonic Structures

Developments in the fundamental understanding of plasmonics and corresponding optical properties stimulate further optimisation of designs for plasmonic nanostructures to fulfil technological requirements and resolve challenges in many fields including medicine, biosensing, imaging, solar energy, catalysis, and optoelectronics [101]. Fabrication of a plasmonic metasurface usually involves lithographic patterning of a nanoscale template and a subsequent metallisation process. Metasurfaces usually have unit cells with subwavelength dimensions, so nanofabrication processing with sub-100 nm resolution is required. Depending on the complexity of the structures, different nanofabrication techniques can be used to manufacture the desired nanostructures. These methods can be separated into two major classes: direct-write and pattern transfer approaches [102].

Conventional photolithography has been widely used in the semiconductor industry owing to its high yield ability, and capacity for large scale mass production. While shorter-wavelength light (such as 193 nm wavelength UV light used in extreme UV/immersion lithography [103]) is preferred for fabricating optical metasurfaces with nanoscale features, such extreme light sources can cause damage to the lens and mask [102]. Alternatively, maskless direct-write lithography utilising particle beams have been demonstrated for the production of nanoscale patterns. Electron-beam lithography (EBL) and focused-ion-beam (FIB) milling are two important examples of conventional, well-established direct-write methods based on particle beams, for the fabrication of optical metasurfaces owing to their nanoscale resolution. In the EBL process, the pattern is predefined on an electron-sensitive resist via electron beam exposure before subsequently undergoing a post-patterning process such as etching, development and/or a metal deposition process. FIB on the other hand, uses a focused beam of ions to mill or remove the desired area of the material (e.g. resist or metallic film) to create a pattern of interest. While templates created by EBL and photolithography usually require a subsequent metal deposition process to finalise the plasmonic device, FIB can directly mill and create nanopatterns on the surface of the metal film. The challenges to EBL and FIB for large-scale manufacturing and commercial purposes are their high operating and maintenance costs, and the fact that they are low-throughput processes which also require a highly stable environment. Additionally, although advanced grayscale technique involving EBL and photolithography allow production of 3D plasmonic nanostructures with interesting optical properties, these approaches require an intricate control of the particle beam and UV light doses to which the resist is exposed.

In order to meet the requirements of scalability and high-throughput large area manufacturing, pattern transfer lithography was developed. In this technique, a predefined pattern on mask or mould is use to replicate the pattern onto another surface. One example of this approach is Nanoimprint Lithography (NIL) which utilises an embossing method using a master mould/stamp comprising nanostructures for pattern transfer onto a polymer resist. Depending on the application and type of polymer resist used, two conventional NIL modes referred to as thermal and UV-assisted NIL are used to cure a polymer-coated substrate while a master mould is being pressed against the substrate. A negative pattern is then formed after the mould is detached from the substrate. NIL has the advantages of high resolution, capacity for large area fabrication and relatively low cost. NIL processes usually leave a residual resist layer at the bottom of the cavity which acts as a cushioning layer to prevent the mould from directly contacting with the substrate when pressure is applied [104, 105]. The residual layer, however, may be undesirable for some applications and therefore, oxygen or argon-oxygen plasma etching is required to remove this layer. Nanosphere lithography (NL) is another straightforward and low-cost pattern transfer approach for large area fabrication. The NL technique involves creating of a monolayer of colloidal self-assembled polystyrene (PS) sphere at an air-water interface. The monolayer is then transferred onto a surface of the substrate as a hard mask [102, 106]. This process is followed by etching or a metal deposition process and removal of the PS spheres to finalise the plasmonic device. One of the shortcomings of the NL technique however, is its limitation to produce simple periodic patterns and constrained to only specific geometries.

After fabricating a template using one of the nanofabrication techniques mentioned above, a layer of metal is deposited onto the template to realise the plasmonic metasurface. Physical deposition methods such as electron beam (e-beam) evaporation and sputtering are some of the commonly used techniques to deposit metallic thin films. E-beam evaporation uses accelerated electron beams, deflected to strike the target material (e.g. metal), converting kinetic energy to heat and thus vaporising the target [107]. The vaporised metal is then deposited onto the surface of the fabricated sample located on top of the target. A sputtering system on the other hand, consists of a metallic anode and cathode inside the chamber and a voltage of the order of several keV is applied to generate the plasma to vaporise the target materials [107]. There are two ways of generating the plasma: (i) direct-current (DC) power generally used for deposition of conducting material while (ii) RF power is suitable for depositing dielectric materials. Ions from the generated plasma are attracted to the target material which has the opposite charge. High energy bombardment by the ions vaporise the target materials which then condense onto the surface of the substrate. Additionally, if the metallisation process involves an assembly of colloidal metallic nanoparticles rather than thin films, an electrophoretic deposition (EPD) technique can be performed [108]. A conductive substrate such as indium tin oxide (ITO) is required in EPD where an electrical potential is applied to electrostatically attract the oppositely charged metallic nanoparticles into the fabricated nanocavities. The voltage can be varied to control the number of particles deposited and their orientation [109].

In conclusion, a high spatial resolution nanofabrication technology with nanoscale precision is required to produce plasmonic structures since their optical properties are highly responsive to their shape and dimensions. State-of-the-art nanofabrication techniques have been demonstrated to produce complex nanostructures with the ability to tailor nanostructure size and shapes on the nanoscale. However, an ideal nanofabrication technique would be inexpensive, have a high throughput, a high resolution, and provide great flexibility for tailoring nanostructure size and shape. Among other techniques, the pattern-transfer techniques have significant advantages for achieving this goal. Therefore, in this thesis, the versatility of the pattern-transfer technique, specifically nanoimprint lithography (NIL) is further explored to maximise its ability to produce plasmonic devices.

2.2.1 Nanoimprint Lithography (NIL): Towards a Versatile and Scalable Nanofabrication Method

The concept of NIL was introduced and demonstrated by Chou et al in the 1990s [110]. The motivation was to develop a low-cost, high-throughput nano-manufacturing technology to overcome the bottleneck in conventional lithography methods used in the semiconductor industry as the demand for high-precision nanolithography techniques to manufacture smaller transistors and higher-density integrated circuits (ICs) increased. To develop a new lithography method that can meet industrial demands, critical issues faced by conventional techniques such as resolution, precision, throughput and reliability need to be addressed. The concept of NIL is relatively simple, analogous to the hot embossing technique, but at the nanoscale level. In the NIL process, a master mould is first fabricated usually using EBL followed by processes such as development, lift off and/or etching (Figure 2.12(a-e)). The fabrication of a mould is usually a one-off process where the same mould can be use for multiple imprinting cycle. The mould is then coated with an anti-sticking layer (trichlorosilane coating) via vapour phase deposition (Figure 2.12(f)). Then by using a nanoimprint tool, the mould is pressed onto a resist-coated substrate to define the nanoscale deformation on a resist film, which is then cured either by heat or UV application (Figure 2.12(g-h)). Once the resist is cured, the mould is detached (or demoulded) and the patterned resist can be used as is or further treated through etching, metal deposition (Figure 2.12(i-j)) or other standard lithographic techniques to finalise the device or to create a daughter mould for further processing [111]. This technique permits rapid pattern replication. Since NIL has been expeditiously developed as an alternative to conventional lithographic technologies, many advances in the NIL technique such as reverse NIL and multilevel NIL, utilising either thermal or UV mode, have been demonstrated due to the demand for more complex nanostructures.

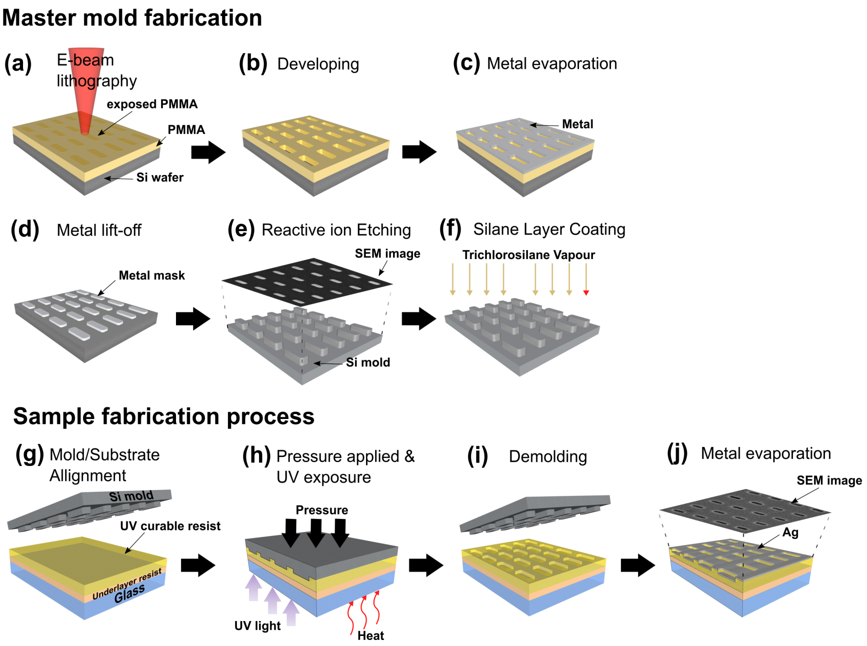

FIGURE 2.12: Nanoimprint process starts with master mould fabrication which involves (a) pre-patterning on resist using electron beam lithography, (b) developing, (c) metal mask evaporation, (d) lift-off, (e) reactive ion etching (RIE) process and (f) silanization of the mould. One the mould is ready, it is used for fabricating the sample via NIL pattern replication process which includes (g) aligning mould and substrate, (h) applying pressure and curing of resist (UV or thermally), (i) demoulding process and (j) metalisation of the replicated pattern.

Conventional NIL uses heat or UV light to cure the polymer resist to enable the pattern to be transferred onto the polymer. Usually, the temperature or the amount of UV light exposed to the polymer resist can be controlled as required by the user. Similarly, other NIL parameters such as imprinting time and the applied pressure can also be tuned, giving more flexibility to the user to control the process and the resultant imprinted structure. However, the pattern transfer process is not only dependent on the NIL parameters but also other factors such as the architecture of the mould (e.g. pattern density and geometries), properties of the surface of the mould and substrate (e.g. surface energy) as well as the chemical or physical properties of the resist [112]. The ability to control all these crucial factors allows us to engineer the desired nanostructures producing 2D or even 3D geometries.

By understanding the surface chemistry, for example, between the substrate, resist and the mould, a reverse NIL can also be employed. In the reverse NIL process shown in Figure 2.13(a), the resist is spin-coated onto the mould first rather than the substrate. The polymer resist is then transferred and bonded onto the surface of preferred substrate in the NIL process due to the difference in surface energy between the mould and the substrate thus creating freestanding micro or nano polymer structures once the resist is cured [113]. A flexible (polymer) mould is preferable for this process due to conformity.

Advantages of this method includes the fact that it produces imprinted structures with no residual layer on various substrates [113] (Figure 2.13(b)). Furthermore, this method can be employed on a pre-patterned substrate (Figure 2.13(c,d)), thus creating structures with a 3D configuration (Figure 2.13(c,e)).

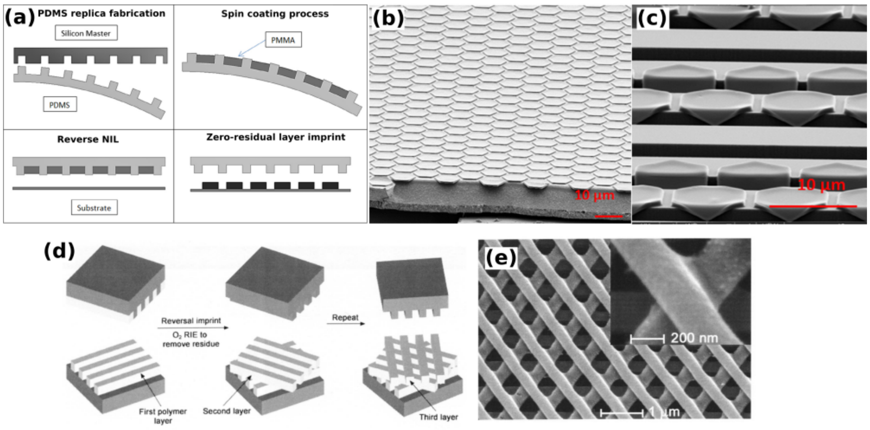

FIGURE 2.13: (a) Schematic shows the reverse NIL process which starts by replicating the flexible PDMS, resist spin-coating on the PDMS mould and reverse NIL to produce the zero-residual layer imprint structures. Cross-sectional SEM images shows the transferred honeycomb structures on (b) a blank substrate and (c) pre-patterned structures. (d) Schematic multilayer reverse NIL process to produce the mesh-like structures shown in SEM image (e) [113].

In NIL a binary or two-level mould is usually used for pattern transfer. This will create a 2D structures with limited tunability over the height of the imprinted structures. Multilevel NIL is one of the earliest approaches used to enable tuning over vertical dimension of the imprinted structures by utilising a grayscale mould (produced using grayscale EBL) which allows production of structures with different heights (grayscale) [114] (Figure 2.14(a,b)). A more creative approach is by combining the EBL and NIL techniques followed by thermal reflow treatement to produce a smooth 3D structure [115] (Figure 2.14(c,d)). With this technique, the complex grayscale EBL process can be avoided.

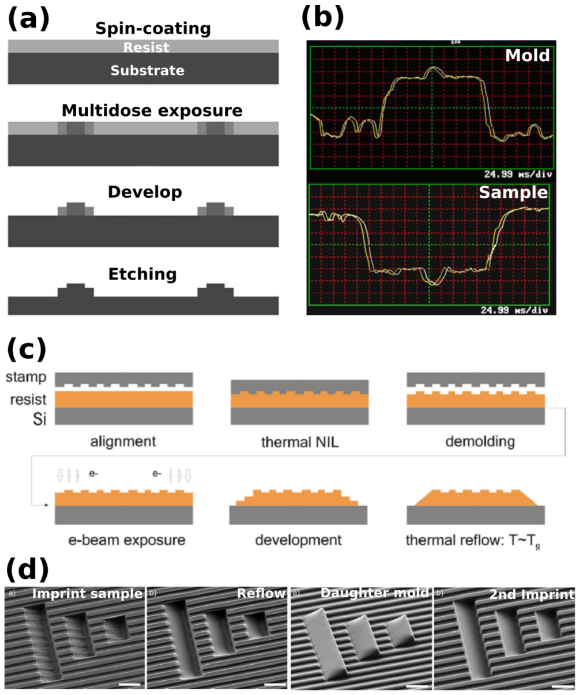

FIGURE 2.14: (a) Fabrication of multilevel NIL mould using grayscale EBL technique and (b) AFM measurement of the mould and imprinted sample.(c) Combined NIL and EBL to produce multilevel structures which then undergone thermal reflow treatment. (d) SEM images shows the imprinted sample and the same sample after thermal reflow process. The sample was used to produce a daughter mould to be used in the second imprint (scale bars refer to 2 μm). Images (a-b) taken from [114] and (c-d) from [115]

Other factors that need to be considered in the NIL process are the chemical composition and physical properties of the resist. The molecular weight of the resist for example, determines the resolution of the pattern as the moulding of nanoscale structures means that single polymer chains have to deform or flow [112]. A lower viscosity resist is a result of the increasing ability of the chains to move freely and enable imprinting to take place easily.

However, the polymer flow during imprinting is also influenced by the density of the structures on the mould as well as the mechanical property of mould. When using a mould comprising multiscale or multidensity structures, nanoimprinting is prone to fail to replicate the desired structures. The defect is mainly caused by the polymer flow behaviour in the multidensity mould producing non-uniform imprint height or residual layer [105, 112, 116]. This effect would be undesirable especially for full pattern replication process, which usually involving a breakthrough etching process to etch away the residual layer and further etch through the substrate.

On the other hand, by using mould with a higher Young's modulus and a resist with a lower viscosity, we can avoid mechanical deformation of the mould. By understanding the dynamics of the resist during nanoimprinting and factors that affect the flow, various plasmonic structure with interesting optical response can be realised using a simple NIL process.

In conclusion, despite being a relatively simple process to execute, there are many factors that can be utilised in the NIL technique in order to produce a broad range of nanostructures, either 2D or 3D. Some of these factors include (i) the NIL parameters, (ii) material and conditions of the mould and substrate, and (iii) chemical and physical properties of the resist. With this motivation in mind, the versatility and ability of the NIL process to produce different plasmonic devices is further explored in this thesis.

2.3 Conclusion

This chapter provided an overview of key concepts central to this thesis. This include a review of naturally occuring structural colour and its origin through some examples from nature. The discussion then focussed on plasmonics-based structural colouration. Part of this chapter was also dedicated to discussing human colour perception, basic colourimetry and colour mapping and the relation of spectral properties to the colour quality (i.e hue, saturation and brightness) which will be important in discussing results later in the thesis. Finally, nanofabrication methods that are conventionally used to realise plasmonic structures were reviewed and compared.

Chapter 3

Fabrication, Characterisation and Numerical Methods

This chapter will discuss all relevant nanofabrication and characterisation techniques as well as numerical methods used throughout this research project. The fabrication of the desired plasmonic structures requires a sequence of processes which involves multiple tools and techniques. Due to the nanoscale nature of the structures, high precision tools and simulations are necessary to successfully design and fabricate the plasmonic metasurfaces presented in this thesis. Lithography techniques such as electron beam lithography (EBL) and nanoimprint lithography (NIL) were the main processes used to pattern the nanostructures developed during this project. Supporting techniques, i.e post-patterning processes such as reactive ion etching (RIE) and thin film evaporation were also used to complete the fabrication of the plasmonic devices. It is worth mentioning that the focus has been on developing the NIL technique, but information about other relevant processes has been included for completeness. It also should be noted that, as discussed in the preface, some aspects of the fabrication required to produce the plasmonic devices were performed by a research fellow in the group, Dr Jingchao Song. The fabricated devices were then characterised using various techniques to determine the morphology and optical response of the samples. Different experimental setups were used to optically characterised the samples including reflectance spectra measurement. Most of the optical measurement presented in this work were undertaken in the School of Physics at the University of Melbourne using tailored benchtop optical systems. The following section discusses various imaging techniques such as scanning electron microscope (SEM), focused ion beam (FIB) milling and atomic force microscopy (AFM) to visualise and measure the morphology and cross-sections of the fabricated nanostructures. Finally, this chapter will outline the numerical methods utilised to simulate the designated plasmonic structures. This was undertaken to aid design and to develop an understanding of the relevant physics and the impact of fabrication artifacts on performance, and to refine designs with the aim of increasing sample fabrication efficiency and reducing the appearance of artefacts.

3.1 Fabrication Techniques

3.1.1 Electron Beam Lithography (EBL)

Electron beam lithography (EBL) is a top-down fabrication method that utilises a focused, high-energy electron beam to define a pre-determined patterns on an electron sensitive polymer film coated on a substrate. A schematic showing a typical EBL system is shown Figure 3.1(a). Energetic electrons from an electron source are focused and controlled by the condenser lens and aperture, before bombarding an electron-sensitive resist film, altering its chemical properties and, thus, allowing selective removal of either the exposed (positive tone resist) or non-exposed (negative tone resist) regions of the resist with a developer [117]. Unlike a photolithography process, the EBL resolution is not limited by light diffraction, thus has a superior patterning resolution with nanoscale precision. With the ability to create structures with dimensions down to several nanometers, EBL is the preferred patterning method for product development, proof-of-concept devices and also for defining patterns for the moulds used for nanoimprint lithography (NIL).

The Vistech EBPG 5000+ EBL tool at the Melbourne Centre for Nanofabrication (MCN) was used to expose the transverse nanostructure patterns as part of the fabrication of the NIL mould used in most of the project presented in this thesis. The tool operates at a 100 kV accelerating potential while the beam current and apertures can be varied from 50 pA to 100 nA and from 200 μm to 400 μm respectively, enabling a balance between the beam spot size and the current used. The tool can produce a minimum beam spot size of 2 nm when the minimum beam current of 200 pA is used with the 200 μm aperture. The system is also equipped with a scattered electron detector thus allowing sample monitoring before and after the beam exposure via SEM images. The tool is incorporated with a control system that allows automatic adjustments for astigmatism and permits sample tilt correction. Additionally, the laser interferometer system detects any changes in the substrate height, adjusting the focal plane as required and automatically realigning samples for multi-exposure processes. The resolution of the pattern, however, is not limited only by the EBL, but also by the resolution of the resists used [118].

Prior to the beam exposure, the patterns were first designed using the open source 2D CAD software, Klayout, which produces an GDSII output file. The Beamer software is then used to convert the GDSII file into the GPF file format recognised by the EBL tool. The software also provides tools for addressing pattern overlap, beam step size adjustment and controlling the distribution of the main and sub-fields. The software has the ability to set the beam step size, address any pattern overlap errors or perform proximity error correction (PEC). The EBL process relies on the use of electron sensitive polymer resists which can be either negative and positive tone resists. The energetic electron flux will either cross link (positive tone) or unlink (negative tone) the exposed resist. A positive tone resist has its chemical properties altered when the portion of the resist is exposed to the electron beam thus become dissolvable to the developer, while the unexposed region of the photoresist remains insoluble to the resist developer. This process is the opposite for the negative tone resist. The main positive resist used in this research is an A-type polymethyl methacrylate (PMMA) dissolved in anisole.

A typical lithography process is shown in Figure 3.1(b-e). Prior to EBL, the substrate was placed in an acetone bath (sonicated), followed by an isopropanol (IPA) bath for 5 minutes to clean the substrate thoroughly. The remaining IPA is rinsed with deionised water and blown dry with nitrogen. PMMA is then spin coated at a particular speed (depending to the desired thickness) and baked at 170°C for 5 minutes. The soft baking process promotes solvent evaporation in the samples thus preventing outgassing in vacuum. Depending on the conductivity and reflectivity of the substrate the resists may need the addition of a 20 nm thin conductive layer of chromium, so that there is no charge build up during e-beam exposure and the laser interferometer has a reflective surface to sense. The pattern was first created on a PMMA resist using a beam of electron to a particular dose (Figure 3.1(b)). The exposed region of the resist is then developed in a mixture of methyl isobutyl ketone (MIBK) and IPA in the ratio of 1:3 (Figure 3.1(c)). The development takes 1 min and is followed by rinsing the sample in fresh IPA. The fabricated pattern is then ready to undergo post-lithography processing such as metal deposition and/or deep reactive ion etching (DRIE) for device finalisation. For DRIE, a 20 nm metal layer (Al or Cr) is then deposited on the developed resist using the electron beam evaporation technique (Figure 3.1(d)) (details of this process will be discussed in the next section). The metal layer thus fills the uncovered region of the substrate. The final step is lifting off the PMMA layer (Figure 3.1(e)) which is performed in 70°C acetone with moderate agitation. This leaves only the metal mask on the substrate for the etching process.

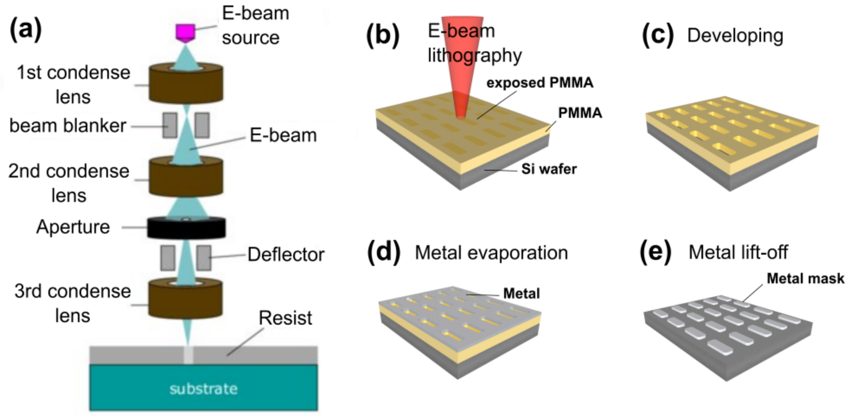

FIGURE 3.1: (a) Schematic of an electron beam lithography (EBL) system [119]. (b-e) Typical EBL process starting with patterning using electron beam on the resist, development, metal evaporation and lift-off to produce a metal mask.

3.1.2 Reactive Ion Etching (RIE)

Reactive ion etching (RIE) is a dry etching method that utilises a plasma to etch through material in certain areas of the sample. The schematic in Figure 3.2(a) shows the typical RIE system. Usually, the exposed area on the sample where no metal mask remains after the developing process will be etched away by the ionised gas (Figure 3.2(b,c)), thus producing micro- or nanoprotrusions (Figure 3.2(d,e)). This permits the fabrication of a silicon-based master mould for NIL applications. The Melbourne Centre for Nanofabrication (MCN) houses an Oxford Instruments PLASMALAB100 ICP380 to perform RIE. A blank silicon wafer is first loaded into the chamber and an oxygen plasma is created to clean the chamber. A Cr coated silicon substrate obtained following EBL and lift-off process, is then loaded into the DRIE chamber and once a vacuum of 5 mTorr is reached, 30 sccm of SF_6 and 70 sccm of C_4F_8 gases are pumped in alternate cycles into the chamber. The etching process takes place once a strong inductively coupled plasma (ICP) of these gases is ignited. The area with no mask on the silicon wafer is etched by SF_6, whilst the C_4F_8 polymer gas acts as a passivation buffer to control the etching rate of the silicon and allow for high aspect ratio etching. Both etching and the deposition of buffer layer are alternately take place during the DRIE process. The depth of the etching depends on the etching time. After the DRIE process is completed the Cr mask is stripped with a 10% HNO_3 30% $(NH_4)_2Ce(NO_3)_6$ solution and the polymer layer removed with a 1:9 $H_2SO_4 : H_2O$ bath for 20 s.

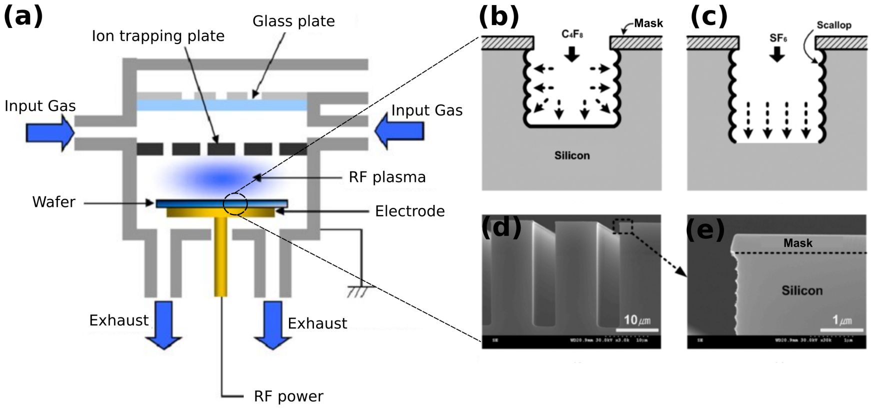

FIGURE 3.2: (a) Schematic of the reactive ion etching system [120]. (b,c) Schematic shows direction of etching using different type of gases. (d) Cross-sectional image shows structures formed after etching of Si wafer and (e) the enlarged image of (d) reveal the scallops formed at the sidewall of the structure due to the etching process [121]

3.1.3 Nanoimprint Lithography (NIL)

Nanoimprint lithography (NIL) is an alternative lithographic technique that permits rapid nanopattern replication by means of mechanical deformation from a master mould onto a polymer surface. NIL offers a straightforward, high-throughput and scalable manufacturing process, suitable for the focus of this thesis. Since NIL does not rely on a photon or a beam of charged particles to change the chemical properties of the resist, it, therefore, can produce structures with spatial dimensions not limited by light diffraction or beam scattering. The schematic in Figure 3.3 illustrates a typical pattern replication process using NIL. The mould and the resist-coated substrate are first aligned in the sample chamber (Figure 3.3(a)). The mould is then pressed onto the resist before a curing process takes place (Figure 3.3(b)). Depending on the type of resist used (e.g. thermoplastic polymer or UV curable), the cross-linking of the resist can be performed via UV exposure or heat treatment. Finally, the mould-substrate stack is demoulded, leaving the replicated patterns (Figure 3.3(c)). Throughout this thesis, either thermal or UV assisted NIL were used to fabricate large area template (> 0.5 cm) for plasmonic devices at high-throughput.

The Nanofabrication Lab at the Advanced Technologies Centre, Swinburne University of Technology houses the Nanonex NX B200 NIL tool which was used throughout the project. The NIL tool is capable of performing both thermal and UV NIL modes. It uses air cushion technology to press the mould onto the polymer-coated substrate which creates a homogeneous pressure distribution and avoids any mould slippage during the imprinting process which occurs commonly during mechanical imprinting. Various parameters such as pumping (vacuum) time, imprint temperature, pressure and time, UV exposure time and venting temperature can be set by the user permitting flexibility in performing nanoimprinting using moulds of various geometries or materials. The temperature and pressure can be set within a range of $0-250°C$ and $0-500$ psi respectively. The imprint and UV exposure time can both be set from 0 to 5 minutes. The sample holder is capable of handling different sizes and irregular shapes and also permits a full-wafer (3 inch) imprinting. Given the focus of this thesis, a detailed discussion of the NIL processes, both thermal and UV assisted, is given in Chapter 4.

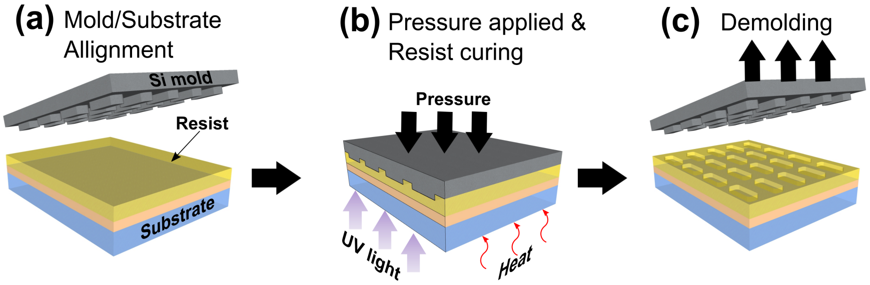

Figure 3.3: The nanoimprint lithography (NIL) process starts with (a) mould/substrate alignment and then (b) pressure is applied while the resist is cured either using UV light or high temperature. The mould/substrate stacks were then manually demoulded producing the replicated pattern (c).

3.1.4 Electron Beam Evaporation

During the fabrication of the plasmonic devices used here, the electron beam (e-beam) evaporation process is employed to deposit a thin layer of metal or dielectric onto the substrate as a mask layer or onto nanostructure patterns obtained from EBL or NIL. E-beam evaporation is commonly used in the plasmonic research community to deposit noble metals such as gold (Au), silver (Ag) and aluminium (Al) as well as dielectric films, such as, titanium dioxide (TiO_2) and silicon dioxide (SiO_2). Figure 3.4 below shows a simplified cross-sectional diagram of the e-beam evaporator illustrating its main components. The evaporation process should be performed in the vacuum environment where the chamber pressure is reduced to 10^{-5} Torr or less to avoid contamination, particularly from water vapour. The source of electrons is a tungsten filament housed in the electron gun. When sufficiently hot, it emits electrons which are then focused and deflected to strike the target material inside the graphite crucible. The high kinetic energy of the accelerated electrons is converted to heat when it hits the target which vaporises the metal target before being deposited onto the surface of the sample/substrate. McPeak et. al [122] provide a concise review of the approach for achieving high-quality plasmonic films. This involves proper control of important parameters such as the chamber pressure and substrate temperature.

Throughout this research project, an 10 kV Intlvac NanoChrome II electron beam evaporation system (located at the Melbourne Centre for Nanofabrication (MCN)) was used to deposit metallic thin films for masking purposes and also following the NIL process to create the resulting plasmonic metasurfaces. The samples were mounted in a central ring within the chamber directly above the crucible containing the target material to avoid shadowing effects due to directional deposition. The chamber is then pumped down to a pressure of about 7×10^{-6} Torr while the sample is rotated at 100 rpm. The target material is then evaporated by the incident electron beam and deposited onto the samples. The deposition rate can be set by the user and varies from $0.2 - 1.5\text{Å}/s$ (depending on material) and the thickness of the film is monitored by an in situ quartz microbalance. This permits production of good quality films with a low roughness. Finally, the sample is left to cool for 5-10 min and the chamber is then vented to atmospheric pressure.

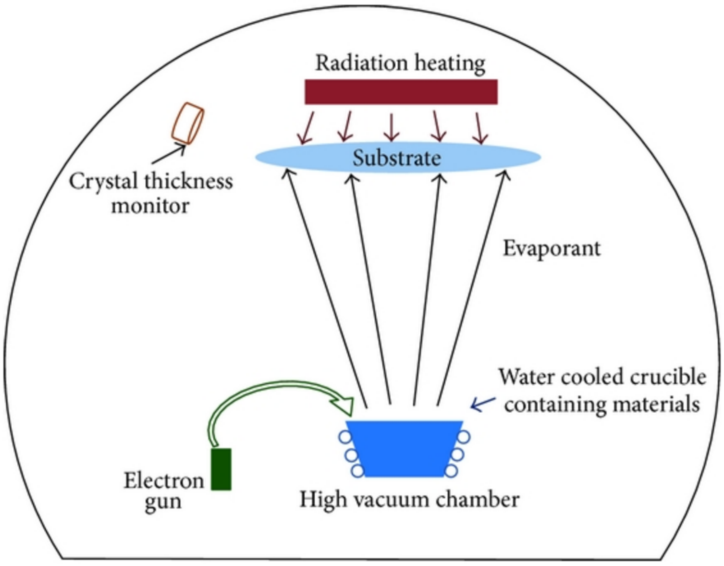

Figure 3.4: Schematic of the electron beam evaporator [123]

3.2 Optical Characterisation

The primary method used to study and characterise the optical performance of the fabricated plasmonic devices under various lighting conditions was optical spectroscopy. The experimental measurements were then compared with corresponding values obtained from simulations.

3.2.1 Bench-top Optical Setup for Reflectance Measurements

Reflectance measurements were obtained with a custom built optical cage setup which offers flexibility for spectral and polarisation sensitive measurements both in reflection and transmission. Figure 3.5 shows a schematic diagram of the reflectance measurement setup. A broadband tungsten-halogen lamp (HL-2000-FHSA, Ocean Insight) was used as a light source (wavelength range from λ = 360 nm to 2000 nm). Unpolarised light passes through the first objective lens (OL 1) of NA=0.15 (10× UPlan, Nikon) and the calcite linear polariser (GTH5M, Thorlabs), producing a collimated, linearly polarised light beam. The polarised light is then focused onto the sample by the second objective lens (OL 2). Ideally, to minimise any non-normal incidence effects, a collimated beam and a low NA lens could be used. However, this needs to be balanced with the size of the investigated area on the sample. The sample was mounted on an xyz mechanical stage (Thorlab, XR25-XZ and XR 50P) for easy navigation. The reflected signal is out-coupled by 50:50 non-polarising beamsplitters (BS 1 and BS 2) (Thorlabs BS016), to a fibre coupled Ocean Optics high quantum efficiency spectrometer (QE65000) and a CCD camera (Thorlab DCC1645C), after being focused by a 50 mm focal length lens (Lens 1 and Lens 2, Thorlabs LA1255-A). The computer-connected spectrometer captured the reflectance signal via *Spectrasuite*, the proprietary Ocean Optics spectrometer interface. A monitor is used to display the image produced from the CCD camera and permits visual navigation of the location of the collection area. For the reflectance measurements, particularly for characterising plasmonic colour, the reflectance from the off-array, unstructured metal film was used as a reference for normalisation. Note that for measurements requiring unpolarised light, the linear polariser can be detached from the cage setup.

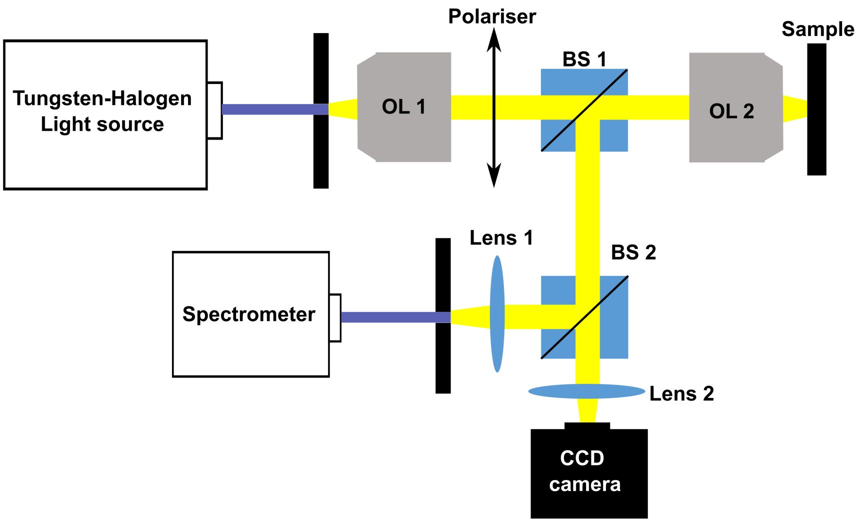

FIGURE 3.5: A schematic diagram of the optical cage set-up for reflectance spectra measurement.

3.3 Topographical Imaging of Fabricated Nanostructures

To inspect the quality and measure both transverse and vertical dimensions of the sample fabricated using electron beam lithography (EBL) and nanoimprint lithography (NIL), their morphology was characterised using a scanning electron microscope (SEM). Cross-sectional images were obtained by milling through the nanostructures using focused ion beam (FIB), integrated with the SEM system. Additionally, atomic force microscopy (AFM) was employed to retrieve the 3-dimensional topography of samples to corroborate measurements from the FIB-SEM system.

3.3.1 Morphological and Cross-sectional Imaging

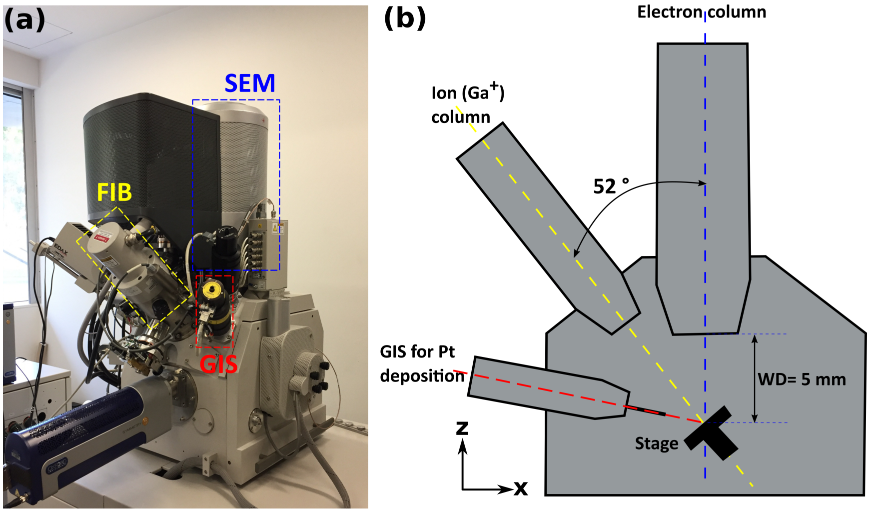

Figure 3.6: (a) Image of a FEI Nova Nanolab 200 comprising the scanning electron microscope (SEM), focused ion beam (FIB) and gas injection system (GIS) for Pt deposition. (b) Simplified schematic diagram of the combined FIB-SEM system in (a) showing the tilt angle and working distance (WD).

The morphology and cross-sectional images of fabricated samples were obtained utilising the scanning electron microscope (SEM) and focused ion beam (FIB) technique. SEM enables high-resolution imaging of structures with nanoscale features, which cannot be obtained with an optical microscope, by scanning a focused electron beam. Since the wavelength of the electron is much smaller than that of visible light, it is not limited by diffraction and can achieve a spatial resolution down to 0.5 nm [124]. The high-energy beam of electrons penetrates the sample to a depth of a few microns, depending on the accelerating voltage and the type of the sample's material. This electron-sample interaction produces several byproduct signals corresponding to secondary electrons, backscattered electrons, and X-rays which are collected by one or more detectors to form images and provide detailed information about the sample including the type of material [124]. Throughout this research project, secondary electron detection is utilised for imaging purposes. Focused ion beam imaging (FIB) on the other hand, has a similar operating principle to the SEM, but uses a beam of ions (e.g. Ga^+ or Ar^+) rather than electrons. While a FIB can permit imaging by using a low beam current [125], the ion-material interaction however, can cause modification to the surface of the sample. A FIB tool uses a focused, high-energy ion beam to mill into the sample surface with nanometer precision. By carefully controlling the energy and intensity of the ion beam, it is possible to vary not only the resulting transverse dimension but also the depth of milling. FIB milling can be used in conjunction with SEM to obtain cross-sectional images of the sample.

Throughout the project, a FEI Nova Nanolab 200 FIB/SEM (a FIB-SEM dual system) tool located at the Bio21 Advanced Microscopy Facility, was used to characterise the morphology and cross-section of the samples (Figure 3.6(a)). The FIB use Gallium (Ga) as the ion source. Figure 3.6(b) shows a simplified schematic diagram of the FIB-SEM dual system. To image the morphology of a non-conductive or electron-sensitive sample using SEM, a layer of gold or silver film (10 nm) was deposited as a conductive layer in conjunction with carbon tape to minimise charging effects i.e accumulation of charges on the surface of the sample, which can produce a distorted image. A focused image of the morphology of the sample was obtained by optimising several SEM parameters such as the voltage, aperture size, working distance and scanning rate to control the electron beam. For electron-sensitive material, a low voltage of 3 kV and aperture size of 68 pA or 0.27 nA were used to minimise the electron penetration depth and hence the reactivity of the material to the electron beam which can be damaging. Then the working distance (WD) is set to 5 mm, which is the optimum distance between the final pole piece of the lens to the sample when the image is in focus (Figure 3.6(b)). Figure 3.7(a) and (b) show representative SEM images of the morphology of rectangular cavities at magnifications of 1000× and 50000× respectively.

To obtain cross-sectional images of the structure, both the FIB and SEM systems are utilised, where the former used for milling into the sample and the latter for imaging. For this purpose, the height of the sample stage needs to be set at the eucentric height. This refers to the height of the sample where the ion beam, electron beam, rotation axis of the sample and the area of interest, intersect as such the observation area and the focus on the sample has minimal shift when the stage is tilted. A combined FIB-SEM system thus allows real time monitoring of the milling process. For FEI Nova FIB/SEM dual system, the eucentric height is optimised to 5 mm similar to the working distance. Then, the stage was tilted at an angle of 52°, which is the optimum tilting angle so that the normal to the sample's surface is parallel to the ion beam but at 52° to the electron beam (Figure 3.6(b)). This allows the milling process to be performed normal to the sample plane while imaging the cross-section at 52° with respect to the normal of the sample. The most important part of this step is to ensure that both beams intersect at the same spot since slight changes in the height of the stage can cause both beams to be misaligned and results in milling into an undesired region. Any required shift can be manually adjusted using the xyz-position knob to move the stage in xyz-direction. Alternatively, the beam shifter can be used to re-aligned the beams. On the other hand, an ion beam with a smaller aperture (98 pA) with a voltage of 30 kV was used over a short time interval image capture to ensure both SEM and FIB were aligned. For milling purposes, a larger aperture 0.4 nA ion beam was used. A layer of platinum (Pt) (300-400 nm) was deposited onto the sample surface prior to the milling process primarily as a protective layer (from the high energy ion beam) while at the same time allowing a clean cut through the structure (Figure 3.7(a) and (c)). A gas injection system (GIS) was used to precisely position the Pt source a few micrometer away from the sample surface. The electron beam was then used to deposit Pt onto the area of interest. To cut a cross-section, a step-like milling pattern was used. Then, the SEM was used to obtained an image of the cross-section and evaluate the depth of the structure. An example of a cross-sectional image of a sample is shown in Figure 3.7 (d) revealing the depth of the cavities.

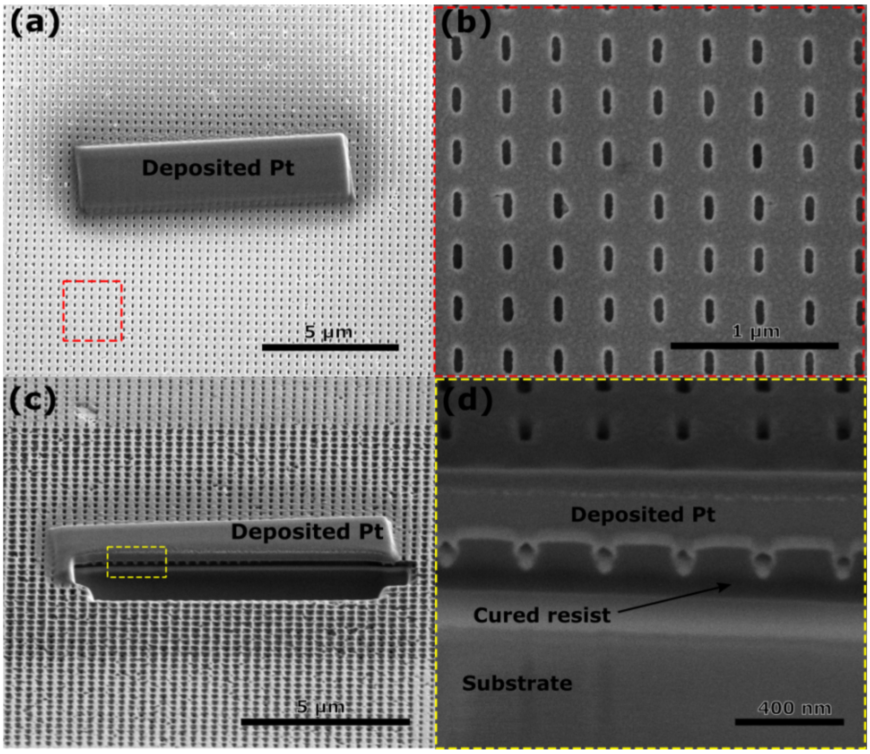

Figure 3.7: Representative SEM images of arrays of rectangular cavities at magnification of (a) 1000 x and (b) 50000x. Also visible in (a) is the deposited Pt layer used as protective layer and to obtain clean milling. (c) Tilted SEM images (at 52°) showing milled area using FIB exposing the cross-section of the structures as shown in (d).

3.3.2 Atomic Force Microscopy (AFM)

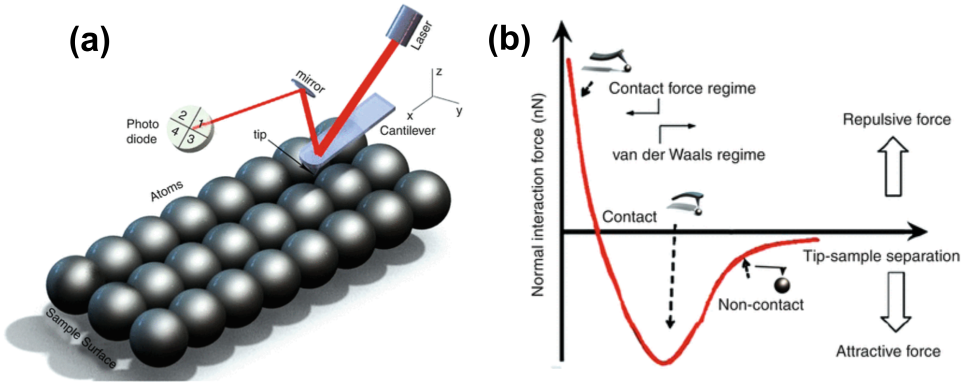

Figure 3.8: (a) Schematic showing the components and mechanism of an AFM. (b) Force curve as function of z-distance of the AFM tip to the sample's surface. [126]

Atomic Force Microscopy (AFM) uses a nanoscale probe to scan a surface to determine the three-dimensional topography on the nanometer scale. AFM has several advantages over optical and electron microscopy for this purpose. For example, electron microscopes generally generate a 2-dimensional image and require cross-sectional imaging to measure the vertical dimension. With AFM, a three-dimensional image of the structures can be acquired in a single scan. State-of-the-art AFM utilises a high aspect ratio tip with a size of 1 nm, thus allowing a resolution comparable to the electron microscope. Since AFM does not use an electron source, the sample can be either conductive or non-conductive.

AFM measures the force between the sharp probe and the surface at a nanoscale separation distance (0.2 nm-10 nm) [127]. The probe, which also known as the tip, has a radius of few nanometers and commonly made from Silicon (Si) or silicon nitride (Si_3N_4) [128], is attached to the end of a flexible cantilever. During scanning, the tip gently touches or taps the surface and the small force between the surface and the probe is recorded. The working principle of AFM can be described by a simple spring model. Using the simple Hooke's law, the amount of force between the tip and sample is highly dependent on the spring constant of the cantilever and their separation distance [127]. A schematic diagram of a typical AFM can be seen in Figure 3.8(a) below. The scanning movement of the tip is controlled by the piezoelectric scanner. The laser (usually at an infrared wavelength) illuminates the reflective back end of the cantilever and is reflected back to the photodiode detector which amplifies the signal and generates an image. The deflection of the cantilever due to the force is measured by a beam bounce method obtained by the detector which then generates a map of the surface topography. There are several types of atomic interaction at the different tip-sample distances as simplified in the force curve shown in Figure 3.8(b). There are three modes of AFM which correspond to the separation distance, i.e contact mode, tapping mode and non-contact mode.

A strong repulsive force (positive force) is dominant when the tip-sample distance reaches few angstroms, and the tip and sample are considered to be in contact. In the repulsive regime, AFM contact mode can be used to scan surface. During this mode, the cantilever bends as result of the force. Thus, by maintaining the deflection – the force between tip and sample's surface while scanning, the magnitude of the force is kept constant and thus an image of the surface can be acquired [128]. AFM contact mode can give a higher resolution and faster scanning but may be destructive as the tip could damage the surface of the sample especially for soft samples such as polymers or, conversely, hard surface can easily wear out the tip.

The non-contact mode corresponds to the situation when the separation distance is in the attractive force regime i.e the tip and surface are further away. This mode, however, is not recommended for topography imaging of the sample's surface as the tip is not in contact with the surface, but oscillates above it. Intermittent mode or tapping mode is an intermediate method between contact and non-contact mode which has the advantage of both approaches. In this mode, the tip lightly taps the sample surface at the cantilever resonant frequency. This mode is capable of producing a high quality image comparable to contact mode and at the same time minimising damage to the sample surface or the tip, since no lateral friction is applied to the sample [128]. The amplitude of the oscillation is maintained during raster scanning so that the image of the surface can be acquired.

In this project, an Asylum AFM MFP 3D with tapping mode was used to measure the topography of moulds produced by electron beam lithography (EBL) and imprinted samples from nanoimprint lithography (NIL). A high-aspect ratio tip with a radius of 1 nm (Budget Sensors, SHR 150) was used to permit the tip to reach as close to the bottom of the cavity as possible while producing high resolution images. The topography provided by AFM allows corroboration with the morphology and cross-sectional images obtained from the SEM and FIB. The tapping mode was used for measurements to avoid introducing defects into the sample and to preserve the lifetime of the tip. Figure 3.9 (a) shows a micrograph of the imprinted square cavities array obtained from an AFM scan in comparison with micrographs produced using SEM (Figure 3.9(b)). Figure 3.9(c) and (d) compares the vertical dimensions (imprint depth) of the sample obtained from AFM and FIB-SEM system respectively, reveal a comparable vertical dimension that is 110 nm of depth.

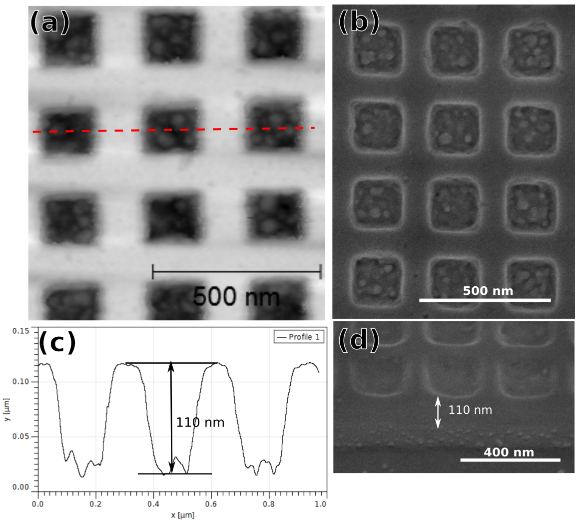

Figure 3.9: Micrographs shows morphologies of imprinted square nanocavities obtained from (a) AFM and (b) SEM, while (c) and (d) shows the vertical dimension i.e imprint depth obtained from both techniques respectively.

3.4 Numerical Methods

The laws of physics often utilise mathematical expressions not only to describe and understand physical phenomena, but also to predict the behaviour according to changes in dependent variables. Differential equations for example, which lie at the core of the laws of physics can be used to describe changes in physical quantities in space and time due to external stimuli. Solving differential equations with given inputs i.e initial conditions, provides predictions on how the physical quantities change at a particular time and point in space. There are two ways to solve differential equations: (i) analytically and (ii) numerically.

Analytic approaches can be used to solve simple ordinary differential equations (ODE) which usually involves derivatives of only one independent variable. Partial differential equation (PDE), however, are differential equations expressed in terms of derivatives of more than one independent variable. In most cases PDEs cannot be solved analytically to give the value of the time or space dependent variables. Therefore, an approximate numerical solution is required to determine solutions to the equations.

Numerical analysis has been widely used to solve complex physical problems represented by PDEs where the analytical solution is either non-existent or inefficient to obtain. With the aid of high powered servers, numerical analysis offers an appropriate way to simulate light-matter interactions including the plasmonic phenomena, with a high accuracy of approximate solutions, and advanced data visualisation. Since the plasmonic devices investigated in this work comprise complex geometries and are composed of material with non-trivial optical properties, numerical analysis, specifically the Finite Element Method (FEM) therefore, offers a solution for this purpose.

3.4.1 Finite Element Method (FEM)

Among numerical techniques, the Finite Element Method (FEM) is one of the most popular method. With recent increases in computational power, FEM has gained its popularity due to its flexibility in modelling a complex geometry by utilising the discretisation strategy. By decomposing the geometric domain of a boundary value problem into solvable finite 'mesh' elements, FEM permits a local increase in accuracy in particular areas of interest. With this strategy, a higher accuracy of approximation can be produced without significantly increasing computational time and memory. Due to its ability to address arbitrary geometries, any desired set of equations and the fact that the user can customise the FEM mesh to conserve computer power, it was chosen over other numerical approaches.

In brief, FEM solver converts the 'infinite' geometric domain to N 'finite' mesh elements. The higher the number of mesh elements, the more accurate the geometrical reconstruction hence the approximation to the solutions. Each of the elements represents a small spatial domain corresponding to the discretised weak form of the relevant PDE which is converted into algebraic expressions. These expressions are then converted into a matrix equation which can be solved. By using this discretised approximation strategy, the FEM solver replaces the original infinite-dimensional problem with a finite version which is then solved using matrix methods. The matrix size depends on the size of the domain over which the PDE operates and the desired approximation accuracy. Solving a large system accurately, therefore, requires solving a large matrix equation due to finer meshing. A rule of thumb employed here is to ensure no mesh element is larger than $\lambda/10$, where λ is the wavelength of the exciting field. A smaller mesh size, however, is required for a model with sub-wavelength dimensions. Since the FEM approach allows customised meshing size in areas of interest, a high mesh density can be applied where the field is changing rapidly with respect to space, such as inside nanoparticles, at metal dielectric boundaries or corners, and therefore can conserve computational power.

Since the FEM approach is a numerical procedure the solution obtained for the physical problems of interest are approximations and it is therefore, necessary to assess the accuracy of the solution. Established analytic results can be used as a reference and reproduced 'numerically' with a similar geometry for comparisons or alternative methods used to validate the results. To obtain sufficiently accurate results, the numerical solution has to be repeated with refined solution parameters (e.g. finer meshes) until variations between parameters of interest vary by less than 1%. It should be noted that the resulting numeric solutions have limitations as it only solves selected a mathematical model i.e PDEs with assigned boundary conditions, thus the prediction or approximations of the physical phenomena made should not be more than the information contained in the mathematical model. It has, therefore inherent discrepancies between the experimental and numerical solutions. The choice of a suitable mathematical model, geometry artefacts and properties of materials are important and completely identifies the insight into the real physical problem that can be obtained from the analysis. This will be discussed further in the next subsection where the FEM-based Wave Optics (WO) module in the COMSOL Multiphysics software is used to simulate light-plasmon interactions.

3.4.2 Wave Optics (WO) Module in COMSOL Multiphysics™

COMSOL Multiphysics™ is FEM-based simulation software used to solve various scientific problems including light-matter interactions. All simulations of the plasmonic devices under investigation in this work were performed by utilising the Wave Optics (WO) module built in the COMSOL Multiphysics™. The simulations were performed on a customised work station equipped with 32 2.6 GHz Intel Xeon E5-2650 cores, 251.9 GB memory and running 64-bit ubuntu 16. Figure 3.10 shows a simplified workflow to establish a simulation.

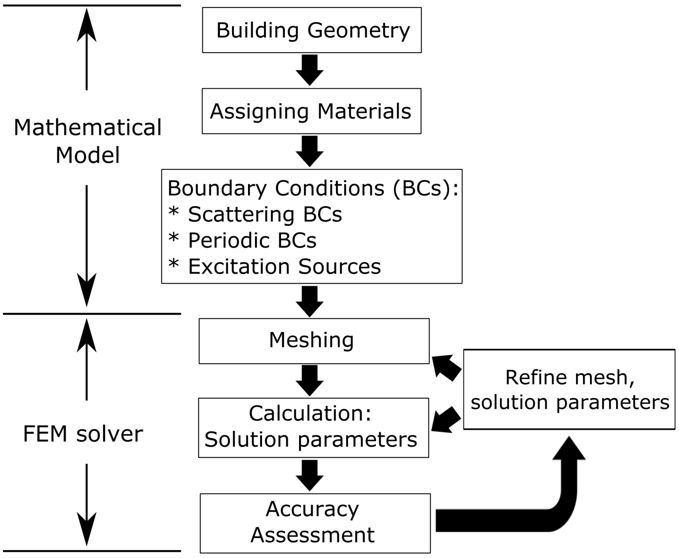

FIGURE 3.10: Typical workflow on designing and executing a FEM simulation on COMSOL (adapted from [129])

First, the geometry of interest is defined using the Geometry tool. The software is capable of solving three-dimensional boundary value problems and has the flexibility to simulate various complex geometries. The next step is to assign materials to the geometric domains created. The WO module solves the inhomogeneous Helmholtz equation:

$$\bigtriangledown \times (\mu_r^{-1} \bigtriangledown \times \vec{E}) - k_0^2 \epsilon_r \vec{E} = 0 \tag{3.1}$$

where μ_r^{-1} and ϵ_r are the relative permeability and permittivity tensor respectively, k_0 is the free space wave number and $\vec{E}$ is the electric field to be calculated. The FEM solver therefore require the input of the optical constants of every materials used in the simulation. In this work, optical constant of metals such as Ag and Al were taken from Rakic [130] as well as dielectric such as SiO_2 and TiO_2 were taken from Jonhson and Christy [131], and are also available in the COMSOL's material library. All materials were considered to be non-magnetic so μ_r was set to 1 in all cases. It is important to designate the boundary conditions on the geometric domain to be solved. Periodic boundary conditions (PBCs) can be applied on the lateral boundaries to simulate the collective optical response of an infinite array. On the other hand, scattering boundary conditions (SBCs) are used to simulate the environment of individual plasmonic structures. SBCs can be assigned with or without an incident field of excitation for a single structure and are transparent to specified wavelengths. Alternatively, a point source such as electric point dipole can be used to simulate the coupling of a quantum light source to a plasmonic structure. For periodic structures, ports can be use as the source of excitation with tailorable properties such as polarisation state and angle of incidence. At the same time, ports also act as a 'detector' to 'measure' the scattered light carried in different diffraction orders while also ensuring that those are not reflected back into the modelled domain. The next important step is to divide the geometric domain into finite sized mesh elements. More mesh elements used means a more faithful reproduction of the geometry. Although this will produce higher accuracy solutions, the trade-off is a longer computational time and the requirement for more memory. Conversely, although larger mesh elements size will reduce the computing time, this comes at the cost of accuracy. Therefore, the size of the elements need to be carefully chosen so that computational time and accuracy can be balanced. In this work, mesh size of $\frac{\lambda}{10}$ to $\frac{\lambda}{5}$ were used where λ is the wavelength of the exciting field. The advantage of the FEM approach is that it permits local mesh size customisation and, as such, particular areas of interest can be designed to have a higher density of mesh to increase local accuracy. Figure 3.11 demonstrates the effect of mesh on the accuracy of the simulation results. Although a finer mesh gives more accurate results but it will require more computational power and longer computational time. For example, a model with a coarser mesh size (30 nm) shown in Figure 3.11(a) took only 14 seconds to complete the calculation in contrast to that with the finer mesh (1 nm) which has completion time of 60 seconds. Finally, calculations can be performed where parametric sweeps are employed if the simulation requires spatial variation of the geometric domain or changes in the initial condition of the excitation source such as the wavelength or angle of incidence.

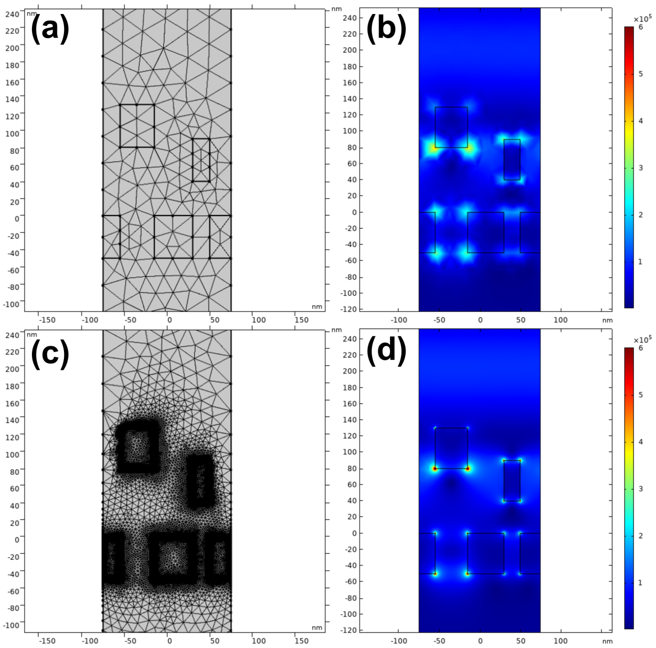

FIGURE 3.11: Different meshing sizes are applied to aperiodic grating simulation. (a) Coarser mesh (30 nm) and (b) the simulated electric field. (c) Finer mesh (5 nm) and (d) the corresponding simulated electric field.

3.5 Conclusion

In summary, to produce specified plasmonic devices, multiple nanofabrication techniques such as electron beam lithography (EBL), reactive ion ethcing (RIE), electron beam evaporation and nanoimprint lithography (NIL) were used. The EBL and post-EBL process (developing, metal mask evaporation and lift-off) were performed to pre-pattern the structure and prepare the substrate for etching. The RIE is used to etch the unmasked region of the substrate thus producing nanoprotrusions on the substrate (usually required for the fabrication of master mould for NIL). The NIL technique is used to replicate patterns from the mould onto a resist-coated substrate followed by the metal evaporation to complete the fabrication of plasmonic devices. The fabricated samples were optically characterised using benchtop setups for reflectance spectra measurement. On the other hand, some of the techniques used for imaging and measuring the morphology/topography of the fabricated samples such as scanning electron microscopy (SEM), focused ion beam (FIB) milling and atomic force microscopy (AFM) were also outlined. Any variations specific to particular experiments will be discussed in the relevant sections. The details of the equipment specifications and parameters are also included to provide sufficient information for reproducibility. Finally, a brief background and discussion of numerical methods i.e the finite element method (FEM) used to simulate the plasmonic structures via COMSOL Multiphysics is also presented in the chapter.

Chapter 4

Nanoimprint Lithography (NIL) Process Optimisation

The nanoimprint lithography (NIL) technique was developed with industry-scale production of nanostructures in mind. Even in the early stages of its development, nanoimprint lithography (NIL) demonstrated high-throughput and wide-area fabrication of nanoscale structures [110, 132]. Since then it has attracted substantial interest as an alternative top-down fabrication approach for both the scientific and industrial community. To ensure excellent quality of pattern replication, there are three particular aspects that need to be considered in the process: (i) the specific details of the NIL process parameters, (ii) the material and conditions of the mould and substrate, and (iii) the chemical and physical properties of the resist. These are the important components of the NIL process which govern the dynamics of the resist during the imprinting process and, hence, the resulting replicated patterns. This chapter will, therefore, discuss the details of the pattern replication process with regards to these aspects, via thermal and UV-assisted NIL, for fabrication of the plasmonic structures presented in this thesis. Both NIL modes were performed on different types of substrates suitable for different applications such as plasmonic colouration and other plasmonic structures. The findings in this chapters also helped in the development of the novel multilevel NIL method and the NIL process sheet (see Figure A2) for future reference.

4.1 Fabrication and Preparation of the Master Mould

Throughout the research presented here a silicon (Si) mould was used for the NIL process due to its high Young's modulus and durability [133]. The schematic in Figure 4.1 shows the fabrication for a Si master mould which starts with the pre-patterning process on a spin-coated PMMA resist on a Si wafer (Figure 4.1(a)), using EBL as described in Chapter 3. The exposed region of the resist is then developed in a mixture of methyl isobutyl ketone (MIBK) and IPA in the ratio of 1:3 (Figure 4.1(b)) before a layer of metal (Al) to act as a mask is deposited, filling the uncovered region of the Si surface (Figure 4.1(c)). Next, the remaining resist is lifted-off using acetone, leaving only the metal mask for the etching process (Figure 4.1(d)). The deep reactive ion etching (DRIE) technique is used to etch the unmasked Si region to create the nanoprotrusions required for the pattern replication process using NIL (Figure 4.1(e)). Before the mould can be used for nanoimprinting, the mould is coated with an anti-stick (trichlorosilane) layer to reduce the surface energy on the Si thus producing a hydrophobic surface (Figure 4.1(f)). This ensures minimum adhesion between the mould and the resist during imprinting.

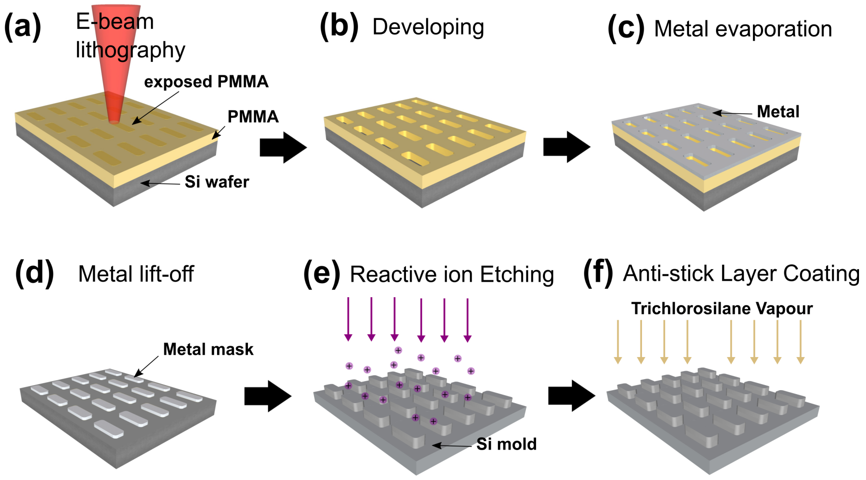

FIGURE 4.1: Schematics showing steps involve in fabrication of Si mould. (a) Pattern writing on PMMA using EBL, (b) developing process to remove exposed resist,(c) evaporation of metal mask using e-beam evaporator, (d) lift-off process to remove PMMA-metal layers, (e) etching via DRIE and (f) anti-stick (trichlorosilane) layer coating via vapor deposition technique.

The details of the trichlorosilane coating process on the Si mould are depicted in the schematic shown in Figure 4.2 . First, the Si mould is treated under an oxygen plasma (Figure 4.2 (a)) (Tergeo Plasma Cleaner, 6 sccm of O_2, 240 mTorr chamber pressure and at power of 100 W for 1 minute) to promote growth of a temporary hydroxyl (OH^-) layer on the surface of the mould which induces a hydrophilic property of the surface. This ensures adhesion of the vapourised silane particles onto the mould surface, thus producing a homogeneous coating. The vapour-phase deposition is then performed in a vacuumised glass bell jar dessicator (Figure 4.2 (b)). A small amount (50-100 μl) of Trichloro(1H,1H,2H,2H-perfluorooctyl)silane (Sigma Aldrich) is dispensed into a small petri dish placed at the bottom of the bell jar, while the Si mould is placed above the petri dish as shown in Figure 4.2 (b). The bell jar is vacuumised for about 1 hour to coat the silane layer. After the deposition, the silane-coated mould is rinsed in isopropanol to remove excess silane followed by rinsing with deionised water (Figure 4.2 (c)). A quick examination can be performed to determine the hydrophobicity of the mould by looking at the contact angle of a drop of water on the Si mould. A contact angle of more than 90° indicates hydrophobicity while if it less than 90° indicates hydrophilicity (schematic in Figure 4.2 (d)).

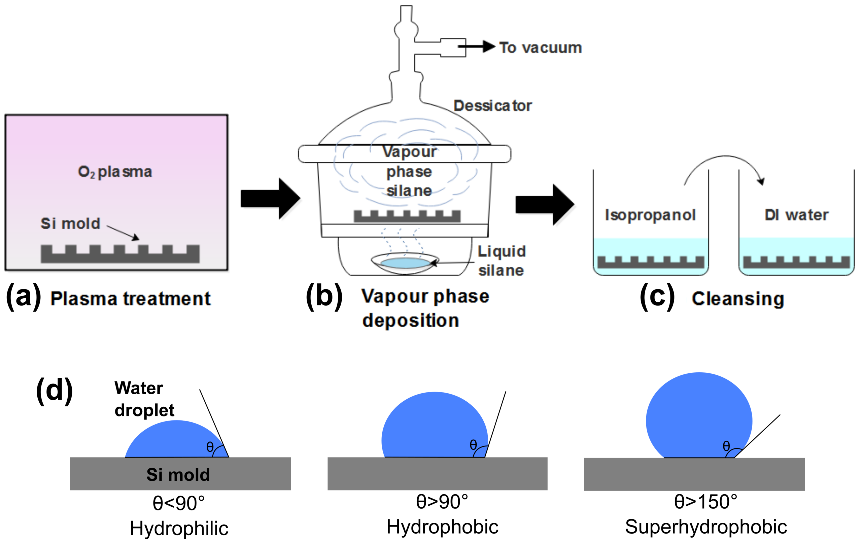

FIGURE 4.2: Schematic of the silanization process starting with (a) oxygen plasma treatment, (b) vapour-phase deposition and end with (c) cleansing process.(d) Schematic shows the relation of the hydrophobicity of the mould surface and the contact angle.

4.2 Thermal and UV-assisted NIL Process

Prior to the pattern replication process, the substrate is first prepared appropriate to the NIL mode to be used i.e thermal or UV. Thermal NIL was utilised to create embossed template on Si substrate coated with a thermopolymer resist i.e Poly(methyl methacrylate) (PMMA, M_w = 15k, Sigma Aldrich). Firstly, the PMMA solution (3 w%) is dispensed onto the substrate before spin coating at 1000 rpm, creating a 130 nm thin PMMA layer. The PMMA-coated Si substrate is then soft-baked at 150°C for 5 minutes to remove remaining solvents, thus solidifying the PMMA layer. On the other hand, for the UV-NIL process, a cleanroom grade glass substrate, transparent to the UV light, is used to permit resist curing via UV exposure. First, a small amount of underlayer resist (NXR-3023, Nanonex) is dispensed onto the glass substrate before spin coating at 4000 rpm to create a thin adhesion layer (150 nm). The substrate is then soft baked at 160°C for 3 minutes to permit the solvent to vaporise. Then, a 100 nm thin UV curable resist (NXR-2030, Nanonex) is coated onto the adhesion layer via spin-coating at 1500 rpm. Layer-by-layer spin coating can be performed if a thicker layer of UV curable resist is needed. Both NXR-3023 and NXR-2030 resist have refractive index of n =1.45.

Figures 4.3 and 4.4 show one of the examples of TNIL and UV-NIL processes and parameters that were used in this study. Generally, the NIL process starts by aligning the resist-coated substrate with the Si mould in the sample chamber of the Nanonex's NX B200 NIL tool (Figure 4.3(a)). Then, air in the chamber is pumped out to create a vacuum (Figure 4.3(e)) to remove trapped air from the sample. This process is important to avoid incomplete resist filling in the cavity (on the mould) due to the trapped air. The vacuum pressure is held for two minutes (by default). If thermal NIL is used, the temperature of the sample is increased to a 'pre-temperature' set by the user (Figure 4.3(b)), which usually slightly lower than the glass transition of PMMA, (T_g = 105 °C) for example 100°C as exemplified in Figure 4.3(e). Then, the temperature is held constant while the pressure applied on the mould is increased to the imprint pressure set by the user (Figure 4.3(c)), which in the case shown in Figure 4.3(e) is 400 psi. At this stage, both the mould and the resist-coated substrate are firmly held in their position due to the increase in temperature and pressure. The temperature is then ramped up to the imprint temperature, for example 150°C, set above the glass transition temperature of PMMA. At this stage, the PMMA layer is 'softened' to its glassy state while both temperature and pressure are held constant (Figure 4.3(c,e)) for a period of time called the imprint time which in this case is set to three minutes. Once the imprinting time is reached, the resist is cooled to about 40°C (this can be adjusted by the user) to solidify the imprinted resist, before the chamber is vented to a atmospheric pressure. The mould-substrate stack is carefully demoulded using a sharp razor blade and a nitrogen gas jet (Figure 4.3(d,e)).

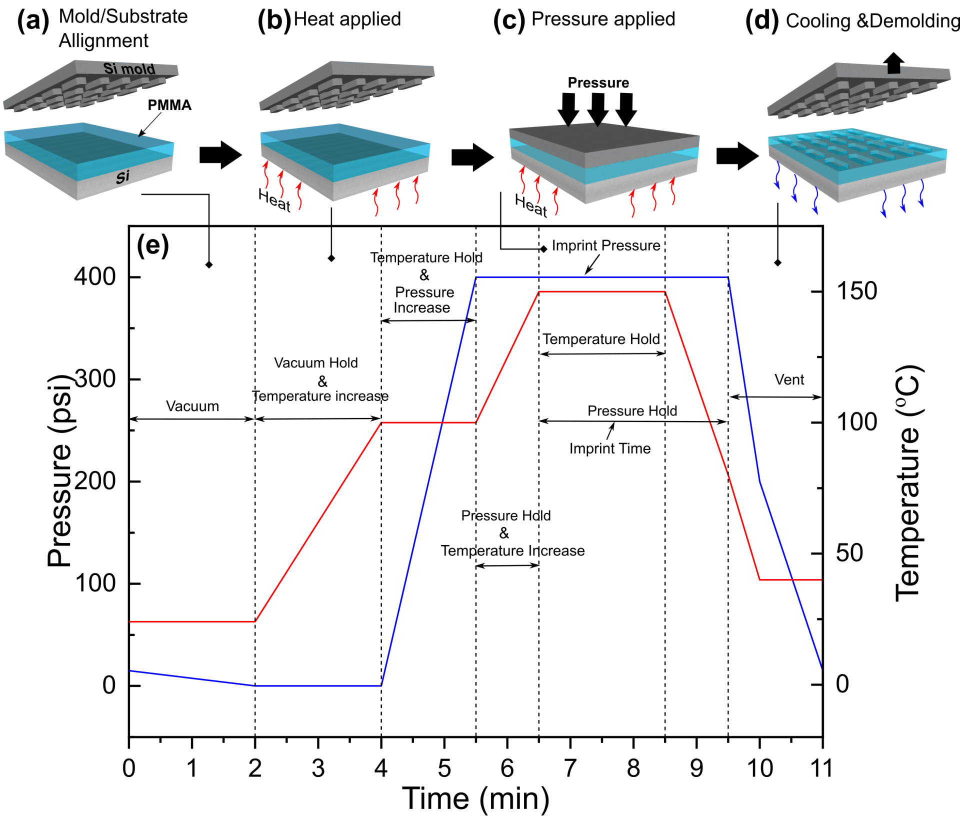

FIGURE 4.3: (a-d) Schematics of thermal nanoimprint lithography (T-NIL) process. (e) The plot shows the steps and parameters of a representative TNIL process which involve the interplay between pressure and temperature variations.

As opposed to thermal NIL, the UV assisted NIL process can be carried out in a room temperature environment as there is no heating involves to cure the resist. After the air is pumped out of the chamber and the vacuum condition is held for two minutes minutes (Figure 4.4(a,d)), nitrogen gas is pumped into the chamber thus increasing the pressure applied onto the mould until it reaches the imprint pressure set by the user. Since the resist used is in the liquid phase and low in viscosity, the pressure needed is relatively small, for example 50 psi. The imprint time set by the user determines the length of time over which the imprint pressure is held. In the representative UV-NIL process shown in Figure 4.4, once the imprinting time reached one minute, the resist is cured under UV light exposure for 45 seconds (this however, depends on the thickness of the resist), while the pressure is still applied onto the mould (Figure 4.4(b,d)). Following the curing process, the chamber is vented and the sample can be demoulded (Figure 4.4(c,d)) as described before. Following the demoulding process, the negative pattern i.e nanocavities created by the mould nanoprotrusions are ready for post-NIL processing such as a metallisation process or etching to complete the fabrication of plasmonic devices.

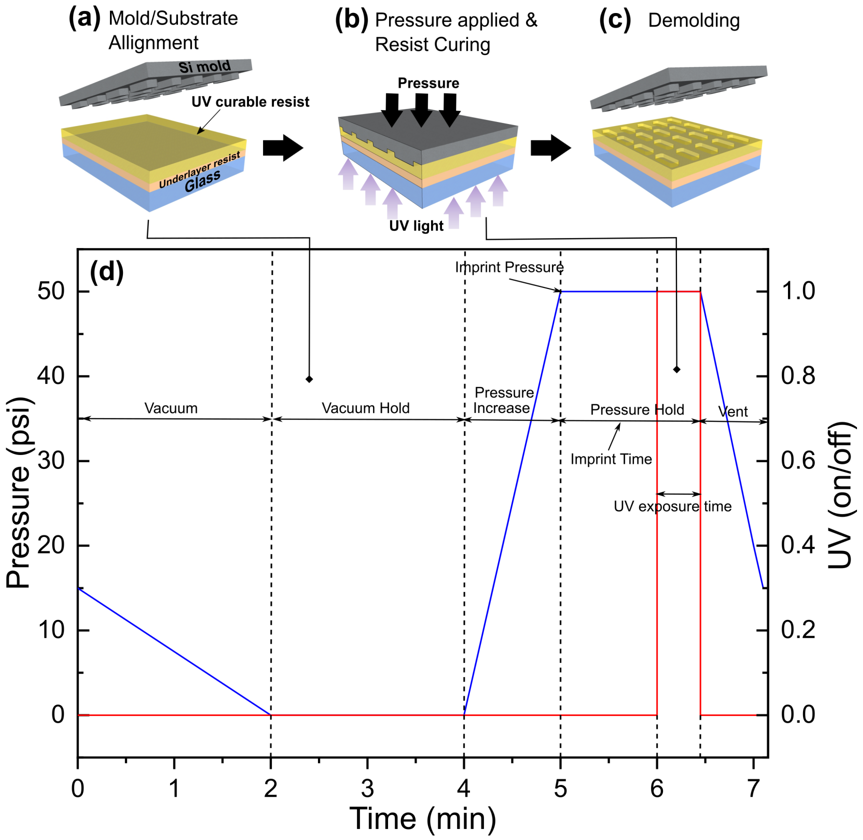

Figure 4.4: (a-c) Schematic of UV-assisted nanoimprint lithography (UV-NIL) process. (d) The plot shows the steps and parameters of a representative UV-NIL process which involve the interplay between pressure and UV exposure.

4.3 Dynamics of Polymer Resist In Imprinting Process

In NIL, the quality and conformity of the replicated lateral and vertical geometry are highly dependent on the flow behaviour of the resist through the nanochannels on the mould upon imprinting i.e the cavity-filling mechanism of the resist. The mould-resist contact results in a net pressure, $P_{contact}$, between the mould and resist, contributed by the external pressure, P_{ex} applied to the mould; and the pressure difference, ΔP_{cp} in the cavity [134], resulting in squeeze flow and capillary flow of the resist respectively, into the channeling on the mould

$$P_{contact} = P_{ex} + \Delta P_{cp}. \tag{4.1}$$

For convenience, we can discuss both types of flow mechanism independently. By considering the polymer resist as an incompressible liquid with constant viscosity and solving the Navier-Stokes equation assuming nonslip boundary conditions on the surface of the stamp and substrate, a basic model for the squeezed polymer flow below the stamp protrusion is obtained. According to this model, the following expression, known as the Stefan equation [133], is considered for a mould consisting of finitely long rectangular protrusions and cavities as shown in Figure 4.5

$$\frac{1}{h_f^2} = \frac{1}{h_0^2} + \frac{2F}{\eta_0 L s^3} t, \tag{4.2}$$

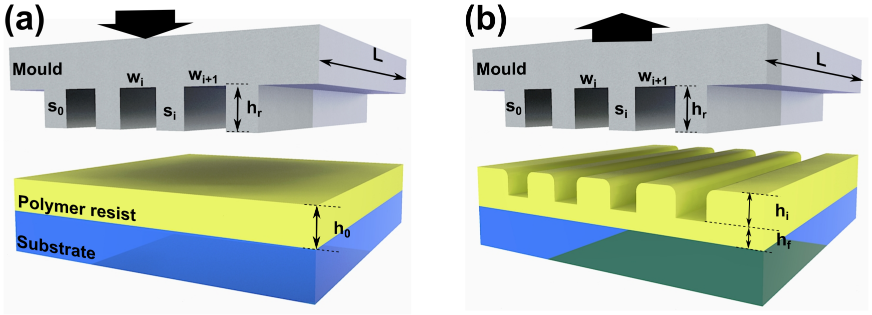

Figure 4.5: Schematic showing the geometrical definitions used to describe the flow of the resist for a mould consisting finitely long rectangular protrusions and cavities (a) before and (b) after the imprinting process. L is the length of the mould, w is the width of the cavities, s is the width of the protrusions, h_r is the height of the protrusions, h_i is the depth of the imprinted structure and h_0 and h_f is the initial and final thickness of the resist polymer respectively (adapted from [112])

where h_f is the final thickness of the film (also referred as the residual layer), h_0 is the initial thickness of the film, F is the applied force, t is the imprint time, η_0 is the viscosity of the polymer, L is the length of the mould and s is the width of the protrusions that in contact with the polymer. For a mould with a constant fill factor, v and assuming that the depth h_i and width w of the cavities and the initial thickness, h_0 are known, the final thickness, h_f of the film after imprinting can be directly deduced from the law of conservation of polymer volume

$$h_f = h_0 - v h_i \quad \text{where} \quad v = \frac{\sum_i w_i}{\sum_i (s_i + w_i)}. \tag{4.3}$$

Considering that the mould is under a constant external applied pressure, P_{ex} as such that $P_{ex} = F/sL$, Stefan's equation (Equation 4.2) above can be simplified and written in terms of the pressure

$$P_{ex} = \frac{\eta_0 w^2}{2t} \left(\frac{1}{h_f^2} - \frac{1}{h_0^2} \right). \tag{4.4}$$

Similarly, for the mould comprised of cylindrical shape protrusion with radius r, Equation 4.4 for pressure can be presented as

$$P_{ex} = \frac{3r^2\eta_0}{4t}\left(\frac{1}{h_f^2} - \frac{1}{h_0^2}\right). \tag{4.5}$$

Another factor that influence the dynamics of the resist is the pressure drop, ΔP_{cp} in a cavity/capillary which governed the capillary flow. The pressure drop can be defined as the pressure difference between two ends of a cavity, $\Delta P_{cp} = P_2 - P_1$, where P_1 and P_2 are the pressure at two points, such as at either end of a cavity. The volumetric flow rate, Q of the viscous polymer into a cavity is directly proportional to the pressure variations, $Q \propto \Delta P_{cp}$. By considering a mould consist of cylindrical-shaped cavity and assuming that the polymer is an incompressible fluid, the relation between Q and ΔP_{cp} can be written as the Hagen–Poiseuille equation [135]

$$\Delta P_{cp} = \frac{8\eta_0 h Q}{\pi r^4}, \tag{4.6}$$

where h and r is the height and radius of the cavity respectively. The Hagen-Poiseuille law, which is analogous to Ohm's law for fluid flow, incorporate the proportionality factor of hydrodynamic resistance also know as viscous resistance, R [136]

$$\Delta P_{cp} = RQ \quad \text{where} \quad R = \frac{8\eta_0 h}{\pi r^4}. \tag{4.7}$$

By considering that the volumetric flow rate, $Q = \frac{dV}{dt}$, where dV is the volume of the polymer which flows through the cross-section of the capillary in the time dt, Equation 4.7 can be rearranged to give

$$dV = \frac{\Delta P_{cp}}{R} dt. \tag{4.8}$$

At the end of any time, t, the liquid will have travelled a distance, h, along the capillary and the meniscus will have arrived at some point where it is moving with the velocity, $\frac{dh}{dt}$. By replacing $dV = \pi r^2 dh$ into Equation 4.7, we can now derive the Lucas-Washburn equation [137]

$$\frac{dh}{dt} = \frac{\Delta P_{cp}}{\pi r^2 R} \tag{4.9}$$

Solving the Lucas-Washburn first-order differential equation will gives the distance the fluid penetrates into the cavity, h. Equation 4.9 also indicate that a smaller cavity leads to a higher viscous resistance and therefore results in a lower filling rate (velocity) of the resist into the cavity.

4.3.1 Factors Affecting the Imprint Quality

Equations 4.2-4.9 above therefore imply that the flow behaviour of the resist during imprinting is regulated by the interplay of three major factors namely (i) the NIL process parameters (e.g. pressure and imprint time), (ii) the chemical and physical properties of the resist (e.g. viscosity of resist), and (iii) the material and conditions of the mould (e.g. dimensions and density of nanostructures) and substrate. These factors will eventually determine the quality of the resulting patterns and therefore need to be taken into account when performing NIL.

To investigate the effect of process parameters to the resist filling behaviour into the cavities during thermal NIL, the imprint temperature and pressure were varied. The thermal NIL process used here was previously discussed in Figure 4.3 in Section 4.2. Other process parameters such as imprint time, 'pre-temperature' and venting temperature were kept constant. During the thermal NIL process, the solid PMMA on the substrate is first 'soften' to its glassy state by heating to a temperature of either 130°C or 150°C before being imprinted with the mould with a pressure varying from 200 psi to 400 psi. Due to the thermoplastic nature of the PMMA resist, its viscosity tends to decrease as the applied temperature increases due to the temperature-dependent viscosity, as expressed by the Arrhenius equation [138]

$$\eta_0 = k \exp(E_0/RT) \tag{4.10}$$

where k is a constant, E_0 is the activation energy, R is the universal gas constant and T is the applied temperature (in Kelvin).

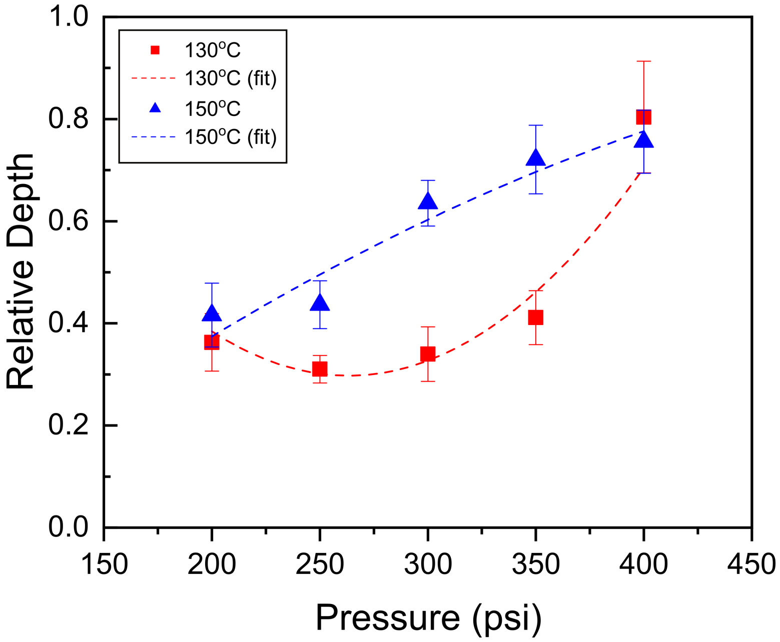

FIGURE 4.6: Plot showing relative depth of imprinted structures obtained from TNIL as a function of imprint pressure for different imprint temperature namely 130°C (red marker) and 150°C (blue marker). The dashed lines represent the line of best fits for corresponding temperatures.

The plot in Figure 4.6 shows the relation between the relative depth for different imprint temperatures and pressures. The height of the protrusion on the mould and the depth of the replicated pattern were measured using AFM. The relative depth, R_d is defined as the ratio of the depth of the imprint, h_i to the actual height of the corresponding feature on the mould, h_0 ($R_d = \frac{h_i}{h_0}$). The closer the value of R_d is to unity, the closer the depth of the imprinted structures to the actual height of the nanoprotrusions thus depicting high replication fidelity. The plot indicates that the relative depth increases with both temperature and pressure. In addition with high applied pressure (400 psi), at a higher temperature of 150°C, the viscosity of the PMMA decreases thus assisting the flow of the resist into the cavities. Figure 4.7 shows SEM images of the morphology of nanostructures comparing various lateral geometries on the mould (Figure 4.7(a-c)) to the resulting patterns imprinted on the substrates (Figure 4.7(d-f)) depicting high fidelity of the lateral geometries. Additionally, the AFM images in Figure 4.8 reveal that the vertical dimension i.e the height of the structures on the mould is comparable to the depth of replicated patterns on the substrate.

Although capable of producing high resolution patterns, thermal NIL, however, is a time consuming process since it requires heating and cooling of the resist. Furthermore, it requires very high temperatures and pressures to achieve a relative depth close to unity, which can be detrimental to the durability of the mould and lead to deterioration of the anti-stick layer on the mould [139]. UV-assisted NIL on the other hand, can be performed at room temperature and require only a relatively low imprint pressure due to the intrinsically low viscosity UV curable resist (NXR-2030, Nanonex) as described by Equation 4.5. The time taken for pattern replication via UV-NIL process, therefore, is much less in comparison to thermal NIL. As shown in the SEM images of Figure 4.9, various patterns have been successfully replicated with high fidelity via UV-NIL using pressure of 50 psi, 1 minute of imprint time and 45 seconds of curing time (UV exposure)(detail of the process is described in Section 4.2 in Figure 4.4). Furthermore, the depth of the imprinted structures is consistent with the height of the nanoprotusions on the mould as measured by AFM as shown in Figure 4.10, indicating high fidelity pattern transfer.

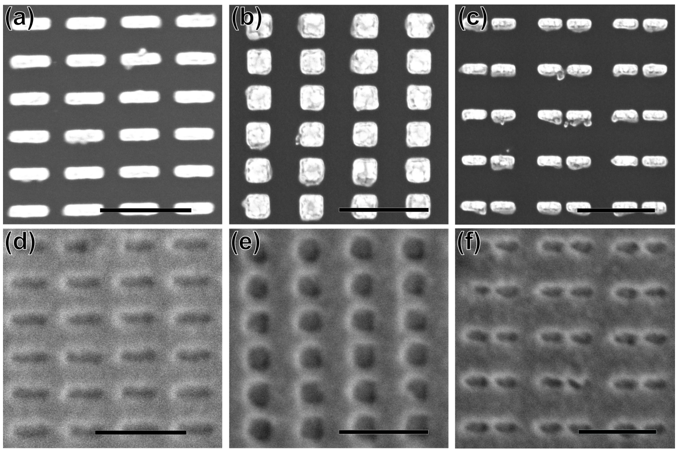

Figure 4.7: SEM images show the morphologies of various nanostructures on (a-c) Si mould and (d-f) replicated patterns on imprinted samples produced via TNIL. Scale bars are 500 nm

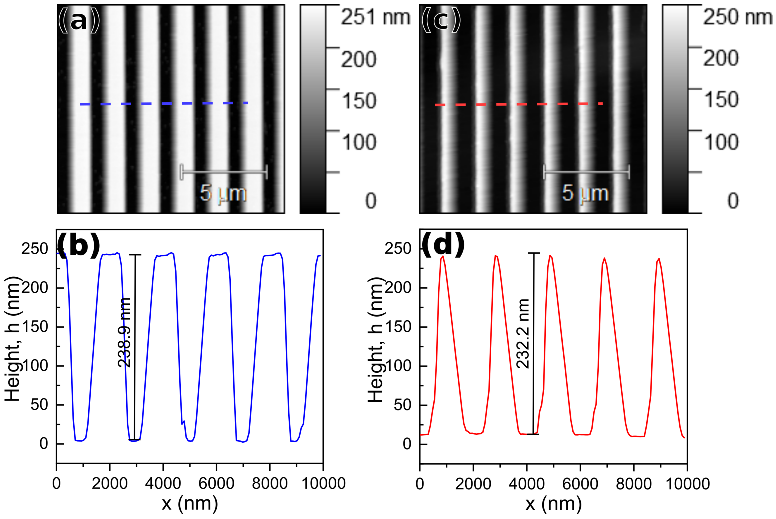

Figure 4.8: AFM images of micrograting on (a) the mould and (c) imprinted sample obtained by using TNIL. Height profile of (b) the mould and (d) imprinted sample from cross-section of image in (a) and (c).

Considering that the NIL parameters have been optimised and the physical and chemical properties of the resist are fixed as per manufacturers specifications, the resulting imprinted structures also depends on the third factor i.e the material and condition of the mould and substrates. In thermal NIL, it is important to have both the mould and the substrate made up of material with similar thermal expansion coefficients, α_L. This is because presence of any anisotropy in heat expansion due to increasing temperature can introduce a thermally-induced defect where one of the materials has a relatively rapid expansion rate [133]. SEM images in Figure 4.11 (a) exhibit slip-like defects occurring on the imprinted structures when a nickel (Ni) mould with $\alpha_L = 13.6 \times 10^{-1} {}^{\circ}C^{-1}$ [140] is used to imprint onto a Si substrate with $\alpha_L = 2.4 \times 10^{-1} {}^{\circ}C^{-1}$ [140] . This issue, however, is not present in UV-NIL. This process, however, requires either the mould or substrate to be transparent to UV light to allow cross-linking of the resist via UV exposure. Another major issue in the NIL process is the presence of particulate contaminants which can create crater-like defects that are larger than the size of the contaminant (Figure 4.11 (b)). Although there are few airborne particles present in a cleanroom environment, particulates usually originate from tools or chemicals used during sample preparation and can be minimised by mounting an ultra-fine filter in the nozzle of the resist dispenser (e.g. 0.1-0.2 μm PTFE syringe filters).

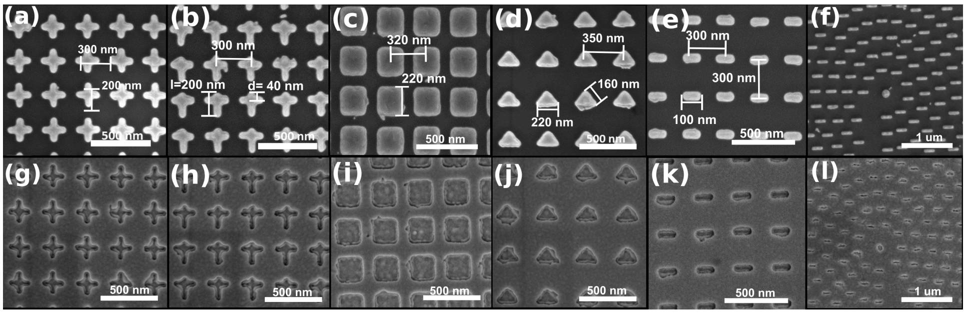

FIGURE 4.9: SEM images show the morphologies of various nanostructures on (a-f) Si mould and (g-l) replicated patterns on imprinted samples produced via UVNIL.

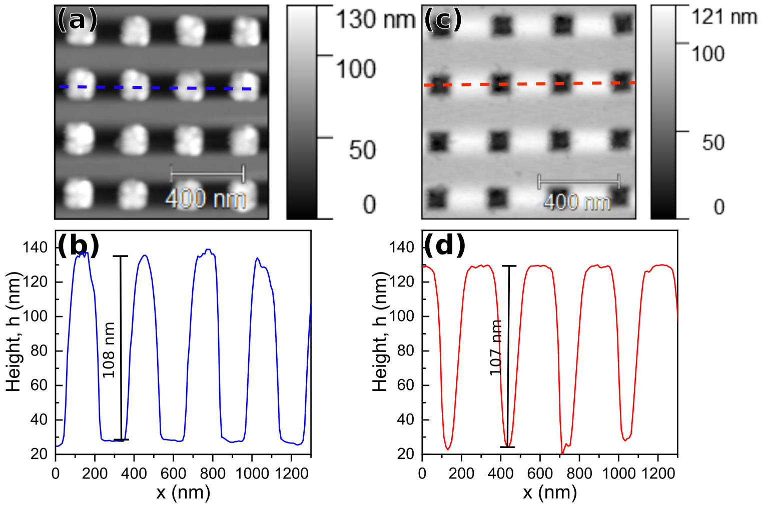

FIGURE 4.10: AFM images of micrograting on (a) the mould and (c) imprinted sample obtained by using UV-NIL. Height profile of (b) the mould and (d) imprinted sample from cross-section of image in (a) and (c).

Additionally, the density of the patterns on the mould can affect the dynamics of the resist during imprinting process. To investigate the effect of architecture of the mould to the dimensions of the resulting structures, a Si mould featuring rod-shaped nanoprotrusions of various densities was used in the UV-NIL process described above. SEM images in Figure 4.12 show a portion of pattern area on the multidensity Si mould. The density of the pattern can be defined as number of features per unit area where in this case the pattern density is varied by adjusting the periodicity of nanoprotrusions in $x-$direction, P_x (Figure 4.12(b-d)). The silicon (Si) master mould shown in Figure 4.12 was fabricated using the process described in Section 4.1. This involves electron beam lithography (EBL) patterning on a 110 nm thick PMMA A4 film (MicroChem) coated on a Si wafer, followed by development, metal mask coating (50 nm of Al), lift-off and etching processes (see Figure 4.1). This produces arrays of rectangular, rod-shaped nanoprotrusions of constant height (h =160 nm) across the mould.

The mould was then used for pattern replication process using the UV-assisted nanoimprint lithography (UV-NIL). Before the nanoimprinting process, a 100 nm thick of underlayer resist (NXR-3023, Nanonex) was spin-coated onto the surface of cleanroom grade glass before the UV curable resist (NXR-2030, Nanonex) was spin-coated at 1000 rpm, twice, layer-by-layer, producing an approximately 200 nm thick film. The pattern replication was performed using the NX B200 NIL tool from Nanonex. The mould was pressed onto the glass substrate by air cushions at a pressure of 50 psi for 3 minutes before the resist was cured under UV exposure for 40 seconds while the pressure is maintained (Figure 4.4(b)). The demoulding process was performed manually using a razor blade (Figure 4.4(c)). Interestingly, this creates a negative of the mould with an imprint depth, h_i that is a function of not only the height of the nanoprotrusions and the selected NIL parameters, but also the pattern density which affects the resist filling during the process. This effect can be exemplified by examination of the cross-sectional images of the imprinted patterns as shown in Figure 4.13 (a-f). The cross-section reveals variations in imprint depth, h_i of a sample imprinted with UV-NIL as a result of non-uniform pattern densities on the mould. The plot in Figure 4.13(g) suggests that the resulting imprint depth, h_i is directly proportional to the incease in periodicity, P_x (or pattern density) and cavity width, W_c on the mould, where $W_c = P_x - W$ and W is the width of the rod-shaped nanoprotrusion (50 nm) (see also Table A1 and Figure A1 in Appendices for detailed analysis of the plot).

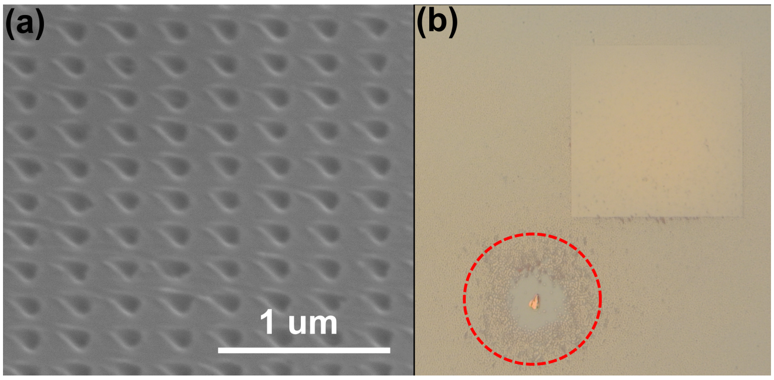

FIGURE 4.11: (a) Slip-like defects induced thermally due to difference in thermal expansion coefficient of mould and substrate. (b) Crater-like defect (in red circle) produced due to the presence of particle contaminant.

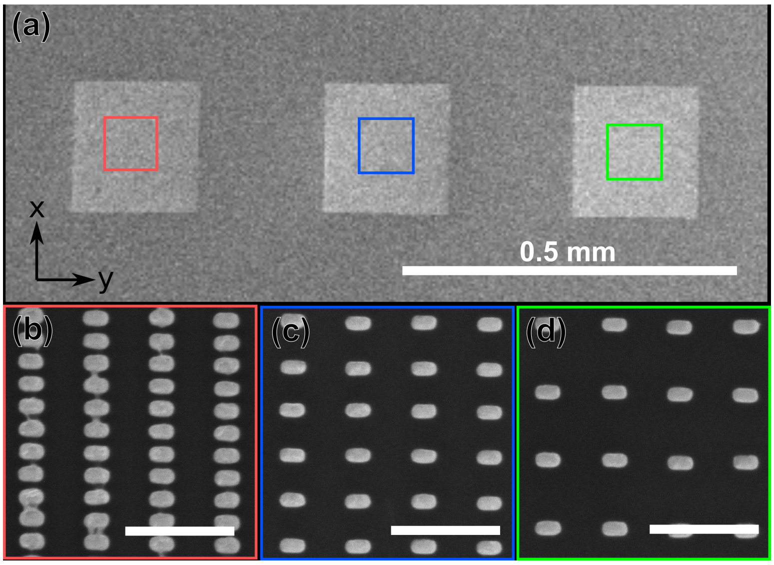

FIGURE 4.12: (a) SEM images of morphologies of a multidensity mould, comprised of rod-shaped nanoprotrusions with various size of lattice period, P_x (b) $P_x = 100$ nm, (c)$P_x = 200$ nm and (d) $P_x = 300$ nm. Scale bar in (b-d) refer to 500 nm.

The mechanism underpinning the production of multiheight structure shown in Figure 4.13 is that for a mould composed of inhomogeneous pattern densities, the resist filling rate can vary greatly across the mould due to the non-uniform distribution of contact pressures (inset Figure 4.13) throughout the imprint area as described by Stefan's equation and the law of conservation of volume (Equation 4.2 and 4.3). Additionally, the pitch size of the nanostructures also influences the volumetric flow rate, Q of the resist into a cavity. The resist fills a smaller cavity at a slower rate due to the higher viscous resistance, R according to the Hagen-Poiseuille law (Equation 4.7). This means that a region with a higher pattern density (i.e smaller cavities and broader nanoprotrusions relative to the size of the unit cell) on the mould produces a shallower imprint depth compared to area with lower pattern densities (i.e larger cavities), thus producing structures with various heights throughout the imprinted area. Although this variation can be undesirable particularly for full pattern transfer involving breakthrough etching (where the residual layer is removed via RIE) [133], the result shown in Figure 4.13 shows that the height/depth of the resulting imprinted structures can be adjusted by harnessing the dynamics of the resist via careful design of the pattern densities on the mould. Depth-varying structures shown in Figure 4.13 (a-f) resemble grayscale structures which are usually created by using complex grayscale lithography technique utilising EBL [141] or photolithography [142], can now be obtained by using UV-NIL. An approximately linear relationship between the depth and periodicity can be seen with a line of best fit given by $h_i(P_x) = 0.33 \pm 0.012 P_x + 32$ This novel multilevel NIL technique can be used for printing plasmonic devices that require multiheight structures. It will be shown in the next chapter that this technique can be used to produce a plasmonic colouration device whereby the hue and saturation of the resulting colours can be controlled through the vertical dimensions of the imprinted structures.

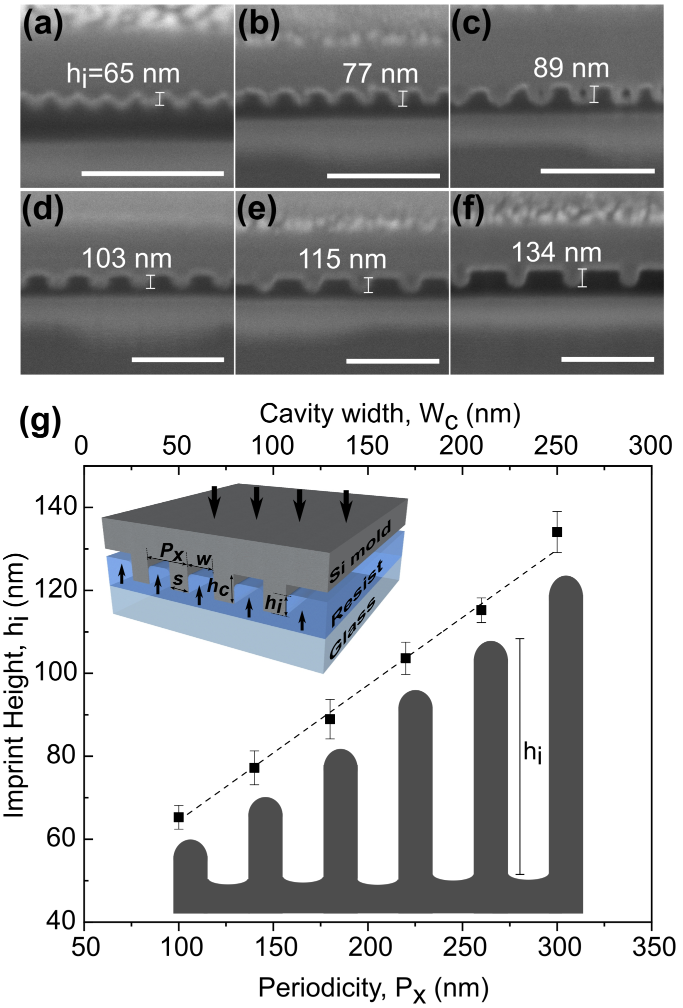

FIGURE 4.13: Cross-sectional images of imprinted structures with various periodicities (a-f)$P_x = 100 - 300$ nm (with 40 nm increment). (g) Plot showing imprint heights as function of periodicities and cavity width of the structures on the mould. The dotted line shows the linear fit of the mean imprint height $[h_i(P_x) = 0.33 \pm 0.012 P_x + 32]$. Inset shows schematic depicting the mechanism of resist flow during imprinting process.

Several approaches, however, have been proposed to reduce global variations in imprint depth such as increasing the applied pressure [143], increasing the imprint time [134, 144], introducing additional microcavities or protrusions in proximity to the original design [105] and utilising a cavity-equalised mould [116]. To address this issue and as part of this project, a novel mesh-like microcavity architecture was introduced to the multi-density mould to facilitate resist flow. The structure considered here has microcavities with a width, $w_{micro} = 5$ μm and periodicity of 25 μm . Figure 4.14 (a) shows the top-view of the mould with mesh-like microcavities, dividing the pixel into sub-pixels while the inset in (a) shows the tilted SEM image of rectangular-shaped nanoprotrusions on the mould with heights of 160 nm. The additional microcavities promote a more uniform distribution of resist by aiding the long-range transport of resist over various pattern densities [145]. At the same time, the resist travels locally into the microstructure to assist cavity filling into the nanostructure in order to compensate and stabilise the filling rate as depicted in Figure 4.14 (b) [134]. This permits an almost constant resist filling rate over the sample producing a consistent imprint depth and resulting gap size in the final structure. Cross-sectional images in Figure 4.14 (c-e) reveal that cavities with almost the same imprint depth were produced regardless of the size of the lattice period through the use of this strategy.

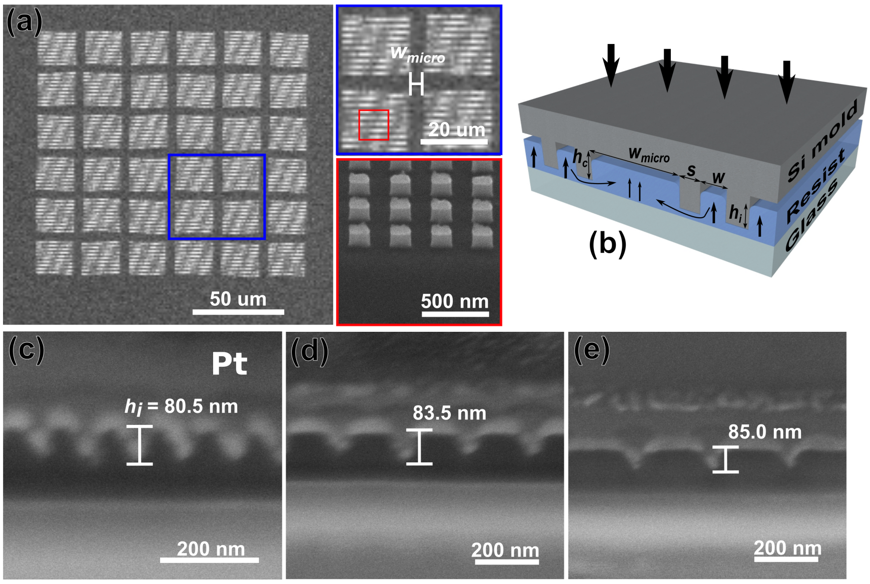

FIGURE 4.14: (a) SEM image showing morphology of a mould with complementary microcavities with $w_{micro} = 5\mu$m. Inserts show the magnified image and cross-sectional image of (a). (b) Schematic showing the mechanism of resist flow using a multidensity mould with complementary microcavity structure. (c-e) Cross-sectional images of imprinted structures of various periodicities ($P_x = 100 - 300$ nm) using the mould with microcavities reveals an almost leveled imprint height regardless of density of the structures.

4.4 Conclusion

To summarize, this chapter covers the fundamentals of nanoimprint lithography (NIL) and discussed three most important aspects that govern dynamics of the resist and thus the quality of the imprinted structures: (i) the NIL process parameters, (ii) the chemical and physical properties of the resist, and (iii) the material, conditions and architecture of the mould and substrate. Throughout the research presented here, a Si mould, coated with anti-stick layer, was used. The fabrication and preparation of the mould were discussed in this chapter. Both thermal NIL and UV-assisted NIL (UV-NIL) were utilised and production of high-resolution nanostructures of various geometry have been demonstrated. However, unlike thermal NIL, UV-NIL can be carried out at room temperature and requires relatively shorter imprint time and low pressure as a result of the low-viscosity UV curable resist and therefore a preferred method for this project.

The optimisation of the imprinting aspects above has lead to the main finding in this chapter which involves the development of a novel multilevel NIL technique for controlling the vertical dimension of the structures (imprint depth) by harnessing the dynamics of the resist. This was achieved by utilising a mould with various pattern densities. It was shown that NIL is a versatile technique that is capable of producing not only 2-dimensional structures, but also structures of various heights (3-dimensional) – a feature that resembles grayscale structures, without relying on charged particles or light beams. Conversely, this effect can be minimised by introducing a novel mesh-like microcavity structure on the multidensity mould. The presence of the microcavities compensate the filling rate of the resist across the mould producing a consistent imprint depth regardless the pattern density. This finding demonstrate a full control of the vertical dimension of the imprinted structure. From a fabrication point-of-view, introducing a microcavity structure into the mould suggests a simple solution to a longstanding issue in NIL. This is particularly important for the production of plasmonic devices which require nanoscale precision across surfaces orders of magnitude larger. It will be shown in Chapter 5 the utilisation of this novel NIL technique for printing of plasmonic colouration device comprising structures of varying height for control of the hue and saturation of the resulting colours.

Chapter 5

Multilevel Nanoimprint Lithography (NIL) for Plasmonic Colour Printing

It was demonstrated in Chapter 4 that multilevel nanoimprint lithography (NIL) capable of controlling the vertical dimension of the nanostructure can be achieved in a single print by careful control of the dynamics of the polymer resist through the strategic design of the architecture of the mould, thus producing multilevel structures. By using this novel multilevel NIL technique, the reliance on complex grayscale technique can be avoided. Additionally, this approach can be adapted in the fabrication of plasmonic devices such as plasmonic colours. This chapter, therefore, pertains to discuss the utilisation of the multilevel NIL for printing of plasmonic colouration device with tunable hue and saturation via simultaneous control of both transverse and vertical dimension of the structure.[1]

Recently, pigment-free colouration based on plasmonic resonances has attracted considerable attention for potential in manufacturing and other applications. Plasmonic colouration originates in the strongly wavelength-dependent scattering and absorption of light which arises from the excitation of surface plasmon resonance (SPR) and localised surface plasmon resonances (LSPR) on the surface of sub-wavelength metallic nanoparticles and nanocavities [48, 51]. For plasmonic colour utilizing the metal-insulator-metal (MIM) configuration, where metallic nanoantenna embedded in a transparent dielectric 'float' above their Babinet complementary screen (Figure 5.1), the resonance are dependent not only on the transverse dimensions of the nanostructures [76, 77, 79, 81, 146], but

---

[1] The research discussed in this chapter has been published in Nanoscale Advances (Shahidan, M. F. S. et. al. (2020). Nanoscale Adv., 2, 2177-2184.)[84]

also the size of the vertical gap (g) between the nanoantenna and the perforated backplane film. This vertical gap controls the nanoantenna-film coupling strength and, hence, the resulting colouration seen in reflection [147]. With the rod-shaped nanantenna-hole structure (Figure 5.1) being the main focus throughout the chapter, the importance of this vertical separation distance in MIM plasmonic colour in tuning the resonance wavelength and hence the resultant colour will be discussed in the first section of this chapter.

While many approaches have been proposed to improve the functionality and quality of the resulting colouration, the key challenge remains controlling both the transverse and vertical dimensions of the nanostructures in a single nanofabrication process. The complexity of conventional fabrication methods such as electron beam lithography (EBL), limits their capacity to simultaneously control these critical parameters. The later part of the chapter, therefore, will demonstrate the straightforward production of plasmonic colour via UV-assisted nanoimprint lithography (NIL) with a simple binary mould to address this issue using the findings of Chapter 4. This approach provides a further avenue for controlling the colour reflected by the resulting plasmonic pixels as an adjunct to the conventional approach of tailoring the transverse dimensions of the nanostructures. The experimental results confirm that a wide colour coverage of the CIE 1931 XY colour space can be obtained through careful control of both the length of the nanorod and size of the lattice period and the resulting vertical gap size of the structure obtained from the nanoimprinting process. Conversely, by introducing complementary microcavities in the vicinity of the nanostructures on the original mould, a fixed gap size can be produced, showing the capacity of this method to fully control the vertical dimension. Moreover, in order to demonstrate scalability, this technique is utilised to perform a large area, centimeter scale imprinting of plasmonic colour.

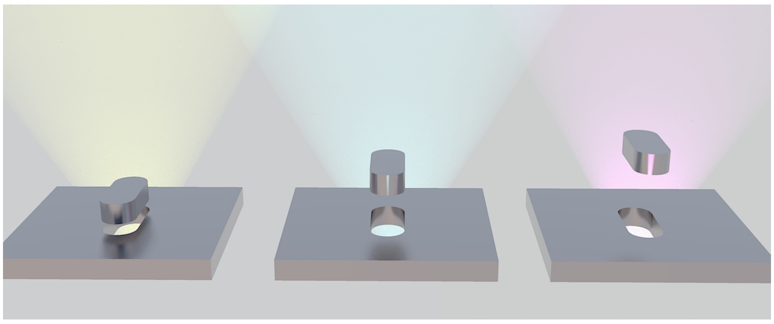

FIGURE 5.1: Artist impression showing metal-insulator-metal (MIM) plasmonic colour comprised of metallic nanoantenna vertically displaced above their Babinet complementary screen with various gap size which produced different colours.

5.1 Dependency of Output Colour to Vertical Gap in Metal-Insulator-Metal (MIM) Plasmonic Colour

Studies in plasmonic colour have explored a vast range of designs to accommodate a wide variety of applications. In general, these designs can be categorised into two main configurations, which are the insulator-metal-insulator (IMI) and metal-insulator-metal (MIM). The IMI configuration composed of a single layer of metal sandwiched in between a dielectric substrate and superstrate. Previous studies have utilised plasmonic metasurfaces comprising metallic nanoantenna arrays of various geometries as plasmonic colour elements in the IMI configuration, owing to their efficiency in coupling free-space radiation to localised surface plasmons, thus enabling wavelength-selective optical response and resulting colouration [14, 73, 148]. In addition to nanoantenna arrays, nanostructured metallic films containing nanoapertures, nanocavities and nanoprotrusions were used to produce plasmonic colour both in transmission and reflection mode [67, 149]. A MIM configuration consists of two layers of metal separated by a thin layer of dielectric. The top metal layer is usually made up of wavelength-selective metasurfaces such as a nanostructured metallic film or a metallic nanoantenna array, with a tunable transverse geometry to regulate the resulting colours [15, 59, 77, 79, 81]. The bottom metallic film, either uniform or perforated, acts as a back-reflector while at the same time allowing near-field interactions with the top plasmonic nanoantenna when in resonance. This interaction induces plasmon hybridzation which consequently results in a shift of the resonance wavelengths compared to isolated nanostructures and even enhance the absorption or reflection of light [16, 150]. Due to the phenomenon of mode hybridization, the vertical dimension i.e. the gap size between the top and bottom metal, g plays an important role in controlling the resonance wavelength. Additionally, when the size of the gap is large enough to decouple the pair, both layers exhibit independent resonances whereby the resonance wavelength corresponds to the Fabry-Perot resonance of the structure. The MIM configuration, therefore, provides an extra degree of freedom in terms of tuning the resulting reflected or transmitted colour in contrast to the IMI configuration, which relies only on the transverse geometries. It is worth mentioning that this feature has been one of the main motivations for the use of the MIM plasmonic colour throughout this project. This section therefore seeks to understand the optical modes present in an MIM device (designed to produce plasmonic colour) comprising a nanoantenna-hole array, explained in terms of plasmon hybridization. The effect of tuning the vertical dimensions of the structure on the reflectance spectra and corresponding colouration will also be discussed to highlight the importance of controlling this critical dimension in the fabrication process.

To analyze the contributions of plasmonic modes to the designed device, Finite Element Method (FEM) simulations of the interaction of light with rod-shaped nanoantennas and nanohole arrays, and the composite structures, were performed (details of the simulation will be discussed in the next section). Figure 5.2 shows the calculated reflectance, transmission and absorption spectrum of each of the structures and the corresponding surface charge distribution at particular wavelengths. All structures have their periodicity, P, rod/hole length, L and rod/hole width, W fixed at 300 nm, 75 nm and 50 nm respectively. The material of the structure is silver (Ag) and its optical constant is taken from Rakic [130]. The refractive index of both the substrate and superstrate were set to n =1.45 and the structures were illuminated at normal incidence with a linearly polarised plane wave with its electric field parallel to the long-axis of the rod or aperture. For the structure consisting of only the rod-shaped nanoantenna array, the reflectance spectrum shows a peak in reflection at a wavelength of 520 nm (Figure 5.2(a)) corresponding to the excitation of the dipole mode of the nanoantenna (see inset). Figure 5.2(b) shows the calculated spectrum for a silver (Ag) film containing a nanohole, exhibiting an almost flat reflectance spectrum of approximately 94%, similar to a bare Ag mirror. There is however, a weak dip in reflection and peak in absorption near 520 nm. In contrast, the reflectance spectrum in Figure 5.2(c) of the composite structure shows an enhanced absorption up to 96%, when the nanoantenna is placed 60 nm above the nanohole, manifested by the near-zero minimum in reflectance at a wavelength of 450 nm. Moreover, the surface charge density (inset Figure 5.2(c)) illustrates the synergistic effect of the coupled nanoholes and nanoantenna, which plays a key role in enhanced absorption. Results shown in Figure 5.2 also suggest that the coupled nanoantenna-hole array configuration behaves as a near-zero reflectance , wavelength-selective absorber, suitable for producing highly saturated colour.

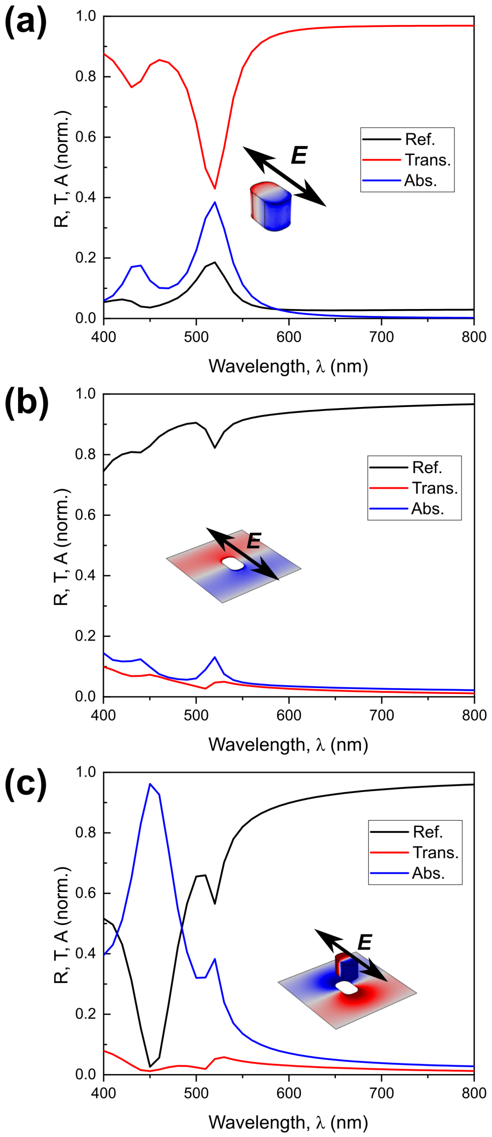

FIGURE 5.2: Simulated reflectance, transmission and absorption spectra of different structures namely rod-shaped (a) nanoantenna, (b) nanohole and (c) coupled nanoantenna-hole. Insets show the surface charge distributions and the direction of linear polarisation.

The resonant absorption exhibited by the nanoantenna-hole structure presented in Figure 5.2(c) can be understood as a plasmon hybridization of the modes associated with the elementary plasmonic structures. Surface charge distributions of the relevant modes for (i) an individual nanoantenna and (ii) its complementary hole shown in the energy diagram in Figure 5.3(a) depicting both structures possessing dipolar resonances on their own. When brought into proximity within the near-field distance, the dipole states supported by the holes hybridize with dipole states of the vertically displaced nanoantennas. The dipole coupling in the nanoantenna-hole pair therefore results in two new resonant modes arising from plasmon hybridization namely ‘bonding’ and ‘antibonding’ modes [15, 16, 150]. A ‘bonding’ mode is characterised by a lower energy (longer wavelength) whereby the charge oscillations in the nanoantenna and the hole are out-of-phase (Figure 5.3(a)(iii)). In contrast, an ‘antibonding’ mode is characterised with a higher energy (shorter wavelength) as such the charge oscillations are in phase (Figure 5.3(a)(iv)).

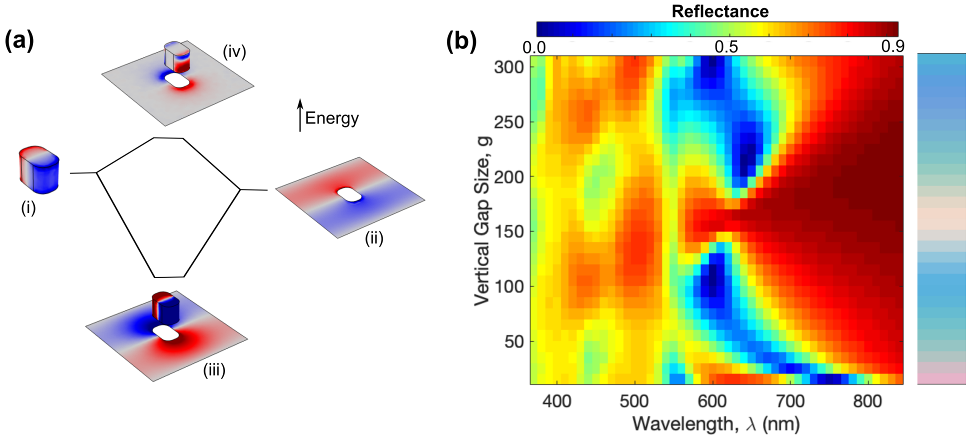

Figure 5.3: (a) Energy diagram illustrating the hybridization of the coupled plasmonic modes of the nanoantenna and holes of the structure into a low energy mode (bonding) and a high energy mode (antibonding). The shown structure is for length, $L = 75$ nm, periodicity, $P = 300$ nm, vertical gap size, $g = 60$ nm (for (iii) and (iv)), and thickness, $t = 50$ nm embedded in material of refractive index of 1.5. (b) Simulated reflectance plot for an 80 nm long nanoantenna-hole array in a 300 nm cell with an increasing gap between the floating dipole and thin film. Inset shows the colour generated due to the varying vertical gap size.

The resulting resonance wavelengths induced by plasmon hybridization are therefore, highly dependent on the vertical distance between the top and bottom metal layers, in addition to the transverse geometries [15]. To show the effect of the vertical gap size on the resulting colour, a FEM simulation based on an array with Ag rod nanoantenna of 80 nm long and 50 nm wide, were performed with the vertical gap between the nanoantenna and perforated film, g varied from 15 to 305 nm. Other parameters such as the metal film thickness and the lattice period are fixed at 50 nm and 300 nm respectively. The direction of the polarisation of the incident light is set parallel to the long-axis of the nanorod. The simulated reflectance spectra collected from the nanoantenna-hole system presented in Figure 5.3(b), show two defined features associated with the increasing vertical gap size. The resonant responses are correlated with the plasmon hybridization of dipole modes exhbited by the nanoantenna and film at distances $g < 125$ nm; and Fabry−Pérot-like effects for gaps, $g > 125$ nm. Within the near field distance ($g < 125$ nm), the increased vertical gap size leads to a weaker coupling strength between the dipole modes and is manifested by the blue shifting of the resonance wavelength. For larger gap sizes ($g > 125$ nm), where significant resonant spectral shifting occurs, the system exhibit a Fabry−Pérot-like behaviour where the nanoantenna and the hole array each acts as isolated ‘mirrors’ with resonant reflection coefficients [16]. Within this regime, the resonance wavelength is red-shifted with increasing vertical gap size, opposite to the response showed when the vertical gap is in the near-field region. In short, the strength of the 'bonding' mode is highly dependent on the shorter gap size (strong coupling) and above $g = 125$ nm the hybridization is not seen in the reflectance spectra. The inset in Figure 5.3(b) shows the simulated variation in colour due to the varying vertical gap size of the structure, demonstrating the significant effect the gap has on the spectral response and hence the colour. For example, at very small nanonatenna-hole gaps (g <20 nm) the structure initially generates a pink colour which dramatically changes to cyan as the gap size increases, exemplifying that slight variations of just a few tens of nanometers in the vertical gap size will lead to transitions in the hue and even lead to desaturation of the output colour. The reflectance map in Figure 5.3(b) therefore demonstrates the importance of controlling the vertical dimension, i.e the gap size in the nanoantenna-hole configuration during the fabrication process in addition to tuning the transverse dimension in order to produce colouration with controllable hue, brightness and saturation. While various fabrication methods have been utilised to precisely control the vertical dimension of the structures, this chapter discusses nanoimprint lithography fabrication as an alternative approach to other complex fabrication process.

5.2 Design and Simulation

The details of the building block of the MIM plasmonic pixel discussed here is shown in Figure 5.4. The structure, which was designed to be easily produced via NIL, comprises Ag nanorods with length varying from L = 75-150 nm and fixed width W = 50 nm, sitting above complementary aperture in a continuous Ag film with the same transverse dimensions. The nanoparticle is supported by the surrounding dielectric. The vertical gap, g between the particle and the metal film is determined by the imprint depth which, in turn, depends on the details of the resist filling process as shown previously in Chapter 4. The particles are arranged in a rectangular lattice with a fixed periodicity in the y-direction, $P_y = 300$ nm, while the periodicity in the x-direction, P_x is varied from $100 - 300$ nm. The thickness of the particle and metal film is fixed at $t = 50$ nm. It is worth mentioning that a relatively thick structure with a larger width is chosen to blue-shift the resonance wavelength of the Ag sample [151] thus ensuring most of the visible spectrum is covered. By varying the length, L and pitch size, P_x of the structure, this generates not only plasmonic colour variations arising from tailored transverse feature sizes but also from the uneven vertical gap size across the imprinted structure resulting from differences in filling rate. Although the ability to vary the gap size of the structure in a single imprint with a simple binary mould is useful in some applications such as surface colouration, this can be problematic in other applications. Therefore, a simple solution to avoid gap size variations in the sample is the introduction of a complementary microcavity mesh into the original mould architecture permitting filling-rate compensation in different pattern densities resulting in an almost constant gap size and, thus, resonance wavelength. This will be further discussed in the later section of the chapter.

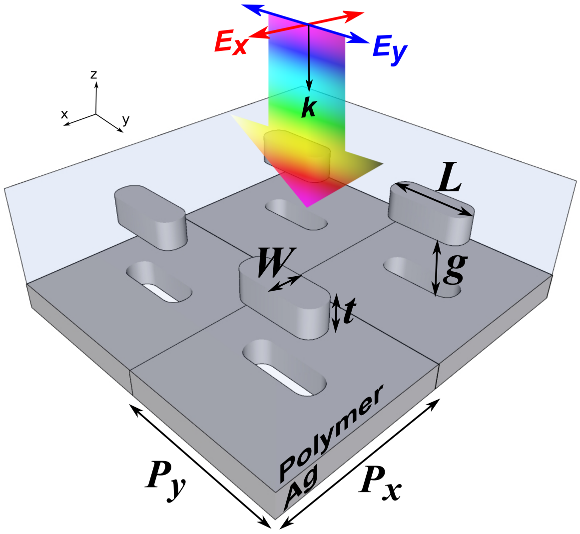

FIGURE 5.4: Schematic design of the plasmonic pixel comprising arrays of the 'floating' Ag nanorod and the complementary screen, arranged in a rectangular lattice. The nanorod has a length L, width W and thickness t. The array has periodicities in the x- and y-directions P_x and P_y, respectively, while the gap between the top of the metal film and the bottom of the Ag nanoparticle is g. Light, linearly polarised in either the x- or y-direction, is incident normally from the nanorod side, while the reflected light is collected from the same side of the sample.

The three-dimensional simulations of nanostructure models shown above were performed using the Finite Element Method (FEM) implemented in the Wave Optics module of COMSOL Multiphysics 5.4. Periodic boundary conditions were used on the sides of the unit cell. The material data for Ag was obtained from Rakic *et al.* [130]. A mesh with maximum element size of 15 nm was used in detailed areas such as the nanorods and nanoaperture. Reflectance spectra were calculated using normal incidence port excitation of a plane wave linearly polarised either parallel or perpendicular to the long-axis of the rods and the zeroth order reflectance calculated from the S–parameter $|S_{11}|^2$. Another port on the rear surface of the model prevented reflections back into the model. The refractive index of the resist and glass were both assumed to be n=1.45. Similar model was used to simulate the rod, hole and their composite structures shown in section 4.1 (Figure 5.2).

5.3 Fabrication and Experimental Methods

In previous studies, a grayscale technique involving electron beam lithography (EBL)[141, 152, 153], focused ion beams (FIB) milling [154] and photolithography (PL) [142] have been utilised to produce grayscale nanostructures (i.e structures with varying height) for structural colouration and three-dimensional (3D) plasmonic devices. The grayscale approach, however, requires meticulous control of electrons, ions and/or photon dosage. Additionally, EBL and FIB have relatively low-throughput, while PL produces structures with feature size limited by the diffraction limit [155]. Nanoimprint lithography (NIL)[110], on the other hand, offers a high-throughput nanopattern replication process by means of mechanical transfer from a mould onto a surface at minimal cost without compromising the nanoscale resolution [156]. Due to these attractive features, different NIL techniques have been developed and are widely used for fabrication of various plasmonic devices [157, 158]. Previously, thermal NIL has been successfully demonstrated to produce high-resolution surfaces exhibiting plasmonic colour [159, 160]. A more scalable approach has been performed by Hojlund *et al.* where thermal roll-to-roll nanoimprint lithography (R2R-NIL) was used to mass-produce devices exhibiting plasmonic colour [47]. Thermal NIL, however, involves heating to high temperatures (typically around 150° C, depending on the type of resist) which not only consumes energy but requires meticulous control over the relevant imprint parameters such as temperature and pressure. The UV-assisted NIL process, on the other hand, requires no heating and can be performed at room temperature and therefore, thermal damage, energy usage and process time can be minimised. Furthermore, the use of low viscosity photocurable resist requires a relatively low pressure (<4 bar) to emboss the structures, thus reducing potential damage to the mould [161].

In NIL, a binary or two-level mould is usually used for pattern transfer. This will create two-dimensional (2D) structures with limited tunability over the height of the imprinted structures. To tune over vertical dimension of the imprinted structures, Alkaisi *et. al.* have performed a multilevel NIL approach by utilising a grayscale mould (produced using grayscale EBL) which allows production of structures with different heights [114]. Although this approach successfully produced 3D structure, the production of the multilevel mould, however, is still depends on the complex grayscale EBL technique. Despite the clear benefits of high-throughput, good quality pattern replication and plasmonic colour production, there has been no discussion in the literature of any capacity of NIL to vary the vertical dimension, including the gap size in the MIM structure, across a sample using a simple, two-step (or 2D) mould.

Generally, the MIM plasmonic structures of interest were fabricated using NIL into a resist followed by a single metallisation step. Since the resulting reflected colour produced by these devices is sensitive to the vertical gap size [147] and this gap correlates directly with the imprint depth, the capacity to vary the imprint depth across a sample provides an additional degree of freedom in NIL-facilitated plasmonic colouration. During the nanoimprint process, the homogeneity of the imprint depth of the replicated structure is highly dependent on the resist filling behaviour in nanoscale cavities on the mould. As discussed in Chapter 4, the mould design/architecture (e.g. the size of the cavities, the density of structures and imprint area) is one of the significant factors affecting the resist filling process into cavities in the mould [112, 134, 161–166]. Previous simulations of the NIL process performed by Yin *et al.* showed that an inhomogeneous imprint depth resulted when a mould composed of both micro- and nanoscale features was used for NIL due to variations across the sample in the resist filling rate [134]. A similar effect was observed when a mould with various pattern densities was used in the NIL process [105]. Although inhomogeneous imprint depths often caused unwanted artefacts appearing in the NIL pattern transfer process [167, 168], this feature however, is an advantage when producing plasmonic colour since it permits another mechanism for control of the vertical dimension and adds another degree of freedom for colour tuning.

The template consisting multilevel nanostructures obtained from the novel multilevel UV-NIL shown previously in Chapter 4 (Section 4.3, Figure 4.13), therefore, is utilised here to demonstrate the capacity of NIL to tune the colour of light reflected from the surface by controlling the vertical gap in the structure in a single print using a binary NIL mould with tailored pattern densities. In addition to experimentally demonstrating the role played by mould architecture in determining the imprint depth, the influence on resulting plasmonic colouration are investigated. The fabrication process of the template have been discussed in detail in previous chapter (Figure 4.1 and Figure 4.4), which involves two major stages: (i) fabrication of a silicon (Si) master mould and (ii) pattern transfer via NIL. The fabricated Si mould consist of arrays of rectangular, rod-shaped nanoprotrusions of constant height (h =160 nm). The NIL process involves embossing of the Si mould onto 200 nm thick UV curable resist, cross-linking via UV exposure and demolding (Figure 5.5(a)-(c)), thus creating negative of the mould (rod-shaped nanocavities). Finally, to complete the device fabrication, the imprinted samples were subsequently coated with 2 nm of Ge as an adhesion layer and 50 nm of Ag film using electron beam evaporation at a rate of 0.05 nm/s, producing a nanoantenna array and its complementary perforated film (Figure 5.5(d)) with various pattern densities and imprinted heights (Figure 5.6(b and c)).

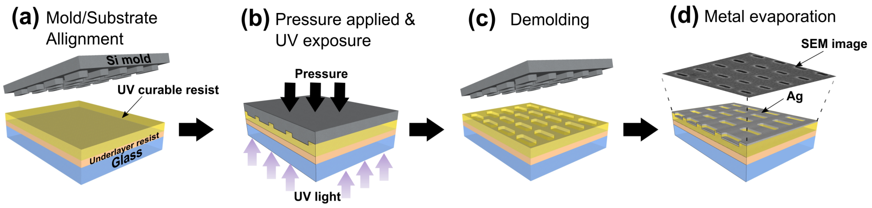

FIGURE 5.5: Schematic of the sample fabrication process. (a) the UV-NIL resist-coated substrate (glass) aligned with silicon mould prepared for NIL process; (b) the substrate contacted with silicon mould with pressure and UV illumination applied; (c) the substrate is delaminated from the silicon mould; (d) substrate after metal evaporation (50 nm Ag). Inset: SEM image of the fabricated glass sample.

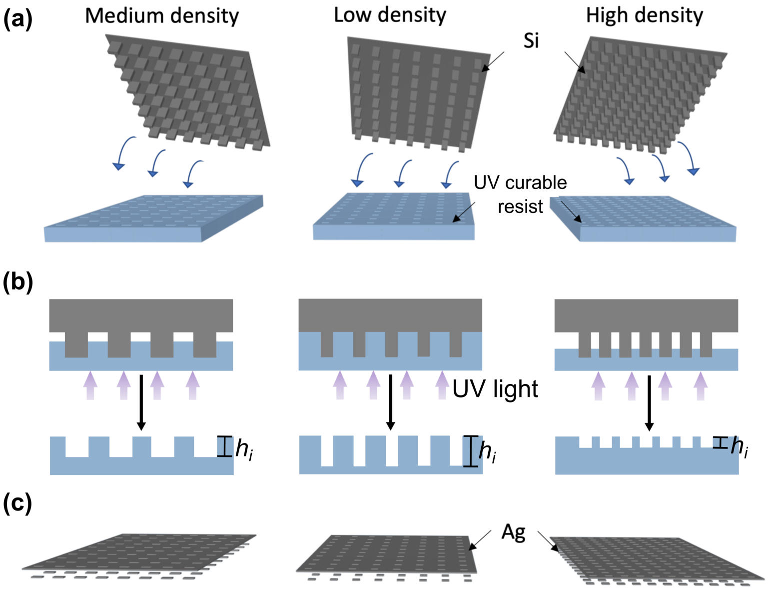

FIGURE 5.6: (a) Schematic of the UV-assisted nanoimprint lithography (UV-NIL) process using a master mould consisting of a multiple density of nanoprotrusions used in the UV-NIL which results in the nanocavity with various imprinting depth, h_i as depicted in (b).(c) Scheme showing the geometry of the Ag 'floating' resonance particle and metal back layer upon metal coating process. Height of the structures in the schematics are not to be scaled.

The morphologies and cross-sectional images of both the mould and imprinted structures were obtained with a FEI Nova Nanolab 200 Dual Beamsystem scanning electron microscope (SEM), integrated with a focused ion beam (FIB) column. For the FIB milling process, firstly, a 400 nm layer of platinum (Pt) was deposited on the structures to protect the soft surface and increase the conductivity. The milling was performed at a 52° stage tilt (perpendicular to the ion beam). Subsequently, the image of the cross-sections were taken at 52° stage tilt. A low electron current of 68 pA was used for SEM imaging through the whole process. Optical images of the patterned surfaces were obtained using a Nikon N1 camera attached to an optical microscope (Olympus BX60) with a halogen lamp as a light source. A rotating linear polariser located in the path of the light source was used to select the linear polarisation state to demonstrate any polarisation sensitivity. Reflectance spectra were measured using a custom built optical cage setup discussed in Chapter 3. A broadband halogen lamp (HL-2000-FHSA, Ocean Optics) was used as a light source. Unpolarised light passed through the first objective lens with NA=0.15 (10x UPlan, Olympus) and the calcite linear polariser (GTH5M, Thorlabs), producing a collimated and linearly polarised light beam. The polarised light passed through the second objective lens of NA=0.5 (20x UPlanFl, Nikon) before illuminating the sample. The light reflected from the sample was split by the first and second 50/50 non-polarising beam splitter cubes (CCM1-BS013, Thorlabs) to a USB CMOS camera (DCC1645C, Thorlabs) and a calibrated spectrometer (QE6500, Ocean Optics Inc.). Reflected light from an unpatterned region of the sample (metal thin film) was acquired as a reference and for normalisation. Reflectance spectra from the nanoparticle side of the resulting structures were then obtained to optically characterise the samples.

5.4 Results and Discussion

The resulting imprinted nanocavities with varying lengths and periodicities are shown in the SEM images of Figure 5.7(a-d). The transverse morphologies of the final fabricated structures are in very good agreement with their counterparts on the mould (Figure 5.7 (e-h)), depicting excellent fidelity of the pattern replication. Insets in Figure 5.7(a-d) show white light optical microscope images taken in reflection of devices after metal coating. A variation in resulting colour is apparent. Additionally, it was showed in previous chapter that the resulting imprint depth, h_i is directly proportional to the increase in periodicity, P_x (or pattern density) and cavity width, W_c on the mould (Figure 4.13). This produces nanocavities with variation in heights as shown previously in cross-sectional images in Figure 4.13 (a-f). Similarly, after evaporating a layer of Ag with thickness, $t = 50$ nm on the fabricated template, the results show that the vertical gap size, g between the film and nanoantenna (where $g = h_i - t$) has an approximately linear relationship to the periodicity, P_x as depicted in the plot in Figure 5.8 (see also Table B1 and Figure B1 in Appendices for detailed analysis of the line fitting). This results in a shift in the resonance wavelength and, hence, the colour of the final structure even if other parameters are held fixed. The dashed line in Figure 5.8 indicate the linear fit of the mean gap size of the structure thus giving a gap-periodicity relation as a linear function of $g(P_x) = 0.34 \pm 0.014P_x - 20$, similar to the depth-periodicity relationship shown previously in Chapter 4 (see Figure 4.13(g)). Slight discrepancy in the gradient values is due to the metallisation of the sample after imprinting.

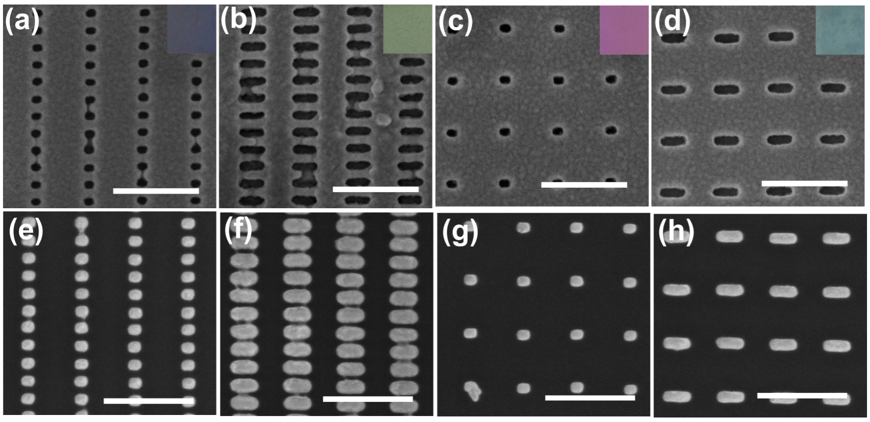

FIGURE 5.7: SEM images showing the morphologies of the nanoimprinted nanocavities and its corresponding nanoprotrusion on mould with different particle geometry: (a,e) L = 75 nm, P_x=100 nm, (b,f) L = 150 nm, P_x=100 nm, (c,g) L = 75 nm, P_x=300 nm and (d,h) L = 150 nm, P_x=300 nm. All scale bars refer to 500 nm. Insets in (a-d) shows bright-field images of colours produced by the samples after metallisation.

As discussed earlier in Chapter 4, for a given resist and fixed NIL parameters, the details of the mould architecture can be used to tune the behaviour of the gap size across the imprinted structure. The cavity-filling mechanism of the resist during imprinting, i.e the dynamics of the liquid phase resist, depend on the net contact pressure between the mould and resist described as the combination of external and capillary pressure [134]:

$$P_{contact} = P_{ex} + \Delta P_{cp} \tag{5.1}$$

where P_{ex} can be described by the Stefan equation (Equation 4.4) while ΔP_{cp} follows the Hagen-Poiseuille law (Equation 4.6). As discussed in Chapter 4, the variation in imprint depth (and the resulting value of g) shown in Figure 5.8 is mainly affected by the nanofluidic channelling behaviour of the resist during the NIL process. During NIL, a feature-rich, multidensity mould composed of various cavity sizes introduces a non-uniform distribution of contact forces between the resist and the mould, resulting in a inhomogeneous filling rate of the resist into the cavities across the mould [134]. The resist fills a smaller cavity volume at a slower rate due to the higher viscous resistance, according to the Hagen-Poiseuille law (Equation 4.6)[169]. This produces a shallower imprint depth, h_i leading to a smaller film/nanorod gap size, g after metallisation as illustrated in inset (ii) of Figure 5.8, consistent with the result shown in Figure 4.13(g). This effect is reversed for a larger cavities. A change in the length of the nanostructure however, introduces a proportionally smaller change in the cavity size thus resulting in a minimal variations in the imprint depths as shown by the SEM images in Figure 5.9(a-d).

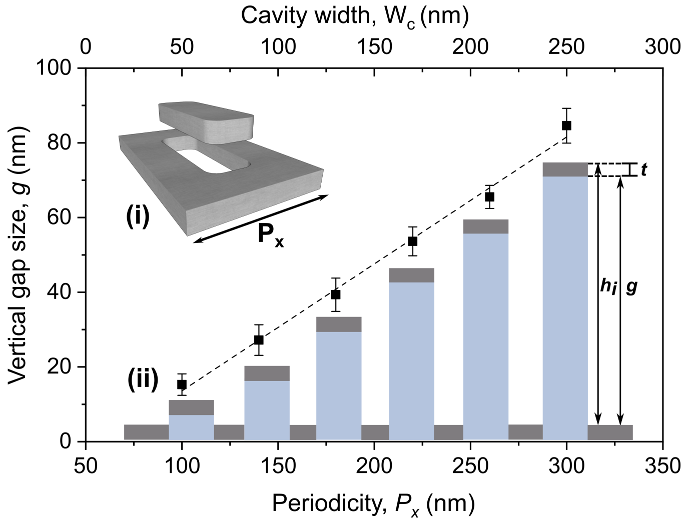

FIGURE 5.8: Plot shows relationship between the periodicity, P_x and the vertical gap size, g. Dotted line indicate the linear fit of mean gap size as function of periodicity. Inset: (i) schematic of the unit cell where P_x is the periodicity in x-direction and (ii) illustration of the metallised structure (metal thickness of t) with varying vertical gap size, g and the imprint depth, h_i.

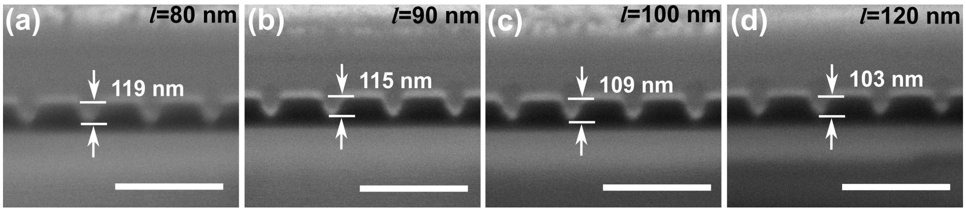

FIGURE 5.9: Cross-sectional images of nanocavities with fixed periodicity of 300 nm reveals the imprint depth of (a) h_i =119 nm,(b) h_i =115 nm, (c) h_i =109 nm and (d) h_i =103 nm for nanocavities with lengths of L =80 nm, L =90 nm, L =100 nm and L =120 nm, respectively. All scale bars refer to 500 nm.

Upon sample fabrication, optical images obtained in reflection with a bright field microscope and accompanying reflectance spectra were obtained across a range of pixel geometries to investigate their optical response. Figure 5.10 shows optical micrographs of the entire colour palette with an imprinted area of 0.6 × 0.4 cm^2 obtained when the structure was illuminated with linearly polarised light with electric field either parallel, (Figure 5.10(a)) or perpendicular to the long-axis, (Figure 5.10(b)) of the nanorods. The columns of the palette correspond to changes in length, L, ranging from 75 nm to 150 nm in 5 nm increments, while the rows represent different periodicities, P_x, ranging from 100 nm to 300 nm in 20 nm increments. The colours are clearly sensitive to the direction of polarisation due to the asymmetric shape of the nanorod. Colour variations were quantified by experimental reflection spectra obtained for nanorods with varying lengths, L but fixed periodicity, P_x =300 nm (colour swatch in the red box). Since the structures in the red box have the same periodicity they also have approximately the same vertical gap size, g = 85 nm (refer Figure 5.8(d)). The measured reflectance spectra in Figure

5.10(c) shows that when the direction of polarisation is parallel to the long-axis of the rod, the resonance red-shifts as the length increases from 75 nm to 150 nm creating distinct colour changes. For example, a pixel appears magenta when the nanorod has a length of 80 nm, but cyan when the length is 130 nm (red box in Figure 5.10(a)). Using the measured gap size obtained from fabricated devices, the simulated spectra also show comparable trends in the corresponding measured spectra as L increases (Figure 5.10(d)), consistent with the trend observed elsewhere [81, 147]. In comparison, the resonance shift resulting from the change in periodicity shown previously in Figure 5.8 resulted in a significant impact on the associated plasmonic colouration as can be seen in the colour variations in the black box in Figure 5.10(a). In contrast to the case where the polarisation is parallel to the long axis of the nanorods, the colours obtained for the orthogonal polarisation show minimal variation with length as the width, W, was held fixed at 50 nm (red box in Figure 5.10(b)). The measured reflectance spectra in Figure 5.10(e) confirm that the position of the resonance minima barely changes as the length of the rods is increased. The simulated results in Figure 5.10(e) are also in good agreement with the measured spectra.

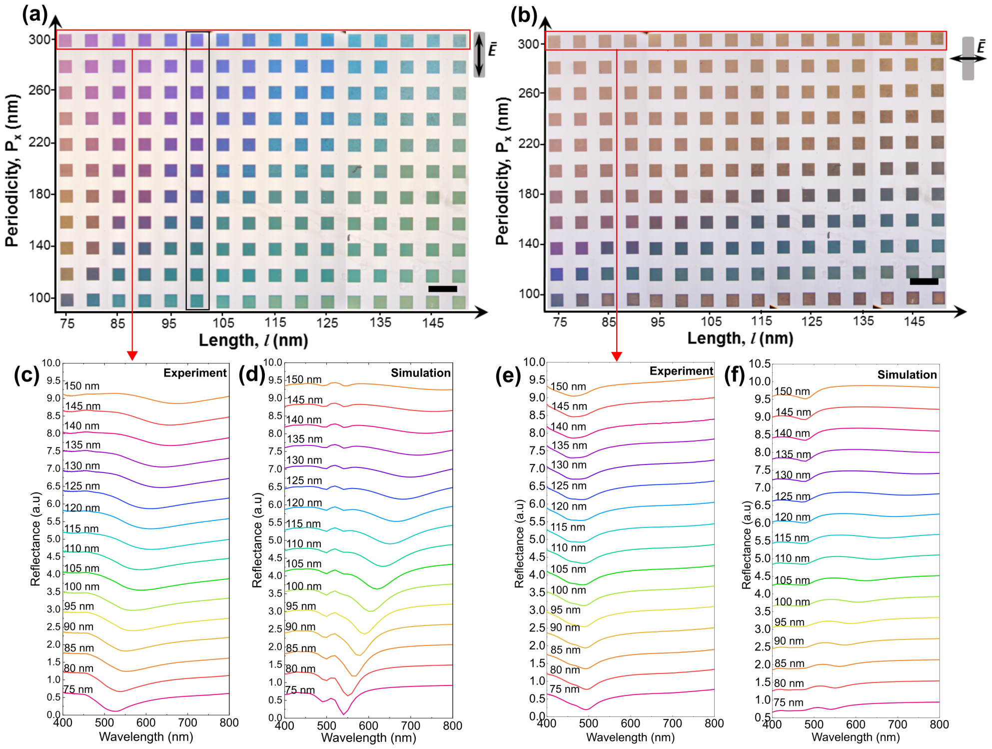

FIGURE 5.10: Bright-field optical micrograph of the colour palettes generated from the nanoimprinted samples under linearly polarised light with direction (a) parallel and (b) perpendicular to the long-axis of the nanorods. Structures in the red boxes have varying length, L and fixed periodicity, P_x=300 nm, while structures in the black box have varying periodicities, P_x and fixed length, L =100 nm. Scale bar refer to 0.4 mm. Corresponding reflectance spectra obtained from experiment and simulation of nanorod with fixed P_x=300 nm and L=75– 150 nm under polarisation direction (c,d) parallel and (e,f) perpendicular to the long-axis of the rod (insets) respectively. The width, W is fixed at 50 nm.

The experimental results exhibit a wide colour coverage covering cyan, magenta and yellow (CMY) in the CIE 1931 XY colour space generated by varying length, L and periodicity, P_x and subsequent vertical gap size, g as shown in Figure 5.11. A repeatability test was also carried out by performing up to eight imprints using the same mould, to check the consistency of the method and resulting colours after several cycles. The results of a repeatability test in Figure 5.12 show the bright field images of colour palettes of reproduced nanoimprinted samples from first to eighth imprints using the same mould. Qualitatively, there is no significant change observed in each of the samples. By measuring the reflectance of the cyan, magenta and yellow coloured swatches and plotting the resonance wavelengths (determine from the reflectance minimum) against number of imprints (Figure 5.12 (b)), the results indicate that the process is capable of reproducing the same colour palette even after multiple imprints. It also demonstrates that colour variations are not due to random defects occurring during the imprint process.

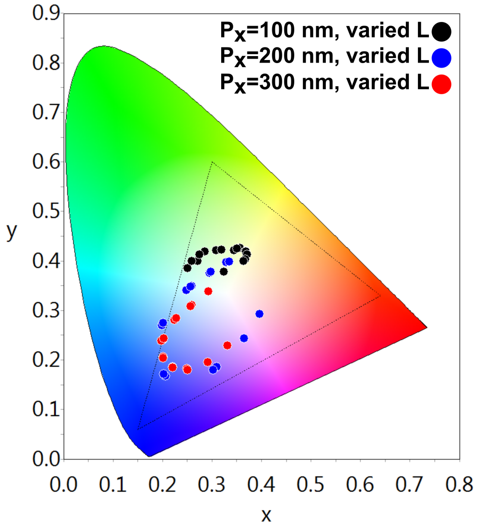

FIGURE 5.11: Position of the resultant colours on CIE 1931 XY colour space produced due to variation in periodicities and lengths of the nanorods when the direction of polarisation is parallel to the long axis of the nanorod. Namely, the black, blue, red dots indicate the colour positions in the CIE space obtained by varying L from 75 — 150 nm, and P_x = 100, 200, 300 nm respectively.

Figure 5.13 (a-c) shows experimentally-obtained two-dimensional reflectance spectra acquired from selected plasmonic pixels with varying periodicity, P_x and vertical gap size, g, at three nanoparticle lengths i.e L =120 nm, 85 nm and 75 nm respectively. The measured reflectance exhibits two minima at shorter and longer wavelengths. For each nanoparticle size, these resonance wavelengths can be tuned by varying the periodicity parallel to the short-axis of the nanorods, P_x, and the associated gap size g. To further understand features in the reflectance spectrum, Finite Element Method (FEM) simulations were performed where the periodicity, the length and vertical gap size of the structure were varied as in the experiments where the geometry was obtained from SEM images. The simulated 2D reflectance plots as a function of periodicity in Figure 5.13 (d-f) show comparable trends in the location of features in the reflectance spectrum (depicted by the dashed lines) as obtained in experiments. The simulations show that for structures with periodicities less than 220 nm, the resonance due to plasmonic coupling between adjacent nanoantennas [50] results in the excitation of a higher-order resonance (a quadrupole mode) as depicted by the charge density distribution (inset (i)) in Figure 5.14). This is accompanied by the appearance of an additional resonance at a shorter wavelength. At larger periodicities ($P_x \geq 220$ nm), the coupling strength between neighbouring nanoantennas becomes weaker as the separation increases (inset (ii) in Figure 5.14). This leaves only the lower-order dipole mode that resonates at longer wavelengths. On the other hand, previous work [147] has shown that when the 'floating' nanoantenna is located at the optimal distance from the metal film, (equal to $(2m + 1)\lambda/4$, where m is an integer and λ is wavelength in the medium) the resulting structure exhibits the strongest resonance (inset (iii) in Figure 5.14). A slight increase in the gap size between the nanoantenna and the film within the near-field distance therefore significantly blue-shifts the wavelength of the dipole mode as a result of weaker plasmonic coupling between film and nanoantenna as depicted in inset (iv) in Figure 5.14. Simulations assuming a structure with a fixed vertical gap size shown in Figure 5.15, however, show either no shift or a red-shift of the dipole mode thus confirming that the blue-shift in resonance wavelengths shown in Figure 5.13 (a,b and c) is due to increasing vertical gap size, g.

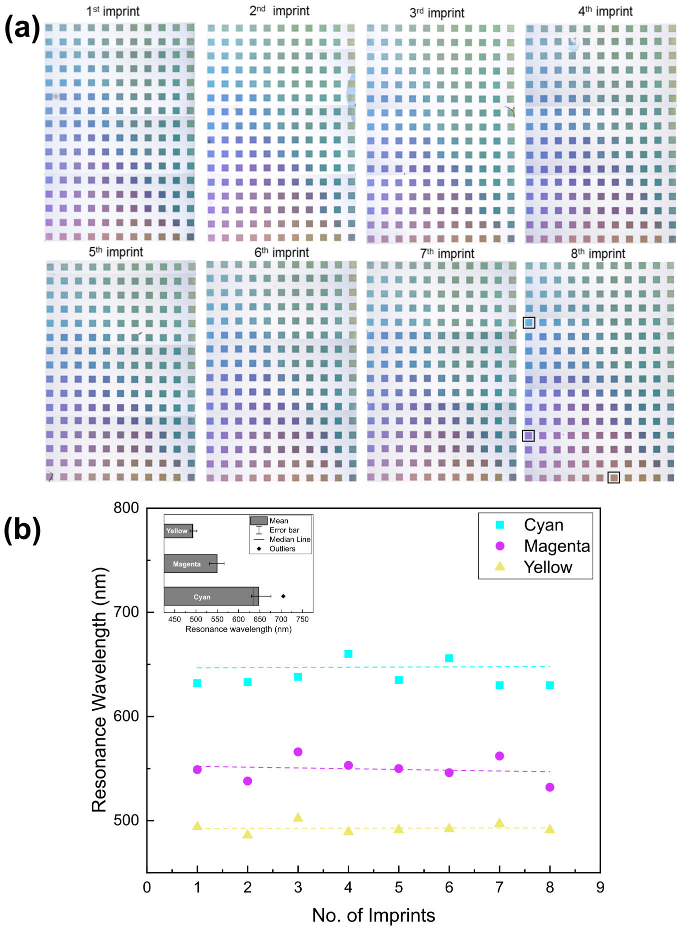

FIGURE 5.12: (a) Bright field image of colour palettes of reproduced nanoimprinted samples from first to eighth imprints under linearly polarised light with direction parallel to the long-axis of the nanorods. (b) The plot of resonance wavelength against number of imprints for cyan, magenta and yellow colours.

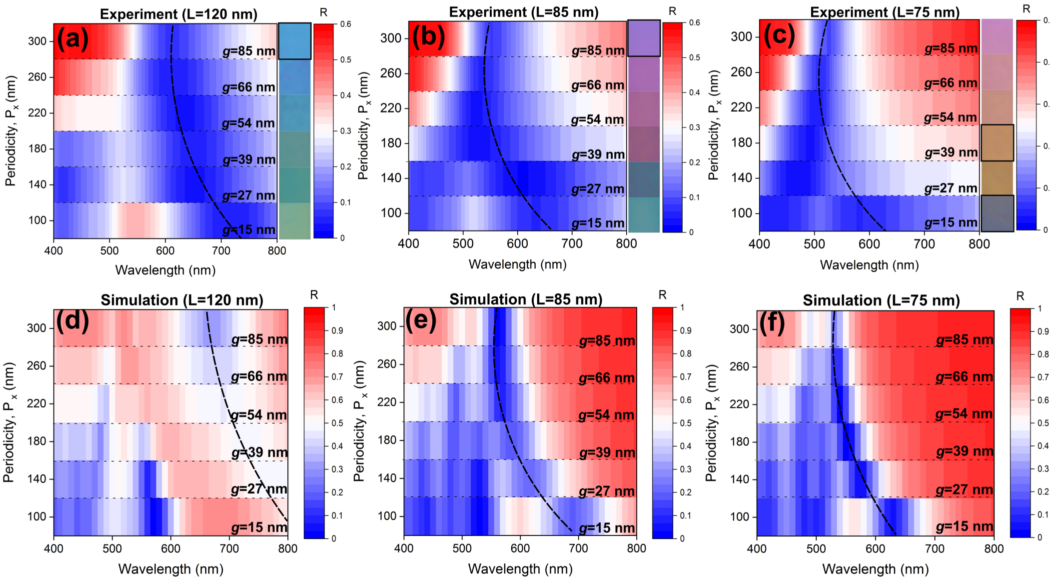

FIGURE 5.13: (a-c) Measured and (d-f) simulated reflectance maps as function of periodicity, P_x and vertical gap size, g for fixed length of nanorod L =120, 85 and 75 nm respectively. Dashed line indicate blue-shift of the resonance wavelength (dipole mode). Insets in (a-c) shows the corresponding colours for each dimensions while colours in black boxes refers to cyan, magenta, yellow and black (CMYK) colours.

Optical images in the insets of Figure 5.13 (a,b and c) show colours of various hue and saturation seen in reflection from the structure with varying transverse and vertical dimensions. The results demonstrate that by optimising the length and the vertical gap size via tailoring the particle spacing, cyan, magenta, yellow and black (CMYK) fundamental colours were able to be produced (colours in black boxes in inset of Figure 5.13 (a,b and c)). The colouration is strongly dependent on the excitation of the quadrupole and dipole mode of the structure. For example, both cyan (inset Figure 5.13 (a)) and magenta (inset Figure 5.13 (b)) colours were produced by adjusting the length of the nanorod to 120 nm (cyan) and 85 nm (magenta), while the periodicity was fixed at 300 nm and the vertical gap size at 85 nm. Decreasing the periodicity, P_x, however, results in a change in the saturation and hue of the reflected colour due to a blue-shift of the dipole mode resonance and the broadband absorption contributed by both dipole and quadrupole mode. A yellow plasmonic pixel (inset Figure 5.13 (c)) was composed of nanorods with a length, L =75 nm, periodicity, P_x =180 nm and vertical gap size, g =39 nm. Similarly, by simply reducing the periodicity, P_x and vertical gap size, g to 100 nm and 15 nm respectively, while maintaining the nanorod length at 75 nm, leads to broadband absorption resulting from the excitation of both modes thus producing ‘black’ (inset Figure 5.13 (c)). The plot in Figure 5.14 shows the resonance wavelength (dipole mode) as a function of periodicity, P_x and vertical gap size, g (obtained from the straight line fit of Figure 5.8 (g)) for devices with nanorods of length, L =85 nm. The plot indicates that the resonance wavelength (dipole mode) is blue-shifted when the periodicity and vertical gap size increases. On the other hand, increasing the length of the rods results in a red-shift of the resonance wavelength as indicated by the position of the dashed line in Figure 5.13 (a,b and c) (see also Figure 5.10 (c and d)). Discrepancies between the measured and simulated reflectance spectra may be due to the presence of the metal deposited on the sidewalls. [89, 170, 171]. This appearance of these artefacts could be minimised by producing nanocavities with more ideally rectangular profiles which is a challenge when using NIL. Some sidewall deposition should be expected as a result of the trapezoidal geometry of the nanocavities and the surface chemistry between the metal and the polymer resist film [171]. In specific applications, balancing performance and scalability requires accommodating these defects in the design process. This approach, therefore, permits fine tuning of the position of the resonance wavelengths to produce a broad colour palette enabled by varying the transverse and vertical dimension.

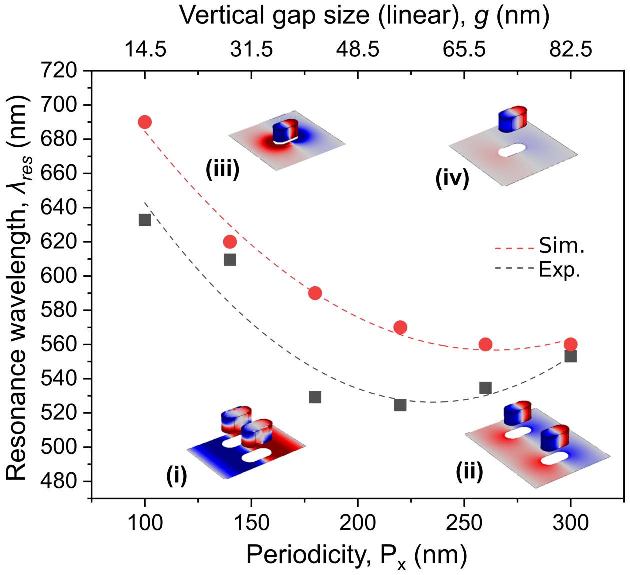

FIGURE 5.14: Plot shows relation between periodicities, P_x, vertical gap size, g (obtained from linear relation shown in Figure 5.8 (e)) and resonance wavelengths, λ_{res} (dipole mode) for nanorod of length of 85 nm. Insets are the surface charge distribution diagram depicting resonance mode and plasmonic coupling strength at (i) shorter and (ii) longer periodicity; and (iii) shorter and (iv)longer gap sizes.

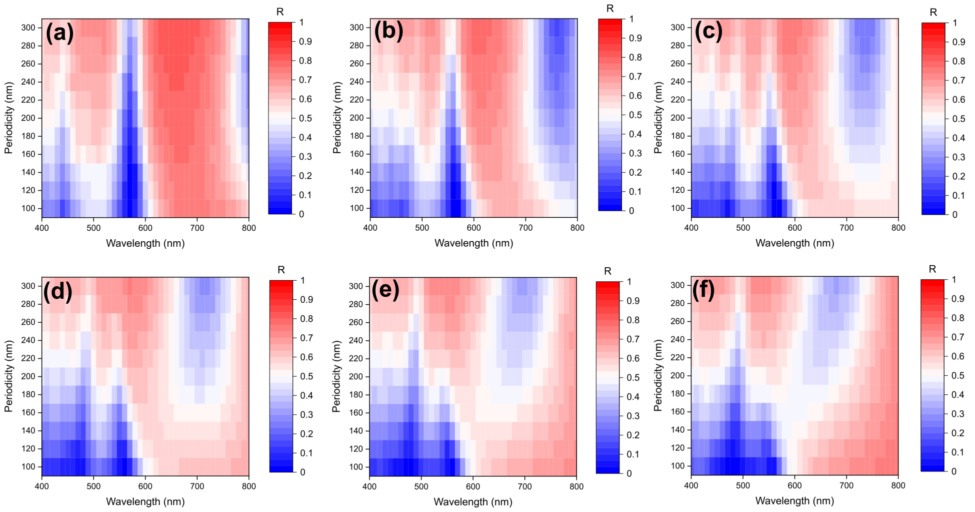

FIGURE 5.15: Simulated reflectance map showing the effect of lattice period, P_x for structure with different vertical gap size, g i.e (a) g=10 nm, (b) g=20 nm, (c) g=30 nm, (d) g=40 nm, (e) g=50 nm and (f) g=60 nm.

Although this approach demonstrate that a variable imprint depth provides an additional degree of freedom in creating plasmonic colouration, in many applications this can be undesirable. As previously shown in Chapter 4, the imprint depth, h_i can be leveled by introducing a mesh-like microcavity architecture to the multidensity mould (Figure 5.16(b)). The supplementary microcavities (width, $w_{micro} = 5\mu$m and periodicity of 25μm) facilitate resist flow by compensating and stabilising the volumetric filling rate of resist into the cavities (Figure 5.16(a)) thus creating a more uniform distribution of resist over various pattern densities [145]. This results in an almost fixed imprint depth and resulting gap size in the final structure as can be seen in the cross-sectional images in Figure 5.16(c-e). Figure 5.16(f) shows the measured reflectance from the metallised nanoimprinted plasmonic pixels using the mould without (dotted lines) and with the microcavity mesh (solid lines), for nanorods with lattice periodicities, P_x = 100 nm, 200 nm and 300 nm. As seen previously, the reflectance spectra exhibit a significant shift in the resonance minimum with increasing periodicity in the absence of the microcavities. In contrast, the spectra in Figure 5.16(f) show no obvious resonance shift with additional microcavities since the gap has almost a constant value (Figure 5.16(e)). There is, however, a reduction in the depth of the reflectance minima as the periodicity increases due to a decrease in structure density resulting in desaturation of the colour. The results show that the mesh-like sub-pixel design is not only applicable to the generation of plasmonic colouration but can be useful for other NIL processes to control imprint depths when utilizing a mould with a pattern of various densities.

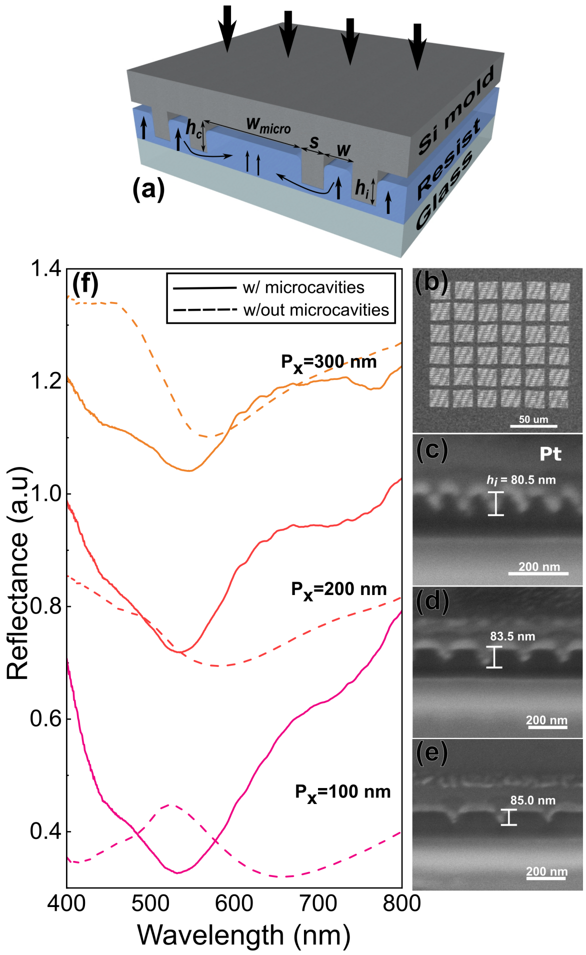

Figure 5.16: (a) Schematic shows resist dynamics during imprinting utilising mould with additional microcavity. (b) SEM image shows top-view of the mould design with additional microcavity mesh superimposed on the original pattern. Cross-sectional images reveals the imprint depth of (c)h =80.5 nm, (d)h =83.5 nm and (e)h =85.0 nm for structure with periodicities, P_x of 100 nm, 200 nm and 300 nm respectively. (f) The measured reflectance of the colours fabricated using design without microcavity (dotted line) and with microcavity (solid line), for nanorod with length of L =100 nm and lattice periodicities of P_x=100, 200, 300 nm.

5.4.1 Large Area Imprinting

To demonstrate the capacity of this technique for large area imprinting, a mould featuring an image composing rectangular nanoprotrusions of various transverse dimensions has been fabricated. The image is reproduced from an artwork entitled 'Landscape' painted by Georges Daniel de Monfreid in 1889 (Figure 5.17 (a)). The original digital image of the painting was converted to a 'graphic data system' (gds) file using a customised *Python* code. The code reconstructs the image with arrays of rectangular nanostructures with lengths and periodicities corresponds to primary cyan, magenta, yellow and black (CMYK). Colour mixing, therefore, is performed by incorporating arrays of nanostructures corresponding to the CMYK. Finally, the gds file is used to pattern the image with total area of 1.8×1.3 cm^2 on a Si wafer using EBL. Figure 5.17 (b) shows the image of the fabricated Si mould. The pattern area on the mould is large as such the cavity volume needed for the resist to fill during imprinting is higher. Therefore, the initial thickness of resist layer was increased to 300 nm to accommodate the larger cavity volume. The imprint time is also increased to 5 minutes to ensure the resist has sufficient time to flow over a large area of the mould. Optical image in Figure 5.18 (b) shows the reproduced image using NIL following the metallisation process with the polarisation direction parallel to the long-axis of the rectangular. Figure 5.18 (c) shows the magnified image of (b) revealing the individual cyan, magenta and yellow pixels. The colours of the reproduced image in (b) are, however, slightly desaturated compared to the original image in (a). This is because the colour mixing using the customised *Python* code produced a large gap between the pixels as can be seen in Figure 5.18 (c). This can be improved by making the gap between the pixels smaller to reduce the 'whiteness'. The imprinted sample also shows a colour contrast as the direction of polarisation is switched in the orthogonal direction due to the asymmetric shape of the rectangular (Figure 5.18 (d)). The morphology and cross-section of the mould and imprint sample are shown in Figure 5.18 (e) and (f) respectively, providing evidence for good pattern transfer in both transverse and vertical dimensions.

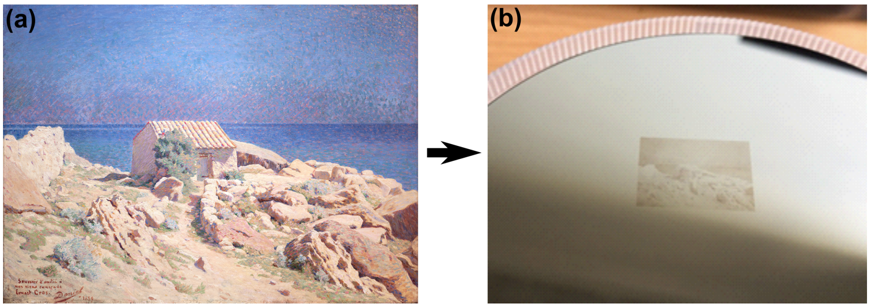

FIGURE 5.17: (a) Original image of an artwork entitled 'Landscape' painted by Georges Daniel de Monfreid in 1889. (b) Fabricated Si mould comprising the reproduced image in (a).

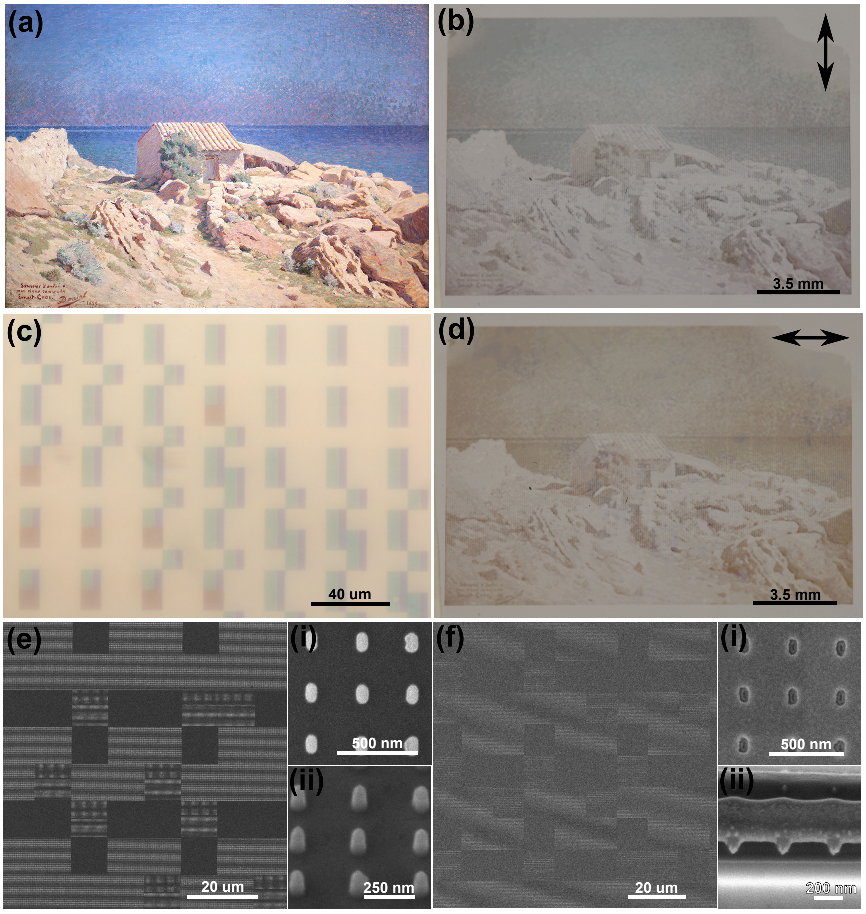

FIGURE 5.18: (a) Original image of an artwork entitled 'Landscape' painted by Georges Daniel de Monfreid in 1889. (b) Metallised nanoimprinted samples shows the reproduced image of painting in (a) utilising plasmonic pixels shown in Figure 5.10 when polarisation direction of incident light is in y-direction. (c) Enlarged image of (b) under 20 × magnification showing combination of pixels corresponds to primary CMY colours used to produce variation of colours of image in (a). (d) Colour switching effect exhibited by the sample in (b) when the direction of polarisation change to x-direction. SEM images show the morphologies of the (e) mould and (f) the imprinted samples (i) and (ii) display the magnified morphologies and cross-section of the structures on mould and the sample.

5.5 Conclusion

In conclusion, this chapter has provided evidence for the importance of the vertical gap size in the MIM-based plasmonic colour in order to control the hue and saturation of the resulting colours. This chapter, therefore, contribute in demonstrating the utilisation of the novel multilevel NIL technique discussed in Chapter 4 to fabricate a MIM plasmonic colouration device with tunable hue and saturation via adjustment of transverse and vertical geometries of the nanostructure. It was shown that the multilevel NIL can be used to tailor the vertical gap size of the structure and thus allow control over plasmonic coupling between film and nanoantenna and thus the resulting colours. Uniquely, the multilevel NIL was performed using a specifically designed binary (2D) Si mould which permit regulation of flow dynamics of the resist during imprinting to produce a grayscale-like (3D) structure in a single print thus producing wide-gamut plasmonic colouration. The process is repeatable and shows that the coupling distance can be tailored by tuning the density of the nanostructures of the mould. On the other hand, it was demonstrated that by introducing additional mesh-like microcavities to the multidensity mould, the filling rate of the resist throughout the sample is compensated regardless of pattern density. Consequently, there was minimal variation in the size of the gap between the top particle and bottom metal layer across the sample, and the resulting colour remains almost constant with periodicity. These methods of plasmonic colour printing has not been reported before and the findings presented in this chapter therefore, offers an alternative, straightforward method for producing plasmonic colouration device with tunable hue and saturation. Overall, this chapter, demonstrates very important findings i.e a full control of the vertical dimension in addition to the transverse dimension, for tuning the hue and saturation of the plasmonic colours. With this understanding, a centimeter scale imprinting was successfully demonstrated by reproducing an image via NIL. The imprinted sample is in good agreement with the original structure on the mould indicating high-fidelity pattern transfer over a large area.

Chapter 6

Polarisation-selective, Multispectral, Iridescent Plasmonic Pixels

Plasmonic nanostructures offer a new mechanism for controlling the relevant properties of the electromagnetic spectrum such as the amplitude and phase of scattered light. As discussed in Chapter 5, plasmonic-based structural colouration arises when particular regions of visible spectrum are selectively absorbed, transmitted and reflected, due to the excitation of localised surface plasmon resonance (LSPR) modes exhibited by the metallic nanostructures [13, 14]. Due to the geometric sensitivity of the relevant plasmonic modes, by using specific shapes and dimensions of nanostructures the colour generated can be modulated to be dynamically responsive to the properties of the incident illumination such as the polarisation direction and angle of incidence. For example, in Chapter 5 it was shown that structures with an asymmetric geometry such as rods [15, 84] and ellipses [81] have shown sensitivity to the direction of polarisation of a linearly polarised light. Furthermore, nanostructures with symmetry breaking configurations, have been shown to exhibit a spectral and associated colour response that are dependent of both the polarisation and angle of incidence [172, 173].

Although some applications demand a static optical effect that is independent of the properties of the incident light such as its polarisation state and angle of incidence, others require dynamically tunable colouration with preferred observation directions. Technologies such as anti-counterfeiting devices, optical security tags and high-density optical data storage are examples of applications that would benefit from this type of optical effect.

However, to date, very few studies, have investigated plasmonic colouration devices that also exhibit multiple resonances beyond the visible spectrum. One of the advantages of having multispectral plasmonic system is the production of a device with a combination of functionalities. For example, an optical security device that works both in visible and infrared wavelengths could have combined overt and covert features in a single structure, thus providing an additional security. Previous studies have shown plasmonic structures with resonances that are tunable across the infrared have significant information encoding potential [174–178]. These plasmonic devices are, however, were uncoloured or demonstrate very limited control of the produced colours in the visible region. In fact, the use of micron size structures and lattice periods reduces the resolution and compactness of the device and results in the production of diffractive colouration. It is worth mentioning here that diffractive colours arise due to interaction of light and a diffraction grating, satisfying the grating equation, $m\lambda = d \sin\theta$ where d is the periodicity of the grating (usually comparable to the wavelength of light), m is the diffraction order and θ is the angle of diffraction, thus results in the colour routing at various angles thus produces a non-controllable iridescent. Diffractive optical effects, however, already widely used and easier to replicate. In comparison, a non-diffractive colours such as plasmonic pixels would depend on the subwavelength geometry of the plasmonic structure in addition to the periodicity of the array. This means that by changing the geometry and the size of the periodic lattice will allow a wavelength-selective absorption, transmission or reflection of visible light thus various colour can be produced. By a careful control of the geometry, therefore, it is possible to create a non-diffractive iridescent effect which is more difficult to be counterfeited.

Here, a novel concept for a multispectral plasmonic device with specific properties in both the visible and near-infrared (NIR) regions is presented and demonstrated. Due to COVID-19 pandemic related restrictions and major instrument failure, however, the fabrication of a viable sample has been unsuccessful and the demonstration here therefore is confined to simulation results. It was shown that in the visible region of the spectrum, the device exhibits plasmonic colouration with a polarisation-selective iridescent feature. The iridescence appears only when the device is illuminated with light with a specific polarisation. Additionally, the device also supports a resonance in the near-infrared (NIR) region. This multispectral system is achieved using the rod-shaped nanoantenna-hole coupled systems discussed in Chapter 5 (Figure 6.1), with a spectral response that depends on the spatial dimensions, particularly the length of the nanostructures. It was shown previously, that the rod-shaped nanoantenna-hole configuration produces colours that are responsive to the direction of linearly polarised light due to the asymmetric rod geometry, but have shown a high tolerance to changes in the angle of incidence [15]. Here, iridescence is achieved by extending the length, L to more than half the size of its periodic lattice, as such $L > P/2$. By doing this, a higher order subradiant mode at a shorter wavelength in the visible can be excited by changing the angle of incidence, i.e by tilting the sample, resulting in a colour rendering effect. Additionally, since the rod-shaped structures are also polarisation sensitive, the iridescence can be achieved only with a specific state of linear polarisation. At normal incidence, however, the device considered here produces a broadband reflectance in the visible region leading to the appearance of an Al mirror, producing a uniform reflectance when viewed at normal incidence. Meanwhile, the elongation of the nanostructure compared to the devices presented in Chapter 5 red-shifts the fundamental resonance mode to the near-infrared region, producing a NIR signature which could be useful for covert data encryption. By identifying the appropriate dimensional parameters through finite element method (FEM) simulations, a plasmonic structure with multispectral property is designed and its performance is demonstrated. The results confirm the potential use of this device particularly in anti-counterfeiting and data encryption technologies.

6.1 Design and Simulation

The plasmonic device under consideration is comprised of an Al rod-shaped nanoantenna displaced vertically over its complementary perforated film as shown in Figure 6.1, similar to the Ag plasmonic colour devices presented in Chapter 5. Nanorods with various length, L are considered with the width fixed at $W = 30$ nm. The nanorod is assumed vertically displaced from the hole by a distance of $g = 60$ nm while the thickness of the Al film is fixed at $t = 50$ nm. The unit cell is arranged in a square array with fixed periodicity of $P = 300$ nm. The metallic structure is sandwiched between a layer of PMMA polymer (on the nanoantenna side) and silica (on the perforated film side). The refractive index of the PMMA and silica layer were both assumed to be n=1.45. The spectral and the colour responses under TM and TE polarised light with varying angles of incidence are systematically investigated via simulation for different lengths of nanorod, from the visible into the near infrared (NIR) region of light spectrum.

The three-dimensional simulations of nanostructure models presented in this work were performed using the Finite Element Method (FEM) implemented in the Wave Optics module of COMSOL Multiphysics 5.6. Periodic (Floquet) boundary conditions were used on the sides of the unit cell. The material data for Al was obtained from Rakic [130]. A mesh with maximum element size of 15 nm was chosen for use in detailed areas such as the nanorods and nanoaperture while 50 nm of mesh size was used in other region. Reflectance spectra were calculated using port excitation of a linearly polarised plane wave located above the nanorod and the reflectance calculated from the

S–parameter $|S_{11}|^2$. It should be noted here that only zeroth order reflectance is taken into account since there are insignificant amount of light being reflected into the other diffraction orders. Another port boundary on the rear surface of the modeled region used to calculate any transmitted power and at the same time to prevent reflections back into the model. For this study, the electric field of the linearly polarised plane wave is aligned and fixed in the y-direction, parallel to the long-axis of the nanorod. For TM and TE polarised illumination, the angle of incidence (in air) is varied from $\theta = 0° - 69°$ whereby the plane of incidence is either parallel or perpendicular to the direction of the incident electric field. The wavelength of the illumination is varied from $\lambda = 400$ nm to $\lambda = 1500$ nm, spanning both the visible and NIR.

The reflectance spectra obtained from simulations were converted to tristimulus xyz values using a customised MATLAB code based on Equations 2.4 and 2.5 given in Chapter 2, assuming illumination from a D65 light source. The xy values are used to plot the position of the corresponding colour on the CIE 1931 XY colour space. The MATLAB code also converts the xyz values to RGB and hsv values based on Equations 2.6 through Equation 2.8. By using these values, the HSV plot and simulated colour swatches can be generated by the MATLAB code. The nanorod-hole structure shown in Figure 6.1 can be straightforwardly fabricated using NIL method as was presented in Chapter 5.

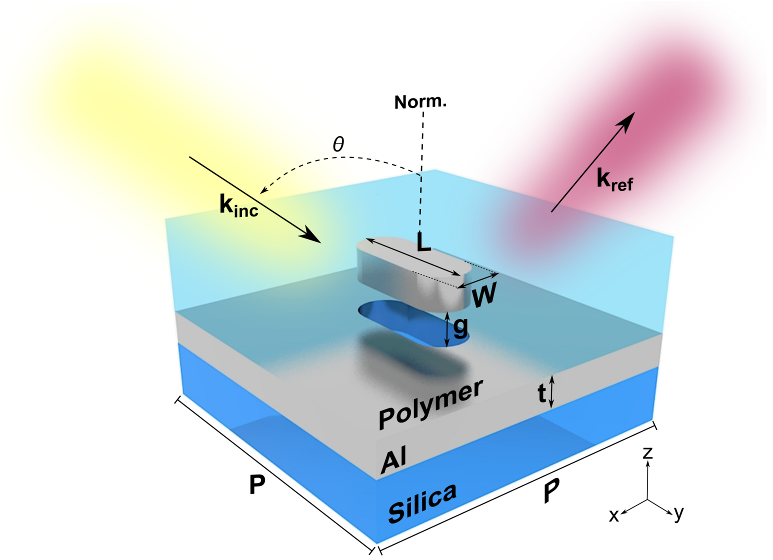

Figure 6.1: Schematic showing the unit cell of the designated multispectral plasmonic pixel comprising the rod-shaped Al nanoantenna and the complementary perforated film, arranged in a square lattice with a periodicity of P. The nanorod has a length L, width W and thickness t while the vertical gap between the top (nanoantenna) and the bottom metal (perforated film) is g. Light, linearly polarised in the y-direction, is incident an angle θ with respect to the normal of the sample.

6.2 Results and Discussion

6.2.1 Influence of the Spatial Dimension to the Angle Dependency of the Spectral Response

The length, L of the structure is varied from 80 nm to 250 nm to investigate its influence on the sensitivity of the optical response to angle of incidence, both in the visible and NIR region of the spectrum. Other spatial parameters are kept fixed. Figure 6.2 shows the simulated reflectance spectrum as a function of the length of the nanorod in the visible region ($\lambda = 400 - 800$ nm), for three different illumination conditions namely normal incidence, TM and TE polarisation. For TM and TE polarised illumination, the angle of incidence is set to $\theta \sim 46^\circ$ and the plane of incidence is either parallel to (TM) or perpendicular to (TE) the direction of the incident electric field, which in this case is kept fixed and aligned along the long axis of the nanorod (inset Figure 6.2). To simplify the discussion, the reflectance map is separated into two regions corresponding to the length, L of the nanorod. The lengths are considered (i) 'short', for L less than half the lattice period ($L < P/2$) ranging from 80 nm to 140 nm and (ii) 'long', when L is larger than half the lattice period ($L > P/2$) ranging from 150 nm to 250 nm.

In the visible part of the spectrum, under normally incident light, nanorods with a length, $L < P/2$ exhibit a red-shift in the resonance wavelength as the length increases from 80 nm to 140 nm, consistent with previous findings [15, 84]. This resonance corresponds to the dipole mode (to be discussed in more detail later) of the structure and is manifested by the expected shift in the position of the reflectance minima from shorter to the longer wavelengths as shown in Figure 6.2(a). This results in a colour change in the reflected light from yellow to blue as displayed by the simulated colour swatch in inset of Figure 6.3(a). To further analyze the produced colour numerically, the spectra are converted to hue, saturation and brightness values (h, s and v). These values are plotted in the two-dimensional hue-saturation (HS) colour space or the HS polar plot shown in Figure 6.3(a-c) which represent the position of the colour according to its hue and saturation, and the brightness (v) plot of Figure 6.3(d). The HS plot in Figure 6.3(a) shows that, under normally incident light, the increase in length towards 140 nm leads to the hue revolving in a clockwise direction from 46.7° (yellow) to 307° (magenta) and finally to 201.7° (near blue), as depicted by the solid blue line. The elongation of the rod also results in a broader bandwidth of the minima as L reached 140 nm, resulting in an improved saturation of the produced colour. The simultaneous red-shifting and broadening in reflectance minima, however, lead to the desaturation of the blue colour when $L = 140$ nm.

As the length of the nanorod increases to $L > P/2$, the resonance wavelength of the dipole mode is further red-shifted toward the near infrared, resulting in an almost flat reflectance across visible wavelengths as L reaches 250 nm. The long nanorods have their reflectance minima located mostly in the green and red regions of the visible spectrum ($\lambda = 520 - 700$ nm), resulting in an insignificant change in the position of the hue, $h \sim 205°$ corresponds to blue as shown in Figure 6.3(a) (depicted by the solid red line). Since almost all wavelengths in the visible region are eventually reflected as the length increases, there is a gradual desaturation of the blue colour as indicated in Figure 6.3(a). The reflected colours therefore are perceived as a transition from a pale blue to almost white (inset Figure 6.3(a)). As a result, at normal incidence, the nanorods with $L < P/2$ produce colours that cover a wide area in the CIE XY colour space compared to those produced by long nanorods as shown in Figure 6.3(e) and (f). The brightness of the colours, however, almost reach unity and remain almost the same despite increasing in length due to the high reflectance efficiency (Figure 6.3(e)).

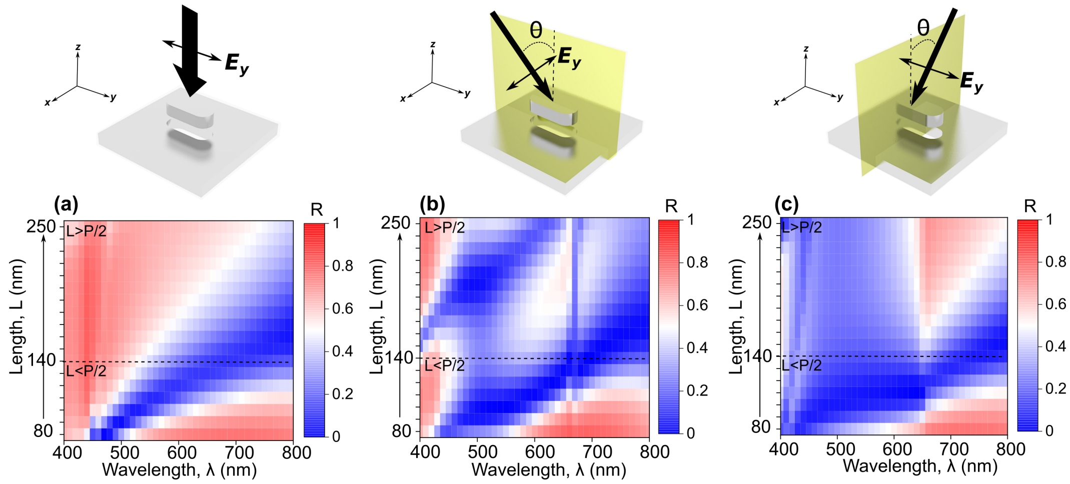

FIGURE 6.2: The simulated reflectance map as function of nanorod's length in the visible region ($\lambda = 400 - 800$ nm), for three different illumination conditions namely (a) normal incidence, (b) TM and (c) TE polarisation. The plot is divided into two regions correspond to the length, L i.e $L < P/2$ and $L > P/2$ (these regions are delineated by a dashed line). Inset shows that the angle of incidence is set to $\theta \sim 46°$ (in air) from the normal of the structure and the direction of polarisation is aligned parallel to the long axis of the nanorod (y-direction).

For the short nanorods, increasing the angle of incidence to $\theta \sim 46°$ results in a significant broadening of the bandwidth of the reflectance minima in the visible region (Figure 6.2(b)). Under TM polarised illumination, this contributes to a minimal change in the hue but an improved saturation for most of the colours especially magenta as indicated by the blue line in Figure 6.3(b). The increase in length, however, leads to a change in hue value from 29° to 223° (clockwise direction) due to the red-shift of the reflectance minimum. In comparison to colours produced under other lighting conditions, the colour generated by the short nanorods under TM polarised light covers a wide area of the CIE XY plot in Figure 6.3(e)(blue dots), suggesting an extensive hue coverage and improved saturation. As a result of simultaneous red-shifting and broadening of the bandwidth of the reflectance minima with the increase in length, however, the saturation and brightness of the blue colour decreases. The variation in hue and saturation of the generated colour associated with the spectral properties of this structure under TM polarisation are depicted in the colour swatch in the inset in Figure 6.3(b).

Interestingly, a further increase in the length of the nanorod to greater than $P/2$ (i.e $L = 150 - 250$ nm) with TM polarised illumination results in the appearance of an additional resonance mode at the shorter wavelengths. For better comparison, Figure 6.4(a) shows a representative reflectance plot from an array with nanorods with length $L = 220$ nm under various illumination conditions. The plot indicates the position of the minimum ($\lambda_1 = 540$ nm) which becomes apparent only when the structure is illuminated with off normal TM polarised light (red line). In contrast, at normal incidence the structure exhibits a broadband reflectance (dashed black line). This additional resonance originates in a higher order longitudinal quadrupole mode exhibited by the nanorod [179] as illustrated by the surface charge density obtained from the simulation and plotted in Figure 6.4(b)(TM pol., $\lambda_1 = 540$ nm). The reflectance map in Figure 6.2(b) shows that the resonance wavelength corresponding to the quadrupole mode is sensitive to the length of the nanorod and red-shifts with an increase in the length. As a result, the hue revolves anticlockwise from 270° to 30° as the length varies from 150 nm to 180 nm (indicated by the red line in Figure 6.3(b)) followed by an increase in saturation resulting in colour transitions from very pale blue to orange (inset Figure 6.3(b)). The value of the hue further moves from 25° to 205° (clockwise) as the length increases towards $L = 250$ nm, producing a wider range of colours covering orange, magenta and blue (see inset Figure 6.3(b)). The colours produced under TM and TE polarised light, however, are less bright than those at normal incidence (Figure 6.3(d)).

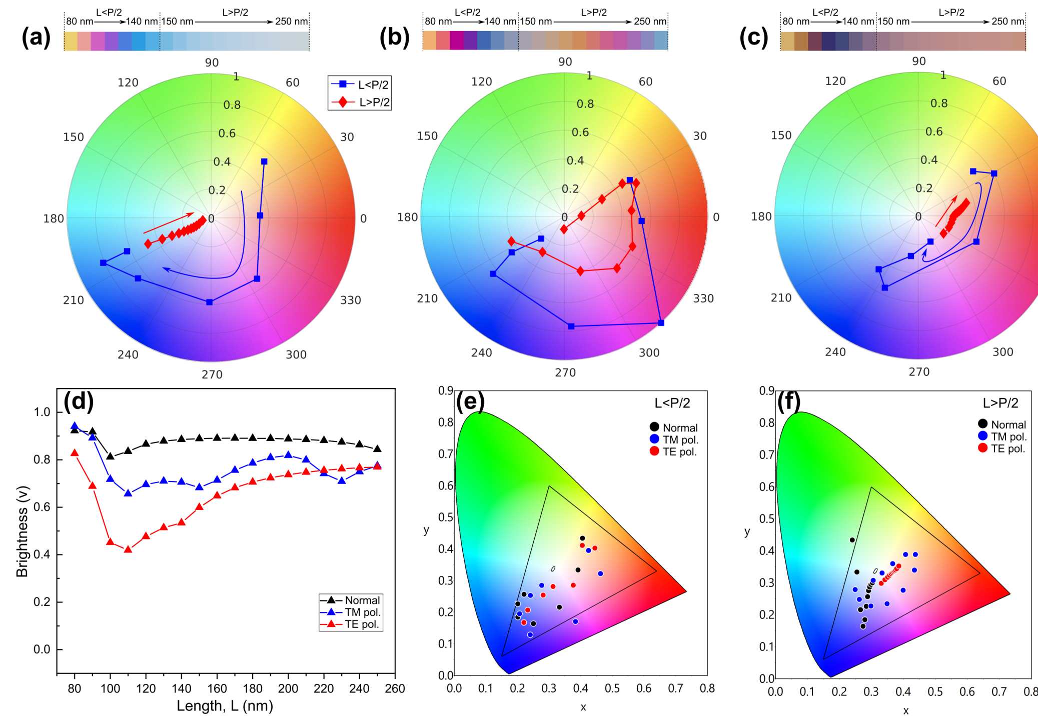

FIGURE 6.3: Hue and saturation (HS) polar plot of the colours produced by the nanorod-hole plasmonic structure of various lengths, under different lighting conditions namely (a) normal incidence, (b) TM and (c) TE polarisation. The azimuthal angle represent different hues while the radius of the plot represent the saturation of the colours. Blue and red lines shows the change in hue and saturation of the colours produced by the short ($L < P/2$) and long ($L > P/2$) nanorods respectively. Insets displays the simulated colour swatches produced by the structure as length increases. (d) Brightness (v) plot of the colours produced by nanorods of different lengths under various illumination conditions. The CIE 1931 XY plot shows the position of the colours produced by (e) short nanorods ($L < P/2$) and (f) long nanorods ($L > P/2$) under various illumination conditions. Black, blue and red markers and lines in (d), (e) and (f) refers to normal incidence, TM and TE polarisation respectively.

Illuminating the structure with TE polarised light (while keeping its electric field parallel to the long axis of the nanorod), leads to a significant broadening of the reflectance minima spanning from 400 nm to 630 nm, in addition to the red-shifting of the resonance wavelength (Figure 6.2(c)). The representative reflectance spectrum plotted (blue line) in Figure 6.4(a) indicates the position of an additional reflection minimum at shorter wavelength (λ_4 = 500 nm) that can be attributed to the sextupole mode induced by TE polarised light as illustrated by the surface charge density in Figure 6.4(b)(TE pol., λ_4 = 500 nm) [179, 180]. This resonance mode, however, is insensitive to the change in the length of the nanorod. Due to the red-shift in the visible region, the shorter nanorods produce a colour with a varying hue, revolving in a clockwise direction from 39° to 295°, covering orange, red and blue colours. However, as a result of the broad suppression in the reflectance across the visible spectrum, less light is reflected thus the generated colours appear darker and less saturated. In contrast to the short nanorod, the long nanorod exhibits very little change in hue, spanning only 50° across the HS plot indicated by the red line in Figure 6.3(c) and covering only the red region. Figure 6.3(f) indicates the positions of the colours produced by nanorods with length $L > P/2$ under various lighting conditions in the CIE XY colour space. The colours generated by the structure covers wider area in the CIE XY plot under TM polarised light than when illuminated at normal incidence or with off-normal TE polarised light, demonstrating the polarisation and angular selective colour response exhibited by the structure.

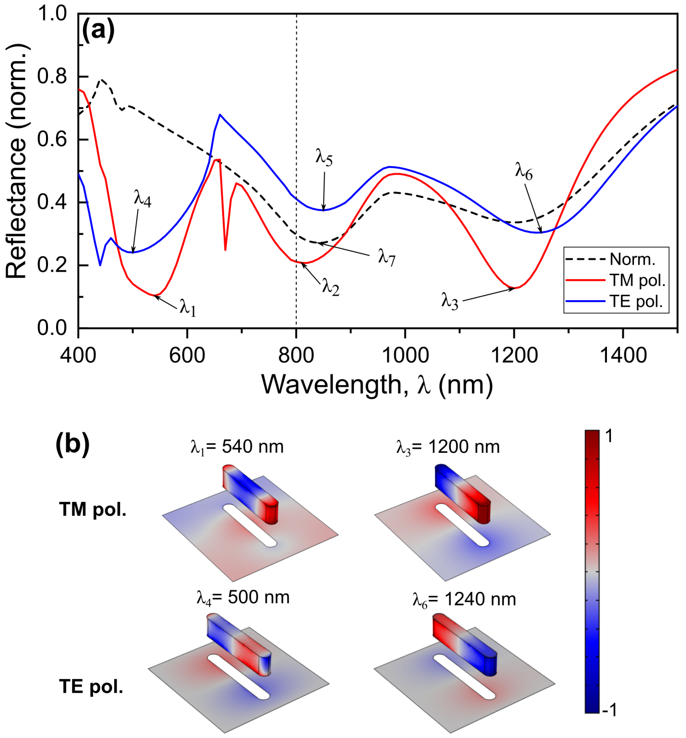

FIGURE 6.4: (a) Simulated reflectance plot for representative nanorod-hole structure with length, $L = 220$ nm under normally incident (dashed black line), TM (red line) and TE polarised (blue line) lights. (b) Normalised surface charge density plots obtained from simulation for nanorod under TM and TE polarised lights, at particular wavelengths, corresponds to the reflectance dips shown in (a).

6.2.2 Near Infrared (NIR) Signature of the Structure

The elongation of the nanorods leads to a shift in the lowest order resonance wavelength to beyond the visible region into the near infrared (NIR). To investigate the resonance of the nanorod-hole structure in the infrared region, the reflectance map in Figure 6.5 is plotted so that the wavelength is now swept from $\lambda = 800 - 1500$ nm. The reflectance map indicates a reflectance minimum in the near infrared (NIR) region exhibited by the structure under normally incident, and off-normal TM and TE polarised illumination. The simulated surface charge distribution on a representative nanorod ($L = 220$ nm) shown in Figure 6.4(b), exemplifies that the reflectance minima at longer wavelengths (i.e $\lambda_3 = 1200$ nm and $\lambda_6 = 1240$ for TM and TE polarisation respectively), are due to the fundamental dipole mode. As expected, the resonance wavelength red-shifts with an increase in the length of the nanorod regardless of the illumination conditions as shown in Figure 6.5. Nanorods with $L < 120$ nm, however, have their fundamental resonance mode in the visible and, therefore, do not appear in the NIR region plotted here. Additionally, there is also a reflectance minimum independent of the length observed at $\lambda \sim 810 - 850$ nm (see λ_2,λ_5 and λ_7 in Figure 6.4(a)), which can be attributed to the interband transition of Al ($\sim$ 1.5 eV) [181]. The position of the dip remains constant despite increases in the length of the nanorod. The position of these minima in the reflectance plot have little response to change in the illumination condition (TM or TE polarisation) at least up to 46° angle of incidence as depicted in Figure 6.5 and also Figure 6.6. The spectral response of the structure beyond this angle, however, will be discussed later. Results shown in Figure 6.5 therefore demonstrate that the plasmonic pixel device comprising nanorod-hole structure with ‘long’ nanorods not only exhibit polarisation and angle-dependent colours in the visible, but also manifest a ‘signature’ in the NIR region. These features are tunable by simply adjusting the length of the nanorod. This multispectral property created by a single structure is ideal for a compact security device possibly with a combined overt and covert feature.

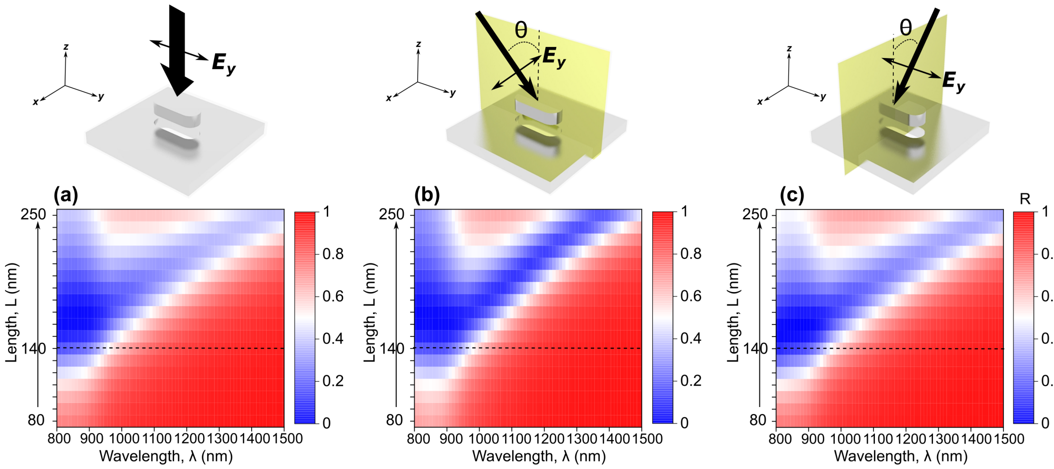

FIGURE 6.5: The simulated reflectance map as function of nanorod’s length in the near infrared (NIR) region ($\lambda = 800 - 1500$ nm), for three different illumination conditions namely (a) normal incidence, (b) TM and (c) TE polarisation. The plot is divided into two regions correspond to the length, L i.e $L < P/2$ and $L > P/2$. Inset shows that the angle of incidence, θ is set to 46° from the normal of the structure and the direction of polarisation is aligned parallel to the long axis of the nanorod.

6.2.3 'Long' Nanorod: Responsiveness of the Output Colour to the Angle of Incidence

To further investigate the responsiveness of the resonances and the resulting colour to changes in angle of incidence, the reflectance is determined for various angles of incidence. Figure 6.6(a) and (c) show the simulated reflectance map of the long nanorod with length, $L = 220$ nm and $L = 250$ nm respectively, under TM illumination, with the angle of incidence (in air) increasing from 0° to 69°. In the visible region ($\lambda = 400 - 800$ nm), both nanorods have a broad reflectance spanning almost entire the visible wavelength range under normally incident light, thus producing a highly desaturated colour close to white (insets Figure 6.6(b) and (d)). Tilting the angle of incidence to 15° excites a higher order subradiant resonance corresponding to the longitudinal quadrupole mode as shown in Figure 6.4. This is manifested by the reflectance minimum at a wavelength of $\lambda = 520$ nm for 220 nm long nanorods (Figure 6.6(a)) and $\lambda = 560$ nm for nanorods with $L = 250$ nm (Figure 6.6(c)). The spectra also indicate that the resonance wavelength exhibited by a longer nanorod is more sensitive to changes in the angle of incidence. This is shown in Figure 6.6 (c) where the resonance wavelength of an array with 250 nm long nanorods is significantly red-shifted from $\lambda = 560$ nm to $\lambda = 620$ nm as the incident angle increases to 46°, while an array of nanorods of $L = 220$ nm exhibits little change in the resonance wavelength. At the same time, the width of the reflectance minima corresponding to the quadrupole mode becomes broader with increasing in incidence angle. Consequently, nanorods of both lengths generate a gradual change in colour (insets Figure 6.6(b) and (d)).

The HS plot in Figure 6.6(b) and (d) indicate the change in hue and saturation for both nanorods as the angle of incidence increases. When the angle of incidence is tilted from 0° to 46°, an array with nanorods of $L = 220$ nm exhibits a hue variation from $h = 205.8°$ to 313.5° (anti-clockwise), producing transition in colour from near white to highly saturared magenta. Similarly, the array with 250 nm long nanorods has a varying hue value changing from $h = 174.4°$ to 205.8° when the angle of incidence changes from 0° to 46°. This results in a colour change from near white to purple and then to dark green. The increasing angle of incidence also results in a broadband absorption for both lengths of nanorod leading to more saturated colours. Meanwhile, the minimum at $\lambda = 800$ nm shows no significant shift with increasing angle of incidence up to 46°. Interestingly, the position of this particular reflectance minimum slightly blue shifts as the angle of incidence further increases to 69° before merging with the minimum corresponding to the quadrupole mode. This produces a broadband minimum, causing a shift in the hue and saturation of the reflected colours. As the incident angle increases towards 69°, the colour produced by an array with nanorods with lengths of 220 nm changes to dark purple, while an array with nanorods with $L = 250$ nm transition to a highly saturated green.

In the NIR region, the resonance wavelength due to the fundamental mode remains almost unchanged as the angle of incidence varies from 0° to 38°, before blue-shifting as the angle further tilts to 69°. Figure 6.6 therefore demonstrates the sensitivity of the resonances exhibited by the structure with $L > P/2$, to changes in the angle of incidence. In the visible, the structure shows a spectral responsivity as soon as the incident angle is tilted to 15°, resulting in an immediate colour change. Further increasing the angle of incidence to 69° results changes in colour i.e iridescence. In contrast, colour produced by nanorods with $L < P/2$ have a high tolerance to the angle of incidence as previously reported [15]. The NIR signature exhibited by the 'long' nanorods on the other hand, has a tolerance up to ∼ 46° angle of incidence. These findings also demonstrate the possibility of incorporating nanorods with different lengths in a single device which can generate NIR-concealed informations such as an image or QR code, hidden within the surface colouration.

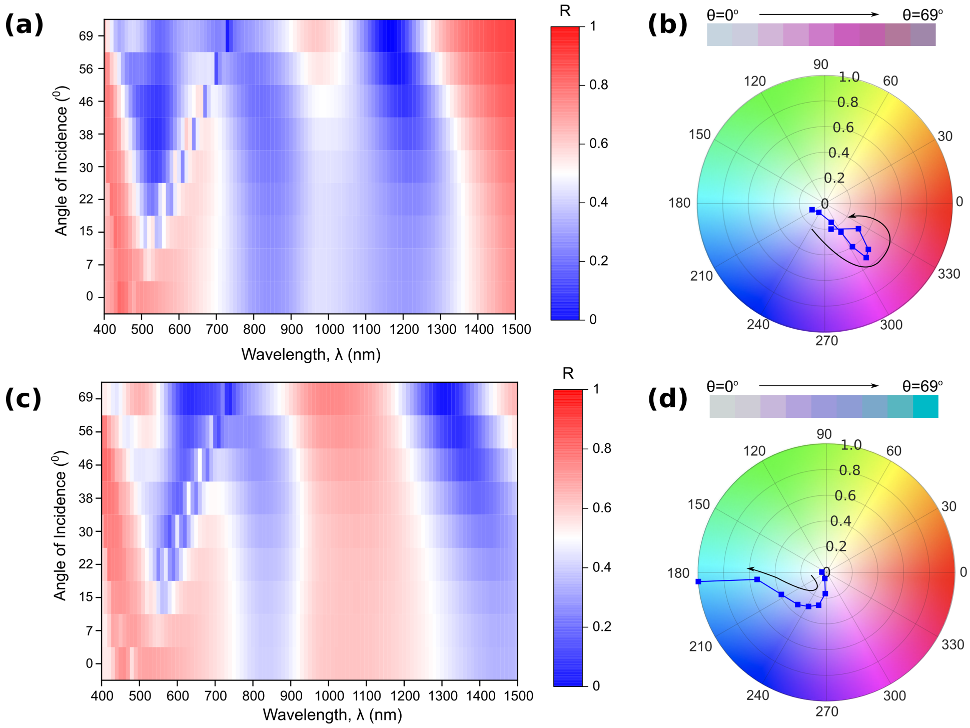

FIGURE 6.6: The simulated reflectance map as function of angle of incidence for nanorods with length, L of (a) 220 nm and (c) 250 nm, under TM polarised light with wavelength spanning the visible ($\lambda = 400 - 800$ nm) and near infrared (NIR) region ($\lambda = 800 - 1500$ nm). The HS polar plot showing hue and saturation of the colours produced by nanorod with length of (b) 220 nm and (d) 250 nm, corresponds to the spectra shown in (a) and (c).

6.2.4 'Long' Nanorod with Hexagonal Array: A comparison

The previous section discussed the spectral and colour response of arrays of long nanorod structures arranged in a square lattice. Positioning such large structure such as the long nanorod (where $L > P/2$) in a square lattice, however, can establish unwanted effects due to plasmonic coupling between adjacent nanorods. Although previous simulations shown in Figure 6.6 indicate no artifacts associates plasmonic coupling between nanorods, but fabricating devices with such closely spaced features can be challenging. This effect can be investigated by considering a hexagonal unit cell where the rod elements are positioned in an interdigitated manner avoiding 'head-to-head' plasmonic coupling. In terms of fabrication, arranging the rectangular nanoprotrusions on the mould in a hexagonal array will introduce a larger cavity size between the nanostructures as compared to square array and can, thus more easily accommodate the flow of resist during the nanoimprinting process. This can avoid the unwanted production of multilevel structures as previously shown in Chapter 5, which can lead to a change in hue and saturation of the colours due to variations in vertical gap size between the nanorods and their complementary holes. Here, the effect of the hexagonal unit cell (Figure 6.7) on the reflectance spectra is investigated and compared to a square-shaped unit cell. The long nanorods under consideration here have lengths of $L = 220$ nm and 250 nm. Other spatial dimensions are kept the same as in the previous section (Figure 6.1). The structure is illuminated with a TM polarised light at various angle while the direction of the electric field is again kept parallel to the long axis of the nanorod.

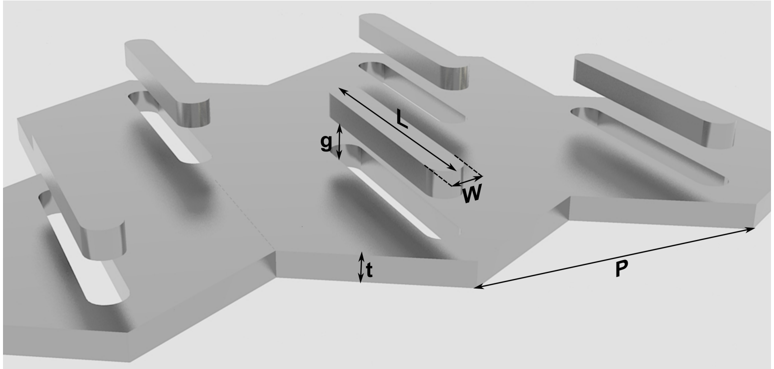

FIGURE 6.7: Schematic showing the long nanorod-hole Al structure arranged in hexagonal lattice with a periodicity of P =300 nm. The nanorod has a length L, width W =30 nm and thickness t =50 nm while the vertical gap between the top (nanoantenna) and the bottom metal (perforated film) is g =60 nm.

Figure 6.8(a) and (c) show the simulated reflectance map of the long nanorod arrays with length, $L = 220$ nm and $L = 250$ nm respectively, arranged in a hexagonal lattice with lattice constant $P = 300$ nm, under TM illumination, with the angle of incidence increasing from 0° to 69°. In the visible region ($\lambda = 400 - 800$ nm), both structures produce a highly desaturated colour when illuminated with normally incident light due to a broad reflectance spanning almost the entire visible range (insets Figure 6.8(b) and (d)). Figure 6.8(a) and (c) also show that the excitation of the longitudinal quadrupole mode takes place as soon as the angle of incidence increased to 7°. This is manifested by the appearance of significant reflectance minima corresponding to higher order resonances at $\lambda = 500$ nm for 220 nm long nanorod arrays and at $\lambda = 580$ nm for nanorod arrays with $L = 250$ nm. In comparison, the structure arranged in a square lattice showed a response once the angle of incidence reached 15° (see Figure 6.6). This indicates that structures arranged in a hexagonal array are slightly more sensitive to changes in incidence angle. In general, the reflectance minima corresponding to the quadrupole mode exhibited by the structure arranged in hexagonal lattice not only red-shifted with an increasing angle of incidence, but also become broader and have a stronger absorption efficiency (see Figure C4). This is due to the higher pattern density achievable using a hexagonal arrangement. Consequently, both nanorod devices generate a gradual change in colour (insets Figure 6.8(b) and (d)).

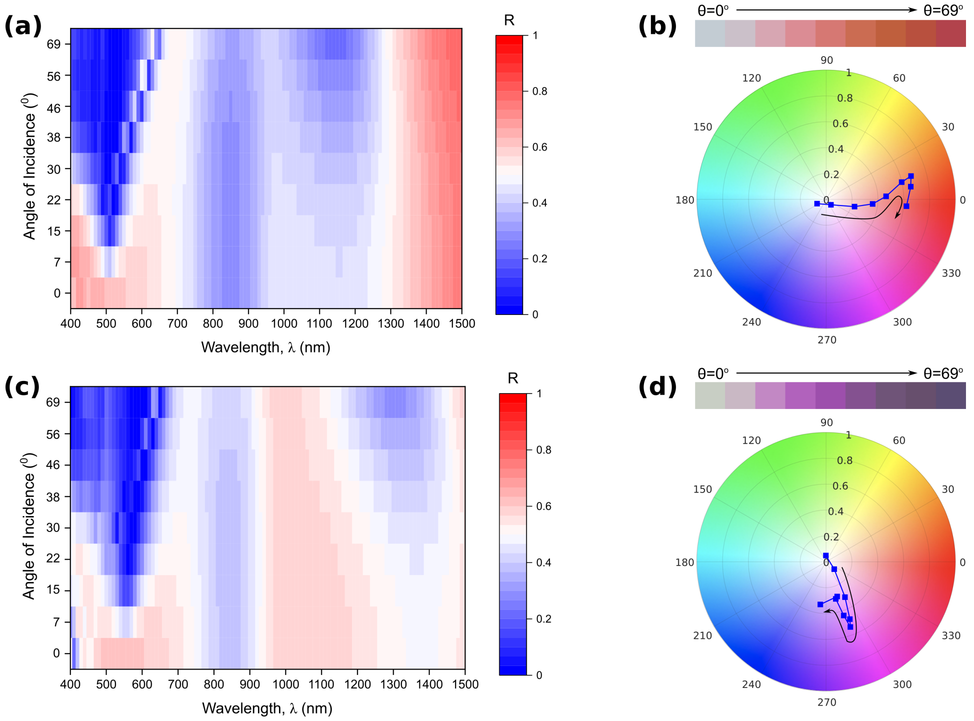

FIGURE 6.8: The simulated reflectance map as function of angle of incidence for nanorods with length, L of (a) 220 nm and (c) 250 nm arranged in hexagonal array, under TM polarised light with wavelength spanning the visible ($\lambda = 400 - 800$ nm) and near infrared (NIR) region ($\lambda = 800 - 1500$ nm). The HS polar plot showing hue and saturation of the colours produced by nanorod in hexagonal lattice with length of (b) 220 nm and (d) 250 nm, corresponds to the spectra shown in (a) and (c).

In terms of colour production, the HS plot in Figure 6.8(b) indicates the change in hue values of the array with nanorods of L =220 nm from h = 205° to 355° (clockwise direction) as the angle of incidence is tilted from 0° to 69°. At the same time, the saturation increases as a result of the broadening of the reflectance minima. As the angle of incidence reached 69°, however, the bandwidth of the spectral minimum spans almost the entire visible region, thus reducing the brightness of the reflected colours. The produced colour, therefore, transitions from near white to dark red. On the other hand, the array with 250 nm long nanorods has a varying hue value revolving from h = 91.5° to 262.3° as the angle of incidence increases from 0° to 69°. This results in a colour change from near white to dark purple. The increasing angle of incidence also produces broadband absorption, thus, increasing the saturation. On the other hand, in the NIR region, the absorption due to the Al interband transition at $\lambda \sim 850$ nm shows no significant shift despite the increase in the angle of incidence. The resonance wavelength due to the fundamental mode at the longer wavelengths blue shifted as the angle of incidence varies from 0° to 69° on a similar manner to that produced by the square array. The increase in angle of incidence also results in the increase of the intensity reflectance minima due to increasing absorption (see Figure 6.9).

Figure 6.8, therefore, demonstrates the sensitivity of the resonances exhibited by the devices with long nanorods in a hexagonal lattice to the changes in angle of incidence. The HS plots in Figure 6.8(b) and (d) also show that the array with nanorods of length L =250 nm has more colour coverage compared to an array with nanorods of length L =220 nm. In comparison, the structure arranged in an hexagonal array has a higher absorption efficiency than the square array. Figure 6.9 shows simulated reflectance and absorption plots of a representative nanorod with length of L =220 nm and L =250 nm arranged in both square (red lines) and hexagonal arrays (black lines), under 30° angle of incidence TM polarised light. In general, the use of hexagonal unit cell leads to a small blue-shift in the resonance wavelengths, both in the visible and the NIR region. It is also shown that by using an hexagonal arrangement, near-perfect absorption can be achieved (dashed lines), resulting in near-zero minima in reflection (solid lines). This is a result of the fact that the hexagonal arrangement has a higher fill factor compared to the square array for the same period, and hence has higher absorption cross-section. However, this is also lead to the decrease in reflectance efficiency of the structure causing the resulting colour to appear darker (inset Figure 6.8(b) and (d)). From a fabrication point-of-view, it is noted that a 30 nm width might be challenging to fabricate. The simulation result shown in Figure C5, however, suggests that increasing the width to 40 nm does not significantly attenuate the performance of the device where the device can still achieve the desired iridescent effect and multiple resonance. In fact, it is feasible to fabricate structure with 40 nm of width as will be shown later in Chapter 7.

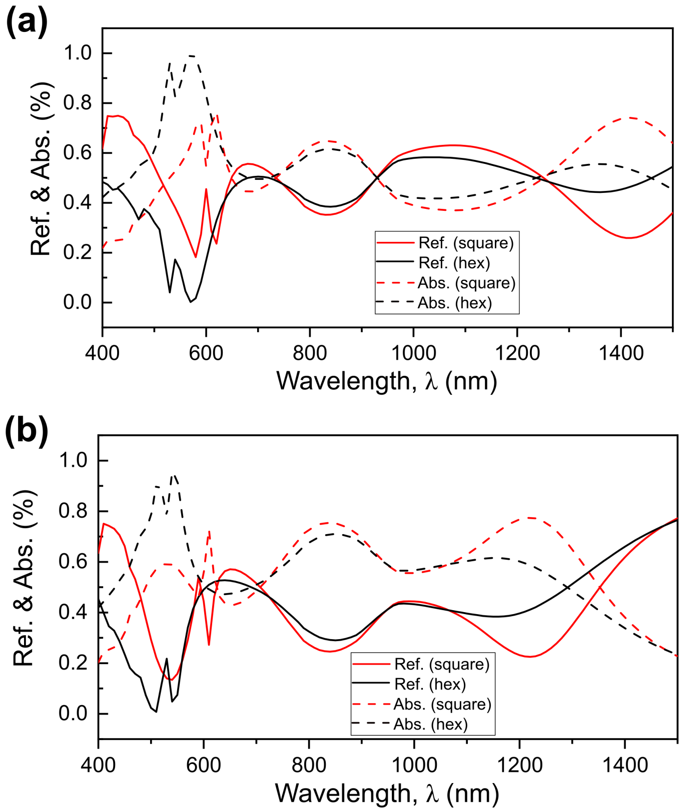

FIGURE 6.9: Simulated reflectance and absorption plots for representative nanorod of length (a)$L = 220$ nm and (b)$L = 250$ nm arranged in a square lattice (red lines) and hexagonal lattice (black lines) under TM polarised light (30°). Solid lines refer the reflectance and dashed lines present the absorption.

6.3 Conclusion

This chapter demonstrated a novel polarisation-selective, iridescent, multispectral plasmonic system comprising the nanorod-hole structure. The complex optical effects are achieved by adjusting the length of the structure to larger than half the size of its periodicity ($L > P/2$). In visible light, the device functions as a polarisation selective, iridescent plasmonic pixel, while at the same time possess a resonance in the NIR region. Simulation results show that increasing the length of the nanorods excites a higher order quadrupole mode which dominates the angle-dependent spectral and colour response in the visible region, while the fundamental dipole mode is red-shifted to the NIR region thus dictating the infrared response. Furthermore, it has been shown previously that this device is amenable to large scale fabrication via nanoimprint lithography. Due to COVID-19 pandemic related restrictions and major instrument failure, however, the fabrication of a viable sample has been unsuccessful and therefore the discussion here are based on simulation results. From a fabrication point-of-view, arranging the rectangular nanoprotrusions on the mould in an hexagonal array provides a larger cavity size between the nanostructures compared to the square array, and thus can accommodate the flow of resist during the nanoimprinting process. This is, therefore, the preferred geometry. The investigation on the effect of the hexagonal unit cell to the spectral response shows minimal shift in the resonance wavelengths. There is, however, an increment in absorption efficiency due to the increasing pattern density, which results in a darker colour. Combined with the ease of scalable fabrication, this multispectral plasmonic device offers a new approach in information encoding technology especially in the optical security device for anti-counterfeiting, with combined overt and covert features. This can be performed by incorporating 'long' nanorods of different lengths to generate encrypted information such as an image or QR code both in visible and NIR regime.

Chapter 7

Vivid Polarisation Independent Plasmonic Colour

Plasmonic colour, depending on the geometry of the constituent nanostructures, can be either dependent or independent of the polarisation state of the incident light. In fact, in nature it is well known that the chiral structure of the elytra of beetles can produce a strong sensitivity to the handedness of circular polarised light [29]. Similarly, as shown previously in Chapters 5 and 6, nanostructures with asymmetric geometries such as rectangular rods [84, 182] or ellipses [183] have shown a responsiveness to the state of linearly polarised light where different colours are generated with illumination or analysis with orthogonal polarisations. Other advanced geometries such as shallow nanogratings [88] and three-dimensional chiral structure [61] have demonstrated excellent colour production with an efficient colour switching ability by changing the handedness of incident circularly polarised light. Although sought-after in various applications discussed previously, polarisation dependent plasmonic colour suffers from 'cross-talk' due to polarisation multiplexing [183], which can lead to undesired colour mixing and colour desaturation particularly when illuminated under bright and unpolarised ambient light. Under these circumstances, the vividness (i.e the saturation and brightness of the colour) becomes degraded and is less visible when viewed in ambient unpolarised light.

Plasmonic colour devices comprising symmetric geometries such as squares [78] and disks [184–186], on the other hand, have a high tolerance to the polarisation state of the incident light thus exhibiting minimal colour change when illuminated under various polarisation states of light. It is therefore advantageous to utilise polarisation insensitive plasmonic structures specifically those with unit cells with symmetric geometries to preserve the hue and vividness of the colour generated particularly under ambient light. This is particularly important in architectural, packaging, automotive [187] and other applications where the surface will be viewed in sunlight or artificial lighting. Previous studies have resorted to simple disk, square and hexagonal shaped nanostructures to produce polarisation independent colours [78, 184, 186]. These designs, however, generate limited range of hue values while the lack of saturation and brightness is rarely discussed. Furthermore these structures are typically fabricated using complex and low-throughput methods such as electron beam lithography (EBL) which is not industrially appropriate for implementation in consumer products.

To resolve the challenge of producing highly saturated and bright colour generation with plasmonic structures under ambient light, a polarisation insensitive symmetric cross-shaped nanoantenna-hole hybrid structure (Figure 7.1), producing vivid subtractive plasmonic colours in reflection is demonstrated here. The structures are fabricated on a glass substrate using a pattern transfer lithography method i.e UV-assisted nanoimprint lithography (UV-NIL) to demonstrate the scalability of the structure. Here, different types of metal, namely silver (Ag), aluminium (Al) and gold (Au) were employed for comparison. The polarisation dependence of the optical response of the cross structure arrays have been comprehensively investigated by illuminating the sample both unpolarised and linearly polarised light and by tuning the spatial dimensions of the structure. The reflectance spectra are converted into hue, saturation and brightness values (hsv) to quantify the vividness of the generated colours. With the capacity for large area fabrication using high-throughput NIL, the proposed plasmonic colour devices are potentially highly attractive for diverse applications, ranging from high-definition displays, high-resolution colour printing, high-density optical data storage and architecture, as well as product-branding applications.

7.1 Design, Simulation and Fabrication

The configuration of the devices under consideration shown in Figure 7.1 comprises a cross-shaped metallic (Ag, Al and Au) nanoantenna and the complementary perforated film of the same material. The cross has a symmetric geometry so both arms have the same length, L and width, W, to minimise any the dependence of the structure's optical response on the direction of polarisation. Various colours are obtained by tuning the arm lengths, L while their width is kept fixed at $W = 40$ nm. The nanoantenna is vertically displaced from the complementary aperture on the film assuming a fixed distance of $g = 65$ nm to permit strong coupling between the plasmonic modes exhibited by both the nanoantenna and the aperture allowing the metasurfaces to behave as a wavelength-selective plasmonic absorber. The thickness of the metal film is fixed at $t = 50$ nm while the unit cell is arranged in a square array with a periodicity of $P = 300$ nm.

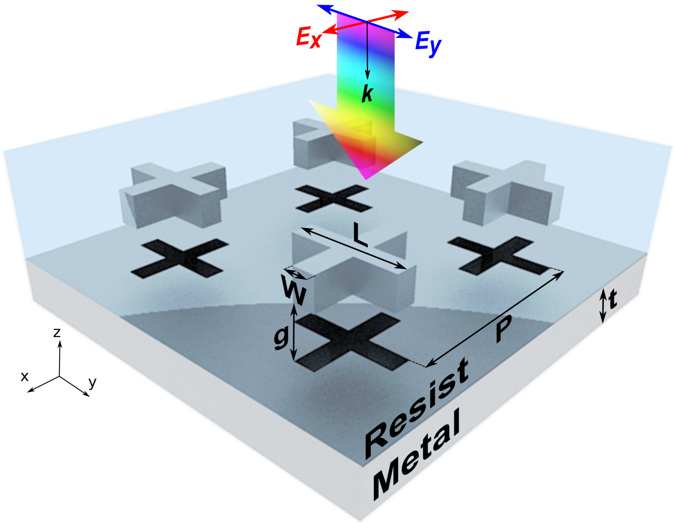

FIGURE 7.1: Schematic of the unit cell of the polarisation independent plasmonic colour comprising cross-shaped metallic nanoantenna vertically displaced $g = 65$ nm above of its complementary perforated film. The cross geometry is symmetric whereby both of its arms have the same length, L and width, W. The unit cells are arranged in a square lattice with periodicity of $P = 300$ nm, while the thickness of the metal is fixed at $t = 50$ nm. The structure is fabricated on a resist-coated glass substrate (both have a refractive index of n=1.45) and the incident light is illuminated from the nanoantenna side of the sample.

To show that the fabrication of the proposed plasmonic structure has the capacity to be scaled up for mass production, we utilise industrially friendly techniques, including UV-assisted nanoimprint lithography (UV-NIL) to first create the pattern template, followed by electron beam evaporation to deposit a layer of metal film on the patterns as shown in Figure 7.2. For NIL, a Si mould comprising arrays of cross-shaped nanoprotrusions was used in the nanoimprinting process to replicate the pattern on a UV-curable resist film spin coated onto a borosilicate glass substrate (Schott)(Figure 7.2 (a)). The Si mould was initially fabricated using electron beam lithography (EBL) where the process is described in Chapter 4 and is usually a one-off process where same mould can be used for multiple imprints as was shown previously in Chapter 5. During NIL, the mould is pressed onto the resist film at a pressure of 50 psi for 3 minutes before being exposed to UV light for 45 seconds for cross-linking of the resist (Figure 7.2 (b)). The mould-substrate stack was then manually demoulded using a razor blade thus leaving a template consisting of an array of cross-shaped nanocavities as shown in Figure 7.2 (c). A 50 nm layer of metal was subsequently evaporated onto the replicated pattern using electron beam evaporation (Figure 7.2 (d)). An adhesion layer with 2 nm thickness (i.e Ge for Ag sample and Cr for Au and Al samples) was also deposited prior to the metal deposition. The final sample, therefore, has the structure partially embedded in the polymer resist film (on the nanoantenna side) that has similar refractive index to the glass substrate (n=1.45) [1]. The SEM image in Figure 7.3 (a) and (c) shows the morphology of a representative sample (Ag) depicting the nanoimprinted cross-shaped nanocavities array after the metal evaporation process which are in very good agreement with their transverse counterparts on the mould in Figure 7.3 (b) and (d), depicting excellent fidelity of the pattern replication. The image of the cross-section in Figure 7.3(e) permits determination of the vertical distance between the top and bottom layer metal (nanoantenna and the perforated film) which is $g = 65 \pm 1$ nm. To study the spectral response to the polarisation of light, the sample is illuminated with both linearly polarised and unpolarised light from the nanoantenna side of the sample and the reflected light is collected as shown in Figure 7.1.

The reflectance spectra of the fabricated devices were measured using a custom optical cage setup discussed in Chapter 3 and 5. Light from a broadband halogen lamp (HL-2000-FHSA, Ocean Optics) illuminated the nanoparticle side of the resulting structures at normal incidence. Reflected light from an unpatterned region of the sample (metal thin film) was acquired as a reference and for normalisation. Optical images of the patterned surfaces were obtained using a Nikon N1 camera attached to an optical microscope (Olympus BX60) with a halogen lamp as a light source. White balance of obtained image is achieved by using a 'standard white' as a reference. A rotating linear polariser located in the path of the light source was used to produce linearly polarised light to determine any polarisation sensitivity exhibited by the device. Three-dimensional simulations of the above nanostructure models were performed using the Finite Element Method (FEM) implemented in the Wave Optics module of COMSOL Multiphysics 5.6. Dimensions included in the model, transverse and vertical, were obtained from SEM images. Periodic boundary conditions were used on the sides of the unit cell. A mesh with a maximum element size of 15 nm was used in detailed areas such as the nanoantenna and nanoapertures while 50 nm of mesh size was used in other region. Reflectance spectra were calculated using port excitation of a linearly polarised plane wave located above the nanorod and the reflectance calculated from the S–parameter $|S_{11}|^2$. Here, only zeroth order reflectance is taken into account since there are insignificant amount of light being reflected into the other diffraction orders. Another port on the rear surface of the model was used to calculate any transmitted power and at the same time prevented reflections back into the model. The unit cell of the structure is illuminated with a normally incident, linearly polarised plane wave with electric field directed parallel to one of the arms of the cross. To emulate unpolarised light, an average reflectance was calculated for each direction of polarisation. The optical constants of Ag and Al were

---

[1] Initial design of the device has a silica coating at the metallic film side of the sample. However, due to restricted access to the fabrication facility during COVID-19 lockdown, evaporation of silica onto the sample could not be performed.

obtained from Rakic *et al.* [130] by , while the optical constants of Au were taken from Johnson and Christy [131].

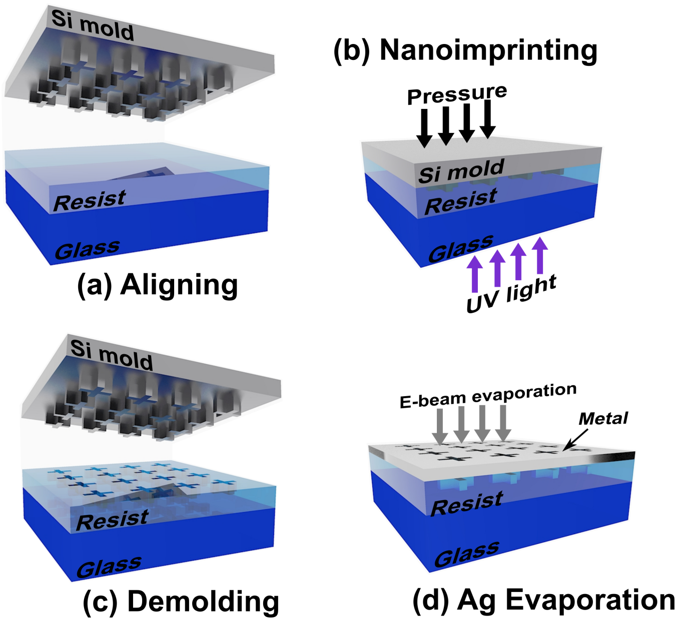

FIGURE 7.2: Schematic shows the fabrication process of the polarisation independent plasmonic colour utilising the cross-shaped structures via nanoimprint lithography and metal deposition. (a) The mould and resist-coated glass substrate were first aligned before (b) the mould is pressed onto the resist while being cured under UV light using UV-assisted nanoimprint lithography (UV-NIL). (c) The mould-substrate stack was then demoulded to complete the pattern transfer process and to obtain the replicated nanopatterns. (d) A 50 nm of metallic film (Ag, Al and Au) was then deposited onto the replicated pattern.

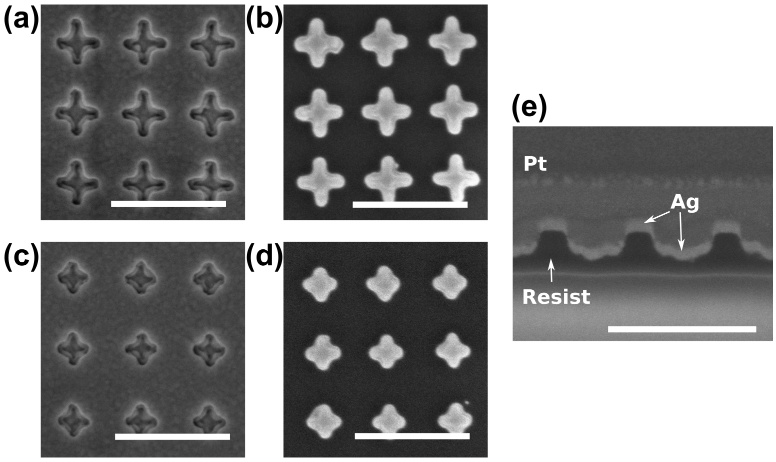

FIGURE 7.3: The representative SEM images shows the morphology of (a) 200 nm and (c) 140 nm long cross-shaped nanocavities after the imprinting and metallisation process. The SEM images in (b) and (d) shows the nanoprotrusions counterpart of the nanocavities in (a) and (c) on the mould respectively. The cross-sectional image shown in (e) reveal the vertical gap size of the structure i.e $g = 65$ nm. All scale bars refer to 500 nm.

7.2 Preserving Hue, Saturation and Brightness of Plasmonic Colour under Ambient Light

The geometry of the plasmonic structure determines the plasmonic modes and the resulting reflected spectrum. The dependence of plasmonic colouration on the polarisation state of light is largely determined by the geometry of the plasmonic elements. To study the influence of the geometry on the polarisation sensitivity of the resulting colours to the state of polarisation, the measured reflectance spectra from an MIM device consisting of arrays incorporating 120 nm long rectangular-shaped Ag nanoantenna or a symmetric cross Ag nanoantenna of the same length are shown in Figure 7.4. Each of the arrays covers 0.5 × 0.5 mm^2. The structures were illuminated with light linearly polarised in either the $x-$ or $y-$direction at normal incidence using the optical setup described above, while the average of the reflectance obtained from both polarisations gives the equivalent spectra for unpolarised illumination. As expected, the device containing rectangular nanostructures exhibits two resonance wavelengths corresponding to directions of polarisation parallel to either the long or short axes of the rectangle as manifested by the minima in the reflectance spectra shown in Figure 7.4(a). When the direction of polarisation is parallel to the long-axis of the rectangle the structure produces a longer resonance wavelength ($\lambda = 610$ nm) and results in a colour close to magenta as depicted in the optical image in the inset of Figure 7.4(a). Conversely, when the polarisation is aligned parallel to the short-axis of the rectangular rods, the resonance wavelength distinctively blue-shifts to a shorter wavelength ($\lambda = 480$ nm) causing the colour to switch closer to orange, as shown in the insets of Figure 7.4(a). The optical images further exemplify that the output colours generated by the rectangular-shaped nanostructures are switchable by simply rotating the polariser positioned in the path of the incident or reflected light. The averaged reflectance from both polarisations, therefore, results in a flatter spectral profile resembling a desaturated colour response produced under unpolarised light as depicted by the optical image in the inset of Figure 7.4(a). This shows that polarisation dependent plasmonic structures exhibit 'cross-talk' [183] when viewed under unpolarised ambient light where there is incomplete suppression of colours intended for one polarisation when observed in the orthogonal polarisation or unpolarised light, leading to undesired colour mixing. Consequently, the resulting colour become less saturated or the surface could even change hue when viewed under ambient lighting conditions.

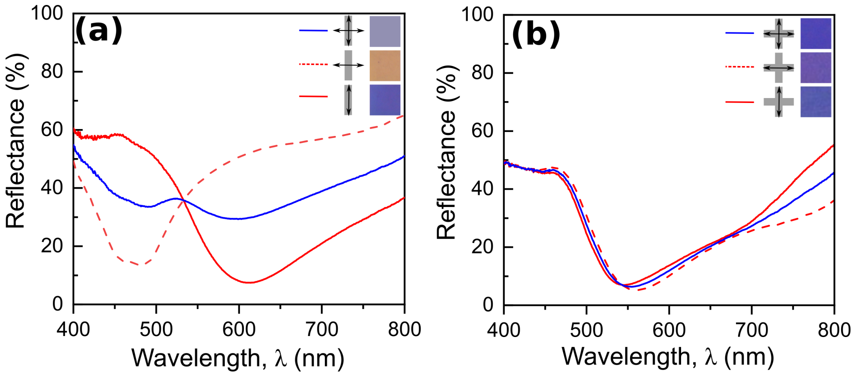

FIGURE 7.4: The measured reflectance plot of the plasmonic colour comprising (a) the asymmetric rectangular-shape nanostructure and (b) the symmetric cross-shaped nanostructure under linearly polarised and unpolarised light. Insets shows the optical images of output colours corresponds to the spectral response.

On the other hand, cross-shaped nanostructures yield almost identical spectral characteristics (Figure 7.4(b)) for both polarisation states where the reflectance minima remain at 550 nm while the reflectance intensity is almost unchanged. In contrast to the device consisting of rectangular elements, the purple colour produced by the cross-shaped structure remain almost unchanged as the polarisation state of the incident light is changed as shown in the optical images in insets of Figure 7.4(b)), indicating that the vividness and hue of the output colour are preserved under ambient light. The strong tolerance to the direction of polarisation of light exhibited by the structure can be attributed to the symmetric geometry of the cross where the same dipole modes are generated by the orthogonal polarisation directions. This feature is highly attractive for use on common consumer products which are normally viewed under bright ambient lighting conditions and require a fixed, specific surface colouration.

To demonstrate production of a wide range of colours with fixed saturation and brightness, the armlength, L of the cross structure was systematically varied, while keeping all other parameters fixed. Measurements of the reflection spectra and bright-field optical images were obtained to investigate the optical responses of the fabricated plasmonic pixels. Figure 7.5 (a) shows the measured reflectance spectra for the Ag 'cross' pixel array, with the length ranging from 80 nm to 200 nm under x- (black dashed-line) and y-polarised light (blue dashed-line) at normal incidence. The spectra shown with solid lines are obtained by averaging the reflectance from both orthogonal polarisations and are equivalent to illumination with unpolarised light. The spectra demonstrate a significant suppression in reflectance at particular wavelengths according to modifications in the length of the cross arms. Figure 7.5 (a) indicates the red-shifting of the resonance wavelength, manifested by the position of the reflectance minimum, from $\lambda = 510$ nm to beyond 800 nm in the near infrared due to the increasing armlength. As the length reached 200 nm, the spectral profile becomes flatter and results in less saturated colour. The simulated reflectance spectra in Figure 7.6(b) show a good agreement with the measured spectra. There is also an additional dip in reflectance at shorter wavelengths corresponding to a high-order quadrupole mode (see Figure D1). This dip however, is less significant in the measured spectra. Plot in Figure D1 also shows that the devices has slightly lower efficiency in reflectance when compared to the simulated spectra due to the presence of the Ge or Cr adhesion layer. Figure 7.6 (a) shows an optical image of colour swatches produced by the symmetric cross structure under polarised and unpolarised light. The colour varies from bright pink to blue to bright greenish-yellow, associated with an increase in armlength of the cross. Qualitatively, the colours are independent of the polarisation state of the light. Figure 7.6 (b) shows the coverage of the colours produced in the CIE 1931 XY plot as a result of the elongation of the arm of the cross. Similarly, the position of the colours in the CIE 1931 XY plot have almost the same coordinates despite the change in polarisation state of light.

To investigate the effect of length on the quality of the resulting colour and validate the optimum dimensions to produce high-purity colours under ambient light, it is more convenient to quantify the colour by converting the spectra to hue, saturation and brightness values (h,s and v). The reflectance spectra corresponding to each armlength were converted to the hsv values and plotted in the 2-dimensional HSV colour space as shown in Figure 7.6 (c) and (d). Figure 7.6 (c) displays the HS polar plot, representing the position of the colour according to its hue and saturation, while Figure 7.6 (d) presents the brightness (v) plot of each colours. For convenience, the saturation (s) and brightness (v) values are normalised to have values ranging from 0 to 1, while the hue (h) revolves from $0°$ to $360°$. The hue produced by the symmetric cross structures has only minimal change with the polarisation state of the light as shown in Figure 7.6 (c). This feature is particularly important to ensure that the hue is preserved under ambient lighting conditions so that the colour perceived does not deviate from the expected colour. Similarly, the saturation (Figure 7.6 (c)) and brightness (Figure 7.6 (d)) also remain almost the same under both polarised and unpolarised light, producing colours with similar shades and vividness. In the case where the armlength is increased, the HS plot in Figure 7.6 (c) shows that the output hue values revolve in a clockwise direction from $h = 284°$ to $111°$, indicating a wide coverage of colours spanning magenta to green. The reflected colours also have a brightness value (v) of greater than 0.6 which can be attributed to the efficiency of the structures with reflectance up to 80%. The brightness, however, remains constant regardless of the polarisation state of the incident light and changes in the size of the armlength. The saturation (s) of the colours however varies with the lengths of the arm consistent with the variation in linewidth of the spectra and absorption intensity (see also Figure D4).

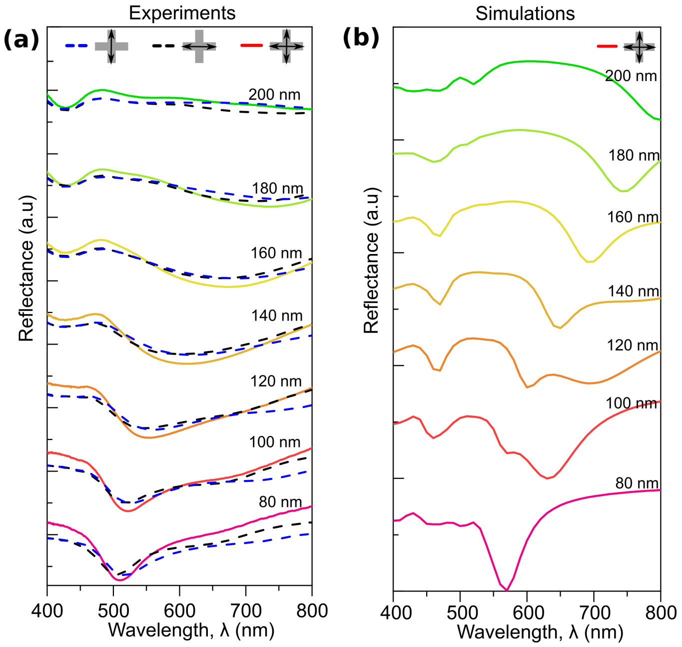

FIGURE 7.5: (a) Measured and (b) simulated reflectance spectra correspond to the cross-shaped Ag structure of increasing armlength, L from 80 nm to 200 nm, with fixed periodicity, $P = 300$ nm, under $x-$ and $y-$polarised light (black and blue dashed lines, respectively). Average of both reflectance (solid lines) represents unpolarised light (solid lines).

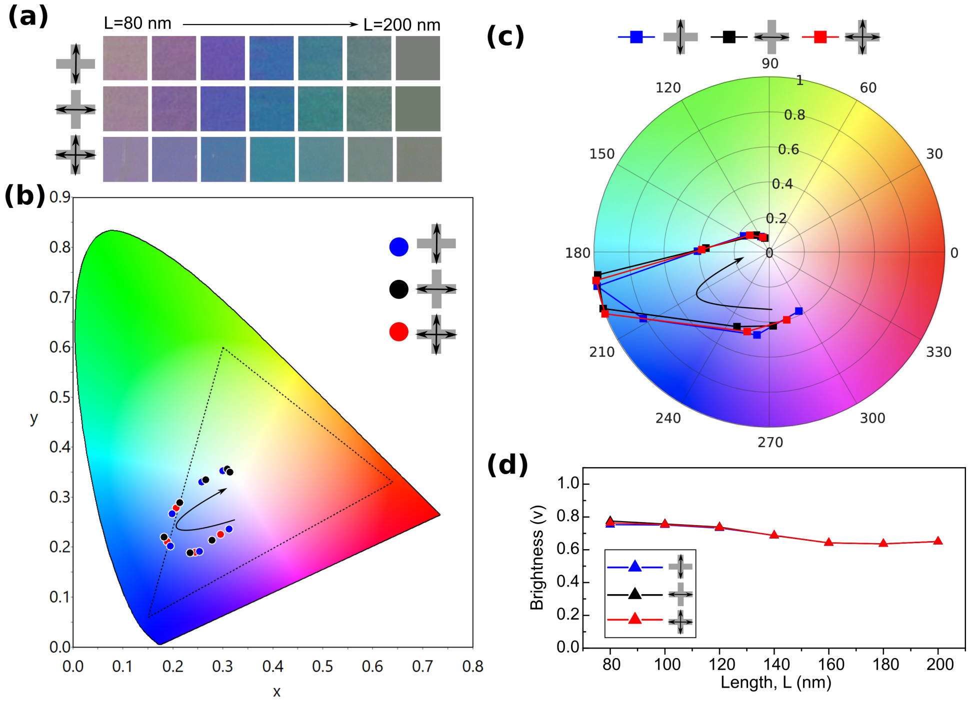

FIGURE 7.6: Properties of colours produced by the Ag device consisting the symmetric cross-shaped nanoantenna-hole structure. (a) Colour swatches as results of the increased armlengths under different light polarisation state. (b) Coordinates of the output colours on the CIE 1931 XY colour space corresponds to the length of the cross and polarisation states of light. (c) The hue-saturation (HS) polar plot and (d) brightness (v) plots associated with the output colours in (a).

In contrast, plasmonic colour produced by the structure with asymmetric rectangular features exhibit a polarisation selective spectral response. Figure 7.7 shows the measured and simulated reflectance spectra of the device consisting of Ag nanorod-hole structure. The measured reflectance plots (Figure 7.7(a)) demonstrate that when the polarisation is parallel to the longer axis of the rod, the resonance wavelength is red-shifted from λ = 510 nm to 710 nm as the lengths of the rods changes from 80 nm to 150 nm. The simulated spectra in Figure 7.7(b) are also in good agreement with the measured spectra. This results in a colour change from magenta to green (Figure 7.8(a)). The properties of the output colour can be further elucidated by plotting the hue, saturation and brightness (hsv) values corresponding to the output colours shown in Figure 7.8(a). Figure 7.8(c) shows that when the incident polarisation is parallel to the long-axis of the rectangle, the hue revolves in a clockwise direction from 262° to 88° (blue line) as the length increases, thus transitioning from magenta to green. The colour, however, becomes desaturated as the suppression in the reflectance at resonance becomes less significant with the increase in length. However, when the direction of polarisation is parallel to the fixed short-axis of the structure, the spectra indicate minimal change in the resonance wavelength since the size of the rods in the direction of the incident polarisation does not change (Figure 7.7(a)) indicating polarisation sensitivity of the output colour. The HS plot in Figure 7.8(c) indicates that the hue revolves in an anti-clockwise direction from $h = 334°$ to 34.2° (black line), covering only a small orange-red region. The produced colours therefore are perceived to be almost identical (a reddish orange) despite the change in length as shown in Figure 7.8(a). Consequently, under unpolarised ambient light, the spectral profile flattens (Figure 7.7(a)) and the colours produced become either desaturated or change in hue as indicated by the red line in Figure 7.8(c). These effects can be seen in the CIE 1931 XY plot where the colours are positioned at quite different coordinates on the plot (Figure 7.8(b)). The output colour however has a brightness of more than 0.6 with minimal changes despite the increase in the length of the rod and change in polarisation state (Figure 7.8(d)).

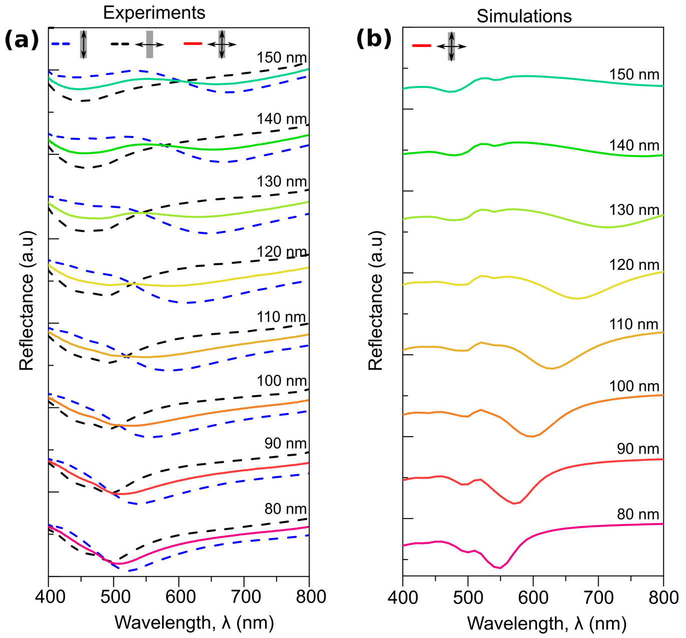

FIGURE 7.7: (a) Measured and (b) simulated reflectance spectra correspond to the rod-shaped Ag structure of increasing length, L from 80 nm to 150 nm, with fixed periodicity, $P = 260$ nm, under $x-$ and $y-$polarised light (black and blue dashed lines, respectively). Average of both reflectance (solid lines) represents unpolarised light (solid lines).

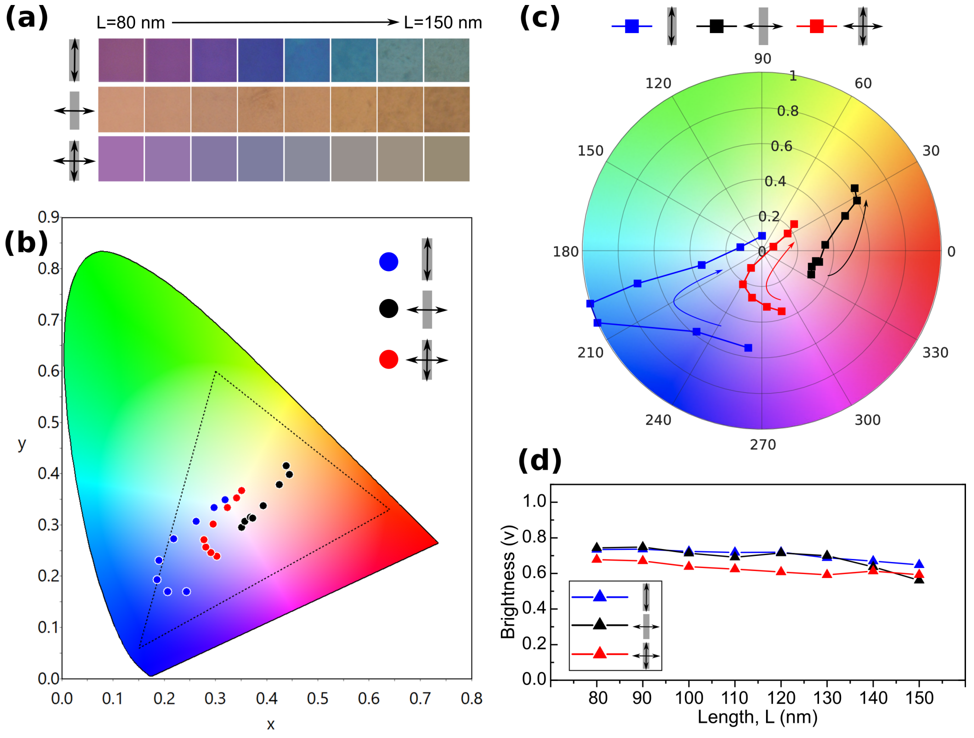

FIGURE 7.8: Properties of colours produced by the Ag device consisting the asymmetric rod-shaped nanoantenna-hole structure. (a) Colour swatches as results of the increased armlengths under different light polarisation state. (b) Coordinates of the output colours on the CIE 1931 XY colour space corresponds to the length of the cross and polarisation states of light. (c) The hue-saturation (HS) polar plot and (d) brightness (v) plots associated with the output colours in (a).

7.3 Cross-shaped Polarisation-Independent Plasmonic Colour Based on Various Metals

Previous results have shown the production of polarisation insensitive plasmonic colour devices based on silver (Ag). Here, the use of aluminium (Al) and gold (Au) to produce a polarisation independent plasmonic colouration device is also demonstrated for comparison. A series of nanoimprinted templates consisting of arrays of symmetric cross-shaped depressions in resist similar to that shown in Figure 7.3 was patterned using nanoimprint lithography (NIL) utilising the same mould used to produce the Ag sample shown in the previous section. The templates then were coated separately with 50 nm of Al and Au. The reflectance spectra of the resulting devices were obtained from simulation and experiments to investigate the optical and colour responses of the fabricated plasmonic pixels.

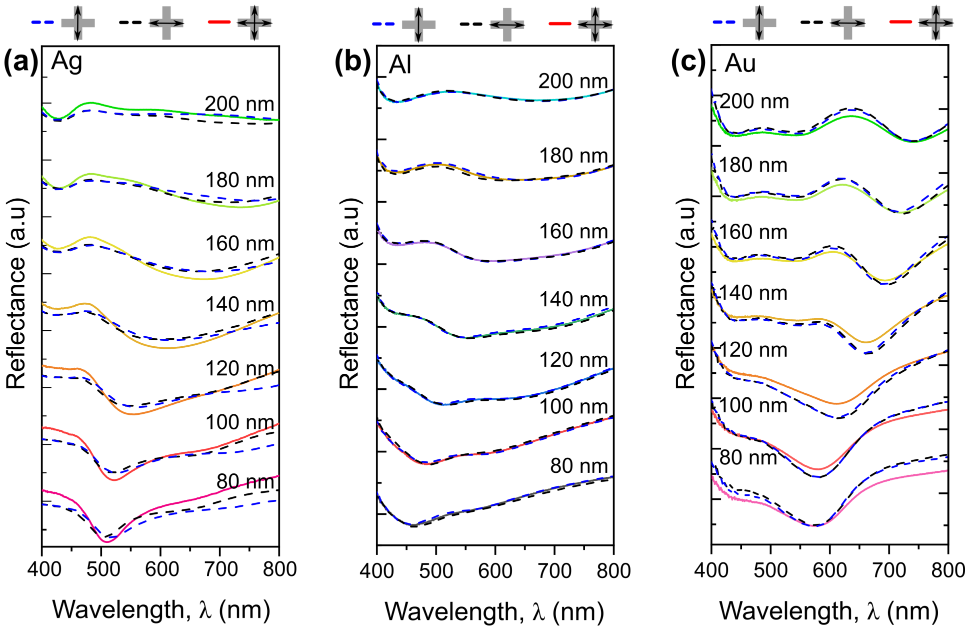

FIGURE 7.9: Measured reflectance spectra correspond to the (a) Ag, (b)Al and (c)Au cross-shaped structure of increasing armlength, $L = 80$ nm$-$200 nm, with fixed periodicity, $P = 300$ nm, under linearly polarised (dashed lines) and unpolarised light (solid lines).

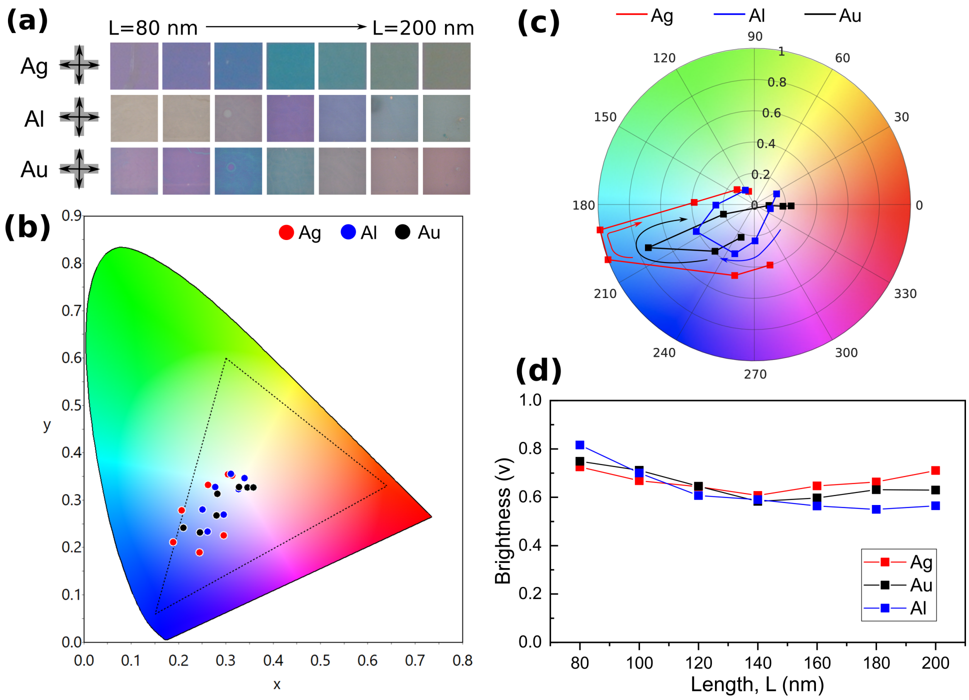

FIGURE 7.10: Properties of colours produced by the device consisting the symmetric cross-shaped nanoantenna-hole structure. (a) Optical images of the output colours under unpolarised light corresponds to various metals. (b) Comparison of the positions of the output colours produced by cross-shaped plasmonic structure of various metals on the CIE 1931 XY colour space. The red, blue and black dots shows the positions of the colours generated by Ag, Al and Au devices respectively. (c) The hue-saturation (HS) plot associated with the output colours produced by the by Ag (red line), Al (blue line) and Au (black line) devices. The direction shown by the arrow indicate the increase in armlength of the cross. (d) The brightness (v) plot of colours produced by Ag (red line), Al (blue line) and Au (black line) devices.

Figure 7.9(a-c) shows the measured reflectance spectra for the Ag, Al and Au-based cross-shaped pixel array respectively, with the length ranging from 80 to 200 nm illuminated with linearly polarised and unpolarised light at normal incidence. The periodicity, P and the vertical gap size, g are fixed at 300 nm and 65 nm respectively. All devices shows only little sensitivity to the direction of polarisation of the incident light (Figure 7.9). Similarly, the colour generated by the devices shows no significant response to the polarisation state of light (see Figure D2), indicating preserved saturation and brightness. As expected, the spectra exhibit red-shifting of the resonance wavelength due to the increasing armlength. This is manifested by the shift in the reflectance minima exhibited by all devices. The simulated spectra shows a good agreement with the spectra collected from experiments (Figure D3). The increase in the armlength of the cross, therefore, results in the production of various colours as depicted in the colour swatch shown in Figure 7.10(a).

As discussed previously, Ag device generate colours that vary from bright pink to bright greenish-yellow as the resonance wavelength shifts from $\lambda = 510$ nm to beyond 800 nm in the near infrared with increasing armlength. For the Al device, the elongation of the armlength leads to colour production covering yellow, magenta and cyan due to a shift in the resonance wavelength from $\lambda = 459$ nm to beyond 800 nm. Figure 7.10(b) indicates the position of the colours produced by the Al device (blue dots) in the CIE XY plot and show that they cover a smaller area in the plot compared to the Ag device (red dots). The HS plot in Figure 7.10(c), however, shows that the hue of the Al device (blue line) revolves in a clockwise direction from $h = 26°$ to 122°, thus indicating that Al device are able to produce a wider range of colours covering yellow, magenta and cyan, complementary colours that cannot be fully achieved using silver. Compared to Ag devices, the Al devices, however, exhibit relatively shallower reflectance minima (due to different optical constants) thus produces less saturated colours compared to those generated by Ag device as seen in Figure 7.10(c).

On the other hand, the Au devices exhibit a suppression in reflectance at relatively longer wavelengths ($\lambda > 550$ nm) due to the fundamental resonance (Figure 7.9(c)). The resonance wavelength red-shifted towards the NIR region as the length of the arm increases. Additionally, there is also appearance of broad reflectance minima at shorter wavelengths ($\lambda < 500$ nm) due to the interband transition of Au ($\sim$ 2.3 eV). These suppressions in reflectance causing most of the light in the blue region of the spectrum to be absorbed or transmitted and is reflected only at longer wavelengths associated with red/orange thus results in a limited colour production. The HS plot in Figure 7.10(c) shows that the hue produced by the Au device changes significantly from $h = 248°$ (bright pink) to 197° (orange), as the armlength increases from 80 nm to 140 nm. As the armlength further increases to 200 nm, the hue, however, shows an almost constant hue value at $h = 357°$, covering only the red region of the plot, exemplifying limited colour coverage by the Au devices. The suppression exhibited by the Au devices at different positions of the reflectance spectra also results in a flatter spectral profile thus producing a less saturated colour. All devices, however, show similar performance in terms of the brightness, with values of over than 0.6 (Figure 7.10(d)).

The results shown in Figures 7.9 and 7.10 concluded that although the Al devices have the widest colour coverage, it produces less saturated colours compared to Ag device. Compared to Ag and Au, the plasma frequency of Al, however, is higher and thus permitting access to the entire visible spectrum. Both Ag and Au, however, are less suitable for mass production due to their relatively high price. Aluminium, on the other hand, is a cost-effective alternative due to its abundance in nature and is also environmentally stable especially for ambient use due to the formation of the native oxide layer. Combined with inexpensive, high-throughput, nanoimprinting fabrication approaches, the use of aluminium is, therefore, highly attractive for large scale production of the plasmonic colour devices. In fact, large area fabrication of this device have also been performed using NIL and are shown in Figure D5 where the region exhibiting the generated plasmonic colour using the device with cross-shaped structure covers an area of more than 1 cm^2. To improve the environmental stability and usability of the device particularly in ambient condition, a thick layer of silica can be coated on the metal surface as a protection layer from oxidation process and fingerprints. This, however, will influence the resulting colour and would need to be accommodated in the design.

7.4 Conclusion

In summary, the important finding in this chapter is the production of a novel polarisation-independent plasmonic colouration device comprising symmetric cross-shaped nanoantenna-hole structure to create vivid colouration under unpolarised ambient light. The structures were fabricated using NIL using the same mould and different metals, namely silver (Ag), aluminium (Al) and gold (Au) were compared. In general, the spectral and colour response exhibited by the cross structures show minimal sensitivity to the polarisation state of the incident light, indicating a high degree of tolerance to polarisation by the device arising from the symmetric nature of the cross structure. A wide colour gamut with high saturation and brightness was successfully produced by simply tuning the armlength of the cross. The quality of the colour produced was quantified by converting the corresponding reflectance spectra into hue, saturation and brightness (HSV) plots. The results show very minimal change in the *hsv* values regardless of the polarisation state of the light indicating preserved hue and vividness of the generated colours. Conversely, the plasmonic colour produced by anisotropic rectangular structures in the unit cell shows a colour response dependent on the direction of polarisation resulting in desaturation and reduced colour gamut affecting their suitability for use under ambient conditions. In terms of material, the colours produced by the Ag devices show a wider coverage of hue in comparison to the Al and Au devices. Au device exhibited intrinsic interband transitions in the visible wavelength thus limiting the range of hue values obtainable. Ag device also produce more saturated colour compared to device made from other metals. For a large scale production, inexpensive Al would be a good candidate. However, other materials could also be employed for different applications. With the capability of large area fabrication using the high-throughput NIL method, the proposed plasmonic colour devices are potentially highly attractive for diverse applications, ranging from high-definition displays, high-resolution colour printing, high-density optical data storage, as well as product-branding applications.

Chapter 8

Future Directions

There were a number of important findings in the course of doing this work that were relevant to the main aims of the project but were unable to be adequately completed due to various factors. This chapter is therefore dedicated to discuss the prospects of these findings for future research. Potential future works resulting from this work are related to NIL-fabricated plasmonic devices and are divided into two parts. The first section is related to a further expansion of experimental work involving nanoimprinted plasmonic colour presented in Chapter 5. The second section discusses utilization of plasmonic nanoantennas coupled to quantum emitters to alter their emission properties.

8.1 Nanoimprinted Colourimetric Sensor for Refractive Index Sensing

The demand for cost-effective, compact and highly sensitive sensors, particularly in the fields of environmental monitoring and medical diagnostics, has drawn attention to plasmonic-based sensors owing to the inherent sensitivity of surface plasmon resonance (SPR) to a small change in the refractive index of its surrounding environment [13, 188]. This means, in addition to tuning the spectral response through the modification of the geometry or dimensions of the plasmonic nanostructure, the resonance of the plasmonic metasurface can be altered by applying a superstrate or substrate of a particular refractive index which leads to a colour variation for visible light. Chapter 5 has discussed a scalable approach to producing bright and distinct plasmonic colours via nanoimprint lithography (NIL). The rod-shaped nanoantenna-hole unit cell design offers interesting features including an ultrathin configuration, is fabrication friendly and in particular the colour generated is responsive to a change in the refractive index of its surrounding environment. These fascinating features will benefit a wide range of applications, including in biomedical sensing [189]. Refractive index sensors based on plasmonic colouration, therefore, provide an alternative for a label-free detection of biological samples especially in the field of bioscience.

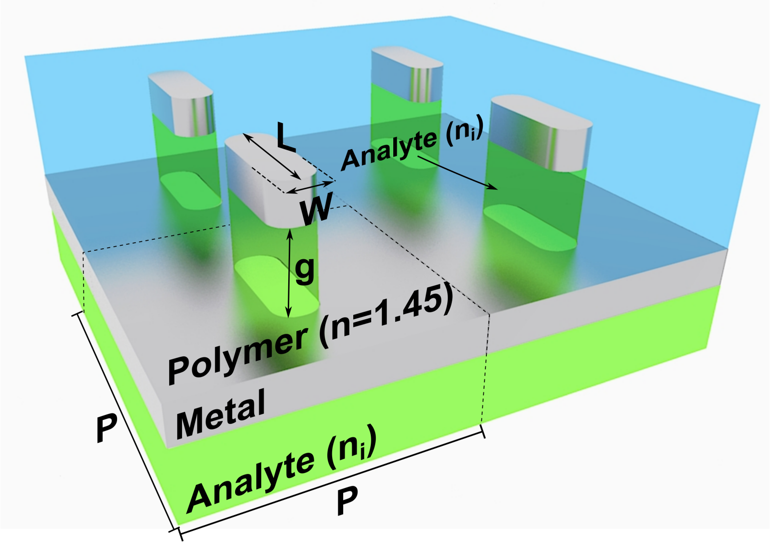

Figure 8.1: Schematic of the colourimetry sensor based on the nanoantenna-hole plasmonic colour design with length of L, width of W, vertical gap size, g and periodicity of P.

Here the potential of the plasmonic colour devices discussed previously in Chapter 5 as a refractive index sensor is investigated. To investigate the optical response of the designed plasmonic colour to the change of surrounding refractive index, a finite element method (FEM) simulation of an array of metallic rod-shaped nanoantenna-hole array (Figure 8.1) with different lengths, L was performed. It should be noted that the same simulation setup described in Chapter 5 is used here, with an addition of a layer of analyte beneath the metal film and it is assumed that the analyte fills the gap (g) between the nanoantenna and its complementary hole. Here, different type of metals, namely silver (Ag), aluminium (Al) and gold (Au) were employed for comparison. As shown in the previous chapter, from a fabrication point-of-view, plasmonic colouration devices based on various metals can be produced straighforwardly using NIL and electron beam evaporation. The optical constants of these metals used in the simulation were taken from Rakic [130] (for Ag and Al devices) and Johnson and Christy [131] (for the Au device). Similar to the device discussed in Chapter 5, the device is designed to have the nanoantenna embedded in the polymer (n =1.45) while the perforated metallic film is exposed to analyte of various refractive indices, n_i. This type of configuration could be used as optical fiber ‘meta-tip’, which utilizes plasmonic metasurface on the fiber tip for sensing refractive index of liquids [190]. This configuration could also be integrated into lab-on-chip microfluidics for in-situ sensor application [191].

The plot in Figure 8.2 (a) shows the resonance wavelengths obtained from calculated reflectance spectra of the Ag device comprising different lengths, L of rod/hole, namely L =75, 85 and 95 nm and width, W = 50 nm. The resonance wavelengths of the device are determined by nonlinear curve fitting of the simulated reflectance spectra. Here both the size of the periodic lattice, P and the vertical gap, g between top and bottom metal are fixed at 300 nm and 85 nm respectively (taken from SEM measurements in Chapter 5), while the surrounding substrate refractive index (analyte) was varied from n_i =1.0 to n_i =2.0 with a step size of 0.1. The plot in Figure 8.2 (a) indicates that for the Ag device consisting of a nanoantenna with length of 75 nm, the resonance wavelength is red-shifted from 577 nm to 618 nm as the refractive index of the analyte increases from n_i =1.0 to n_i =2.0. The hue-saturation (HS) plot in Figure 8.2 (b) shows that the output hue values of the colours generated from the 75 nm long nanoantenna revolve in a clockwise direction from h = 204.6° to 183° (blue marker and line), indicating colour coverage from light blue to cyan (see inset Figure 8.2 (a)) with the increase in the analyte refractive index. Additionally, the colour becomes more saturated as the refractive index of the analyte increases from n_i =1.0 to n_i =1.8 as a result of the broadening of the reflectance spectra (see Figure E1). Similarly, for 85 nm and 95 nm long Ag nanoantenna, the resonance wavelengths of each nanoantenna are red-shifted from 602 nm to 656 nm and from 633 nm to 691 nm respectively, as the refractive index of the analyte increases. The HS plot in Figure 8.2 (b) however shows that the hue of these nanoantennas falls in the cyan region of the plot and has a negligible change (red line for L =85 nm and black line for L =95 nm. This is because the elongation of the nanoantenna also lead to red-shifting of the resonance wavelength beyond the visible region, resulting in desaturation of colours rather than change in hue when refractive index of analyte changes. Additionally, the resonance wavelengths exhibited by both nanoantennas are mostly in the red region of the visible spectrum, which means most of the red is absorbed while blue is reflected. This deficiency however can be fixed by a careful design of the vertical gap size between the top and bottom metal. By reducing the gap size, the resonance wavelength can be blue-shifted (as shown in Chapter 5). Alternatively, the material can be changed to aluminum which has a plasma frequency in the UV region.

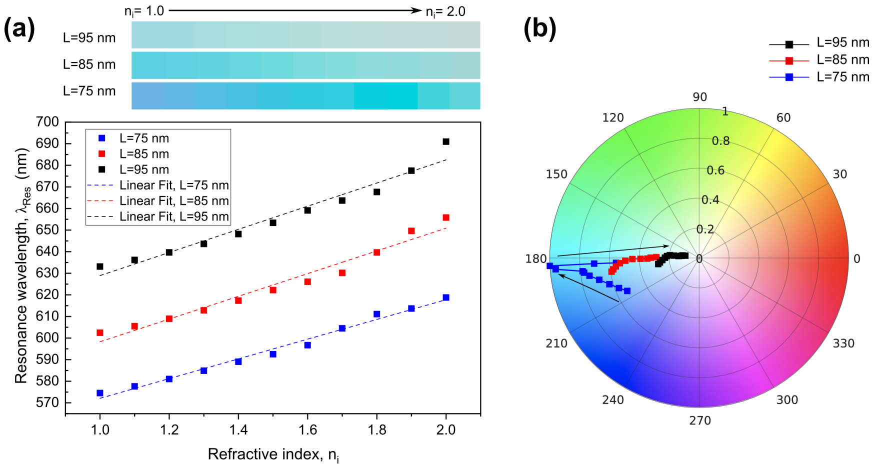

FIGURE 8.2: (a) Calculated resonance wavelengths obtained from reflectance spectra as function of refractive indices of analyte, for Ag device consisting nanorod-hole with length of L = 75 nm, L = 85 nm and L = 95 nm. Inset shows the simulated colour corresponds to the plot. (b) Hue-saturation (HS) plot of the colours generated by the Ag device consisting nanorod-hole of various lengths. The arrow indicates direction of increasing index.

By plotting the resonance wavelength as a function of refractive index as shown in Figure 8.2(a), the sensitivity, S which is described as a shift of peak resonance wavelength (λ_{res}) per unit index change (see Equation 8.1 below) can be evaluated from the gradient of the the linear fit of the plot shown in Figure 8.2(a) (details of the data analysis is shown in Figure E2 in Appendix).

$$S = \frac{\partial \lambda_{res}(nm)}{\partial n_s(RIU)} \tag{8.1}$$

The sensitivity, S of the Ag device consisting arrays of nanorods with length of L =75, 85 and 95 nm are $S = 45.7 \pm 1.76$ nm per RIU, $S = 52.6 \pm 3.35$ nm per RIU and $S = 53.6 \pm 3.67$ nm per RIU respectively. This shows that increasing the length of the nanoantenna could leads to an increase in the sensitivity to variations in the local refractive index of the environment. For comparison, the resonance wavelengths exhibited by the Al and Au devices are also plotted as function of the analyte's refractive index. The plot in Figure 8.3 (a) shows that for the Al device consist of nanoantennas with lengths of 85 nm, 95 nm and 105 nm, the resonance wavelengths of each nanoantenna are red-shifted from 466 nm to 488 nm, from 485 nm to 510 nm and from 505 nm to 534 nm respectively, as the refractive index of the analyte increases from n_i =1.0 to n_i =2.0. The change in the resonance wavelength for Al devices, however, is very small ($\Delta\lambda_{res} \sim 26$ nm) despite increasing refractive index of the analyte. This leads to a little change in the output colours as indicated in the simulated colour swatches in Figure 8.3 (a). From the linear fit of the plot in Figure 8.3 (a), the sensitivity of the Al device with different lengths of nanoantenna is calculated where $S = 22 \pm 1.2$ nm per RIU for 85 nm long nanorod, $S = 25.3 \pm 1.19$ nm per RIU for 95 nm long nanorod and $S = 28.8 \pm 1.25$ nm per RIU for nanorod with length of 105 nm. This shows that the Al device is much less sensitive than the Ag device. This can be attributed to the small change in resonance wavelength exhibited by the Al device as shown in Figure 8.3 (a).

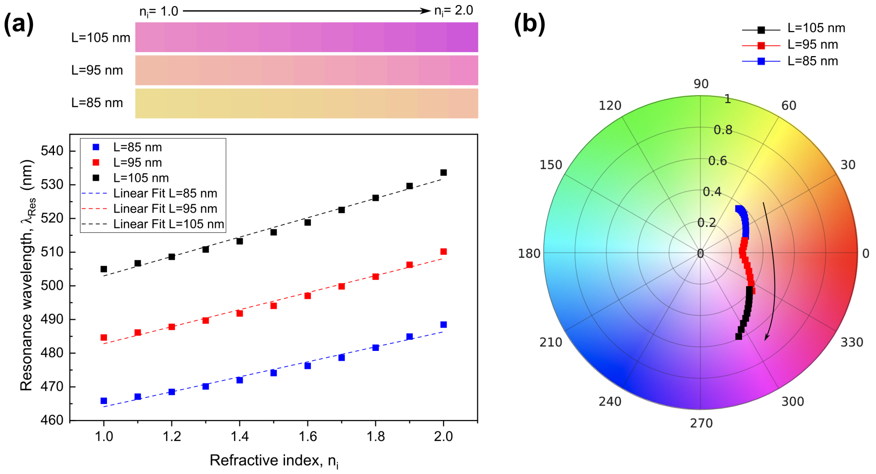

FIGURE 8.3: (a) Calculated resonance wavelengths obtained from reflectance spectra as function of refractive indices of analyte, for Al device consisting nanorod-hole with length of L = 85 nm, L = 95 nm and L = 105 nm. Inset shows the simulated colour corresponds to the plot. (b) Hue-saturation (HS) plot of the colours generated by the Al device consisting nanorod-hole of various lengths. The arrow indicates direction of increasing index.

The hue-saturation (HS) plot in Figure 8.3 (b) shows that the output hue values of the colours generated from the Al device has minimal change. For the 85 nm long nanorod device, the hue revolves in a clockwise direction from $h = 49°$ to 20° (blue marker and line), remain in only orange, while the saturation remains almost unchanged with the increase in analyte refractive index. This results in insignificant colour change despite increase in the refractive index (see inset Figure 8.3 (a)). For the device composed of 95 nm long Al nanoantennas, the red-shift in the resonance wavelength results in hue changes from $h = 15°$ to 323° (clockwise) as shown in the HS plot of Figure 8.3 (b) (red marker and line) which results in a colour transition from orange to light magenta as the refractive index increases from n_i =1.0 to n_i =2.0. The saturation, however, remains almost unchanged. Similarly, for nanorods with L =105 nm, the increase in refractive index leads to the hue revolving in a clockwise direction from $h = 323°$ to 294° (black marker and line), corresponding to a change from red-orange to magenta, followed by the slight increase in saturation from $s = 0.39$ to 0.58. As a result, the colour of the device changes from a light red-orange to a saturated magenta with the increase in analyte refractive index.

In comparison, the plot in Figure 8.4 (a) shows the resonance wavelengths exhibited by the Au device as a function of the analyte refractive index. The sensitivities of the Au devices are $S = 37.6 \pm 1.19$ nm per RIU for that with 75 nm long nanorod, $S = 44.8 \pm 3.18$ nm per RIU for that with 85 nm long nanorod and $S = 55.8 \pm 4.43$ nm per RIU for that with nanorod of length 95 nm. This shows that the Au device is more sensitive to changes in refractive index of its surroundings compared to the Ag and Al device. The Au device, however, exhibits interband transition in the blue region (400–500 nm) of the visible spectrum manifested by the broad minima in the reflectance spectra in conjunction with the minimum associated with the dipole mode at the longer wavelength (see Figure E5). This results in a minimal hue change and colour coverage as can be seen in the HS plot in Figure 8.4 (b) despite the increase in nanorod length and analyte refractive index. For devices with nanorods with a length of 75 nm, the hue change (clockwise) from $h = 147°$ to $117°$ covering mostly green. The Au device consisting 85 nm and 95 nm long nanorods, on the other hand, each exhibits a hue change from $h = 75.6°$ to $46°$ (red marker and line) and from $h = 44°$ to $39°$ (black marker and line) respectively, resulting in a colour change from green to a desaturated orange. The HS plot also indicate that the Au devices produces smaller range of colours compared to Ag and Al devices.

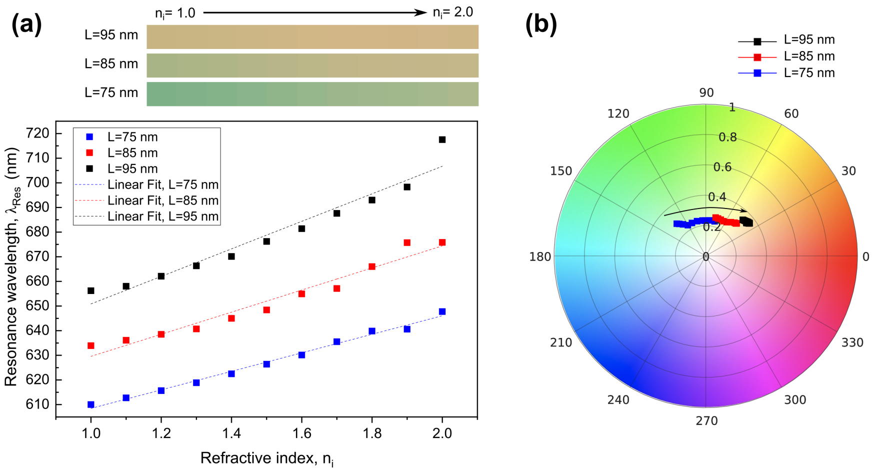

FIGURE 8.4: (a) Calculated resonance wavelengths obtained from reflectance spectra as function of refractive indices of analyte, for Au device consisting nanorod-hole with length of $L = 75$ nm, $L = 85$ nm and $L = 95$ nm. Inset shows the simulated colour corresponds to the plot. (b) Hue-saturation (HS) plot of the colours generated by the Au device consisting nanorod-hole of various lengths.The arrow indicates direction of increasing index.

In order to verify the results obtained from the simulation, the spectra need to be measured experimentally. However, due to to restricted access to the relevant nanofabrication facilities during the COVID-19 lockdowns, there are very limited samples that were fabricated and, therefore, provide insufficient data. Only few samples were able to be fabricated using the NIL and subsequent metal coating process as was discussed previously in Chapter 5. Optical images in Figure 8.5 shows preliminary results that demonstrates a promising colour response exhibited by the nanoimprinted plasmonic colour of various lengths when refractive index of the analyte is either (a) $n_i = 1.0$ (air) or (b) $n_i = 1.5$ (immersion oil) where the immersion oil was applied on sample (a) via drop-casting. Measuring the resulting resonance wavelength of the plasmonic colour covered with analytes of various refractive indices requires a broadband light source and a spectrometer equipped in the bench-top optical setup described in the Chapter 3. Calibration and normalisation can be performed by measuring the reflectance from a standard (e.g. unpatterned region of the sample). From the simulation results, it was shown that with a proper selection of material and the length of the nanorod-hole structure, the plasmonic colouration device discuss in Chapter 5 can exhibit significant colour shift, easily distinguished by the unaided eye, with the change in the refractive index. Although aluminium is more cost-effective and more environmentally stable due to the formation of the native oxide layer, it has the least sensitivity to the change in refractive index of the analyte. On the other hand, gold has the advantage of stability for ambient use due to its inherent inertness. The Au device also shows higher sensitivity to the change of the refractive index. However, it is expensive and exhibits poor colour coverage. The Ag device has a good sensitivity to the change in the analyte refractive index and has a greater colour coverage. Silver, however, is known to be easily oxidized when exposed to the ambient condition which can deteriorate its lifetime. Overall, the results demonstrate that the nanorod-hole structure has suitable properties for colourimetric refractive index sensing, which can be potentially mass produced using NIL fabrication method discussed in Chapter 4, 5 and 7. The sensitivity of the devices, however, can be improved by switching the position of the nanorod and nanohole (in Figure 8.1) so that the nanorod is embedded in the analyte layer allowing more contact area with the nanorod-hole structure. Their design, however, requires substantial further work.

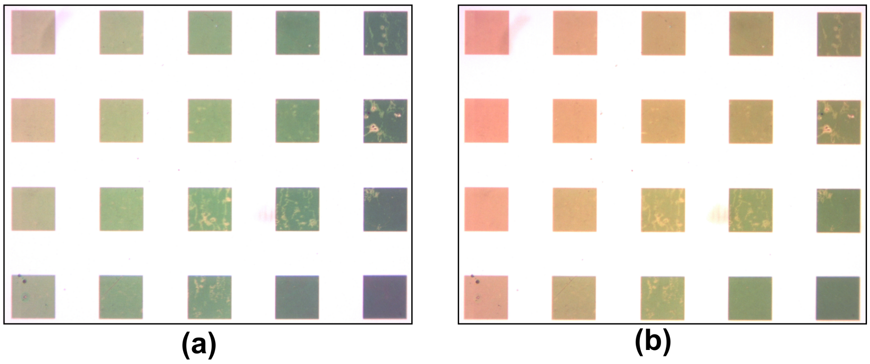

FIGURE 8.5: Optical images demonstrates colour response exhibited by the nanoimprinted plasmonic colour when refractive index of the analyte change from (a) $n_i = 1.0$ (air) to (b) $n_i = 1.5$ (immersion oil).

8.2 Plasmonic Nanoantenna for Controlling Emission Properties of Quantum Emitters

Plasmonic structures can also be used to alter the radiation properties of a quantum emitter through the Purcell effect [192]. Emitters such as quantum dots (QDs) are known to have fixed emission properties upon the synthesis process and cannot be controlled directly thus limiting their versatility [193]. Thus the development of approaches to engineering the optical local density of states (DOS) of quantum emitters is of great interest for controlling their emission properties post-synthesis. One approach is to incorporate quantum emitters into the vicinity of the source of surface plasmons i.e plasmonic structures, allowing coupling between plasmon and exciton (a quasi-particle made up of electron-hole pair, bound by Coulombic attraction) which results in tunable optical emission properties such as the radiation directionality, polarization state and lifetime [194]. There are two types of exciton-plasmon coupling with regards to the extent of the perturbation to their wavefunctions; (i) strong exciton-plasmon coupling caused by the perturbation of wave functions that results in the creation of another quasi-particle called a plexiton which has properties distinct from the original particles, and (ii) weak exciton-plasmon coupling, when there is no perturbation of the wave function [195]. The effects of weak coupling such as surface-enhanced Raman scattering (SERS), surface plasmon enhanced absorption, fluorescence enhancement and changes in lifetime decay, have been widely discussed in the literature [195]. Here we focus on weak interactions between excitons in semiconductor quantum dots coupled to plasmonic structures.

Additionally, the exciton-plasmon interaction adds another degree of freedom to control the emission properties via resonances in plasmonic structures to produce optical effects such as tailored polarisation and/or directional emission and increases in quantum yield. By placing the quantum emitter in proximity to a nanocavity with an asymmetric shape such as a rectangle, so that the resonance is polarisation dependent, not only is the emission intensity enhanced, but also preferentially polarised [196–198]. Furthermore, it is also possible to control the beam shape or directionality of the emission of quantum emitters using a specific nanoantenna design such as the bullseye structure. The plasmonic bullseye nanoantenna has been demonstrated to shape the far-field radiation patterns of dipole emitters including nitrogen-vacancy centers in diamond [199], colloidal quantum dots [200–202] and fluorophores [87, 203]. The bullseye structure is not only useful for shaping the emission directionality, but also collecting radiation. There is a need, however, to improve the bullseye nanoantenna design in order to collect or collimate polarised emission from QDs. Furthermore, the use of a scalable fabrication technique could lead to widespread adoption of these devices.

8.2.1 Cavity-based Plasmonic Bullseye Antenna for Polarised and Directional Emission of Quantum Dots

Plasmonic nanoantennas have the ability to confine incident electromagnetic (EM) field in a subwavelength volume via a localised surface plasmon resonance (LSPR), which enables efficient conversion of EM field from the far- to the near-field and vice versa. LSPRs generated by a plasmonic nanoantenna are highly dependent on their geometry, and, hence their light-matter interactions. Thus, careful design of the nanostructures will allow manipulation of optical responses, which results in alteration of the properties of scattered or emitted light such as the directionality and polarisation state. It is known that quantum emitters such as quantum dots (QDs) radiate as dipole emitters. An ensemble of QDs, therefore, will produce isotropic, unpolarised radiation. An appropriate design of the geometry of the nanoantenna, therefore will allow control over the directionality of the produced emission with preferential polarisation state [204–206]. One example of a nanoantenna for the production of a directional beam is the bullseye structure which comprises concentric circular corrugations of fixed periodicity. The periodic circular corrugation functions as an antenna to concentrate the electromagnetic energy at the aperture located at the centre of the bullseye and enable control of the directionality of the radiated light [87].

Recent studies have successfully employed the bullseye nanoantenna to shape the far-field radiation patterns of dipole emitters including nitrogen-vacancy centers in diamond [199], colloidal quantum dots [200–202] and fluorophores [87, 203]. As previously mentioned, quantum emitters such as quantum dots suffers from several limitations. Their intrinsic symmetrical spherical or cylindrical shape permits only non-directional emission, which not only causes emission losses but also inefficiency in collecting emitted photon with low to medium numerical aperture (NA) microscope objectives and optical fibres [200, 201]. Thus the use of conventional bulk optics is always a challenge, and also against the global trend in miniaturization of devices. Another limiting factor is that QDs have relatively long emission lifetime. Plasmon modes coupled to QDs can induce lifetime shortening by providing a higher density of optical states, thus potentially increasing the total photon flux from the QDs [197, 200]. Previous studies have used plasmonic bullseye nanoantennas demonstrating capability to collect or collimate emission from QDs efficiently while enhancing the intensity [200, 201, 207]. Such properties are highly sought after particularly for detecting fluorescence emission from single quantum dots [87] and also to collimate light into optical fibres.

While the bullseye nanoantenna shows excellent control over directionality of a beam, however, they have poor control of the polarization state of the produced emission. While polarisers are commonly used as a straightforward method to produce polarized light, it leads to power loss and reduces the output intensity. Furthermore, the intrinsic bulkiness of typical polarisers add weight to a device and require additional space. Although wet chemical methods can be used to produce semiconductor QDs that directly generate linearly polarised emission [208, 209], a more simple approach using rectangular plasmonic nanocavities has proven to produce polarised emission accompanied by intensity enhancement via Purcell effect and enhancement of electric field using ordinary QDs [197, 198]. Therefore, there is a need to impove the bullseye nanoantenna design in order to collimate (or collect) a polarised emission from QDs.

The aim of this investigation, therefore, is to design and fabricate a plasmonic bullseye nanoantenna comprising arrays of rectangular-shaped metallic nanocavities arranged in particular orientations used to not only enhance the emission of QDs, but also control the polarisation state and directionality of the QDs emission. A schematic of the device considered here is shown in Figure 8.6. For this purpose, the plasmonic bullseye lens is designed as such the usual corrugations were replaced with linearly oriented rectangular nanocavities. High quantum efficiency graded alloy CdSe/CdS/ZnS quantum dots were spread over the nanocavities. Due to unavoidable limitations arising during the completion of this work, only the near-field emission was able to be partially characterised. The concept, however, is sufficiently promising that preliminary results are included here.

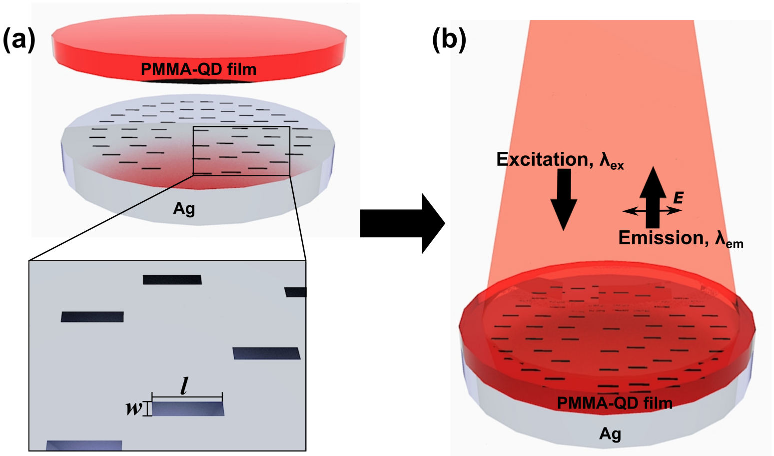

Figure 8.6: (a) Schematic of the silver (Ag) bullseye nanoantenna comprising Ag film with nanocavities arranged in polar array coated with a layer of PMMA mixed with quantum dots. Each nanocavities have a length of l =200 nm, width of w =40 nm and depth of d =220 nm. (b) Schematic illustrates the device can be excited using unpolarised light source with wavelength of λ_{ex}=530 nm and will result in a collimated, linearly polarised emission with wavelength of λ_{em}=640 nm.

Fabrication

The schematic in Figure 8.7 shows the fabrication process used to produce the nanoantenna and incorporation of QDs. First, UV assisted nanoimprinting lithography was used to fabricate the template (Figure 8.7 (a-c)). This creates a circular array of rectangular nanocavities, each with length, l = 200 nm, width, w = 40 nm and depth of, d = 220 nm. Then, the patterned template is coated with 250 nm of Ag before spin-coating with a layer of PMMA mixed with QDs dissolved in dichlorobenzene. SEM images of the fabricated bullseye nanoantenna (without the PMMA-QDs coating) are shown in Figure 8.7 (f) and (g)).

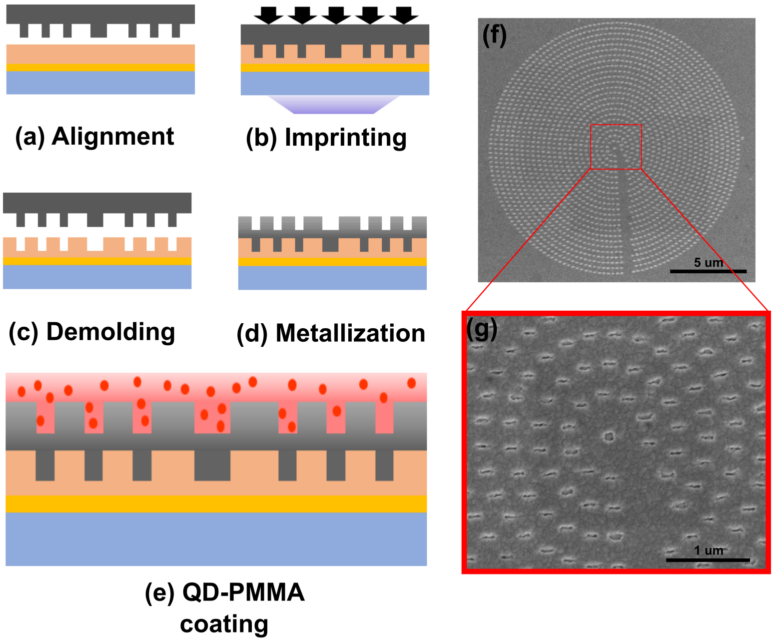

Figure 8.7: Fabrication of the cavity-based bullseye nanoantenna coupled to QDs: (a-c) UV nanoimprint lithography, (d) Metal deposition and (e) Coating of QDs-mixed PMMA layer.(f) SEM image of the nanoimprinted bullseye nanoantenna. (g) A magnified image of (f).

Optical Measurement

In order to characterise the local effect of the rings of nanocavities on the emission properties of the quantum emitters, the spatial distribution of the fluorescence was mapped using fluorescence laser scanning confocal microscopy (FLSCM) (near-field distribution). The schematic of the setup is shown in Figure 8.8. The microscope chassis employed for the FLSCM setup is a Nikon Ti-80i Eclipse inverted microscope fitted with 0.9 NA 100× objective lens and a Mad City Labs Nanodrive xy piezostage. The excitation source is a Fianium 450-SC supercontinuum source and the required wavelength and bandwidth is selected using a Fianium SuperChrome tunable filter. Here, the type of quantum emitters used are quantum dots (QDs) which have an absorption peak 530 nm and emission wavelength near 640 nm. To reduce noise from the background emission coming from off-structure QDs, the concentration of the QDs has been optimised and thin QD-PMMA film of 155 nm thickness was used. Spectrally filtered light (530 nm central wavelength and 10 nm linewidth) is focused by an objective lens (L1, 40× 0.6 NA Olympus Plan) onto the tip of a single mode fibre (Thorlabs SM450) and then collimated by a collimator (L2, Thorlabs F260FC-A) to an opening at the back of the microscope.

The FLSCM setup utilises a single point confocal configuration. In this configuration, small apertures were used to spatially filter the illuminated and collected light. Throughout the project, confocal scanning and a binning techniques were employed since typical wide-field fluorescence microscopy produced fluorescence images with poor noise-to-signal ratio due to stray emission from the out-of-focus areas of the sample. The computer-controlled piezostage was used to perform a serpentine scanning mode with resolution of 100 nm and scan areas of 25 μm. A Perkin Elmer SPCM-AQRH-14-FC avalanche photo diode (APD) was incorporated into the setup to collect and bin the emission from the QDs. In this setup, the collimated light from L2 passed through an 50μm aperture attached at an opening at the back of the microscope before being focused onto the sample using an objective lens of 0.9 NA (100× CFI Plan Achromat, Nikon). The fluorescence is collected with the same objective lens and spectrally filtered using a 532 nm long pass (LP) dichroic beam splitter (DM, Semrock Brightline 540) redirected to a second 50μm aperture placed in front of the APD. Both the first and second apertures have the same size to ensure the detector images a similar volume to that being illuminated. Light from outside this volume is focused either before or after the plane of the aperture and hence is blocked by the aperture. A Thorlab USB CCD camera (Thorlab DCC1645C) was also attached to the setup for navigation purposes but is not shown in the figure. A half waveplate (HWP, Thorlabs AHWP05M-600) and linear polarizer is placed in front of the APD to obtain a polarisation resolved fluorescence image from QD-plasmonic coupled samples.

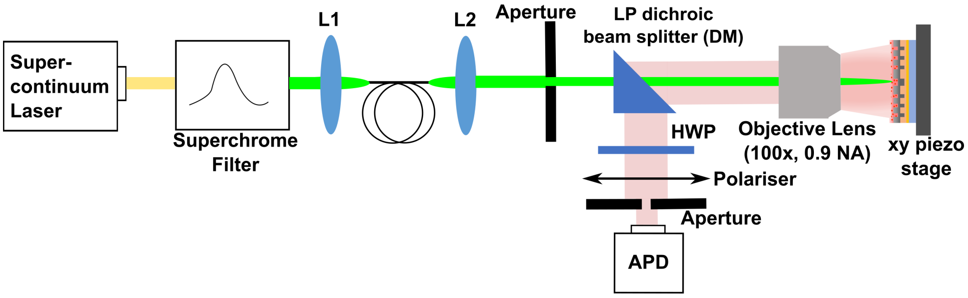

FIGURE 8.8: Schematic of the fluorescence laser scanning confocal microscopy (FLSCM) used for obtained the fluorescence image of the bullseye-coupled QDs nanoantenna.

Preliminary results

Figure 8.9 shows the resulting intensity, I, of near-field scans resolved as I_x and I_y when the analyser is in the x- and y-polarisation orientations, respectively, and normalised to the background fluorescence. For the x-polarised scan, the bullseye device shows minimal signal above the fluorescence background (Figure 8.9(a)). The y-polarised scan, however, shows a bright circular region with almost twice the intensity of the fluorescence background (Figure 8.9(b)). Although the results shown here are preliminary, the fabricated device shows ability to produce linearly polarised emission owing to the shape and orientation of the cavities. To investigate the influence of the cavity-based plasmonic bullseye nanoantenna on the radiation pattern and directionality of the emission beam from the quantum dots, k-space reflection microscopy can be utilised [210]. This permits the measurement of the far-field radiation intensity and determination of the angular distribution of the emitted light. However, further fluorescent imaging and k-space measurement however, was unable to be performed due to lack of laboratory access and to the laser failure following the COVID-19 lockdown period.

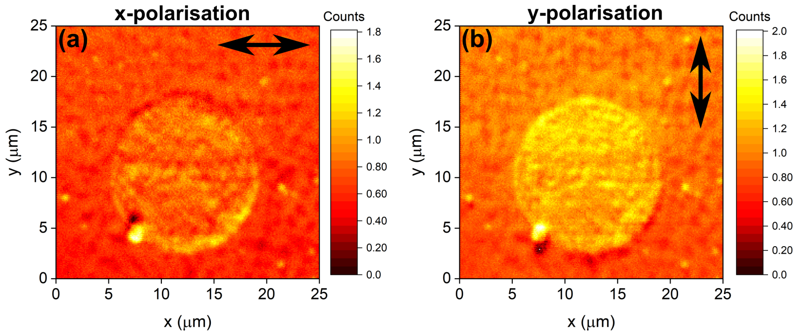

FIGURE 8.9: Fluorescence images of the bullseye-coupled QDs obtained from (a) x-polarised scan and (b) y-polarised scan of FLSCM

8.3 Conclusion

In conclusion, this chapter discusses some potential other interesting plasmonic devices that can be fabricated using the nanoimprint lithography (NIL) technique. Some promising preliminary results and simulation results were presented in this chapter. Potential future work resulting from this research are a plasmonic colourimetric sensor for refractive index sensing and a plasmonic slot-based bullseye structure for controlling the emission properties of quantum dots and other emitters. The plasmonic colourimetric sensor is an extension of experimental work of the nanoimprinted plasmonic colour presented in Chapters 5. A colourimetric sensor device consist of nanorod-hole made of three different materials namely Ag, Al and Au, were compared in terms of their sensitivity and colour production with the change in the refractive index of analyte. Simulation results shows that by choosing appropriate materials and geometry, the device can perform as a sensitive refractive index sensor with a distinguishable colour transition. A preliminary experimental result based on Ag plasmonic colour was also presented where a colour change was observed when the refractive index of the analyte is changed from $n_i = 1.0$ to $n_i = 1.5$. Furthermore, a slot-based Ag bullseye nanoantenna has also been fabricated using NIL and coated with a layer of PMMA mixed with quantum dots (QDs). The device was expected to produce a polarised and collimated beam emitted by the QDs while at the same time enhance the emission of the QDs. Preliminary fluorescence images obtained from experiments show the near-field effect of the nanoantenna on the QD emission. This provide evidence that the emission has been enhanced and has a tailored direction of polarisation. The preliminary results shown in this section demonstrate the diversity of next-generation plasmonic devices that can be fabricated using NIL.

Chapter 9

Conclusions

9.1 Research Outcomes

This thesis has discussed the capability and versatility of nanoimprint lithography (NIL) technique for fabrication of plasmonic devices exhibiting surface colouration on a large scale. One of the main outcomes of this thesis is the understanding and optimisation of some important aspects of the NIL process which impacts the resulting structures. In conjunction to the study on the NIL process, a major outcome of this work also revolves around the conception and characterisation of NIL fabricated plasmonic-based structural colouration with specific responses to the properties of incident light.

A large portion of this project was centered on nanofabrication, particularly NIL as discussed in Chapter 4. A significant amount of time, therefore, was spent on development of a robust NIL process and attempting to repeatably produce viable samples. The development and refinement of the NIL process which are the key enabling process for the fabrication of the samples in Chapter 5, 6 and 7, required a significant investment in time at the Nanofabrication Lab, Swinburne University of Technology. As a result, a NIL process sheet has been developed (see Figure A2) and while not publishable, will remain available to successive researchers. One important factor in the development of the NIL process that requires consideration is the dynamic flow of the resist during nanoimprint process. This involves investigation of three crucial aspects of NIL namely: (i) the NIL parameters, (ii) material and conditions of the mould and substrate, and (iii) chemical and physical properties of the resist. These are the factors that govern the flow of the resist and thus impact the quality and conformity of the replicated lateral and vertical geometry. The result of optimisation of these aspects of NIL is presented in Chapter 4 of this thesis. It was shown that high temperature and pressure is required in thermal NIL to replicate the height of the actual nanoprotrusions on the mould (see Figure 4.6). This is due to intrinsic high-viscosity and thermoelastic nature of the PMMA resist. Since the use of high temperature and pressure in thermal NIL results in a longer process time and can be detrimental to the shelf-life of the mould and potentially damaging the substrate, UV-assisted NIL was used as a the main fabrication method which offers less than a minute curing time, low operating temperature and imprint pressure is reduced by 8 fold.

Additionally, the choice of material for the substrate and mould is also important. Thermal NIL requires both mould and substrate to have the same thermal expansion coefficient in order to avoid thermally induced defects. UV-NIL on other hand, requires either the mould or substrate to be transparent to UV light to aid the curing process. While the replication of lateral geometry is more straightforward, controlling the vertical dimension of the imprinted structure is non-trivial. Remarkably, given that the chemical and physical properties of the resist is fixed, the density of the nanoprotrusions on the mould play important role in controlling the flow of the resist. It was shown that by varying the periodicity of the nanoprotrusions on the same mould, it is possible to tune the vertical height of the imprinted structures. The results demonstrate that height increase linearly with the spacing between the unit cells which can be attributed to the variation in viscous resistance as the size of the cavity varies (see Figure 4.13). Consequently, multi-height structures, a feature that resembles a grayscale structure, was produced. This important finding thus demonstrates a novel multilevel NIL process to produce a three-dimensional structure using only a binary, two-dimensional mould by harnessing only the dynamics of the resist, without relying on the intricate control of charged particles or light beam dosage as in EBL and UV lithography. Another important finding in Chapter 4 is that the variation in imprinted heights resulting from the use of multidensity mould can be minimised if required by introducing complementary mesh-like microcavities into the mould, thus producing structures with almost constant imprint heights (see Figure 4.14). This demonstrates a capability to have complete control of this vertical dimension of the imprinted structure. At the same time, this approach will serve as a great alternative solution to produce same-height structures which has been a challenge in using NIL when utilizing a mould of varying structure density.

The results from the investigation of multilevel NIL in Chapter 4 was utilised in plasmonic colour printing and presented in Chapter 5. It is known that the resonance wavelength exhibited by plasmonic colour device comprising metallic nanoantennas coupled to its complementary perforated film, is highly sensitive to the vertical gap between the top (nanoantenna) and bottom (perforated film) metal. This vertical gap controls the nanoantenna-film coupling strength and, hence, the resulting colouration seen in reflection. Chapter 5, therefore, demonstrated the utilisation of the multilevel NIL developed in Chapter 4 to produce plasmonic colouration using the Ag MIM nanorod-hole coupled system, with the ability to control not only the resulting structure's transverse dimension but also the vertical gap size by adjusting the periodicity of the structure on the mould. The use of multilevel NIL method for controlling the vertical gap size and hence the resonance wavelength of plasmonic colouration device adds an additional degree of freedom for controlling the hue and saturation of the resulting colours. Consequently, a palette consisting of a wide colour gamut over CMYK colours was successfully produced as a result of the interplay between the length, periodicity and vertical gap size (see Figure 5.10). Additionally, it was also shown that the introduction of complementary microcavities in the vicinity of the nanostructures on the original mould, a fixed gap size, hence the position of the resonance wavelength can be produced (see Figure 5.16). Finally, with the improved understanding of resist flow and colour production, a centimeter scale plasmonic colour printing was successfully demonstrated using NIL (see Figure 5.18).

One of the interesting applications of plasmonic colour devices are their capacity to function as optical security features. Dynamically tunable plasmonic colours involve switching colour by changing the polarisation state of incident light or/and tilting the sample and are thus suitable as overt optical security features. In addition, plasmonic device with an IR signature have the ability to conceal information which can be decoded only using a special IR detection tools. The work presented in Chapter 6, therefore, revolves around a novel concept of combining a dynamically tunable plasmonic colour with an IR signature as both overt and covert features. In Chapter 6, a concept of multispectral polarisation sensitive, iridescent plasmonic colour with an IR signature was discussed. This includes an investigation of the plasmonic colour comprising the Al nanorod-hole configuration as an optical security feature with combined overt-covert feature. This device was designed to be easily fabricated using NIL as has been demonstrated in Chapter 5. However, due to restricted access to relevant nanofabrication facilities during COVID-19 lockdowns, the investigation was performed through simulations. From these simulation results,it was shown that nanorods with length, $L > P/2$, i.e relatively large features in the unit cell, exhibit colours that are sensitive to the tilting of angle of incidence, only when under TM polarisation. This is due to the excitation of a higher order resonance (a quadrupole mode) exhibited by the long nanorod 'activated' only with off-normal illumination, while the direction of electrical field is maintained parallel to the long axis of the nanorods. These 'long' nanorods, however, exhibit an almost flat reflectance spectra, resembling a silver mirror, when illuminated at normal incidence. Consequently, there is a colour transition with the change in angle of incidence thus creating an iridescent effect (see Figure 6.3). Furthermore, as a result of increase in the length, the nanorods exhibit electric dipole resonance in the IR region, with subradiant high order resonances at shorter wavelengths (see Figure 6.5). Interestingly, this dipole mode has a relatively high tolerance to the change in angle of incidence. This multiresonance feature envisages the use of nanorod-hole configuration as an polarisation selective iridescent overt feature while having a covert IR attribute.

A dynamically tunable plasmonic colouration device, specifically one that is polarisation dependent, however, is less suitable for use in conditions that require a fixed surface colouration under unpolarised ambient lighting conditions. This is because polarisation-dependent plasmonic colour suffers from 'cross-talk' which can lead to undesired colour mixing and colour desaturation when illuminated under unpolarised ambient light. Chapter 7 therefore presents an important finding involving the design and fabricatation of a plasmonic device that exhibits surface colouration robust to the polarisation state of the incident light thus preserving its vividness under ambient light. This involves the utilisation of plasmonic devices with unit cells comprising symmetric cross-shaped nanoantenna-hole structures, where the length of the cross arms is the same. The devices were again fabricated using NIL and coated with various metals namely Ag, Al and Au. It was shown that the spectral profile of the structure in reflectance is largely insensitive to the state of polarisation. As a result, the reflected colours shows insignificant changes regardless of the polarisation state of light. The quantified hue (H), saturation (S) and brightness (V) plots shows that the *hsv* values remain almost constant for both polarised and unpolarised light. This is however, not the case for nanorod structures where the spectral response exhibits a distinct shift in the position of the resonance wavelength when illuminated with orthogonal linear polarisation resulting in a colour change. Consequently, the colour produced under unpolarised ambient light experienced desaturation. Although there are studies that have utilised other symmetric geometries to create polarisation independent plasmonic colours, there are no reports detailing colour preservation strategies using a nanoimprinted polarisation-insensitive plasmonic colouration device. The use of different metals, however, has both pros and cons and can be employed to suit different applications. With the capability of large area fabrication using the high-throughput NIL method, the proposed plasmonic colour devices are potentially highly attractive for diverse applications.

The penultimate chapter, Chapter 8, discuss the prospects of the findings presented in this thesis for potential future research. This includes an extension of experimental work involving nanoimprinted plasmonic colour devices in Chapter 5 for the use as the cost-effective colourimetric sensor which can be useful especially in the fields of environmental monitoring and medical diagnostics. Additionally, a preliminary demonstration of a novel NIL-fabricated, slot-based bullseye plasmonic nanoantenna which is capable of manipulating the polarisation and directionality of emission of quantum emitters, is also shown in this chapter. The use of NIL as a fabrication method would be beneficial in the mass production of such devices. The preliminary results shown in Chapter 8 therefore demonstrate the diversity of next-generation plasmonic devices that can be fabricated using NIL. In addition, the multiresonance plasmonic device consisting the 'long' nanorods structure proposed in Chapter 6 shows a promising performance as a state-of-the-art optical security device once it comes to a realisation. Furthermore, from fabrication point-of-view, the nanofluidics behaviour of polymer resist during imprinting presented in Chapter 4 can be further explored to produce more complicated three-dimensional plasmonic structures with interesting optical properties.

9.1.1 Summary of Research Outcomes

This thesis has demonstrated the utilisation and versatility of nanoimprinting lithography (NIL) as a scalable technique for producing plasmonic devices. Notable contributions to knowledge emerging from this research are summarised as below:

1. Development of novel multilevel NIL in producing 3-dimensional structures (in addition to 2-dimensional) via harnessing the nanofluidics dynamics of the resist using only a binary mould. (Chapter 4)
2. Demonstration of the utilisation of multilevel NIL as a method for printing of plasmonic colouration devices with gap-tunable hue and saturation. (Chapter 5 and reference [84])
3. A proposal for a novel multispectral, polarisation selective, iridescent plasmonic pixels with an IR signature for potential optical security features. (Chapter 6)
4. Development and fabrication of a novel polarisation independent scalable plasmonic colour device comprising symmetric cross-shaped structure to preserve the vividness of the colours under ambient light. (Chapter 7)
5. Demonstration of scalable production of plasmonic colour devices using NIL. (Chapter 5 and Chapter 7)
6. Development of a process sheet for conventional and multilevel NIL process for future references. (Chapter 4 and Appendix Figure A2)

Appendices

A Nanoimprint Lithography (NIL) Process Optimisation

Periodicity, P_x	**100**	**140**	**180**	**220**	**260**	**300**
Cavity Width, W	50	90	130	170	210	250
Mean Imprint Height, h_i	65.2	77.2	88.9	103.6	115.2	134.1
Std. Dev. of h_i	2.86	4.09	4.75	3.87	2.97	4.94

TABLE A1: Table showing the vertical dimension before metal coating i.e imprint height, h_i of the imprinted structure with various periodicities and cavity widths obtained from cross-sectional SEM images.

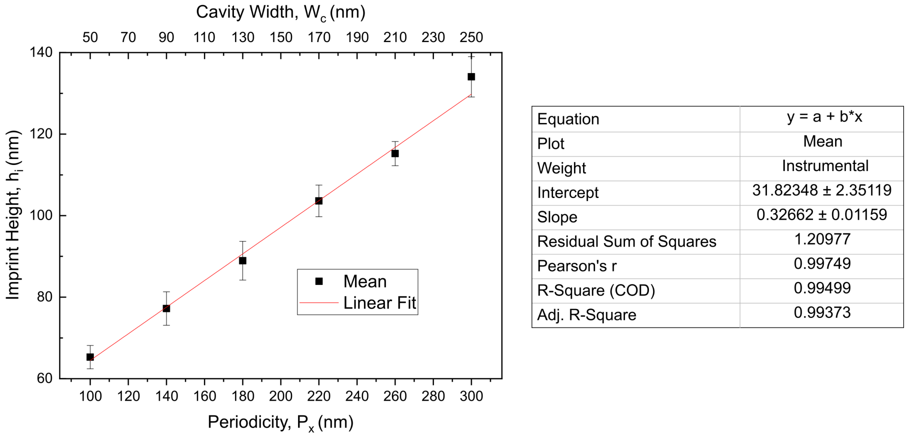

Equation	y = a + b*x
Plot	Mean
Weight	Instrumental
Intercept	31.82348 ± 2.35119
Slope	0.32662 ± 0.01159
Residual Sum of Squares	1.20977
Pearson's r	0.99749
R-Square (COD)	0.99499
Adj. R-Square	0.99373

FIGURE A1: The linear fit plots of the mean imprint height, h_i as function of periodicity, P_x and cavity width, W_c. Tables at right hand side shows the detail of analysis of the plots.

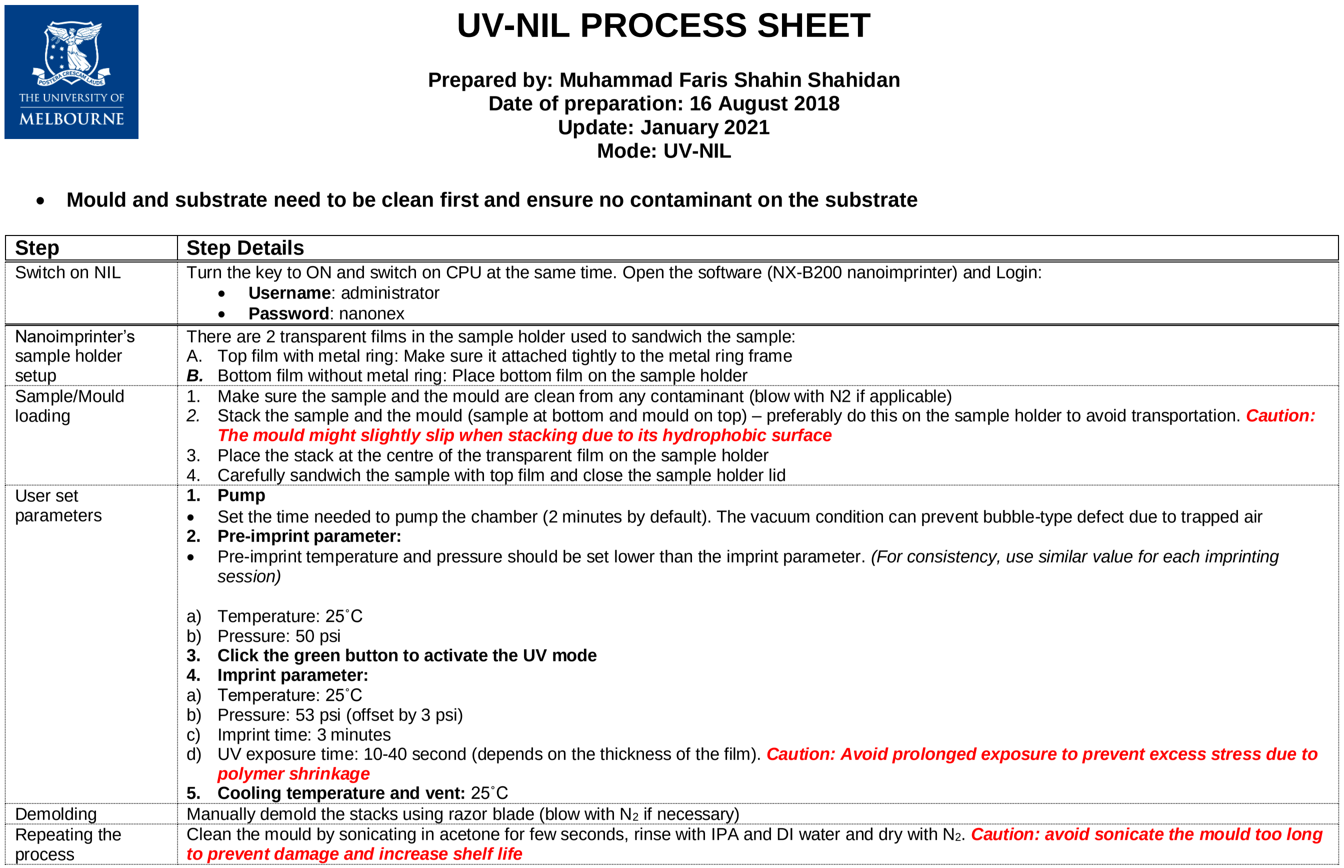

UV-NIL PROCESS SHEET

Prepared by: Muhammad Faris Shahin Shahidan
Date of preparation: 16 August 2018
Update: January 2021
Mode: UV-NIL

- **Mould and substrate need to be clean first and ensure no contaminant on the substrate**

Step	**Step Details**
Switch on NIL	Turn the key to ON and switch on CPU at the same time. Open the software (NX-B200 nanoimprinter) and Login: • **Username**: administrator • **Password**: nanonex
Nanoimprinter's sample holder setup	There are 2 transparent films in the sample holder used to sandwich the sample: A. Top film with metal ring: Make sure it attached tightly to the metal ring frame ***B.*** Bottom film without metal ring: Place bottom film on the sample holder
Sample/Mould loading	1. Make sure the sample and the mould are clean from any contaminant (blow with N2 if applicable) *2.* Stack the sample and the mould (sample at bottom and mould on top) – preferably do this on the sample holder to avoid transportation. ***Caution: The mould might slightly slip when stacking due to its hydrophobic surface*** 3. Place the stack at the centre of the transparent film on the sample holder 4. Carefully sandwich the sample with top film and close the sample holder lid
User set parameters	**1. Pump** • Set the time needed to pump the chamber (2 minutes by default). The vacuum condition can prevent bubble-type defect due to trapped air **2. Pre-imprint parameter:** • Pre-imprint temperature and pressure should be set lower than the imprint parameter. *(For consistency, use similar value for each imprinting session)* a) Temperature: 25˚C b) Pressure: 50 psi **3. Click the green button to activate the UV mode** **4. Imprint parameter:** a) Temperature: 25˚C b) Pressure: 53 psi (offset by 3 psi) c) Imprint time: 3 minutes d) UV exposure time: 10-40 second (depends on the thickness of the film). ***Caution: Avoid prolonged exposure to prevent excess stress due to polymer shrinkage*** **5. Cooling temperature and vent:** 25˚C
Demolding	Manually demold the stacks using razor blade (blow with N_2 if necessary)
Repeating the process	Clean the mould by sonicating in acetone for few seconds, rinse with IPA and DI water and dry with N_2. ***Caution: avoid sonicate the mould too long to prevent damage and increase shelf life***

Figure A2: Nanoimprint lithography process sheet developed after process optimisation for future reference.

B Multilevel Nanoimprint Lithography (NIL) for Plasmonic Colour Printing

Periodicity, P_x	**100**	**140**	**180**	**220**	**260**	**300**
Cavity Width, W	50	90	130	170	210	250
Mean Gap Size, g	15.2	27.2	39.0	53.6	65.5	84.6
Std. Dev. of g	2.86	4.09	4.46	3.87	3.08	4.65

TABLE B1: Table showing the vertical dimension after metal coating i.e vertical gap size, g of the structure with various periodicities and cavity widths obtained from cross-sectional SEM images.

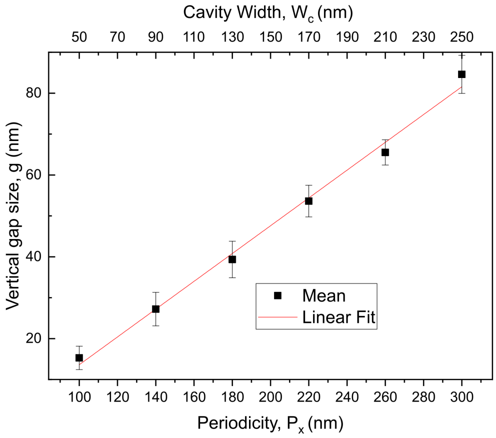

Equation	y = a + b*x
Plot	Mean
Weight	No Weighting
Intercept	-20.37114 ± 2.87136
Slope	0.33981 ± 0.01359
Residual Sum of Squares	20.67324
Pearson's r	0.99682
R-Square (COD)	0.99365
Adj. R-Square	0.99206

FIGURE B1: The linear fit plots of the mean gap size, g as function of periodicity, P_x and cavity width, W_c. Tables at right hand side shows the detail of analysis of the plots.

C Polarisation-selective, Multispectral, Iridescent Plasmonic Pixels

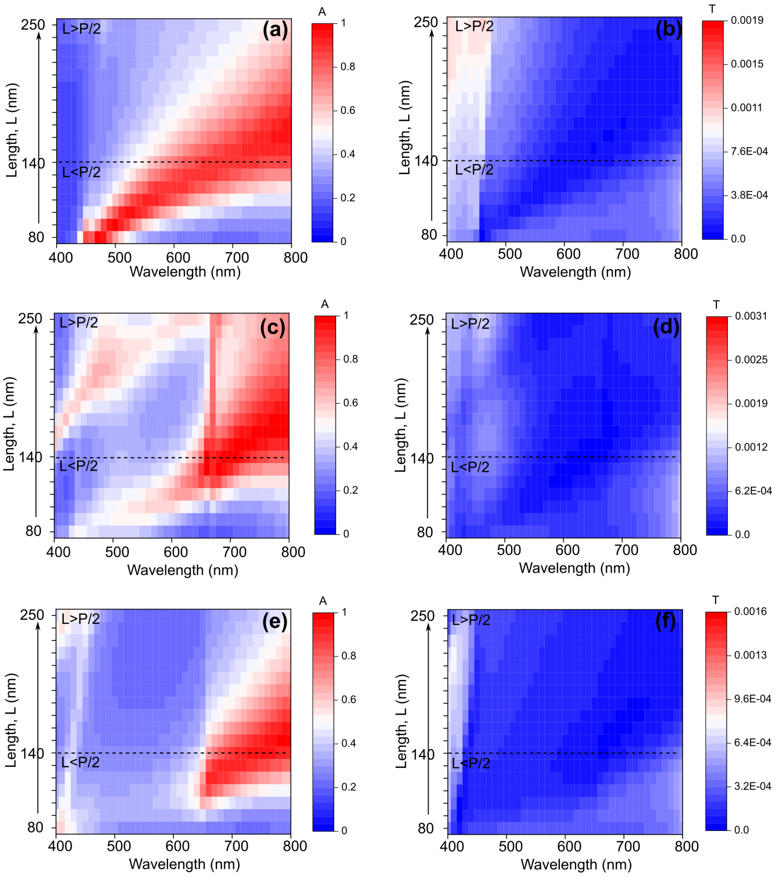

FIGURE C1: The simulated absorption map as function of nanorod's length in the visible region ($\lambda = 400 - 800$ nm), for three different illumination conditions namely (a) normal incidence, (c) TM and (e) TE polarisation. The simulated transmittance map as function of nanorod's length in the visible region ($\lambda = 400 - 800$ nm), for three different illumination conditions namely (b) normal incidence, (d) TM and (f) TE polarisation. The plot is divided into two regions correspond to the length, L i.e $L < P/2$ and $L > P/2$ (these regions are delineated by a dashed line).

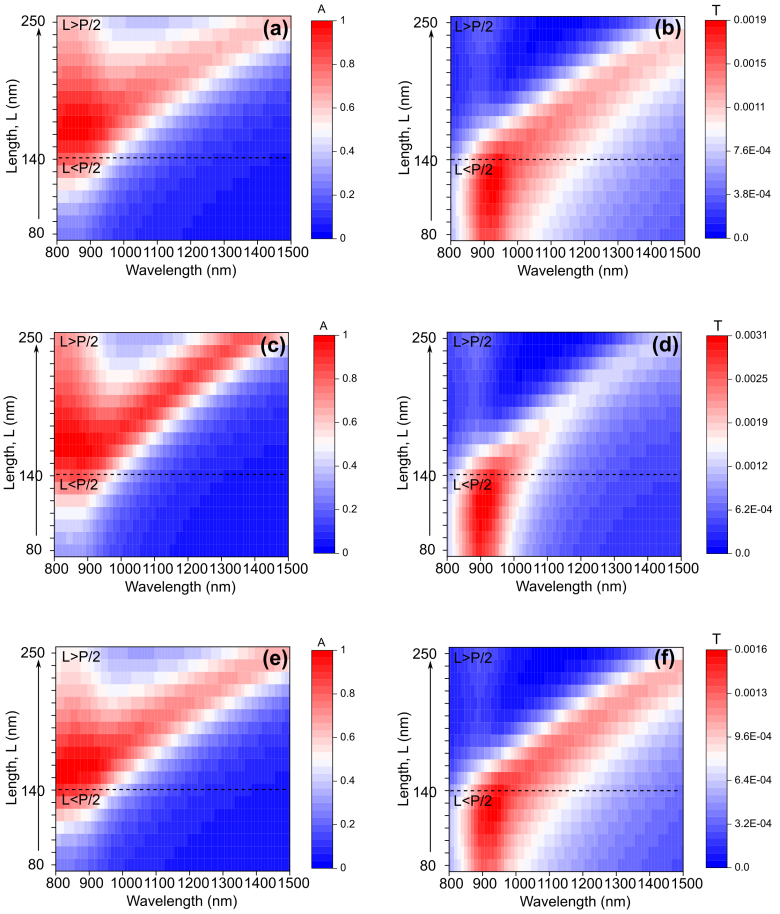

FIGURE C2: The simulated absorption map as function of nanorod's length in the near infrared (NIR) region ($\lambda = 800 - 1500$ nm), for three different illumination conditions namely (a) normal incidence, (c) TM and (e) TE polarisation. The simulated transmittance map as function of nanorod's length in the NIR region, for three different illumination conditions namely (b) normal incidence, (d) TM and (f) TE polarisation. The plot is divided into two regions correspond to the length, L i.e $L < P/2$ and $L > P/2$ (these regions are delineated by a dashed line).

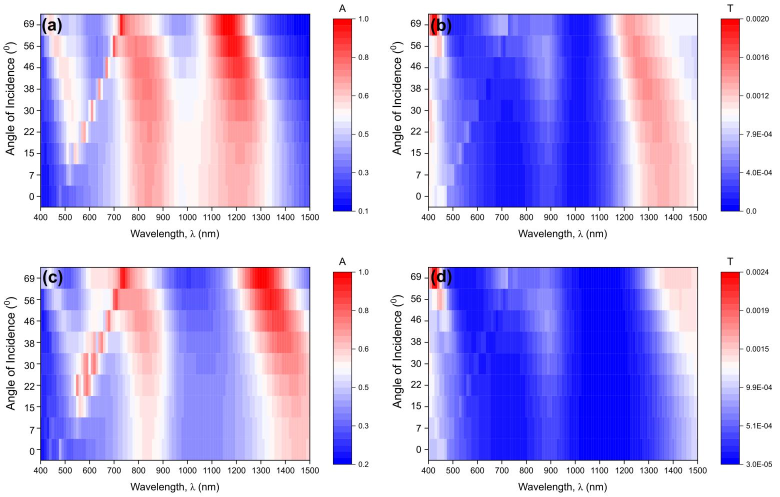

Figure C3: The simulated absorption and transmittance maps as function of angle of incidence for nanorods in square lattice with length, L of (a,b) 220 nm and (c,d) 250 nm respectively, under TM polarised light with wavelength spanning the visible ($\lambda = 400 - 800$ nm) and near infrared (NIR) region ($\lambda = 800 - 1500$ nm).

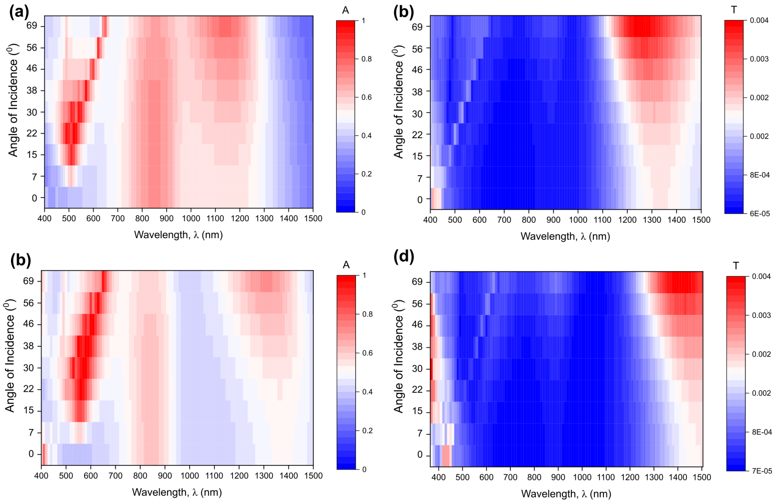

Figure C4: The simulated absorption and transmittance maps as function of angle of incidence for nanorods in hexagonal lattice with length, L of (a,b) 220 nm and (c,d) 250 nm respectively, under TM polarised light with wavelength spanning the visible ($\lambda = 400 - 800$ nm) and near infrared (NIR) region ($\lambda = 800 - 1500$ nm).

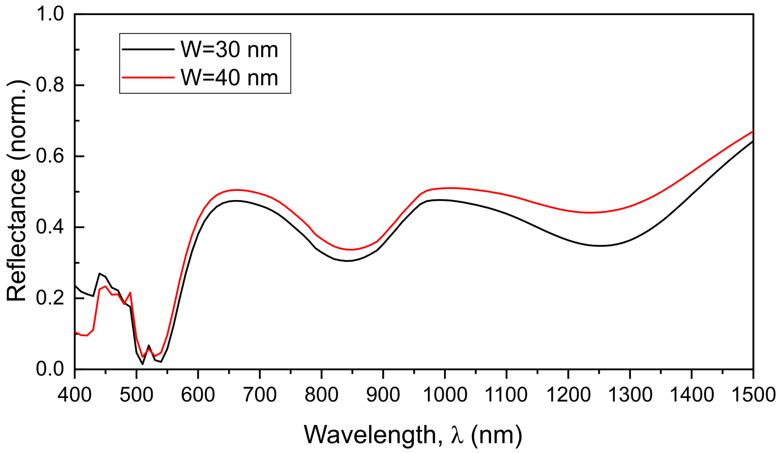

FIGURE C5: The simulated reflectance spectra of the 'long' nanorod with length of $L = 220$ nm with different widths, W, arranged in a hexagonal array, illuminated by TM polarised light at 46° angle of incidence.

D Vivid Polarisation Independent Plasmonic Colour

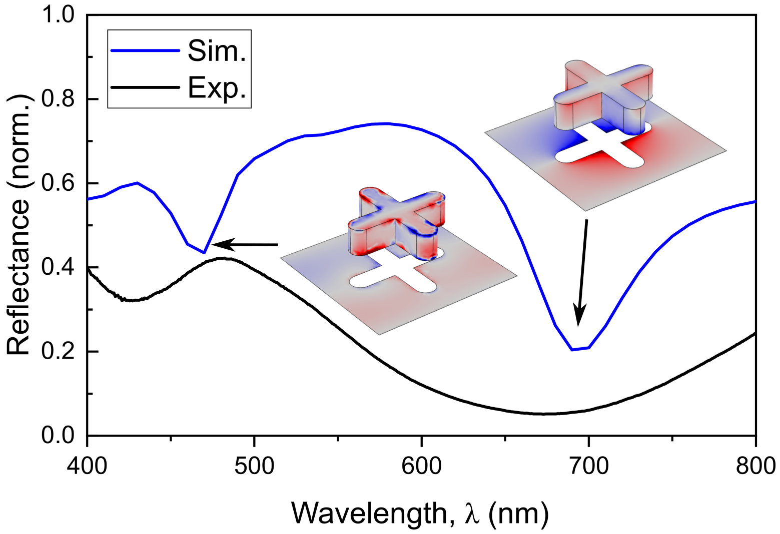

FIGURE D1: Simulated and measured reflectance spectra for a cross-shaped nanostructures with length of L =160 nm showing two distinct minimum at $\lambda = 470$ nm and $\lambda = 690$ nm. Insets show the normalised surface charge density plot corresponds to the resonance wavelengths.

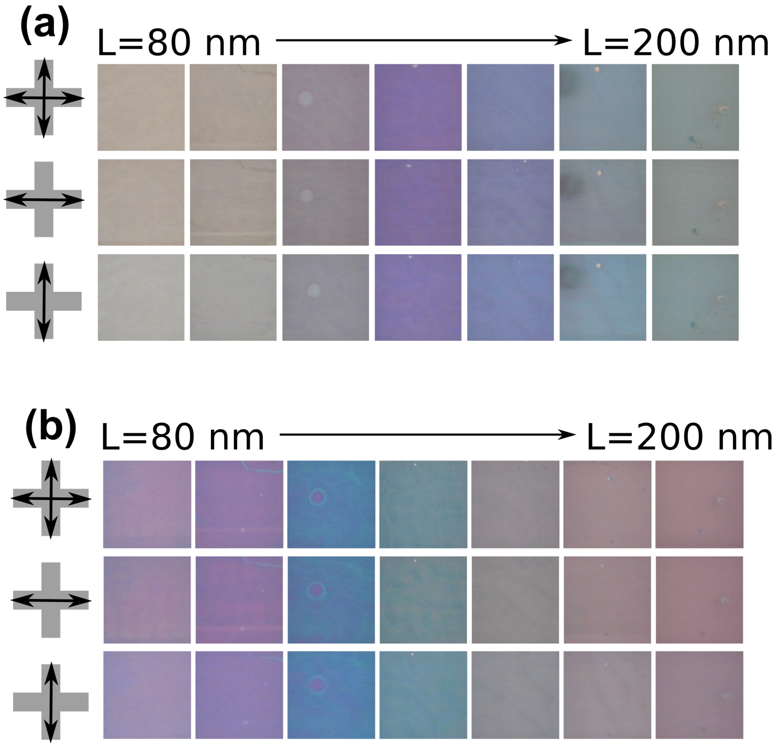

FIGURE D2: Optical images of the colour swatches produced by the (a) Al and (b) Au 'cross' plasmonic pixels of various armlength, illuminated under unpolarised and linearly polarised light.

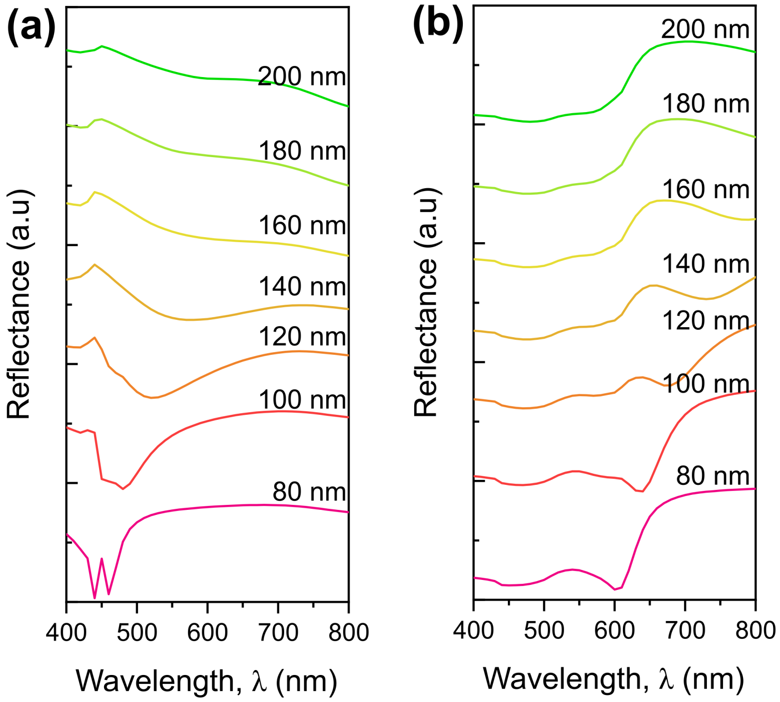

FIGURE D3: Simulated reflectance spectra of the (a) Al and (b) Au cross-shaped plasmonic structure with different armlength under unpolarised light.

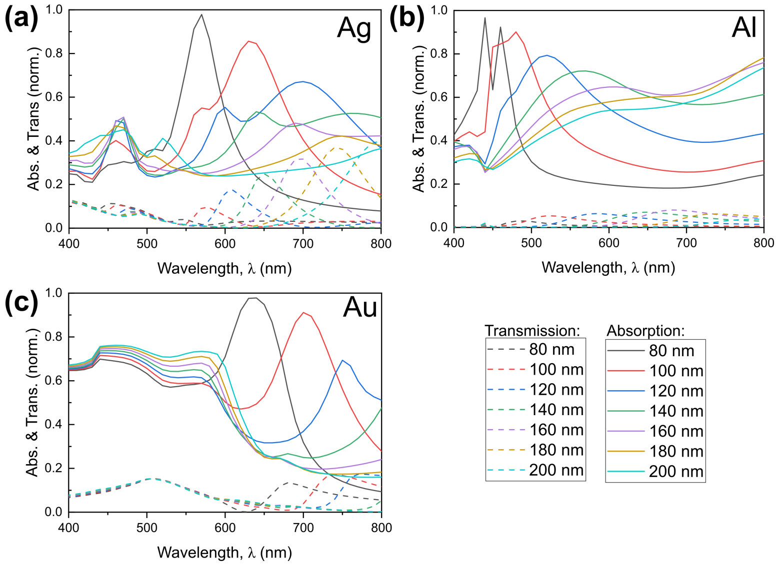

FIGURE D4: Simulated absorption (solid lines) and transmission (dashed lines) spectra of the (a) Ag, (b) Al and (c) Au cross-shaped plasmonic structure with different armlength under unpolarised light.

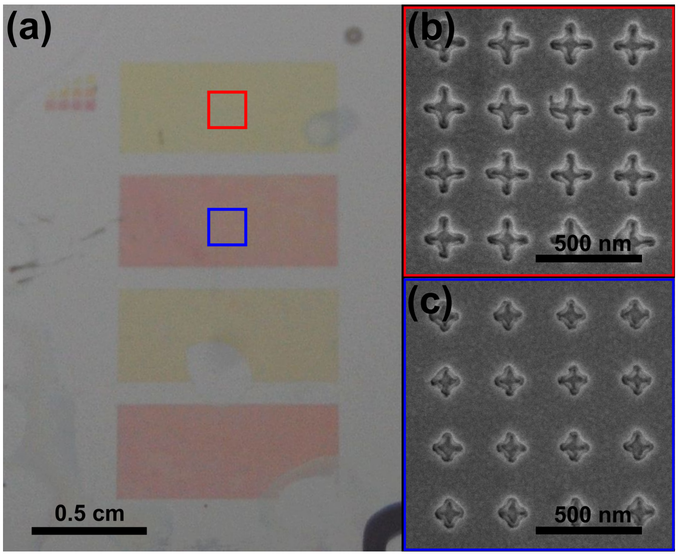

FIGURE D5: (a) Optical image of large area plasmonic pixels produced by NIL consisting symmetric cross-shaped structures with length of (b) $L = 200$ nm and (c) $L = 140$ nm.

E Future Directions

E.1 Nanoimprinted Colourimetric Sensor for Refractive Index Sensing

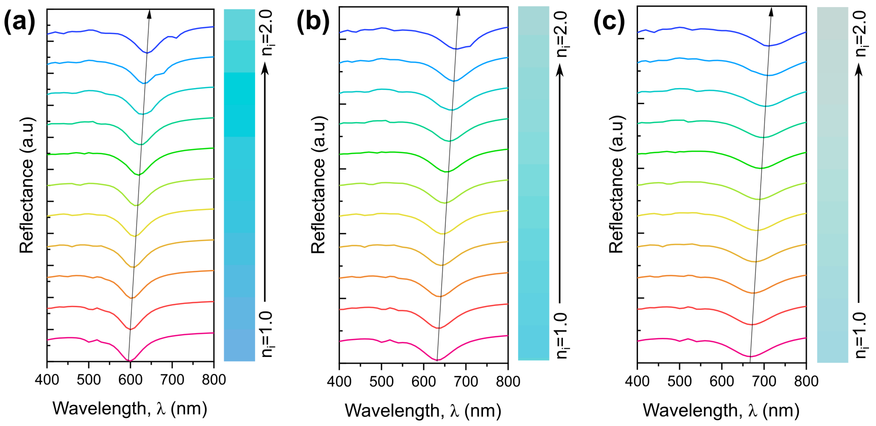

FIGURE E1: Calculated reflectance spectra for Ag based refractive index sensor device consisting nanorod with length, L of (a) L =75 nm, (b) L =85 nm and (c) L =95 nm as function of refractive index of analyte, n_i. Insets are the simulated colour swatches corresponds to the reflectance spectra.

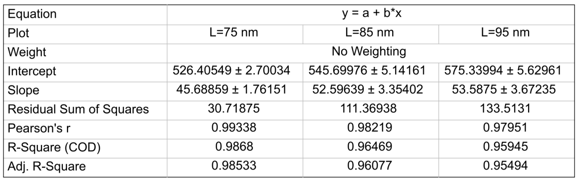

Equation	y = a + b*x		
Plot	L=75 nm	L=85 nm	L=95 nm
Weight	No Weighting		
Intercept	526.40549 ± 2.70034	545.69976 ± 5.14161	575.33994 ± 5.62961
Slope	45.68859 ± 1.76151	52.59639 ± 3.35402	53.5875 ± 3.67235
Residual Sum of Squares	30.71875	111.36938	133.5131
Pearson's r	0.99338	0.98219	0.97951
R-Square (COD)	0.9868	0.96469	0.95945
Adj. R-Square	0.98533	0.96077	0.95494

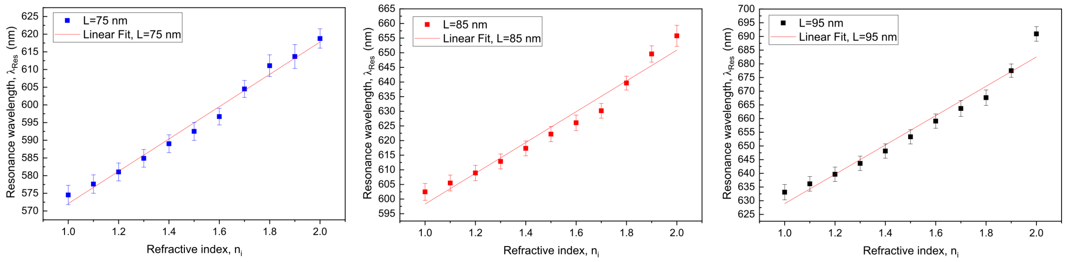

FIGURE E2: The linear fit plots of the resonance wavelengths as function of analyte's refractive index, n_i for Ag-based device consisting nanorod with length, L =75 nm (left), L =85 nm (middle) and L =95 nm (right). Table on the top shows the detail of analysis of the plots.

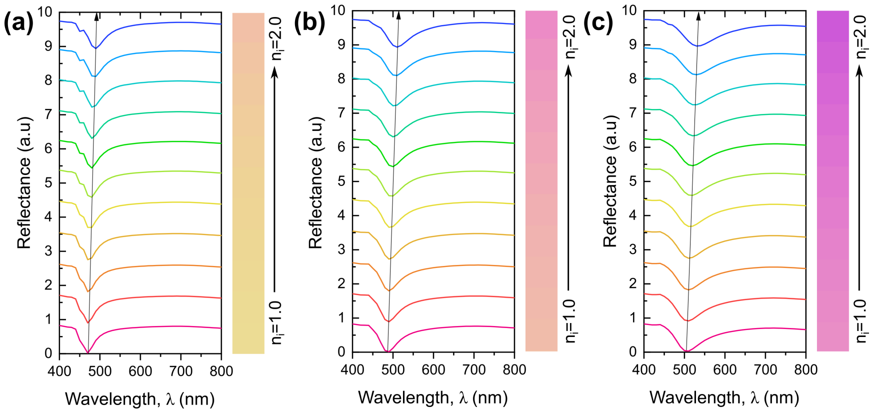

FIGURE E3: Calculated reflectance spectra for Al based refractive index sensor device consisting nanorod with length, L of (a) L =85 nm, (b) L =95 nm and (c) L =105 nm as function of refractive index of analyte, n_i. Insets are the simulated colour swatches corresponds to the reflectance spectra.

Equation	y = a + b*x		
Plot	L=85 nm	L=95 nm	L=105 nm
Weight	No Weighting		
Intercept	441.82334 ± 1.84283	457.52229 ± 1.82515	474.15058 ± 1.92964
Slope	22.26397 ± 1.20213	25.28869 ± 1.1906	28.79542 ± 1.25876
Residual Sum of Squares	14.30663	14.03342	15.68628
Pearson's r	0.98713	0.99017	0.99151
R-Square (COD)	0.97443	0.98044	0.98309
Adj. R-Square	0.97159	0.97827	0.98121

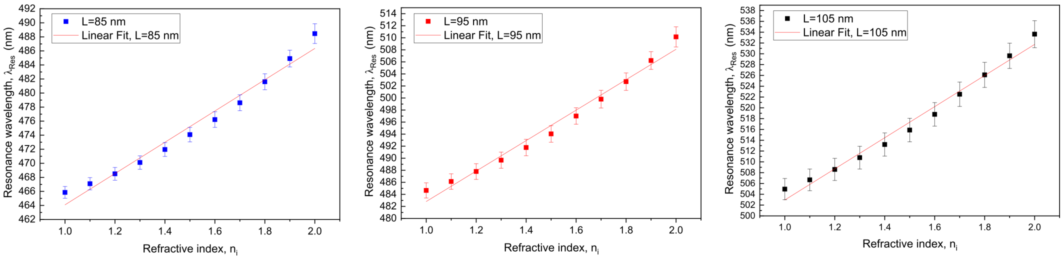

FIGURE E4: The linear fit plots of the resonance wavelengths as function of analyte's refractive index, n_i for Al-based device consisting nanorod with length, L =85 nm (left), L =95 nm (middle) and L =105 nm (right). Table on the top shows the detail of analysis of the plots.

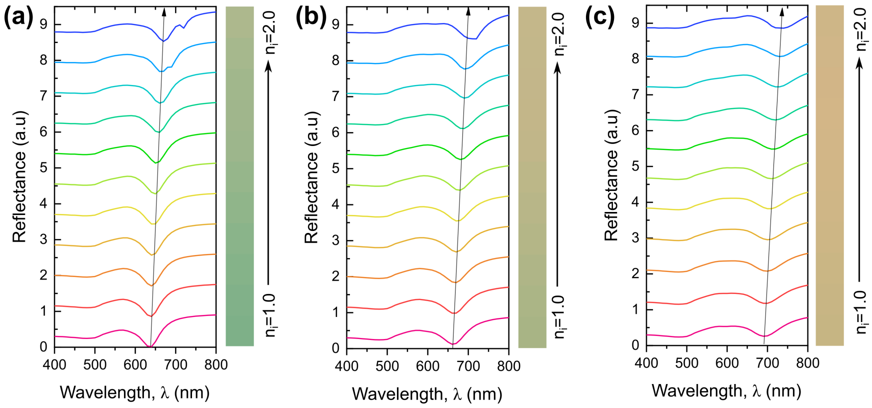

FIGURE E5: Calculated reflectance spectra for Au based refractive index sensor device consisting nanorod with length, L of (a) L =75 nm, (b) L =85 nm and (c) L =95 nm as function of refractive index of analyte, n_i. Insets are the simulated colour swatches corresponds to the reflectance spectra.

Equation	y = a + b*x		
Plot	L=75 nm	L=85 nm	L=95 nm
Weight	No Weighting		
Intercept	570.88958 ± 1.83638	584.76818 ± 4.88272	595.02273 ± 6.78925
Slope	37.58595 ± 1.19792	44.82727 ± 3.18513	55.84545 ± 4.42882
Residual Sum of Squares	14.20666	100.43627	194.18282
Pearson's r	0.99546	0.97803	0.97285
R-Square (COD)	0.99094	0.95654	0.94643
Adj. R-Square	0.98993	0.95171	0.94048

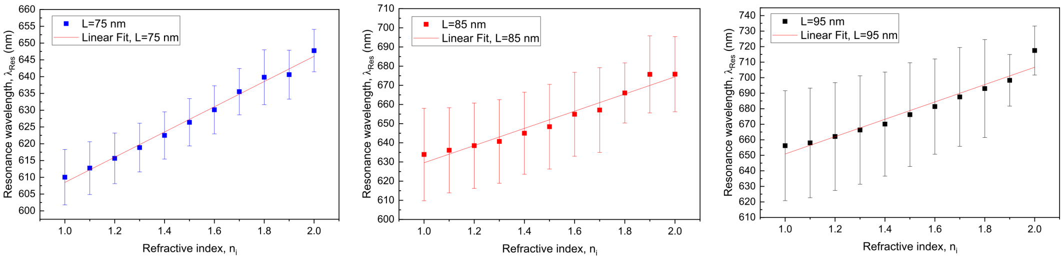

FIGURE E6: The linear fit plots of the resonance wavelengths as function of analyte's refractive index, n_i for Au-based device consisting nanorod with length, L =75 nm (left), L =85 nm (middle) and L =95 nm (right). Table on the top shows the detail of analysis of the plots.

Bibliography

[1] Hou-Tong Chen, Antoinette J Taylor, and Nanfang Yu. A review of metasurfaces: physics and applications. *Reports on Progress in Physics*, 79(7):076401, 2016.

[2] Nina Meinzer, William L Barnes, and Ian R Hooper. Plasmonic meta-atoms and metasurfaces. *Nature Photonics*, 8(12):889–898, 2014.

[3] Viktor G Veselago. The electrodynamics of substances with simultaneously negative values of ϵ and μ. *Soviet Physics Uspekhi*, 10(4):509, 1968.

[4] Bo Xiong, Lin Deng, Ruwen Peng, and Yongmin Liu. Controlling the degrees of freedom in metasurface designs for multi-functional optical devices. *Nanoscale Advances*, 1(10):3786–3806, 2019.

[5] Yang Zhao, Xing-Xiang Liu, and Andrea Alù. Recent advances on optical metasurfaces. *Journal of Optics*, 16(12):123001, 2014.

[6] Wei Zhou and Teri W Odom. Tunable subradiant lattice plasmons by out-of-plane dipolar interactions. *Nature Nanotechnology*, 6(7):423–427, 2011.

[7] G Vecchi, V Giannini, and J Gómez Rivas. Shaping the fluorescent emission by lattice resonances in plasmonic crystals of nanoantennas. *Physical Review Letters*, 102(14):146807, 2009.

[8] Nanfang Yu, Patrice Genevet, Mikhail A Kats, Francesco Aieta, Jean-Philippe Tetienne, Federico Capasso, and Zeno Gaburro. Light propagation with phase discontinuities: generalized laws of reflection and refraction. *Science*, 334(6054): 333–337, 2011.

[9] Manuel Decker, Nils Feth, Costas M Soukoulis, Stefan Linden, and Martin Wegener. Retarded long-range interaction in split-ring-resonator square arrays. *Physical Review B*, 84(8):085416, 2011.

[10] Michael Christian Gwinner, Elisabeth Koroknay, Liwei Fu, Piotr Patoka, Witold Kandulski, Michael Giersig, and Harald Giessen. Periodic large-area metallic split-ring resonator metamaterial fabrication based on shadow nanosphere lithography. *Small*, 5(3):400–406, 2009.

[11] Andrey E Nikolaenko, Francesco De Angelis, Stuart A Boden, Nikitas Papasimakis, Peter Ashburn, Enzo Di Fabrizio, and Nikolay I Zheludev. Carbon nanotubes in a photonic metamaterial. *Physical Review Letters*, 104(15):153902, 2010.

[12] Wei Wu, Evgenia Kim, Ekaterina Ponizovskaya, Yongmin Liu, Zhaoning Yu, Nicholas Fang, Y Ron Shen, Alexander M Bratkovsky, William Tong, Cheng Sun, et al. Optical metamaterials at near and mid-ir range fabricated by nanoimprint lithography. *Applied Physics A*, 87(2):143–150, 2007.

[13] Mehdi Hedayati and Mady Elbahri. Review of metasurface plasmonic structural color. *Plasmonics*, pages 1–17, 2016. ISSN 1557-1955. doi: 10.1007/s11468-016-0407-y. URL `http://dx.doi.org/10.1007/s11468-016-0407-y`.

[14] Anders Kristensen, Joel KW Yang, Sergey I Bozhevolnyi, Stephan Link, Peter Nordlander, Naomi J Halas, and N Asger Mortensen. Plasmonic colour generation. *Nature Reviews Materials*, 2:16088, 2016.

[15] Timothy D James, Paul Mulvaney, and Ann Roberts. The plasmonic pixel: large area, wide gamut color reproduction using aluminum nanostructures. *Nano Letters*, 16(6):3817–3823, 2016.

[16] Jeppe S Clausen, Emil Højlund-Nielsen, Alexander B Christiansen, Sadegh Yazdi, Meir Grajower, Hesham Taha, Uriel Levy, Anders Kristensen, and N Asger Mortensen. Plasmonic metasurfaces for coloration of plastic consumer products. *Nano Letters*, 14(8):4499–4504, 2014.

[17] Maowen Song, Di Wang, Samuel Peana, Sajid Choudhury, Piotr Nyga, Zhaxylyk A Kudyshev, Honglin Yu, Alexandra Boltasseva, Vladimir M Shalaev, and Alexander V Kildishev. Colors with plasmonic nanostructures: A full-spectrum review. *Applied Physics Reviews*, 6(4):041308, 2019.

[18] Ahu Gümrah Dumanli and Thierry Savin. Recent advances in the biomimicry of structural colours. *Chemical Society Reviews*, 45(24):6698–6724, 2016.

[19] Yulan Fu, Cary A Tippets, Eugenii U Donev, and Rene Lopez. Structural colors: from natural to artificial systems. *Wiley Interdisciplinary Reviews: Nanomedicine and Nanobiotechnology*, 8(5):758–775, 2016.

[20] Yuanjin Zhao, Zhuoying Xie, Hongcheng Gu, Cun Zhu, and Zhongze Gu. Bio-inspired variable structural color materials. *Chemical Society Reviews*, 41(8):3297–3317, 2012.

[21] Jiyu Sun, Bharat Bhushan, and Jin Tong. Structural coloration in nature. *RSC Advances*, 3(35):14862–14889, 2013.

[22] Stephanie L Burg and Andrew J Parnell. Self-assembling structural colour in nature. *Journal of Physics: Condensed Matter*, 30(41):413001, 2018.

[23] S. Kinoshita, S. Yoshioka, and J. Miyazaki. Physics of structural colors. *Reports on Progress in Physics*, 71(7):076401, 2008. ISSN 0034-4885 1361-6633. doi: 10.1088/0034-4885/71/7/076401.

[24] Palmer Christopher and E Loewen. Diffraction grating handbook. *Newport Corporation*, pages 67–69, 2005.

[25] Heather M Whitney, Mathias Kolle, Piers Andrew, Lars Chittka, Ullrich Steiner, and Beverley J Glover. Floral iridescence, produced by diffractive optics, acts as a cue for animal pollinators. *Science*, 323(5910):130–133, 2009.

[26] Abigail L Ingram, Virginie Lousse, Andrew R Parker, and Jean Pol Vigneron. Dual gratings interspersed on a single butterfly scale. *Journal of the Royal Society Interface*, 5(28):1387–1390, 2008.

[27] TL Tan, D Wong, and Paul Lee. Iridescence of a shell of mollusk haliotis glabra. *Optics Express*, 12(20):4847–4854, 2004.

[28] Thomas F Anderson and A Glenn Richards Jr. An electron microscope study of some structural colors of insects. *Journal of Applied Physics*, 13(12):748–758, 1942.

[29] Ainsley E Seago, Parrish Brady, Jean-Pol Vigneron, and Tom D Schultz. Gold bugs and beyond: a review of iridescence and structural colour mechanisms in beetles (coleoptera). *Journal of the Royal Society Interface*, 6(suppl_2):S165–S184, 2009.

[30] Matija Crne, Vivek Sharma, Jung O Park, and Mohan Srinivasarao. Structural origin of circularly polarized iridescence in jeweled beetles. *APS*, 2010:D17–002, 2010.

[31] Doekele G Stavenga, Hein L Leertouwer, N Justin Marshall, and Daniel Osorio. Dramatic colour changes in a bird of paradise caused by uniquely structured breast feather barbules. *Proceedings of the Royal Society B: Biological Sciences*, 278 (1715):2098–2104, 2011.

[32] Stéphanie M Doucet, Matthew D Shawkey, Geoffrey E Hill, and Robert Montgomerie. Iridescent plumage in satin bowerbirds: structure, mechanisms and nanostructural predictors of individual variation in colour. *Journal of Experimental Biology*, 209(2):380–390, 2006.

[33] MH Amiri and Huda M Shaheen. Chromatophores and color revelation in the blue variant of the siamese fighting fish (betta splendens). *Micron*, 43(2-3):159–169, 2012.

[34] Shinya Yoshioka, B Matsuhana, S Tanaka, Y Inouye, N Oshima, and S Kinoshita. Mechanism of variable structural colour in the neon tetra: quantitative evaluation of the venetian blind model. *Journal of the Royal Society Interface*, 8(54):56–66, 2011.

[35] Daniel J Brink, Nic G van der Berg, and Andre J Botha. Iridescent colors on seashells: an optical and structural investigation of helcion pruinosus. *Applied Optics*, 41(4):717–722, 2002.

[36] DJ Brink and NG Van Der Berg. An investigation of green iridescence on the mollusc patella granatina. *Journal of Physics D: Applied Physics*, 38(2):338, 2005.

[37] Lydia M Mäthger, Eric J Denton, N Justin Marshall, and Roger T Hanlon. Mechanisms and behavioural functions of structural coloration in cephalopods. *Journal of the Royal Society Interface*, 6(suppl_2):S149–S163, 2009.

[38] Silvia Vignolini, Paula J Rudall, Alice V Rowland, Alison Reed, Edwige Moyroud, Robert B Faden, Jeremy J Baumberg, Beverley J Glover, and Ullrich Steiner. Pointillist structural color in pollia fruit. *Proceedings of the National Academy of Sciences*, 109(39):15712–15715, 2012.

[39] Sunil Mehla, Jagannath Das, Deshetti Jampaiah, Selvakannan Periasamy, Ayman Nafady, and Suresh K Bhargava. Recent advances in preparation methods for catalytic thin films and coatings. *Catalysis Science & Technology*, 9(14):3582–3602, 2019.

[40] Joanna Aizenberg, Vikram C Sundar, Andrew D Yablon, James C Weaver, and Gang Chen. Biological glass fibers: correlation between optical and structural properties. *Proceedings of the National Academy of Sciences*, 101(10):3358–3363, 2004.

[41] Joanna Aizenberg and Gordon Hendler. Designing efficient microlens arrays: lessons from nature. *Journal of Materials Chemistry*, 14(14):2066–2072, 2004.

[42] Victoria Welch, Jean Pol Vigneron, Virginie Lousse, and Andrew Parker. Optical properties of the iridescent organ of the comb-jellyfish beroë cucumis (ctenophora). *Physical Review E*, 73(4):041916, 2006.

[43] Andrew R Parker, Ross C McPhedran, David R McKenzie, Lindsay C Botten, and Nicolae-Alexandru P Nicorovici. Aphrodite's iridescence. *Nature*, 409(6816): 36–37, 2001.

[44] Shinya Yoshioka and Shuichi Kinoshita. Effect of macroscopic structure in iridescent color of the peacock feathers. *FORMA-TOKYO-*, 17(2):169–181, 2002.

[45] Eunok Lee, Hang Lee, Junpei Kimura, and Shoei Sugita. Feather microstructure of the black-billed magpie (pica pica sericea) and jungle crow (corvus macrorhynchos). *Journal of Veterinary Medical Science*, pages 1003030180–1003030180, 2010.

[46] Victoria Welch, Virginie Lousse, Olivier Deparis, Andrew Parker, and Jean Pol Vigneron. Orange reflection from a three-dimensional photonic crystal in the scales of the weevil pachyrrhynchus congestus pavonius (curculionidae). *Physical Review E*, 75(4):041919, 2007.

[47] Emil Højlund-Nielsen, Jeppe Clausen, Tapio Mäkela, Lasse Højlund Thamdrup, Maksim Zalkovskij, Theodor Nielsen, Nello Li Pira, Jouni Ahopelto, N Asger Mortensen, and Anders Kristensen. Plasmonic colors: toward mass production of metasurfaces. *Advanced Materials Technologies*, 1(7):1600054, 2016.

[48] Stefan A. Maier. *Plasmonics: Fundamentals and Applications*. Springer. Springer, New York, 1 edition, 2007. ISBN 978-0387-33150-8. URL http://scholar.google.com/scholar?q=Plasmonics:FundamentalsandApplications&btnG=&hl=en&num=20&as_sdt=0%2C22.

[49] Phillip Manley. *Simulation of Plasmonic Nanoparticles in Thin Film Solar Cells*. PhD thesis, Department of Physics, Freie Universitat Berlin, 7 2016.

[50] S. D. Rezaei, J. Ho, R. J. H. Ng, S. Ramakrishna, and J. K. W. Yang. On the correlation of absorption cross-section with plasmonic color generation. *Optics Express*, 25(22):27652–27664, 2017. ISSN 1094-4087 (Electronic) 1094-4087 (Linking). doi: 10.1364/OE.25.027652. URL https://www.ncbi.nlm.nih.gov/pubmed/29092236.

[51] Ian Freestone, Nigel Meeks, Margaret Sax, and Catherine Higgitt. The lycurgus cup — a roman nanotechnology. *Gold Bulletin*, 40(4):270–277, 2007. doi: https://doi.org/10.1007/BF03215599.

[52] G Ali Mansoori and TA Fauzi Soelaiman. Nanotechnology—an introduction for the standards community. *Journal of ASTM International*, 2(6):1–22, 2005.

[53] Gilles Lérondel, Sergei Kostcheev, and Jérôme Plain. Nanofabrication for plasmonics. In *Plasmonics*, pages 269–316. Springer, 2012.

[54] Joel Henzie, Jeunghoon Lee, Min Hyung Lee, Warefta Hasan, and Teri W Odom. Nanofabrication of plasmonic structures. *Annual Review of Physical Chemistry*, 60, 2009.

[55] Soroosh Daqiqeh Rezaei, Zhaogang Dong, John You En Chan, Jonathan Trisno, Ray Jia Hong Ng, Qifeng Ruan, Cheng-Wei Qiu, N Asger Mortensen, and Joel KW Yang. Nanophotonic structural colors. *ACS Photonics*, 2020.

[56] Min Gu, Xiangping Li, and Yaoyu Cao. Optical storage arrays: a perspective for future big data storage. *Light: Science & Applications*, 3(5):e177–e177, 2014.

[57] Peter Zijlstra, James WM Chon, and Min Gu. Five-dimensional optical recording mediated by surface plasmons in gold nanorods. *Nature*, 459(7245):410–413, 2009.

[58] Søren Raza, Cristian Lavieja, Xiaolong Zhu, and Anders Kristensen. Resonant laser printing of bi-material metasurfaces: from plasmonic to photonic optical response. *Optics Express*, 26(16):20203–20210, 2018.

[59] Karthik Kumar, Huigao Duan, Ravi S Hegde, Samuel CW Koh, Jennifer N Wei, and Joel KW Yang. Printing colour at the optical diffraction limit. *Nature Nanotechnology*, 7(9):557–561, 2012.

[60] SOROOSH DAQIQEH REZAEI. *Structural Colors For Plasmonic Color Prints, Analyte Sensing, And Display Technologies*. PhD thesis, Department of Mechanical Engineering, National University of Singapore, 8 2019.

[61] HL Liu, Bing Zhang, Tian Gao, Xijun Wu, Fayi Cui, and Wei Xu. 3d chiral color prints for anti-counterfeiting. *Nanoscale*, 11(12):5506–5511, 2019.

[62] Kevin TP Lim, Hailong Liu, Yejing Liu, and Joel KW Yang. Holographic colour prints for enhanced optical security by combined phase and amplitude control. *Nature Communications*, 10(1):1–8, 2019.

[63] Ray Jia Hong Ng, Ravikumar Venkat Krishnan, Zhaogang Dong, Jinfa Ho, Hailong Liu, Qifeng Ruan, Kin Leong Pey, and Joel KW Yang. Micro-tags for art: covert visible and infrared images using gap plasmons in native aluminum oxide. *Optical Materials Express*, 9(2):788–801, 2019.

[64] Jin Xiang, Jingdong Chen, Sheng Lan, and Andrey E Miroshnichenko. Nanoscale optical display and sensing based on the modification of fano lineshape. *Advanced Optical Materials*, page 2000489, 2020.

[65] Bo Xiao, Sangram K. Pradhan, Kevin C. Santiago, Gugu N. Rutherford, and Aswini K. Pradhan. Enhanced optical transmission and fano resonance through a nanostructured metal thin film. *Scientific Reports*, 5(1):10393, 2015. doi: 10.1038/srep10393. URL http://dx.doi.org/10.1038/srep10393.

[66] Bo Xiao, Sangram K. Pradhan, Kevin C. Santiago, Gugu N. Rutherford, and Aswini K. Pradhan. Topographically engineered large scale nanostructures for plasmonic biosensing. *Scientific Reports*, 6(1):24385, 2016. ISSN 2045-2322. doi: 10.1038/srep24385. URL http://dx.doi.org/10.1038/srep24385.

[67] Xiao Goh, Ray Ng, Sihao Wang, Shawn J. Tan, and Joel K. W. Yang. Comparative study of plasmonic colors from all-metal structures of posts and pits. *ACS Photonics*, 3(6):1000–1009, 2016. ISSN 2330-4022. doi: 10.1021/acsphotonics.6b00099. URL http://dx.doi.org/10.1021/acsphotonics.6b00099.

[68] Zhigang Li, Wei Wang, Daniel Rosenmann, David A Czaplewski, Xiaodong Yang, and Jie Gao. All-metal structural color printing based on aluminum plasmonic metasurfaces. *Optics Express*, 24(18):20472–20480, 2016.

[69] Richard Bartholomew, Calum Williams, Ammar Khan, Richard Bowman, and Timothy Wilkinson. Plasmonic nanohole electrodes for active color tunable liquid crystal transmissive pixels. *Optics Letters*, 42(14):2810–2813, 2017.

[70] Q Chen, D Das, D Chitnis, K Walls, TD Drysdale, S Collins, and DRS Cumming. A cmos image sensor integrated with plasmonic colour filters. *Plasmonics*, 7(4):695–699, 2012.

[71] Zhibo Li, Alasdair W Clark, and Jonathan M Cooper. Dual color plasmonic pixels create a polarization controlled nano color palette. *ACS Nano*, 10(1):492–498, 2016.

[72] Eugeniu Balaur, Catherine Sadatnajafi, Shan Shan Kou, Jiao Lin, and Brian Abbey. Continuously tunable, polarization controlled, colour palette produced from nanoscale plasmonic pixels. *Scientific Reports*, 6:28062, 2016.

[73] Tal Ellenbogen, Kwanyong Seo, and Kenneth B Crozier. Chromatic plasmonic polarizers for active visible color filtering and polarimetry. *Nano Letters*, 12(2):1026–1031, 2012.

[74] XL Hu, LB Sun, Beibei Zeng, LS Wang, ZG Yu, SA Bai, SM Yang, LX Zhao, Q Li, M Qiu, et al. Polarization-independent plasmonic subtractive color filtering in ultrathin silver nanodisks with high transmission. *Applied Optics*, 55(1):148–152, 2016.

[75] Claudio U Hail, Gabriel Schnoering, Mehdi Damak, Dimos Poulikakos, and Hadi Eghlidi. A plasmonic painter's method of color mixing for a continuous red–green–blue palette. *ACS Nano*, 14(2):1783–1791, 2020.

[76] Masashi Miyata, Hideaki Hatada, and Junichi Takahara. Full-color subwavelength printing with gap-plasmonic optical antennas. *Nano Letters*, 16(5):3166–3172, 2016. ISSN 1530-6984. doi: 10.1021/acs.nanolett.6b00500. URL `http://dx.doi.org/10.1021/acs.nanolett.6b00500`.

[77] Alexander S. Roberts, Anders Pors, Ole Albrektsen, and Sergey I. Bozhevolnyi. Subwavelength plasmonic color printing protected for ambient use. *Nano Letters*, 14(2):783–787, 2014. ISSN 1530-6984. doi: 10.1021/nl404129n. URL `http://dx.doi.org/10.1021/nl404129n`.

[78] Vivek R Shrestha, Sang-Shin Lee, Eun-Soo Kim, and Duk-Yong Choi. Aluminum plasmonics based highly transmissive polarization-independent subtractive color filters exploiting a nanopatch array. *Nano Letters*, 14(11):6672–6678, 2014.

[79] Renilkumar Mudachathi and Takuo Tanaka. Up scalable full colour plasmonic pixels with controllable hue, brightness and saturation. *Scientific Reports*, 7, 2017.

[80] Shawn J Tan, Lei Zhang, Di Zhu, Xiao Ming Goh, Ying Min Wang, Karthik Kumar, Cheng-Wei Qiu, and Joel KW Yang. Plasmonic color palettes for photo-realistic printing with aluminum nanostructures. *Nano Letters*, 14(7):4023–4029, 2014.

[81] Xiao Ming Goh, Yihan Zheng, Shawn J Tan, Lei Zhang, Karthik Kumar, Cheng-Wei Qiu, and Joel KW Yang. Three-dimensional plasmonic stereoscopic prints in full colour. *Nature Communications*, 5:5361, 2014.

[82] Hao Wang, Xiaolong Wang, Chen Yan, Hua Zhao, Jingwen Zhang, Christian Santschi, and Olivier JF Martin. Full color generation using silver tandem nanodisks. *ACS Nano*, 2017.

[83] Masashi Miyata, Hideaki Hatada, and Junichi Takahara. Full-color subwavelength printing with gap-plasmonic optical antennas. *Nano Letters*, 16(5):3166–3172, 2016. ISSN 1530-6984. doi: 10.1021/acs.nanolett.6b00500. URL `http://dx.doi.org/10.1021/acs.nanolett.6b00500`.

[84] Muhammad Faris Shahin Shahidan, Jingchao Song, Timothy D James, and Ann Roberts. Multilevel nanoimprint lithography with a binary mould for plasmonic colour printing. *Nanoscale Advances*, 2020.

[85] Tingbiao Guo, Julian Evans, Nan Wang, and Sailing He. Monolithic chip-scale structural color filters fabricated with simple uv lithography. *Optics Express*, 27 (15):21646–21651, 2019.

[86] Wei Hong, Zhongke Yuan, and Xudong Chen. Structural color materials for optical anticounterfeiting. *Small*, 16(16):1907626, 2020.

[87] Heykel Aouani, Oussama Mahboub, Eloïse Devaux, Hervé Rigneault, Thomas W Ebbesen, and Jérôme Wenger. Plasmonic antennas for directional sorting of fluorescence emission. *Nano Letters*, 11(6):2400–2406, 2011.

[88] Maowen Song, Xiong Li, Mingbo Pu, Yinghui Guo, Kaipeng Liu, Honglin Yu, Xiaoliang Ma, and Xiangang Luo. Color display and encryption with a plasmonic polarizing metamirror. *Nanophotonics*, 7(1):323–331, 2018.

[89] Swathi Murthy, Henrik Pranov, Nikolaj A Feidenhans, Jonas S Madsen, Poul Erik Hansen, Henrik C Pedersen, and Rafael Taboryski. Plasmonic color metasurfaces fabricated by a high speed roll-to-roll method. *Nanoscale*, 9(37):14280–14287, 2017.

[90] Mark D Fairchild. *Color appearance models.* John Wiley & Sons, 2013.

[91] Brand Fortner and Theodore E Meyer. *Number by colors: a guide to using color to understand technical data.* Springer Science & Business Media, 2012.

[92] Angelo V. Arecchi, Tahar Messadi, and R. John Koshel. *Field Guide to Illumination.* Society of Photo-Optical Instrumentation Engineers (SPIE), USA, 2007. ISBN 0819467685.

[93] James M Palmer. The measurement of transmission, absorption, emission, and reflection. *Handbook of Optics*, 2:25–1, 1995.

[94] Linda Shapiro. *Computer vision and image processing.* Academic Press, 1992.

[95] Alexander D Logvinenko. The color cone. *Journal of the Optical Society of America A*, 32(2):314–322, 2015.

[96] David L MacAdam. Color-matching functions. In *Color Measurement*, pages 178–199. Springer, 1981.

[97] Chris Wyman, Peter-Pike Sloan, and Peter Shirley. Simple analytic approximations to the cie xyz color matching functions. *Journal of Computer Graphics Techniques*, 2(2):1–11, 2013.

[98] C Poynton. The cie system of colorimetry. *Digital Video and HDTV: Algorithms and Interfaces*, pages 211–231, 2003.

[99] Max K.. Agoston. *Computer Graphics and Geometric Modeling: Implementation and Algorithms*. Springer, 2005.

[100] Tieling Chen, Jun Ma, and Zhongmin Deng. Attributes of color represented by a spherical model. *Journal of Electronic Imaging*, 22(4):043032, 2013.

[101] Sujan Kasani, Kathrine Curtin, and Nianqiang Wu. A review of 2d and 3d plasmonic nanostructure array patterns: fabrication, light management and sensing applications. *Nanophotonics*, 8(12):2065–2089, 2019.

[102] Vin-Cent Su, Cheng Hung Chu, Greg Sun, and Din Ping Tsai. Advances in optical metasurfaces: fabrication and applications. *Optics Express*, 26(10):13148–13182, 2018.

[103] KS Moore. Euv lithography finally ready for chip manufacturing. *IEEE Spectrum*, 5, 2018.

[104] L Jay Guo. Nanoimprint lithography: methods and material requirements. *Advanced Materials*, 19(4):495–513, 2007.

[105] Hiroshi Hiroshima. Nanoimprint with thin and uniform residual layer for various pattern densities. *Microelectronic Engineering*, 86(4-6):611–614, 2009.

[106] Woo Kyung Jung and Kyung Min Byun. Fabrication of nanoscale plasmonic structures and their applications to photonic devices and biosensors. *Biomedical Engineering Letters*, 1(3):153, 2011.

[107] Asim Jilani, Mohamed Shaaban Abdel-Wahab, and Ahmed Hosny Hammad. Advance deposition techniques for thin film and coating. *Modern Technologies for Creating the Thin-film Systems and Coatings*, 2:137–149, 2017.

[108] Heyou Zhang, Yawei Liu, Muhammad Faris Shahin Shahidan, Calum Kinnear, Fatemeh Maasoumi, Jasper Cadusch, Eser Metin Akinoglu, Timothy D James, Asaph Widmer-Cooper, Ann Roberts, et al. Direct assembly of vertically oriented, gold nanorod arrays. *Advanced Functional Materials*, page 2006753, 2020.

[109] Malika Ammam. Electrophoretic deposition under modulated electric fields: a review. *RSC Advances*, 2(20):7633–7646, 2012.

[110] Stephen Y Chou, Peter R Krauss, and Preston J Renstrom. Nanoimprint lithography. *Journal of Vacuum Science & Technology B: Microelectronics and Nanometer Structures Processing, Measurement, and Phenomena*, 14(6):4129–4133, 1996.

[111] Helmut Schift, Christian Spreu, Arne Schleunitz, Jens Gobrecht, Anna Klukowska, Freimut Reuther, and Gabi Gruetzner. Easy mask-mold fabrication for combined nanoimprint and photolithography. *Journal of Vacuum Science & Technology B: Microelectronics and Nanometer Structures Processing, Measurement, and Phenomena*, 27(6):2850–2853, 2009.

[112] Helmut Schift. Nanoimprint lithography: An old story in modern times? a review. *Journal of Vacuum Science & Technology B: Microelectronics and Nanometer Structures Processing, Measurement, and Phenomena*, 26(2):458–480, 2008.

[113] Ariadna Fernández, Juan Medina, Christian Benkel, Markus Guttmann, Brian Bilenberg, Lasse H Thamdrup, Theodor Nielsen, Clivia M Sotomayor Torres, and Nikolaos Kehagias. Residual layer-free reverse nanoimprint lithography on silicon and metal-coated substrates. *Microelectronic Engineering*, 141:56–61, 2015.

[114] MM Alkaisi, W Jayatissa, and M Konijn. Multilevel nanoimprint lithography. *Current Applied Physics*, 4(2-4):111–114, 2004.

[115] Arne Schleunitz, Christian Spreu, Marko Vogler, Hakan Atasoy, and Helmut Schift. Combining nanoimprint lithography and a molecular weight selective thermal reflow for the generation of mixed 3d structures. *Journal of Vacuum Science & Technology B, Nanotechnology and Microelectronics: Materials, Processing, Measurement, and Phenomena*, 29(6):06FC01, 2011.

[116] Sung-Won Youn, Kenta Suzuki, and Hiroshi Hiroshima. Chip-scale pattern modification method for equalizing residual layer thickness in nanoimprint lithography. *Japanese Journal of Applied Physics*, 57(6S1):06HG03, 2018.

[117] Nezih Pala and Mustafa Karabiyik. Electron beam lithography (ebl). *Encyclopedia of Nanotechnology*, pages 718–740, 2012.

[118] Anushka S Gangnaik, Yordan M Georgiev, and Justin D Holmes. New generation electron beam resists: a review. *Chemistry of Materials*, 29(5):1898–1917, 2017.

[119] Alongkorn Pimpin and Werayut Srituravanich. Review on micro-and nanolithography techniques and their applications. *Engineering Journal*, 16(1):37–56, 2012.

[120] Chenxi Wang and Tadatomo Suga. Investigation of fluorine containing plasma activation for room-temperature bonding of si-based materials. *Microelectronics Reliability*, 52(2):347–351, 2012.

[121] Chang Kun Kang, Sang Min Lee, Im Deok Jung, Phill Gu Jung, Sung Jin Hwang, and Jong Soo Ko. The fabrication of patternable silicon nanotips using deep reactive ion etching. *Journal of Micromechanics and Microengineering*, 18(7): 075007, 2008.

[122] Kevin M McPeak, Sriharsha V Jayanti, Stephan JP Kress, Stefan Meyer, Stelio Iotti, Aurelio Rossinelli, and David J Norris. Plasmonic films can easily be better: Rules and recipes. *ACS Photonics*, 2(3):326–333, 2015.

[123] Shideh Ahmadi, Nilofar Asim, MA Alghoul, FY Hammadi, Kasra Saeedfar, Norasikin Ahmad Ludin, Saleem H Zaidi, and Kamaruzzaman Sopian. The role of physical techniques on the preparation of photoanodes for dye sensitized solar cells. *International Journal of Photoenergy*, 2014, 2014.

[124] Natasha Erdman, David C. Bell, and Rudolf Reichelt. *Scanning Electron Microscopy*, pages 229–318. Springer International Publishing, Cham, 2019. ISBN 978-3-030-00069-1. doi: 10.1007/978-3-030-00069-1_5. URL `https://doi.org/10.1007/978-3-030-00069-1_5`.

[125] J. Orloff. Focused ion beam characterization techniques. In *Reference Module in Materials Science and Materials Engineering*. Elsevier, 2016. ISBN 978-0-12-803581-8. doi: https://doi.org/10.1016/B978-0-12-803581-8.03523-2. URL `http://www.sciencedirect.com/science/article/pii/B9780128035818035232`.

[126] Reza Shahbazian-Yassar. *Atomic Force Microscopy (AFM)*, pages 129–133. Springer US, Boston, MA, 2013. ISBN 978-0-387-92897-5. doi: 10.1007/978-0-387-92897-5_1213. URL `https://doi.org/10.1007/978-0-387-92897-5_1213`.

[127] Vector Bellitto (ed.). *Atomic Force Microscopy: Imaging, Measuring and Manipulating Surfaces at the Atomic Scale (ed. by Vector Bellitto)*. Intech, 2012. ISBN 978-953-51-0414-8.

[128] Huaiyu Wang and Paul K Chu. Surface characterization of biomaterials. In *Characterization of Biomaterials*, pages 105–174. Elsevier, 2013.

[129] Klaus-Jürgen Bathe. *Finite element procedures*. Klaus-Jurgen Bathe, 2006.

[130] Aleksandar D Rakić, Aleksandra B Djurišić, Jovan M Elazar, and Marian L Majewski. Optical properties of metallic films for vertical-cavity optoelectronic devices. *Applied optics*, 37(22):5271–5283, 1998.

[131] Peter B Johnson and R-WJPrB Christy. Optical constants of the noble metals. *Physical review B*, 6(12):4370, 1972.

[132] Stephen Y Chou, Peter R Krauss, Wei Zhang, Lingjie Guo, and Lei Zhuang. Sub-10 nm imprint lithography and applications. *Journal of Vacuum Science & Technology B: Microelectronics and Nanometer Structures Processing, Measurement, and Phenomena*, 15(6):2897–2904, 1997.

[133] Helmut Schift and Anders Kristensen. Nanoimprint lithography–patterning of resists using molding. In *Springer Handbook of Nanotechnology*, pages 271–312. Springer, 2010.

[134] Minqi Yin, Hongwen Sun, and Haibin Wang. Resist filling study for uv nanoimprint lithography using stamps with various micro/nano ratios. *Micromachines*, 9(7): 335, 2018.

[135] Salvatore P Sutera and Richard Skalak. The history of poiseuille's law. *Annual Review of Fluid Mechanics*, 25(1):1–20, 1993.

[136] Carolyn G Conant, J Tanner Nevill, and Cristian Ionescu-Zanetti. Live cell analysis under shear flow. In *Microfluidic Cell Culture Systems*, pages 357–383. Elsevier, 2013.

[137] Edward W Washburn. The dynamics of capillary flow. *Physical Review*, 17(3): 273, 1921.

[138] Takushi Saito and Hiroshi Ito. Nanopattern transfer technology of thermoplastic materials. *Nanoimprint Technology: Nanotransfer for Thermoplastic and Photocurable Polymers*, pages 17–50, 2013.

[139] Hongwen Sun. Recent progress in low temperature nanoimprint lithography. *Microsystem Technologies*, 21(1):1–7, 2015.

[140] H Schift. Napanil-library of processes. *Berlin: NaPANIL consortium*, 2012.

[141] Zhengmei Yang, Yiqin Chen, Yanming Zhou, Yasi Wang, Peng Dai, Xupeng Zhu, and Huigao Duan. Microscopic interference full-color printing using grayscale-patterned fabry–perot resonance cavities. *Advanced Optical Materials*, 5(10): 1700029, 2017.

[142] Calum Williams, George SD Gordon, Timothy D Wilkinson, and Sarah E Bohndiek. Grayscale-to-color: Scalable fabrication of custom multispectral filter arrays. *ACS Photonics*, 6(12):3132–3141, 2019.

[143] Heon Lee. Effect of imprinting pressure on residual layer thickness in ultraviolet nanoimprint lithography. *Journal of Vacuum Science & Technology B: Microelectronics and Nanometer Structures Processing, Measurement, and Phenomena*, 23 (3):1102–1106, 2005.

[144] Minqi Yin, Hongwen Sun, and Haibin Wang. Effect of stamp design on residual layer thickness and contact pressure in uv nanoimprint lithography. *Micro & Nano Letters*, 13(6):887–891, 2018.

[145] Hayden Taylor and Duane Boning. Towards nanoimprint lithography-aware layout design checking. In *Design for Manufacturability through Design-Process Integration IV*, volume 7641, page 76410U. International Society for Optics and Photonics, 2010.

[146] JiaoRong Fan and WenGang Wu. Metal-dielectric-metal plasmonic nanohelms as broad-color-gamut tunable pixels for vivid display. In *Micro Electro Mechanical Systems (MEMS), 2016 IEEE 29th International Conference on*, pages 226–229. IEEE, 2016.

[147] Timothy D. James, Paul Mulvaney, and Ann Roberts. The plasmonic pixel: Large area, wide gamut color reproduction using aluminum nanostructures. *Nano Letters*, 16(6):3817–3823, 2016. doi: 10.1021/acs.nanolett.6b01250.

[148] Jana Olson, Alejandro Manjavacas, Lifei Liu, Wei-Shun Chang, Benjamin Foerster, Nicholas S King, Mark W Knight, Peter Nordlander, Naomi J Halas, and Stephan Link. Vivid, full-color aluminum plasmonic pixels. *Proceedings of the National Academy of Sciences*, 111(40):14348–14353, 2014.

[149] Fei Cheng, Jie Gao, Ting S. Luk, and Xiaodong Yang. Structural color printing based on plasmonic metasurfaces of perfect light absorption. *Scientific Reports*, 5(1):11045, 2015. doi: 10.1038/srep11045. URL `http://dx.doi.org/10.1038/srep11045http://www.nature.com/articles/srep11045.pdf`.

[150] Emil Prodan, Corey Radloff, Naomi J Halas, and Peter Nordlander. A hybridization model for the plasmon response of complex nanostructures. *Science*, 302 (5644):419–422, 2003.

[151] Yueqiang Hu, Xuhao Luo, Yiqin Chen, Qing Liu, Xin Li, Yasi Wang, Na Liu, and Huigao Duan. 3d-integrated metasurfaces for full-colour holography. *Light: Science & Applications*, 8(1):1–9, 2019.

[152] Yasi Wang, Mengjie Zheng, Qifeng Ruan, Yanming Zhou, Yiqin Chen, Peng Dai, Zhengmei Yang, Zihao Lin, Yuxiang Long, Ying Li, et al. Stepwise-nanocavity-assisted transmissive color filter array microprints. *Research*, 2018:8109054, 2018.

[153] Keith Wilson, Cristian A Marocico, Esteban Pedrueza-Villalmanzo, Christopher Smith, Calin Hrelescu, and A Louise Bradley. Plasmonic colour printing by light trapping in two-metal nanostructures. *Nanomaterials*, 9(7):963, 2019.

[154] Yang Chen, Xiaodong Yang, and Jie Gao. 3d janus plasmonic helical nanoapertures for polarization-encrypted data storage. *Light: Science & Applications*, 8(1):45, 2019.

[155] Wenbin Huang, Xingtao Yu, Yanhua Liu, Wen Qiao, and Linsen Chen. A review of the scalable nano-manufacturing technology for flexible devices. *Frontiers of Mechanical Engineering*, 12(1):99–109, 2017.

[156] L. J. Guo. Nanoimprint lithography: Methods and material requirements. *Advanced Materials*, 19(4):495–513, 2007. doi: 0.1002/adma.200600882.

[157] Andrea Cattoni, Petru Ghenuche, Anne-Marie Haghiri-Gosnet, Dominique Decanini, Jing Chen, Jean-Luc Pelouard, and Stéphane Collin. $\lambda 3/1000$ plasmonic nanocavities for biosensing fabricated by soft uv nanoimprint lithography. *Nano Letters*, 11(9):3557–3563, 2011.

[158] Alexandra Boltasseva. Plasmonic components fabrication via nanoimprint. *Journal of Optics A: Pure and Applied Optics*, 11(11):114001, 2009.

[159] Karthik Kumar, Huigao Duan, Ravi S. Hegde, Samuel C. W. Koh, Jennifer N. Wei, and Joel K. W. Yang. Printing colour at the optical diffraction limit. *Nature Nanotechnology*, 7:557–561, 2012. doi: 10.1038/nnano.2012.128. URL https://www.nature.com/articles/nnano.2012.128.

[160] B. R. Lu, C. Xu, J. Liao, J. Liu, and Y. Chen. High-resolution plasmonic structural colors from nanohole arrays with bottom metal disks. *Optics Letter*, 41(7):1400–3, 2016. ISSN 1539-4794 (Electronic) 0146-9592 (Linking). doi: 10.1364/OL.41.001400. URL https://www.ncbi.nlm.nih.gov/pubmed/27192246.

[161] Jun Taniguchi, Yasuhiro Kamiya, Takeshi Ohsaki, and Nobuji Sakai. Technique for transfer of high-density, high-aspect-ratio nanoscale patterns in uv nanoimprint lithography and measurement of the release force. *Microelectronic Engineering*, 87 (5-8):859–863, 2010.

[162] Achille Francone. *Materials and anti-adhesive issues in UV-NIL*. PhD thesis, Institut National Polytechnique de Grenoble-INPG, 2010.

[163] Ki-Don Kim, Hyo-Joong Kwon, Dae-guen Choi, Jun-Ho Jeong, and Eung-sug Lee. Resist flow behavior in ultraviolet nanoimprint lithography as a function of contact angle with stamp and substrate. *Japanese Journal of Applied Physics*, 47(11R): 8648, 2008.

[164] Sandra Gilles, Matthias Meier, Michael Prömpers, Andre van der Hart, Carsten Kügeler, Andreas Offenhäusser, and Dirk Mayer. Uv nanoimprint lithography with

rigid polymer molds. *Microelectronic Engineering*, 86(4-6):661–664, 2009. ISSN 01679317. doi: 10.1016/j.mee.2008.12.051.

[165] Kentaro Ishibashi, Hiroshi Goto, Jun Mizuno, and Shuichi Shoji. Large-scale atmospheric step-and-repeat uv nanoimprinting. *Journal of Nanotechnology*, 2012, 2012.

[166] Yoshihiko Hirai. Uv-nanoimprint lithography (nil) process simulation. *Journal of Photopolymer Science and Technology*, 23(1):25–32, 2010.

[167] SV Sreenivasan. Nanoimprint lithography steppers for volume fabrication of leading-edge semiconductor integrated circuits. *Microsystems & Nanoengineering*, 3:17075, 2017.

[168] Qing Wang, Hiroshi Hiroshima, Hidemasa Atobe, and Sung-Won Youn. Residual layer uniformity using complementary patterns to compensate for pattern density variation in uv nanoimprint lithography. *Journal of Vacuum Science & Technology B, Nanotechnology and Microelectronics: Materials, Processing, Measurement, and Phenomena*, 28(6):C6M125–C6M129, 2010.

[169] Jingxuan Cai and Wen-Di Li. Modeling of capillary force-induced mold deformation for sub-10 nm uv nanoimprint lithography. *arXiv preprint arXiv:1811.05103*, 2018.

[170] Peng Dai, Yasi Wang, Xupeng Zhu, Huimin Shi, Yiqin Chen, Shi Zhang, Wenhong Yang, Zhiquan Chen, Shumin Xiao, and Huigao Duan. Transmissive structural color filters using vertically coupled aluminum nanohole/nanodisk array with a triangular-lattice. *Nanotechnology*, 29(39):395202, 2018.

[171] Selina Goetz, Martin Bauch, Theodoros Dimopoulos, and Stephan Trassl. Ultrathin sputter-deposited plasmonic silver nanostructures. *Nanoscale Advances*, 2(2): 869–877, 2020.

[172] Luc Duempelmann, Daniele Casari, Angélique Luu-Dinh, Benjamin Gallinet, and Lukas Novotny. Color rendering plasmonic aluminum substrates with angular symmetry breaking. *ACS Nano*, 9(12):12383–12391, 2015.

[173] Kuang-Yu Yang, Ruggero Verre, Jérémy Butet, Chen Yan, Tomasz J Antosiewicz, Mikael Käll, and Olivier JF Martin. Wavevector-selective nonlinear plasmonic metasurfaces. *Nano Letters*, 17(9):5258–5263, 2017.

[174] Daniel Franklin, Sushrut Modak, Abraham Vázquez-Guardado, Alireza Safaei, and Debashis Chanda. Covert infrared image encoding through imprinted plasmonic cavities. *Light: Science & Applications*, 7(1):1–8, 2018.

[175] Chunxiang Sheng, Yidan An, Jun Du, and Xiaofeng Li. Colored radiative cooler under optical tamm resonance. *ACS Photonics*, 6(10):2545–2552, 2019.

[176] Yusai Zhou, Gui Zhao, Jingming Bian, Xiaoli Tian, Xuejun Cheng, Hong Wang, and Hongyu Chen. Multiplexed sers barcodes for anti-counterfeiting. *ACS Applied Materials & Interfaces*, 12(25):28532–28538, 2020.

[177] Yan Cui, In Yee Phang, Yih Hong Lee, Mian Rong Lee, Qi Zhang, and Xing Yi Ling. Multiplex plasmonic anti-counterfeiting security labels based on surface-enhanced raman scattering. *Chemical Communications*, 51(25):5363–5366, 2015.

[178] Yejing Liu, Yih Hong Lee, Mian Rong Lee, Yijie Yang, and Xing Yi Ling. Flexible three-dimensional anticounterfeiting plasmonic security labels: Utilizing z-axis-dependent sers readouts to encode multilayered molecular information. *ACS Photonics*, 4(10):2529–2536, 2017.

[179] Timothy J Davis, Kristy C Vernon, and Daniel E Gómez. Effect of retardation on localized surface plasmon resonances in a metallic nanorod. *Optics Express*, 17 (26):23655–23663, 2009.

[180] Zehui Yong, Dang Yuan Lei, Chi Hang Lam, and Yu Wang. Ultrahigh refractive index sensing performance of plasmonic quadrupole resonances in gold nanoparticles. *Nanoscale Research Letters*, 9(1):187, 2014.

[181] H Ehrenreich, HR Philipp, and B Segall. Optical properties of aluminum. *Physical Review*, 132(5):1918, 1963.

[182] Timothy D James, Paul Mulvaney, and Ann Roberts. The plasmonic pixel: large area, wide gamut color reproduction using aluminum nanostructures. *Nano Letters*, 16(6):3817–3823, 2016.

[183] Xiao Ming Goh, Yihan Zheng, Shawn J Tan, Lei Zhang, Karthik Kumar, Cheng-Wei Qiu, and Joel KW Yang. Three-dimensional plasmonic stereoscopic prints in full colour. *Nature Communications*, 5(1):1–8, 2014.

[184] Alexander S Roberts, Anders Pors, Ole Albrektsen, and Sergey I Bozhevolnyi. Subwavelength plasmonic color printing protected for ambient use. *Nano letters*, 14(2):783–787, 2014.

[185] Soroosh Daqiqeh Rezaei, Jinfa Ho, Ray Jia Hong Ng, Seeram Ramakrishna, and Joel KW Yang. On the correlation of absorption cross-section with plasmonic color generation. *Optics Express*, 25(22):27652–27664, 2017.

[186] Jiancun Zhao, Xiaochang Yu, Xiaoming Yang, Quan Xiang, Huigao Duan, and Yiting Yu. Polarization independent subtractive color printing based on ultrathin hexagonal nanodisk-nanohole hybrid structure arrays. *Optics Express*, 25(19): 23137–23145, 2017.

[187] The all-new lexus lc structural blue edition — lexus europe. https://www.lexus.eu/discover-lexus/lexus-news/lc-structural-blue. (Accessed on 03/03/2021).

[188] Yinghong Gu, Lei Zhang, Joel KW Yang, Swee Ping Yeo, and Cheng-Wei Qiu. Color generation via subwavelength plasmonic nanostructures. *Nanoscale*, 7(15): 6409–6419, 2015.

[189] Ayoung Choe, Jeonghee Yeom, Ravi Shanker, Minsoo P Kim, Saewon Kang, and Hyunhyub Ko. Stretchable and wearable colorimetric patches based on thermoresponsive plasmonic microgels embedded in a hydrogel film. *NPG Asia Materials*, page 1, 2018.

[190] H Nguyen, F Sidiroglou, SF Collins, TJ Davis, A Roberts, and GW Baxter. A localized surface plasmon resonance-based optical fiber sensor with sub-wavelength apertures. *Applied Physics Letters*, 103(19):193116, 2013.

[191] Lisa Plucinski, Manas Ranjan Gartia, William R Arnold, Abid Ameen, Te-Wei Chang, Austin Hsiao, Gang Logan Liu, and Aditi Das. Substrate binding to cytochrome p450-2j2 in nanodiscs detected by nanoplasmonic lycurgus cup arrays. *Biosensors and Bioelectronics*, 75:337–346, 2016.

[192] Edward Mills Purcell. Spontaneous emission probabilities at radio frequencies. In *Confined Electrons and Photons*, pages 839–839. Springer, 1995.

[193] RJ Moerland, HT Rekola, G Sharma, A-P Eskelinen, AI Väkeväinen, and P Törmä. Surface plasmon polariton-controlled tunable quantum-dot emission. *Applied Physics Letters*, 100(22):221111, 2012.

[194] Chaitanya Indukuri, Deepika Chaturvedi, and Jaydeep K Basu. Plasmonic control of spontaneous emission of quantum dots in sub-wavelength photonic templates. *Plasmonics*, 11(3):787–795, 2016.

[195] En Cao, Weihua Lin, Mengtao Sun, Wenjie Liang, and Yuzhi Song. Exciton-plasmon coupling interactions: from principle to applications. *Nanophotonics*, 7 (1):145–167, 2018.

[196] K Tanaka, E Plum, Jun-Yu Ou, Takashi Uchino, and NI Zheludev. Multifold enhancement of quantum dot luminescence in plasmonic metamaterials. *Physical Review Letters*, 105(22):227403, 2010.

[197] Jasper J Cadusch, Evgeniy Panchenko, Nicholas Kirkwood, Timothy D James, Brant C Gibson, Kevin J Webb, Paul Mulvaney, and Ann Roberts. Emission enhancement and polarization of semiconductor quantum dots with nanoimprinted plasmonic cavities: towards scalable fabrication of plasmon-exciton displays. *Nanoscale*, 7(33):13816–13821, 2015.

[198] Mengxin Ren, Mo Chen, Wei Wu, Lihui Zhang, Junku Liu, Biao Pi, Xinzheng Zhang, Qunqing Li, Shoushan Fan, and Jingjun Xu. Linearly polarized light emission from quantum dots with plasmonic nanoantenna arrays. *Nano Letters*, 15(5):2951–2957, 2015.

[199] Hamed Sattari, Alireza R Rashed, Ekmel Ozbay, and Humeyra Caglayan. Bright off-axis directional emission with plasmonic corrugations. *Optics Express*, 25(25): 30827–30842, 2017.

[200] Nitzan Livneh, Moshe G Harats, Shira Yochelis, Yossi Paltiel, and Ronen Rapaport. Efficient collection of light from colloidal quantum dots with a hybrid metal–dielectric nanoantenna. *ACS Photonics*, 2(12):1669–1674, 2015.

[201] Moshe G Harats, Nitzan Livneh, Gary Zaiats, Shira Yochelis, Yossi Paltiel, Efrat Lifshitz, and Ronen Rapaport. Full spectral and angular characterization of highly directional emission from nanocrystal quantum dots positioned on circular plasmonic lenses. *Nano Letters*, 14(10):5766–5771, 2014.

[202] Young Chul Jun, Kevin CY Huang, and Mark L Brongersma. Plasmonic beaming and active control over fluorescent emission. *Nature Communications*, 2:283, 2011.

[203] Heykel Aouani, Oussama Mahboub, Nicolas Bonod, Eloïse Devaux, Evgeny Popov, Hervé Rigneault, Thomas W Ebbesen, and Jérôme Wenger. Bright unidirectional fluorescence emission of molecules in a nanoaperture with plasmonic corrugations. *Nano Letters*, 11(2):637–644, 2011.

[204] A Femius Koenderink, Andrea Alu, and Albert Polman. Nanophotonics: shrinking light-based technology. *Science*, 348(6234):516–521, 2015.

[205] Jon A Schuller, Edward S Barnard, Wenshan Cai, Young Chul Jun, Justin S White, and Mark L Brongersma. Plasmonics for extreme light concentration and manipulation. *Nature Materials*, 9(3):193, 2010.

[206] Shobhit K Patel and Christos Argyropoulos. Plasmonic nanoantennas: enhancing light-matter interactions at the nanoscale. *arXiv preprint arXiv:1511.03140*, 2015.

[207] Hamza A Abudayyeh and Ronen Rapaport. Quantum emitters coupled to circular nanoantennas for high-brightness quantum light sources. *Quantum Science and Technology*, 2(3):034004, 2017.

[208] Dan Wang, Dan Wu, Di Dong, Wei Chen, Junjie Hao, Jing Qin, Bing Xu, Kai Wang, and Xiaowei Sun. Polarized emission from cspbx 3 perovskite quantum dots. *Nanoscale*, 8(22):11565–11570, 2016.

[209] Anders Lundskog, Chih-Wei Hsu, K Fredrik Karlsson, Supaluck Amloy, Daniel Nilsson, Urban Forsberg, Per Olof Holtz, and Erik Janzén. Direct generation of linearly polarized photon emission with designated orientations from site-controlled ingan quantum dots. *Light: Science & Applications*, 3(1):e139, 2014.

[210] Clara I Osorio, Abbas Mohtashami, and A Femius Koenderink. K-space polarimetry of bullseye plasmon antennas. *Scientific Reports*, 5:9966, 2015.